ABSTRACT

Title of dissertation: OPTICAL LATTICES AND
                              QUANTUM DEGENERATE ^{87}RB
                              IN REDUCED DIMENSIONS

                              John Howard Huckans
                              Doctor of Philosophy, 2006

Dissertation directed by: Professor William D. Phillips
                              Dr. James V. Porto
                              Department of Physics

This dissertation is about the physics of dilute gaseous Bose-Einstein condensates (BECs) confined to lower dimensions by optical lattices. The central theme of the effects of reduced dimensionality is explored within various one-dimensional (1D) and two-dimensional (2D) systems. We create a 2D BEC by adiabatically increasing the confinement of a trapping potential in one direction to the point where motion in that direction is frozen out. Doing this in two directions, we create a 1D BEC. Two experiments examine the ground state properties of a 1D and 2D system. In the 1D system (Chap. 9), a reduction in three-body recombination signals an increase in correlation resulting in a partial "fermionization" of the Bose gas. In the 2D system (Chap. 8), we measure temperature-dependent condensate phase fluctuations in the vicinity of the Berezinskii-Kosterlitz-Thouless transition.

Other experiments investigate dynamic properties of reduced dimension systems. Strongly inhibited transport of a 1D gas in a lattice is observed in one ex-

periment (Chap. 9). Another 2D experiment measures suppressed collisional decay rates due to the reduced dimensionality (Chap. 9). A final experiment (Chap. 7) examines quantum/classical correspondence in the effectively 1D dynamics of a 3D BEC. The dynamics is effectively 1D in the sense that the experiment is over before motion in the radial directions (which are *not* frozen out) can occur.

This dissertation also describes the design and implementation of a novel 1D "accordion lattice" (Chaps. 5-6) which greatly facilitated the Berezinskii-Kosterlitz-Thouless experiment, the quantum/classical correspondence experiment, and a "superlattice" experiment conducted to assist in the calibration of the accordion lattice.

OPTICAL LATTICES AND QUANTUM DEGENERATE ^{87}RB IN REDUCED DIMENSIONS

by

John Howard Huckans

Dissertation submitted to the Faculty of the Graduate School of the
University of Maryland, College Park in partial fulfillment
of the requirements for the degree of
Doctor of Philosophy
2006

Advisory Commmittee:

Professor William D. Phillips, Chair/Advisor
Dr. James V. Porto, Co-Advisor
Professor Wendell T. Hill
Professor Bei-Lok B. Hu
Professor Christopher J. Lobb
Professor Stephen L. Rolston

DEDICATION

οικος

לביתי

para mi familia

ACKNOWLEDGMENTS

I want to first thank Bill Phillips for inviting me to be a part of his Laser Cooling and Trapping familiy. Thanks also to my co-advisor, Trey Porto and the other members of the Laser Cooling and Trapping "central committee" : Kris Helmerson, Paul Lett, Steve Rolston and its newest member Ian Spielman. I have benefitted from a steady stream of talented postdocs flowing through the laboratory who were always willing to share knowledge and insight, most notably Bruno Laburthe Tolra, Ken O'Hara, and Chad Fertig. I am also very lucky that Ennio Arimondo was here for my final year.

My greatest source of strength is, of course, my family. And, I never would have been able to return to graduate school after working in industry for fourteen years and succeed without the constant love, support and encouragement of Debbie.

TABLE OF CONTENTS

x

xi

Chapter 1

Introduction

Bose-Einstein condensation (BEC) in a dilute atomic gas was first achieved at JILA in Boulder, Colorado in 1995 in the group of Carl Weiman and Eric Cornell [1]. First predicted by Albert Einstein [18–21], who was generalizing the work of Satyendra Nath Bose [22], its creation was a watershed event in atomic physics. BEC has enabled the exploration of fundamental quantum mechanical issues using systems that are accessible and highly flexible. The use of lasers to create periodic light shift potentials (standing waves of light or "optical lattices") for atoms in a BEC has permitted many fascinating condensed matter-analog experiments in which the experimentalist has exquisite control over properties such as the geometry of the lattice potential, its strength, disorder, and periodicity. This has opened up a new era of research to atomic, molecular, and optical physicists allowing detailed investigations into the many-body properties of quantum mechanical systems. The ease and speed with which we can spatially and temporally modulate laser light intensity and polarization can be exploited to allow us to explore the ground state properties as well as the dynamics of the atoms in the lattice with unprecedented precision.

1.1   3D BEC in a Uniform, Ideal Gas

The phenomenon of Bose-Einstein condensation was first described theoretically for ideal (non-interacting) bosons in a uniform potential. However, the first realization of a gaseous BEC occurred with weakly interacting bosons in a three-dimensional (3D) harmonic trap. Given these differences, it is remarkable how closely the initial experiments can be understood in terms of the early theory. Unlike a classical phase transition, BEC does not rely on atom-atom interaction for its occurrence. It is a result that depends only on Bose statistics and the density of states of the system. Its explanation for an ideal Bose gas in a uniform (also referred to as homogeneous) potential is contained in many statistical mechanics textbooks [31]. A brief explanation of the theory in 3D along the lines of Ref [31] follows.

Consider N non-interacting indistinguishable bosons, each with mass M, in thermodynamic equilibrium at temperature T. The average occupation n_i of an energy level with energy ϵ_i is easiest to calculate in the grand canonical ensemble. According to Bose statistics, it is

$$n_i = \frac{1}{e^{(\epsilon_i - \mu)/k_B T} - 1},$$

(1.1)

where k_B is Boltzmann's constant and μ is the chemical potential. The chemical potential can be thought of as a Lagrange multiplier whose value changes with temperature in such a way as to keep the average total number of particles, determined

by summing over all energy level occupations, equal to N.

$$N = \sum_i n_i. \tag{1.2}$$

If we consider the energy of the lowest level to be zero, we see that μ must be negative to avoid a negative occupation of the lowest level at finite T. In addition, as the temperature decreases toward zero, it is apparent that μ must also approach zero (from below) to keep N constant. However, since μ goes to zero faster than T goes to zero, this forces the population in the lowest energy level to diverge. At this point, the standard procedure is to write Eq. (1.2) as an integral with the ground state occupation separated out as N_0. This ability to write this as an integral is justified if N is large and $k_B T$ is much larger than the typical energy level spacing [31].

$$N = N_0 + \int_0^\infty \gamma(\epsilon) \frac{1}{e^{(\epsilon-\mu)/k_B T} - 1} d\epsilon. \tag{1.3}$$

Here $\gamma(\epsilon)$ is the density of states, which for a 3D box with volume V is

$$\gamma(\epsilon) = \frac{V M^{3/2} \epsilon^{1/2}}{\sqrt{2}\hbar^3 \pi^2}. \tag{1.4}$$

Substituting this expression for $\gamma(\epsilon)$ into Eq. (1.3), we arrive at the following

$$N = N_0 + \frac{V}{\lambda_{\text{th}}^3} g_{3/2}(z), \tag{1.5}$$

where $\lambda_{\text{th}} = \sqrt{2\pi\hbar^2/M k_B T}$ is the thermal deBroglie wavelength, $z = e^{\mu/k_B T}$ is the

3

fugacity and $g_{3/2}(z)$ is the Bose function

$$g_{3/2}(z) = \sum_{l=1}^{\infty} \frac{z^l}{l^{3/2}}. \qquad (1.6)$$

The phenomenon of Bose-Einstein condensation can now be understood as follows. First, observe that as T decreases, λ_{th} increases. As the temperature T of the system is reduced from an initial temperature high enough that μ is initially much less than zero, we see that μ initially has the ability to increase toward zero, thus allowing $g_{3/2}(z)$ to keep up with the increasing λ_{th}^3 in order to maintain fixed N (without N_0 having to be macroscopically occupied). However, keeping in mind the fact that μ can never exceed zero, we see that at $z = 1$ (where $g_{3/2}(1) = 2.612$) the second term in Eq. (1.5) cannot hold all N atoms. At this point the first term in Eq. (1.5) is forced to start holding a significant number of the atoms. As T continues to decrease, it holds increasingly more. The transition occurs when $z = 1$ and Eqs. (1.3) and (1.5) cannot be satisfied with $N_0 = 0$. Using the value of $g_{3/2} = 2.612$ at this point and requiring the first term in Eq. (1.5) to be zero together define the onset of BEC:

$$N = 2.612 \frac{V}{\lambda_{\text{th}}^3}, \qquad (1.7)$$

or simply $n\lambda_{\text{th}}^3 = 2.612$ where n is the spatial number density of the gas. In the next section, we will discuss a more general definition of BEC that relates to the amount of phase fluctuations in the system.

1.2 The Role of Interactions, Trapping, and Dimensionality

Previously we talked about BEC as being the macroscopic occupation of a quantum state. Although this is a valid definition, an often more useful definition involves the phase coherence properties of the system as originally emphasized by Penrose and Onsager [2]. They considered the single-particle density matrix $\rho(\vec{r}, \vec{r}')$ which characterizes the correlation properties at points $\vec{r}$ and $\vec{r}'$. If $\vec{r} = \vec{r}'$, then this function returns the system density; but as $|\vec{r} - \vec{r}'|$ increases, the function goes to zero for a non-condensed system. Macroscopic occupation of a quantum state implies that $\rho(\vec{r}, \vec{r}')$ remains finite even in the limit $|\vec{r} - \vec{r}'| \rightarrow \infty$. Calling the wavefunction of the state that is macroscopically occupied $\psi(\vec{r})$, then the fact that $\rho(\vec{r}, \vec{r}')$ remains finite even in the above limit means that the phase of $\psi(\vec{r})$ must be correlated over the entire system. This phase coherence is another definition of BEC, and is commonly referred to as *off-diagonal long-range order* (ODLRO). For a trapped finite-size system, the limit $|\vec{r} - \vec{r}'| \rightarrow \infty$ does not exist, however phase coherence across the size of the condensate is a meaningful definition of BEC.

The first order corrections to degeneracy temperatures and ground state occupations due to the effects of harmonic trapping and weak atom-atom interactions in a 3D BEC were calculated in a seminal paper by Bagnato, Pritchard, and Kleppner [3]. As mentioned above, these corrections were rather minor so that the uniform, ideal gas theory was a good guide to the early experiments. However, for BEC in one and two dimensions (1D, 2D), the effects of weak interactions and harmonic trapping are very pronounced. For instance, in a 1D uniform ideal gas, BEC only

occurs at zero temperature [5]; however, with interactions it cannot occur even at $T = 0$ [5]. For a 2D uniform ideal gas, BEC also only occurs at $T = 0$ [106, 107]. However, unlike the 1D case, weak interactions do not destroy the 2D BEC at $T=0$ in a uniform gas. Instead, the effect of interactions is to create a finite T superfluid (SF) transition associated with the formation of bound vortex pairs below the critical temperature T_{BKT} [12–17] (the Berezinskii-Kosterlitz-Thouless temperature). Above T_{BKT} the system is normal (non-superfluid); below T_{BKT} the system is SF and referred to as a quasi-condensate because although density fluctuations are suppressed, the phase still fluctuates on a length scale which is smaller than the system size. The above conclusions can be reached by simple density of (plane wave) states arguments for the non-interacting uniform 1D and 2D gases. For the interacting gases, the arguments are more subtle.

The presence of a confining potential alters these conclusions to the point where Bagnato and Kleppner showed that 2D BEC is possible at finite T for an ideal gas in a power-law trap of any positive power [4]. They further showed that in the thermodynamic limit, 1D BEC is possible at finite T for an ideal gas in a power-law trap as long as the exponent is higher than two. However, exploring finite-number effects in trapped systems, Ketterle and van Druten [47] theoretically demonstrated, by using a definition of the thermodynamic limit which was different than the standard definition, that 1D finite T BEC is in fact possible for an ideal gas in a harmonic trap.

The role of interactions in trapped lower dimensional systems is quite complicated. For a 1D harmonically trapped system, interactions that are weak compared

to the harmonic energy $\hbar\omega$ do not destroy BEC at $T=0$. However these interactions do destroy a sharp transition to a 1D trapped BEC at finite T if the interaction energy is not less than approximately $\hbar\omega/N$ where N is the number of atoms [105]. For interactions that are strong compared to $\hbar\omega$, a 1D gas in its ground state becomes a highly correlated string of impenetrable bosons (a Tonks-Girardeau gas) [6–9] if the healing length ξ_h (where $\xi_h = \sqrt{8\pi na}$, n being the 3D density, and a the s-wave scattering length) is less than the average interparticle separation. If the healing length is greater than the average separation (and the interactions are still larger than $\hbar\omega$), then this (weakly interacting) gas in its ground state has a phase that does not appreciably vary over its spatial extent. This is known as a quasicondensate above a critical temperature T_ϕ and it becomes a true BEC below T_ϕ [129]. Interestingly, interactions in a 1D gas becomes increasingly important the lower the 1D density.

For a 2D harmonically trapped system with interactions, it has not yet been established under which conditions a normal BEC transition (long range order, as described in this chapter) occurs versus a Berezinskii-Kosterlitz-Thouless transition (quasi-long range order, as described in Chap. 8). These two transition temperatures are expected to be very close to each other for most weakly-interacting, trapped systems [131]. In general, if a finite T trapped 2D BEC exists for a system with weak repulsive interactions, the critical temperature is lower than for the corresponding ideal system. Bagnato, Pritchard, and Kleppner have calculated critical temperature corrections based on changes to the density of states due to a mean-field effective potential [3].

See Table 1.1 for a brief summary of the above discussion giving (where applicable) degeneracy temperatures and ground state occupations as a function of temperature for 1D, 2D, and 3D, uniform and trapped, with and without interactions. Note that within Table 1.1, n and g refer to spatial number density and coupling strength for the relevant dimensionality, i.e. their forms change depending on the dimensionality. The interactions are assumed to be repulsive (i.e. the s-wave scattering length, a, is positive). Also, ω refers to the trap frequency for the harmonic cases. In the case of an anisotropic trap, it is the geometric average of the two or three frequencies. The harmonic oscillator ground state size is denoted a_{ho}. Finally, the thermodynamic limit is assumed throughout Table 1.1 with the exception of the 1D harmonically trapped ideal gas where finite N is assumed. All references are contained in the text of this chapter.

System	1D Gnd State	1D Occupation	2D Gnd State	2D Occupation	3D Gnd State	3D Occupation
Uniform, ideal	BEC, T=0	$N_0 = N$	BEC, T=0	$N_0 = N$	BEC, $T_c^{0,u} = \frac{2\pi\hbar^2}{mk_B}\left(\frac{n}{2.612}\right)^{\frac{2}{3}}$	$\frac{N_0}{N} = 1 - \left(\frac{T}{T_c}\right)^{\frac{3}{2}}$
Uniform Weak Int	No BEC	—	BEC, T=0, SF, $T_{BKT} = \frac{\pi\hbar^2 n}{2mk_B}$	—	BEC, $T_c = T_c^{0,u} - O(na^3)$	—
Uniform Strong Int	Tonks gas	—	—	—	—	—
Harmonic, ideal	BEC, $T_c^{0,h} = \frac{\hbar\omega}{k_B}\frac{N}{\ln 2N}$	$\frac{N_0}{N} = 1 - \frac{T}{T_c}$ for large N	BEC, $T_c^{0,h} = \frac{\hbar\omega}{k_B}\left(\frac{N}{\pi^2/6}\right)^{\frac{1}{2}}$	$\frac{N_0}{N} = 1 - \left(\frac{T}{T_c}\right)^2$ for large N	BEC, $T_c^{0,h} = 0.94\frac{\hbar\omega}{k_B}N^{\frac{1}{3}}$	$\frac{N_0}{N} = 1 - \left(\frac{T}{T_c}\right)^3$
Harmonic Weak Int	$gn \ll \frac{\hbar\omega}{N} \Rightarrow$ BEC, $T_c^{0,h}$ $gn \gg \frac{\hbar\omega}{N} \Rightarrow$ BEC, T=0	—	BEC, $T_\phi \approx \frac{T_c^{0,h}}{\ln N}\left(\frac{4\pi\hbar^2}{mg}\right)^{\frac{1}{2}}$ SF, $T_{\mathrm{BKT}} = T_c^{0,h}\left(1 - \frac{3\nu}{\pi^2}\ln^2\nu\right)$ where $\nu = a/a_{ho}$	—	BEC, $T_c = T_c^{0,h} - 1.3\frac{a}{a_{ho}}N^{\frac{1}{6}}$	—
Harmonic Strong Int	Tonks gas	—	—	—	—	—

Table 1.1: Some important thermodynamic quantities at quantum degeneracy for 1D, 2D, and 3D uniform and harmonically-trapped systems. The occupation number is for below the transition temperature. In the case of the uniform ideal system in 1D and 2D, there is no functional relationship since BEC only exists at $T = 0$. Where there are no entries, either there are no simple expressions or the theory is incomplete. References are contained in Chap. 1 of the doctoral dissertation of J. H. Huckans.

1.3 Thesis Overview

This thesis is about the physics of dilute gaseous BECs confined to lower dimensions by optical lattices. We create a 2D BEC by increasing the confinement of a trapping potential in one direction to the point where motion is frozen out. If we do this in two directions, we create a 1D BEC. The experiment on BEC diffraction beyond the Raman-Nath regime (Chap. 7) uses a 1D lattice; however the atomic system is not 1D. Because the experiment takes place over a timescale which is short compared to the time for motion in the weak radial directions, it can be considered an experiment about the effective 1D dynamics of a 3D BEC.

The criterion for freezing out a dimension in order to reduce the dimensionality of a system is that the separation between the ground state and the first excited state in the tight direction must be much larger than the temperature and the chemical potential of the gas. Because of the extremely cold temperatures (tens of nK) and low densities (a few times 10^{13} cm^{-3}) involved in these experiments, this criterion is met using optical lattices created by a laser with approximately 1W power (with beam waists of approximately 200 μm).

The overview of this dissertation is as follows. Chap. 2 provides a conceptual summary of the steps necessary to a achieve a dilute gaseous BEC and a description of the resulting harmonically-trapped wavefunction. Chap. 3 provides the theory of the optical dipole potential, optical lattices, and Bloch bands. Chap. 4 describes those aspects of the ^{87}Rb BEC apparatus for which I was responsible during its reconstruction. However, since one of the purposes of this dissertation is to docu-

ment the apparatus for those who will continue to use it, I have also described some parts of the apparatus in whose construction I did not play a major role. Chap. 5 describes the implementation of a specialized 1D optical lattice whose periodicity can be dynamically changed during an experiment—an "accordion" lattice. The theory of heating and adiabaticity issues in this accordion lattice are also considered. Chap. 6 contains descriptions of the ways in which we performed periodicity calibrations of the accordion lattice, touching on mean-field effects during the expansion of the BEC. Chap. 7 describes an experiment using the accordion lattice which explores the effective 1D dynamics of a BEC in a deep 1D optical lattice as a function of different fixed lattice periodicities. Interesting connections between classical and quantum physics relating to the observation of phase space caustics are investigated. Chap. 8 describes an experiment investigating the low-lying excitations of the ground state of a 2D BEC observed by matter wave interference. The resultant phase fluctuations and occasional phase dislocations provide important evidence on the existence and location of the Berezinskii-Kosterlitz-Thouless transition in a trapped 2D system as well as the nature of the correlations as the temperature of the system approaches zero. Chap. 9 summarizes three experiments which led to publications in peer-reviewed scientific journals. These publications are provided in the appendices. The first experiment relates to the ground state of a 1D trapped gas in which the strength of the atom-atom interactions resulted in partial "fermionization" as evidenced by reduced three-body recombination. The second experiment continues the theme of reduced dimensionality by exploring transport of a 1D gas through optical lattices of varying depth. The third experiment in-

vestigates the discrete vibrational decay of an ensemble of 2D gases which we had previously Raman-excited from the ground state to higher vibrational levels in the tight (initially frozen) direction. Chap. 10 is a summary of the thesis and a forward look at the unsolved problems in ultra-cold and condensed matter physics that might be elucidated using Bose-Einstein condensates and optical lattices.

Chapter 2

The Path to BEC

This chapter provides a conceptual overview of the steps along the path to making a Bose-Einstein condensate (BEC). The path to BEC is not narrow; different laboratories have developed different techniques for achieving the same result. The following description is specific to the way we make a ^{87}Rb BEC in our laboratory. This chapter also gives a brief description of the final condensate wavefunction in the magnetic trap. It is assumed that the reader is generally familiar with atomic and optical physics techniques.

2.1 Laser Cooling and Trapping

2.1.1 Zeeman Slowing

The first step in the process of making our ^{87}Rb BEC is to slow the hot ^{87}Rb atoms being emitted from the oven with radiation pressure. The atoms are effusively emitted at approximately 420K from the oven in the direction of the magneto-optical trap (MOT). In order to be captured by the MOT, they must be slowed to below the capture velocity of the MOT (a few m/s).

Since the atoms coming out of the oven have a typical initial velocity of several hundred m/s and they need to be reduced to a velocity of a few m/s to be captured by the MOT, a scheme is needed to keep the atoms always nearly resonant with

the Doppler-shifted frequency of the slowing light. To accomplish this, we use the Zeeman effect and change the atomic level splitting with a time-independent, position-dependent magnetic field along the path of the atoms. For a two-level atom, a magnetic field **B** Zeeman-shifts the energy levels by a relative amount $\Delta E_{\text{zm}} = \mu_B B[g_e m_e - g_g m_g]$ where μ_B is the Bohr magneton, g is the Landé g-factor, subscripts g and e refer to the ground and excited states, and m is the magnetic quantum number. The Zeeman slower is designed to have a magnetic field profile whose direction is constant along its axis, but whose magnitude varies so that $\Delta E_{\text{zm}} = \hbar[(\omega - \omega_0) + kv(x)]$ where ω and k are the frequency and k-vector of the slowing laser, ω_0 is the atomic transition frequency and $v(x)$ is the position-dependent velocity of the atoms.

The slowing laser is detuned from the atomic transition frequency so that it is not resonant with the stationary atoms collecting in the MOT which it passes through. The detuning is red (as opposed to blue) which means that for a given maximum velocity class of slowed atoms, the magnitude of the Zeeman magnetic field is smaller. Thus, there is a reverse part of the slower to make the field negative before the atoms arrive at the MOT. Finally, we have a compensator on the other side of the MOT to bring the magnetic field to zero at the MOT location.

2.1.2 Doppler Cooling

We now discuss schemes for cooling the atoms after the Zeeman slower using laser light. We generally follow the treatment in Ref. [25]. Consider a two-level

atom with velocity v interacting in one dimension with two counterpropagating low intensity laser beams at the same frequency. The total light scattering force on the atom is [25]

$$F = \frac{\hbar k \gamma}{2} s_0 \left[\frac{1}{1 + s_0 + 4(\frac{\delta + kv}{\gamma})^2} - \frac{1}{1 + s_0 + 4(\frac{\delta - kv}{\gamma})^2} \right], \qquad (2.1)$$

where γ is the decay rate of the atom, $s_0 = I/I_0$ is the saturation parameter of one beam, and δ is the laser detuning from the atomic transition. In the definition of s_0, the saturation intensity, $I_0 \equiv 2\pi^2 \hbar \gamma c / 3\lambda^3$ where λ is the wavelength of the light. In the above expression for F, we ignore the effects of stimulated emission and cross-saturation (in which one beam saturates the transition for the other beam). For small velocities where terms of order $(kv/\gamma)^4$ and higher are neglected, we can simplify the above expression to

$$F \simeq \frac{8\hbar k^2 \delta s_0 v}{\gamma[1 + s_0 + (2\delta/\gamma)^2]^2}. \qquad (2.2)$$

We see that for $\delta < 0$ this is a velocity-dependent (dissipative) force, which can cool the atoms. Since this force is nearly linear with velocity if $|v| < \gamma/k$ (when $s_0 \ll 1$ and $\delta = -\gamma/2$), we can define a capture velocity $v_c = \gamma/k$. Below this velocity, the damping rate (term in front of v) is $s_0 \hbar k^2$. By using three intersecting pairs of counterpropagating beams, we can achieve Doppler cooling in three directions.

The above damping is accompanied by heating arising from the randomness

in the discrete absorptions and emissions. The atoms are heated because these recoils occur in random directions and at random time intervals between events. Equating this heating rate to the Doppler cooling rate $F \cdot v$, the steady-state Doppler temperature is reached, which is equal to [25]

$$T = \frac{\gamma}{8k_B} \frac{1 + 4\delta^2/\gamma^2}{-\delta/\gamma}, \tag{2.3}$$

where k_B is Boltzmann's constant. This temperature has its minimum when $\delta = -\gamma/2$ and the resulting temperature is called the Doppler cooling limit:

$$T_{\mathrm{D}} = \hbar\gamma/2k_B. \tag{2.4}$$

For ^{87}Rb, T_{D} is approximately 140 μK. T_{D} was long considered to be the limit in cooling a gas of atoms. However, this barrier was soon broken because of processes that will be described in the next section.

2.1.3 Sub-Doppler Cooling

The above treatment ignores important processes relating to the multi-level character of the atom, the polarization of the light, and optical pumping. These processes can take away kinetic energy from the atom by converting it to potential energy as described below resulting in much lower temperatures. Here, we follow the treatment detailed in Ref. [27]. As an example, consider the case of a multi-level atom ($J = 1/2$ ground state, $J = 3/2$ excited state) with velocity v interacting in

one dimension with two counterpropagating low intensity laser beams at the same frequency. Now, assume that both beams are linearly polarized but with perpendicular polarization vectors (lin ⊥ lin configuration). The resultant polarization along the beam axis varies from linear to circular to orthogonal linear to opposite circular. Say that it starts out where the polarization is σ^+ meaning that it is naturally pumped to the $m_g = +1/2$ sublevel. As it moves from this point, the light first smoothly changes to linear polarization and then starts to become σ^-. During this time, it will be moving up a potential hill due to the dependence of the light shift on the Clebsch-Gordan coefficient. When it reaches the location where the polarization of the light is fully σ^-, a slowly moving atom will tend to be optically pumped to the $m_g = -1/2$ sublevel where it starts the process of going up a hill again. This picture is referred to as "Sisyphus" cooling based on Greek mythology. A similar process occurs for the actual (more complicated) atom we have in our experiments which is not $J = 1/2$ to $J = 3/2$.

This sub-Doppler Sisyphus cooling is limited by the "graininess" of the light field, i.e. the fact that interactions take place via photons. We can associate a temperature with the photon recoil energy equal to

$$T_{\rm R} = \frac{\hbar^2 k^2}{M k_B}. \tag{2.5}$$

For ^{87}Rb, $T_{\rm R}$ is equal to 400 nK. In practice, the lowest temperatures achieved using standard sub-Doppler cooling techniques are approximately a factor of 10 higher than this. However, the recoil limit, $T_{\rm R}$, has been broken via techniques such

as velocity-selective coherent population trapping [28] and Raman cooling [29].

2.1.4 The Magneto-Optical Trap

The techniques so far discussed do not involve spatial trapping of the atoms. A magneto-optical trap is a hybrid technique which uses the light scattering force in conjunction with a spatially varying magnetic field which shifts atoms increasingly into resonance with inwardly-directed laser beams depending on how far away from the origin the atoms are [30]. Even though the MOT has nothing to do with the dipole force (described in Chap. 3) which is based on light-shifting the atomic levels, it mimics a conservative potential in the sense that it results in a spatially-dependent force.

In the simplest case, in one dimension, an atom with a $J = 0$ ground state and $J = 1$ excited state is placed between two counter-propagating red-detuned laser beams, circularly polarized in opposite directions (σ^+ and σ^- with respect to the +x axis). Along this axis and near the origin, the projection of a 3D quadrupolar magnetic field results in a linear field with its 0 at the origin and a direction which is along the axis. The sign of the slope of this magnetic field is chosen so that if the atom moves toward the source of the σ^+ beam, its $m_e = +1$ excited state is Zeeman-lowered, which, because of the light's red-detuning, favors excitation by the σ^+ beam over the oppositely-directed σ^- beam. Roles are reversed if the atom moves toward the σ^- beam and so the atom remains near the origin. The process works for more complicated atoms as well.

The same principle can be applied for the remaining two axes to get 3D confinement. The beams along the axis of the quadrupolar field have opposite handedness circular polarization from the beams in the plane of the field. Finally, because the light is red-detuned in a MOT, in addition to a restoring force we obtain cooling as described in the Doppler cooling section above.

2.2 Evaporative Cooling

Typically, when trying to get high normalized phase space densities using the above laser cooling and trapping techniques, in the case of ^{87}Rb we are limited to approximately $n\lambda_{\text{th}}^3 \simeq 10^{-4}$ based on temperatures in the range of tens of μK with $n \simeq 10^{11}$ cm^{-3} (λ_{th} is the thermal deBroglie wavelength). Various tricks such as creating a "dark spot" on the MOT have been able to push the spatial densities up to approximately $n \simeq 10^{12}$ cm^{-3} by reducing light scattering pressure. So far, however, no one has been able to achieve a BEC without evaporative cooling.

The principle of evaporative cooling is very simple. First, atoms are conservatively confined by either a magnetic trap (which is what we do) or by a far-detuned light trap so that spontaneous scattering (almost) never occurs, so that one is not subject to the T_{R} limit. Second, the height of the potential confining the atoms is gradually brought down (at the periphery of the trap) in order to permit the highest energy atoms to escape. The lowest energy atoms do not reach the edge of the trap, and so they are retained. As long as this process of cutting the tail of the Maxwell-Boltzmann distribution is done slowly enough to allow the remaining

atoms to collide and re-thermalize, the tail will continually regrow and cooling will take place. Some of the collisions between the atoms may cause the colliding atoms to change their internal states and be lost from the trap. In the case of ^{87}Rb, these "bad" collisions are rare and the "good" collisions, which lead to rethermalization, dominate. Although evaporative cooling does increase phase space density and is a proven path to BEC, its main disadvantage is that one ends up with typically 0.1% of the initial number of atoms there were at the start of the evaporation.

2.3   The Gross-Pitaevskii Equation

We now turn to a description of the Bose-Einstein condensate wavefunction in the magnetic trap. The following treatment borrows heavily from Ref [23]. A way to derive the condensate wavefunction based on the Hartree-Fock method, which is relevant when one needs to account for the trapping potential, leads to the well-known Gross-Pitaevkii (GP) equation [23, 24]. The time-dependent form of the GP equation is often used for direct simulation of condensate dynamics; we implement the time-dependent GP equation in Chap. 6 as a comparison for our experimental results.

By taking the many-body wavefunction as a product of N (where N is the number of atoms in the condensate) identical single-particle wavefunctions $\Psi(\mathbf{x_1}, \mathbf{x_2}, ..., \mathbf{x_N}) = \chi(x_1)\chi(x_2)...\chi(x_N)$, and minimizing the total energy functional

$$\mathcal{H}(\psi) = N \int d\mathbf{x}\chi^*(\mathbf{x})\Big(-\frac{\hbar^2}{2M}\nabla^2 + U_{ext}(\mathbf{x})\Big)\chi(\mathbf{x}) + \frac{N(N-1)}{2}g \int d\mathbf{x}|\chi(\mathbf{x})|^4, \quad (2.6)$$

subject to the normalization constraint

$$\int d\mathbf{x} |\chi(\mathbf{x})|^2 = 1, \tag{2.7}$$

we obtain the GP equation:

$$-\frac{\hbar^2}{2M} \nabla^2 \chi + U_{ext}\chi + g(N-1)|\chi|^2 \chi = \frac{\lambda}{N}\chi, \tag{2.8}$$

where $U_{ext}(\mathbf{x})$ is the external trapping potential and λ is a Lagrange multiplier. If we define the order parameter [24] as $\psi(\mathbf{x}) = \sqrt{N}\chi(\mathbf{x})$ and the chemical potential $\mu = \lambda/N$, also noting $N - 1 \simeq N$ for large N, we obtain

$$-\frac{\hbar^2}{2M} \nabla^2 \psi + U_{ext}\psi + g|\psi|^2 \psi = \mu\psi. \tag{2.9}$$

In the above expressions, g is related to the strength of the two-body interaction potential. For a delta function interaction between two atoms, g is just the strength of the interaction. For s-wave scattering in the Wigner threshold limit, with a scattering length a, it is given by:

$$g = \frac{4\pi\hbar^2 a}{M}. \tag{2.10}$$

To see why μ is called the chemical potential, we can rewrite the constrained functional minimization problem in terms of ψ. With a normalization constraint of

21

N instead of 1, it follows that the minimized $\mathcal{H}$ and the corresponding μ (i.e. the total ground state energy) satisfies $\mu = \partial \mathcal{H}/\partial N$ [23].

In the Thomas-Fermi regime, the mean-field energy $g|\psi|^2$ dominates over the kinetic energy term in Eq. (2.9). If we ignore the kinetic energy term altogether, we obtain an equation for the Thomas-Fermi profile of the condensate:

$$U_{ext} + g|\psi|^2 = \mu, \qquad (2.11)$$

which for a harmonic trap $U_{ext} = \frac{1}{2}M(\omega_x^2 x^2 + \omega_y^2 y^2 + \omega_z^2 z^2)$ gives the density profile $n(x,y,z) = N|\psi|^2$

$$n(x,y,z) = \frac{1}{g}(\mu - \frac{M}{2}(\omega_x^2 x^2 + \omega_y^2 y^2 + \omega_z^2 z^2)). \qquad (2.12)$$

Therefore, in this limit, a harmonically-trapped condensate has an inverted parabolic density distribution with Thomas-Fermi radii:

$$R_i = \sqrt{\frac{2\mu}{M\omega_i^2}}, \qquad (2.13)$$

where $i = x, y, z$. The Thomas-Fermi approach is typically a very good approximation except at the edge of the condensate where the kinetic energy is larger than the mean-field energy. Here, the density goes smoothly to zero instead of abruptly as given by the Thomas-Fermi profile. For a given N, in the Thomas-Fermi approximation, μ is determined by the normalization condition that $N = \int d\mathbf{x}\, n(\mathbf{x})$

giving

$$\mu = \frac{1}{2}\left[15Na\sqrt{M}\hbar^2\omega_x\omega_y\omega_z\right]^{\frac{2}{5}}, \tag{2.14}$$

again where a is the s-wave scattering length. Finally, in the Thomas Fermi regime

$$\mu = \frac{1}{2}M\omega_i^2R_i^2 \gg \hbar\omega_i, \tag{2.15}$$

for any i. This inequality is equivalent to

$$R_i \gg \sqrt{\frac{\hbar}{M\omega}}, \tag{2.16}$$

which means that the condensate wavefunction has a spatial extent much greater than the single-particle ground state in the harmonic trap. So, in our experiments with a typical harmonic frequency of 20 Hz and atom numbers of roughly 10^5, the single-particle ground state in the harmonic trap has a size of approximately 2 μm whereas the Thomas-Fermi radius of the cloud is approximately an order of magnitude larger.

Chapter 3

Optical Lattices

Some of the earliest experiments using periodic optical potentials in conjunction with cold neutral atoms were in the contexts of atom diffraction [90] and atomic cooling (optical molasses) [38]. The idea that a standing wave of light could be used to scatter [64] and trap [39] neutral atoms had been proposed more than a decade earlier. At the time of the early experiments, the term "optical lattice" was not in use. In fact, in the case of the first optical molasses experiments [38], although the researchers realized that they had created a standing wave of light, the importance of the periodic potential in helping to achieve extremely low temperatures was not even appreciated initially.

The term "optical lattice" was coined in the early 1990s to suggest the idea of atomic confinement and localization at the nodes (or antinodes) of the periodic potential (within the optical lattice). Although it did not use the term "optical lattice," the experiment described in Ref. [40] was one of the first to demonstrate this localization. Since that time, there has been an explosion of interest in the use of optical lattices with ultracold neutral atoms. Many of the experiments in the early 1990s focussed on understanding and improving the atomic confinement and localization within a lattice [41][42][43]. With increasingly sophisticated cooling techniques (such as Raman sideband cooling), wave packet momentum spreads

began to shrink below the width of Brillouin zones, thus allowing demonstrations of predicted (and hitherto very difficult to observe) single-particle condensed matter phenomena such as Bloch oscillations [33] and its counterpart in the frequency domain [36]. With the advent of BEC, the theme of using optical lattices and ultracold atoms to simulate important condensed matter tools and phenomena such as Bragg scattering [95], band structure [49], Mott insulators [50, 52, 53, 123], Tonks-Girardeau gas "fermionization" [51, 54–56] etc., has continued. As of the writing of this thesis, we are at the point where important, unsettled questions in condensed matter physics (such as the nature of the 2D Kosterlitz-Thouless transition in trapped systems, [126] and whether high T_c superconductivity is contained within the Hubbard model [158]) may be settled using ultracold neutral atoms in optical lattices.

3.1   Optical Dipole Potential and Light Scattering Theory

To understand optical lattices, it is important to better understand the interaction between light and atoms. Following is a very brief overview of this interaction in which the light is considered to be a classical field. In fact, for extremely far-detuned light (as is typically used in optical lattices) processes such as spontaneous emission and saturation can often be safely ignored and thus even the atom can be treated classically with conclusions that are the same as the semi-classical predictions (in which the atom is treated quantum-mechanically and the light is treated classically). This is the starting viewpoint we take in presenting the following very

simple model of the light-atom interaction. In essence, the quantum part of the interaction is only important when the correct form of the damping coefficient is required. This presentation borrows heavily from an excellent presentation by Grimm, Weidemüller, and Ovchinnikov [37].

Consider an atom with a dipole moment $\vec{d}$ induced by an electric field $\vec{E}(\vec{r}, t) = \hat{e} E_0 e^{i\vec{k}\cdot\vec{r}} e^{-i\omega t} + c.c..$ The dipole moment oscillates at the same frequency ω as the electric field with a response given by $\vec{d} = \alpha \vec{E}$ where the polarizability α is a tensor whose elements are in general complex. If we assume that the unit polarization vector, $\hat{e}$, of $\vec{E}$ and $\vec{d}$ are collinear, then α is a rank-0 tensor (i.e., just a complex scalar). We now express the interaction potential between the atom and the light field as

$$U_{\text{dip}} = -\frac{1}{2}\left\langle \vec{d}\cdot\vec{E}\right\rangle = -\frac{1}{2\epsilon_0 c}Re(\alpha)I, \tag{3.1}$$

where I is the light intensity, the brackets indicate a time average over a cycle and the factor of $\frac{1}{2}$ in front reflects the fact that the atomic dipole is induced and not permanent. Given the way we have expressed the electric field above, the relationship between the amplitude of $\vec{E}$ and the intensity of the electric field is $I = 2\epsilon_0 c|E_0|^2$. The imaginary part of α is excluded because it gives the part of $\vec{d}$ which is oscillating out of phase with $\vec{E}$ and thus does not contribute to U_{dip} after time averaging. Throughout this chapter, SI units are being used.

The part of the light-atom interaction due to the imaginary part of α is dissipative. The atom absorbs a photon from the electric field and then emits a photon spontaneously in a random direction (in accordance with the appropriate spatial

26

distribution function) into the vacuum (scattering). Considering the light to be a stream of photons, the scattering rate Γ_{sc} can be expressed as the ratio of the power absorbed by the atom to the energy per photon.

$$\Gamma_{\text{sc}} = \frac{\left\langle \frac{d}{dt}(\vec{d}) \cdot \vec{E} \right\rangle}{\hbar\omega} = \frac{\omega \text{Im}(\alpha)2|E_0|^2}{\hbar\omega} = \frac{\text{Im}(\alpha)I}{\hbar\epsilon_0 c}. \tag{3.2}$$

We can now derive an expression for the atomic polarizability α using Lorentz's model of the light-electronic cloud interaction as a classical driven damped oscillator of mass M_{e} and charge e elastically bound to the nucleus with a resonant frequency ω_0 (equal to the optical transition frequency). The driving force is $e\vec{E}$.

$$\alpha = \frac{e^2}{M_{\text{e}}} \frac{1}{\omega_0^2 - \omega^2 - i\omega\Gamma(\omega)}. \tag{3.3}$$

An expression for the damping rate $\Gamma(\omega)$ is obtained by dividing Larmor's formula for the power radiated by an accelerating charge [58] by $M_{\text{e}}v^2$ where v is the instantaneous magnitude of the maximum velocity of the electron.

$$\Gamma(\omega) = \frac{e^2\omega^2}{6\pi\epsilon_0 M_{\text{e}}c^3}. \tag{3.4}$$

The classical functional dependence of Γ on ω allows us to express α as

$$\alpha = 6\pi\epsilon_0 c^3 \frac{\Gamma_0/\omega_0^2}{\omega_0^2 - \omega^2 - i(\omega^3/\omega_0^2)\Gamma_0}, \tag{3.5}$$

27

where Γ_0 is the on-resonance damping rate. At this point, we can add quantum mechanics onto the classical expression for α and consequently our expressions for U_{dip} and Γ_{sc} by equating the on-resonance classical damping rate to the quantum-mechanical expression for the two-level excited state population decay rate γ (the inverse of the excited state natural lifetime, τ). This gives us the scalar part of the light shift applicable to systems without any fine or hyperfine structure:

$$\gamma = \frac{\omega_0^3}{3\pi\epsilon_0\hbar c^3}|\langle\phi_{\text{e}}|\hat{\mu}|\phi_{\text{g}}\rangle|^2, \tag{3.6}$$

where $\langle\phi_{\text{e}}|\hat{\mu}|\phi_{\text{g}}\rangle$ is the matrix element connecting the ground and excited state of the atom for the dipole matrix $\hat{\mu} = -e\hat{r}$. We now can write down expressions for U_{dip} and Γ_{sc} in which we assume that $\delta \equiv (\omega - \omega_0) \gg \gamma$

$$U_{\text{dip}} = -\frac{3\pi c^2}{2\omega_0^3}\Big(\frac{\gamma}{\omega_0 - \omega} + \frac{\gamma}{\omega_0 + \omega}\Big)I. \tag{3.7}$$

$$\Gamma_{\text{sc}} = \frac{3\pi c^2}{2\hbar\omega_0^3}\Big(\frac{\omega}{\omega_0}\Big)^3\Big(\frac{\gamma}{\omega_0 - \omega} + \frac{\gamma}{\omega_0 + \omega}\Big)^2 I. \tag{3.8}$$

If $\delta \ll \omega$, we can make the rotating wave approximation (RWA) [59] in which we neglect the second term in Eqs. (3.7) and (3.8) and set $\left(\frac{\omega}{\omega_0}\right)^3 = 1$, thereby leaving

$$U_{\text{dip}} = \frac{3\pi c^2}{2\omega_0^3}\frac{\gamma}{\delta}I. \tag{3.9}$$

$$\Gamma_{sc} = \frac{3\pi c^2}{2\hbar\omega_0^3}\left(\frac{\gamma}{\delta}\right)^2 I. \tag{3.10}$$

We see that for a negative (positive) detuning, atoms are attracted toward regions of high (low) intensity and that the scattering rate does not depend on the sign of the detuning. Also, we can relate Γ_{sc} to U_{dip} as follows

$$\Gamma_{sc} = \frac{\gamma}{\delta}\frac{U_{dip}}{\hbar}. \tag{3.11}$$

To preserve coherence and not heat the atoms, this relationship points out the need to go to very large detunings (relative to the power broadened γ) to minimize the spontaneous scattering events. However, as the detuning is increased, the laser intensity needs to increase proportionately to maintain the same potential depth.

As previously mentioned, the above simple treatment ignores several important aspects of the interaction between light and real atoms. For one, the effect of saturating the transition is completely missed whereas a two-level atom (which is an approximation to the system) shows saturation; however this is almost completely irrelevant given our typical detunings and powers. We also miss the important fact that according to second order perturbation theory the light shifts the upper and lower state energy levels in equal and opposite directions, which is obtained even for a two-level system. We can identify the lower state energy shift with the classical dipole potential which we just derived. In fact, including the rotating wave approximation, the results are identical. However, there is no classical effect

29

corresponding to the shift of the upper state (because classically there is no "upper state"). The quantum result comes out very easily in the "dressed" picture of the atom [61].

A far more important aspect of the problem is that the atom in our experiment, ^{87}Rb, has internal structure which cannot be captured via a two-level model. This gives rise to state-dependent light shifts that depend on the internal structure of the atom. Let us now specialize to the atom we use in our experiment. For ^{87}Rb, the excited states we work with can be grouped into two separate manifolds, $^2P_{1/2}$ and $^2P_{3/2}$, split several THz by electron spin-orbit coupling (fine structure). (Relative to the ground state, these manifolds have transition wavelengths of roughly 795 nm and 780 nm, respectively. The ground state has no fine structure because it has no orbital angular momentum.) Each of these excited state manifolds is further split by nuclear spin coupling into sub-manifolds separated on the order of 100 MHz (hyperfine structure). The ground state is also split into 6.8 GHz separated manifolds by the nuclear spin coupling. Furthermore, all of the ground state and excited state hyperfine manifolds and sub-manifolds can be even further split by an externally applied magnetic field. These Zeeman shifts are (in the weak field limit) proportional to the magnitude of the applied field and the projection of the total angular momentum of the atom onto the direction of the field, given by the quantum number m_F. The F subscript denotes total angular momentum. If the laser detuning is large with respect to the excited state hyperfine splitting (approximately 200-300

MHz in the case of ^{87}Rb), then we can derive the following expression for U_{dip} [37]:

$$U_{\text{dip}} = \frac{\pi c^2 \gamma}{2\omega_0^3} I \left(\frac{2 + P g_F m_F}{\delta_{2,F}} + \frac{1 - P g_F m_F}{\delta_{1,F}} \right), \tag{3.12}$$

where $P = 0, \pm 1$ for linearly and circularly $\sigma^\pm$ polarized light, g_F is the Landé g-factor, m_F is the magnetic quantum number of the ground state (with respect to the polarization axis for linearly polarized light, but with respect to the propagation axis for circularly polarized light), and the detunings are relative to the transitions between the ground state and the $^2P_{3/2}$ and $^2P_{1/2}$ manifolds, respectively.

We can simplify the expression for U_{dip} even further if the laser detuning is large with respect to fine structure. In this case, the expression reduces to

$$U_{\text{dip}} = \frac{3\pi c^2 \gamma}{2\omega_0^3 \delta} I \left(1 + \frac{1}{3} P g_F m_F \frac{\delta_{FS}}{\delta} \right), \tag{3.13}$$

where the detuning δ is with respect to the center "of gravity" of the D-line doublet and δ_{FS} is the fine structure splitting. For linearly polarized light, this expression is just

$$U_{\text{dip}} = \frac{3\pi c^2 \gamma}{2\omega_0^3 \delta} I = \frac{\hbar \gamma^2}{8\delta} \frac{I}{I_0}, \tag{3.14}$$

which is the same as Eq. (3.9). If the system were a two-level atom, $I_0 = \hbar\gamma\omega_0^3/12\pi c^2$

31

is the laser intensity at which the zero-detuned light scattering rate is half the maximum $\gamma/2$. We may also express U_{dip} as

$$U_{\mathrm{dip}} = \frac{\hbar|\Omega_0|^2}{4\delta}, \tag{3.15}$$

where $\Omega_0 = \left\langle \hat{\mu} \cdot \hat{E} \right\rangle / \hbar$ is the on-resonance Rabi frequency and $|\Omega_0|^2 = \gamma^2 I / 2 I_0$. The key point is that the atomic potential is proportional to the light intensity. Any intensity pattern we make with the light becomes a corresponding potential for the atoms.

3.2   Optical Potentials

In order to trap atoms conservatively with light, an optical potential gradient must be established. Simply by using a single red-detuned Gaussian laser beam, one obtains radial (transverse to propagation direction) confinement because the intensity decreases as one moves away from the central axis of propagation. If the beam is focussed, one also obtains axial confinement at the focus. By combining two (or more) coherent laser beams in space such that some component of their k-vectors ($k = 2\pi/\lambda$ is the magnitude of this vector; λ is the wavelength of the light) are anti-parallel to each other, a standing light wave is created with a minimum spatial periodicity of half the laser wavelength. The intensity gradients within this optical lattice may trap ultra-cold atoms.

3.2.1 Focussed Traps

Consider a single far red-detuned Gaussian beam with linear polarization, total power P, focussed to a minimum waist w_0 (giving a Rayleigh length $z_R = \pi w_0^2/\lambda$). Using Eq. (3.15) the potential seen by an atom in the beam is

$$U_{\text{dip}} = \frac{\hbar \gamma^2}{8\delta I_0} \frac{2P}{\pi w_0^2 (1 + (z/z_R)^2)} \exp \frac{-2r^2}{w_0^2 (1 + (z/z_R)^2)}, \qquad (3.16)$$

where z is the coordinate along the beam axis and r is in the radial direction (perpendicular to the beam direction). We may define the dimensionless trap depth

$$s = \frac{1}{E_R} \frac{\hbar \gamma^2}{8\delta I_0} \frac{2P}{\pi w_0^2}, \qquad (3.17)$$

where $E_R = \hbar^2 k^2 / 2M$ is the single photon recoil energy, which is the energy imparted to a ^{87}Rb atom, initially at rest, by the absorption or emission of a single photon. Using this definition, for small displacements away from the focus of the beam we use the harmonic approximation and derive classical trapping frequencies of

$$\omega_R = \frac{\sqrt{8}\sqrt{s}}{k w_0} \left(\frac{E_R}{\hbar} \right), \qquad (3.18)$$

in the radial direction and

$$\omega_A = \frac{2\sqrt{s}}{k z_R} \left(\frac{E_R}{\hbar} \right) = \frac{4\sqrt{s}}{k^2 w_0^2} \left(\frac{E_R}{\hbar} \right) = \left(\frac{\sqrt{2}}{k w_0} \right) \omega_R, \qquad (3.19)$$

in the axial direction. For most of the work in this thesis $kw_0 \gg 1$, and so the axial trapping frequency is negligible.

3.2.2 Optical Lattices

If we now consider two superimposed counterpropagating far red-detuned Gaussian beams with parallel linear polarization, total power P in each beam, and both focussed to the same minimum waist w_0 at the same location in space, we create a 1D optical lattice whose potential is

$$U_{\mathrm{dip}} = \frac{\hbar\gamma^2}{8\delta I_0} \frac{8P}{\pi w_0^2(1 + (z/z_{\mathrm{R}})^2)} \sin^2(kz) \exp \frac{-2r^2}{w_0^2(1 + (z/z_{\mathrm{R}})^2)}, \qquad (3.20)$$

with z and r defined as above. Notice that the light intensity at the maxima (antinodes) of the $\sin^2$ modulation is four times the intensity in a single beam due to constructive interference. Radial confinement at the focus is still provided by the Gaussian profile of the light and so $\omega_{\mathrm{R}} = \frac{\sqrt{8}\sqrt{s}}{kw_0}\left(\frac{E_{\mathrm{R}}}{\hbar}\right)$ as before (although s for the two beams is four times as large as s for the single beam). At the focus in the axial direction however, in addition to the confinement envelope provided because the intensity decreases as one moves away from the focus, a fine-scale confinement is created because of the standing wave. Thus, we still have an envelope curvature in the axial direction of

$$M\omega_{\mathrm{A}}^2 = M\left[\frac{4c\sqrt{s}}{k^2 w_0^2}\left(\frac{E_{\mathrm{R}}}{\hbar}\right)\right]^2, \qquad (3.21)$$

34

where s for the two beams is twice s for the single beam and c is explained below. In addition, we have, on a fine scale, a parallel array of microtraps (a stack of "pancakes") each of which, in the deep lattice limit where we ignore tunneling between neighbors, has an axial frequency

$$\omega_{\mathrm{L}} = 2\sqrt{s}\Big(\frac{E_{\mathrm{R}}}{\hbar}\Big), \tag{3.22}$$

(where s for the two beams is four times s for a single beam). The factor c in the expression for the envelope curvature in the axial direction accounts for the fact that as the depth of the lattice increases, the wavefunction increasingly is confined to the deepest parts of the potential at the antinodes, thus seeing more of the intense parts of the light. In the deep lattice limit, $c = 2 - \frac{1}{\sqrt{s}} \simeq 2$ [35].

If we now modify the 1D optical lattice created by two counterpropagating beams by changing the angle between their propagation axes such that the centers of their minimum waists are still superimposed and their polarizations are still parallel, we create a new 1D optical lattice with periodicity larger than $\lambda/2$ (see the description of the "accordion lattice" in Chap. 5). For this lattice, we define the x-axis to be along the line bisecting the angle θ between the two beams. The z-axis is the lattice axis, which is perpendicular to the x-axis and in the plane of the two beams. The y-axis is perpendicular to both the x-axis and the z-axis. For a deep lattice, the trapping frequencies in the $\hat{x}$ and $\hat{y}$ direction and the envelope curvature

in the $\hat{z}$ direction are given by

$$\omega_x = \frac{\sqrt{8}\sqrt{s}}{kw_0} \frac{E_R}{\hbar} \sqrt{\sin^2\frac{\theta}{2} + \frac{2\cos^2\frac{\theta}{2}}{k^2 w_0^2}}, \tag{3.23}$$

$$\omega_y = \frac{\sqrt{8}\sqrt{s}}{kw_0} \frac{E_R}{\hbar}, \tag{3.24}$$

$$M\omega_z^2 = M\left[\frac{\sqrt{8}\sqrt{s}}{kw_0} \frac{E_R}{\hbar} \sqrt{\cos^2\frac{\theta}{2} + \frac{2\sin^2\frac{\theta}{2}}{k^2 w_0^2}}\right]^2. \tag{3.25}$$

In the above expressions, s is the depth of the potential in units of the single photon recoil energy E_R (and is four times s for a single beam). For our experiments, the second term under both square roots is very small (due to the Rayleigh length). Also, $k = 2\pi/\lambda$ is the magnitude of the light wavevector (not half the magnitude of the reciprocal lattice vector). This other wavevector is convenient to use in defining the lattice recoil. We may recast the deep lattice expression Eq. (3.19) as

$$\omega_L = 2\sqrt{s_L}\left(\frac{E_L}{\hbar}\right), \tag{3.26}$$

in which s_L is now the lattice depth in units of the *lattice* recoil energy E_L where

$$E_L = \hbar^2 \kappa_L^2 / 2M, \tag{3.27}$$

and $\kappa_L = \frac{\pi}{d}$ (half the reciprocal lattice vector). Here d is the optical lattice period-

icity. This definition for the lattice recoil energy gives the same value as the photon recoil energy when the two beams are counterpropagating (i.e. $\kappa_{\mathrm{L}} = k$).

We can create a 2D optical lattice by intersecting two 1D lattices (for a total of four beams). Assuming the two 1D lattices intersect at a right angle, the potential for this lattice (ignoring the Gaussian character of the beams and the overall phase differences between the two lattices) can be expressed as

$$U_{\mathrm{dip}} = sE_{\mathrm{R}}\Big[\cos^2 kx + \cos^2 kz + 2\hat{e}_1 \cdot \hat{e}_2[\cos(\omega_1 + \omega_2)t + \cos(\omega_1 - \omega_2)t]\cos kx \cos ky\Big].$$

(3.28)

This expression is valid in the limit that the light is linearly polarized and its detuning is large with respect to the upper state hyperfine splitting *or* the light is circularly polarized and its detuning is large with respect to the fine structure splitting. The lattice depth, s, again is four times s for a single beam. The cross term in the above expression vanishes if the polarizations of the two lattices, $\hat{e}_1, \hat{e}_2$ are exactly perpendicular. Alternatively, if the frequencies of the two lattices, ω_1, ω_2 are sufficiently detuned from each other, then the atom will not be able to respond to the rapidly changing value of the cross term, and it will time-average to zero. Since it is in practice very difficult to ensure polarization orthogonality, frequency detuning is the standard method to kill the cross term and it is the way we create the 2D optical lattices described in Chap. 9. The term containing the sum frequency goes away for the same reason.

There are important corrections to the simple expression (Eq. 3.22) we have given relating the lattice trapping frequency to the depth of the optical lattice.

First, this expression is based on considering only the quadratic term in the Taylor expansion of a sinusoid, which approximates each lattice site as an infinitely deep harmonic well. The next order correction is to include the quartic term in the Taylor expansion. This correction weakens the trap at higher vibrational energy, subtracting $[n(n+1)/2]E_{\mathrm{R}}$ from the energy of state n, defining the energy of state $n = 0$ to be zero. For instance, including the quartic term the excitation energy between the ground and first excited state is $(2\sqrt{s} - 1)E_{\mathrm{R}}$. Between the first and second excited state, the energy difference would be $(2\sqrt{s} - 2)E_{\mathrm{R}}$.

Another effect, due to atom-atom interactions, decreases the depth from the "bare" (single-atom) depth of the potential within the context of the Gross-Pitaevskii equation. In the weakly interacting limit where interactions can be treated as a mean field, for a repulsive interaction between the atoms, a spatially-varying positive mean-field energy equal to

$$U_{\mathrm{int}} = \frac{4\pi\hbar^2 a}{M}n, \tag{3.29}$$

where M is the atomic mass, a is the s-wave scattering length of the atom, and n is the number density, makes the potential more shallow because for a red-detuned lattice U_{int} is most positive where U_{dip} is most negative. The resultant potential is called the "effective potential."

Another correction, mainly affecting the radial trapping frequency, is due to the coupling between the confinement in the radial and axial directions which causes the Schrödinger equation to not be truly separable. One way to handle this is to

treat the energy of the zero point motion due to confinement in one direction as a pseudopotential added to the confining potential in an orthogonal direction. For instance, relative to the bottom of the potential, the ground state energy level due to the axial lattice confinement is highest along the z-axis ($r = 0$) and decreases monotonically as one moves out toward the edges of the beam ($r > 0$). This has the effect of making the potential in the radial direction shallower. The radial trapping frequency (for small displacements from the z-axis) is accordingly reduced by

$$\frac{\sqrt{2}}{2kw_0} \frac{1}{2\sqrt{s}} \frac{E_{\mathrm{R}}}{\hbar}. \tag{3.30}$$

All of the above has ignored tunneling between lattice sites. When the lattice is not very deep, tunneling must be taken into account. When this is done, each originally single energy level is split into a band of m closely spaced levels where m is the number of lattice sites. Within each band, each closely spaced level has associated with it a quasimomentum q which is proportional to the amount of phase difference between neighboring sites. The purpose of the next section is to describe and explain this part of the picture more clearly.

3.3   Bloch Band Theory

Following is a brief exposition of one-dimensional Bloch band theory which may be suitably amplified by any standard condensed matter textbook [57]. Consider the Schrödinger equation for a single particle in a one-dimensional spatially periodic

potential $U_{\mathrm{L}}(x) = U_{\mathrm{L}}(x + d)$ where d is the periodicity of the potential.

$$H\psi = \left(-\frac{\hbar^2}{2M}\nabla^2 + U_{\mathrm{L}}(x)\right)\psi = \epsilon\psi. \tag{3.31}$$

According to Bloch's theorem, the eigenstates of the Hamiltonian can be written as the product of a plane wave and a spatially periodic wavefunction with the same periodicity as the potential:

$$\psi_{nq}(x) = e^{iqx/\hbar}u_{nq}(x). \tag{3.32}$$

For a finite lattice, the index q called the "quasimomentum" ranges from $+\infty$ to $-\infty$ in steps of $2\pi\hbar/md$, again where m is the number of lattice sites and d is the lattice constant. However, q is usually defined modulo $2\pi\hbar/d$. The band index n is the absolute value of the integer part of the quasimomentum (in the extended zone scheme) divided by $2\pi\hbar/d$. If we insert $\psi_{nq}(x)$ into the Schrödinger equation, we get an equation for $u_{nq}(x)$:

$$H\psi = \left[\frac{1}{2M}\left(-i\hbar\nabla + q\right)^2 + U_{\mathrm{L}}(x)\right]u_{nq}(x) = \epsilon_{nq}u_{nq}(x). \tag{3.33}$$

We now Fourier decompose $u_{nq}(x)$ using a single lattice spacing as the basic Fourier interval:

$$u_{nq}(x) = \sum_l c_l^{nq}e^{il2\kappa x}. \tag{3.34}$$

In the case of an optical lattice, the periodic potential is sinusoidal which we express as $U_{\mathrm{L}}(x) = U_0 \sin^2(kz)$. It can be written in a form that makes evaluation of its matrix elements in the plane wave basis spanned by the reciprocal lattice vectors (parameterized by a particular q value) transparent,

$$U_{\mathrm{L}}(x) = \frac{U_0}{2} - \frac{U_0}{4}\left(e^{i2kx} + e^{-i2kx}\right). \tag{3.35}$$

The kinetic energy operator in this basis is

$$\frac{1}{2M}\left(-i\hbar\nabla + q\right)^2 = \frac{(2\hbar kl + q)^2}{2M}. \tag{3.36}$$

And thus the Hamiltonian H_0 expressed as a $(2l_{\mathrm{max}}+1) \times (2l_{\mathrm{max}}+1)$ matrix (where l_{max} is chosen to truncate the basis set) becomes

$$\begin{pmatrix}
\cdots & -\frac{U_0}{4} & 0 & 0 & 0 & 0 & 0 \\
-\frac{U_0}{4} & \frac{(4\hbar k + q)^2}{2M} & -\frac{U_0}{4} & 0 & 0 & 0 & 0 \\
0 & -\frac{U_0}{4} & \frac{(2\hbar k + q)^2}{2M} & -\frac{U_0}{4} & 0 & 0 & 0 \\
0 & 0 & -\frac{U_0}{4} & \frac{q^2}{2M} & -\frac{U_0}{4} & 0 & 0 \\
0 & 0 & 0 & -\frac{U_0}{4} & \frac{(-2\hbar k + q)^2}{2M} & -\frac{U_0}{4} & 0 \\
0 & 0 & 0 & 0 & -\frac{U_0}{4} & \frac{(-4\hbar k + q)^2}{2M} & -\frac{U_0}{4} \\
0 & 0 & 0 & 0 & 0 & -\frac{U_0}{4} & \cdots
\end{pmatrix}$$

plus an offset of $U_0/2$. For each choice of q, diagonalization of this matrix leads to

41

a spectrum of $2l + 1$ eigenvalues. If this is done for all values of q between $-\hbar k$ and $+\hbar k$, the set of spectra can be displayed in the usual reduced zone scheme where only the first Brillouin zone is shown. Figures 3.1, 3.2 and 3.3 display the resultant band structures for sinusoidal potentials of various depths. Notice that as the lattice gets deeper, the bands become increasingly flat (starting with the lowest bands) and their separations become increasingly uniform at a value given by the harmonic frequency as described above. Each one of the eigenvectors $u_{nq}(x)$ associated with a particular value of q will be expressed as a linear combination of plane waves (as in Eq. (3.33)). When multiplied by $e^{iqx/\hbar}$ (as in Eq. (3.31)), these final solutions are known as Bloch states. It is convenient to express the wave function of an atom in an optical lattice in the Bloch state basis. Assuming that the Bloch states representing a particular atom all reside in the same band n and have quasimomenta q clustered tightly around a central value q_0, we can define an effective mass for the atom [57].

$$m^* = \hbar^2 \Big[\frac{\partial^2 \epsilon}{\partial q^2}\Big]_{q=q_0}^{-1}. \tag{3.37}$$

We use the concept of effective mass in our experiment on transport (dipolar damping) of an array of 1D BECs.

3.4 Atom-Atom Interactions and Overall Confinement

The theory presented above is for a single particle in a uniform periodic potential (one with no overall confinement). The effect of atom-atom interactions and
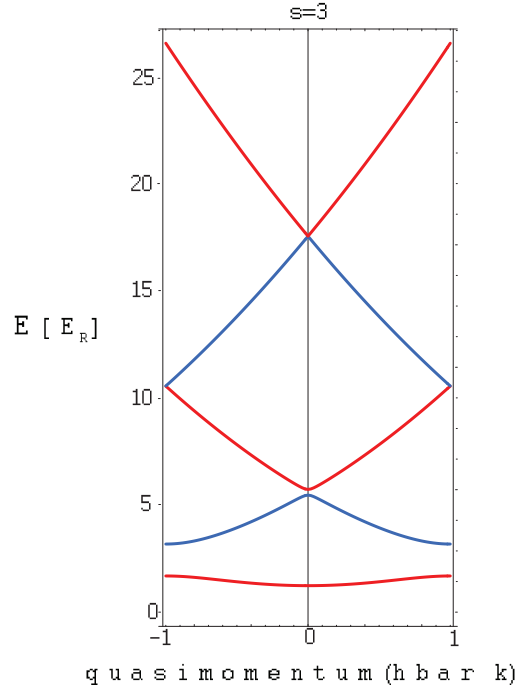
Figure 3.1: Band structure for a 3 E_R deep lattice formed from counterpropagating beams so that $d = \lambda/2$. Energy is given in units of E_R, the single photon recoil energy; quasimomentum is in units of $\hbar k$ with the edges of the bands at ± 1
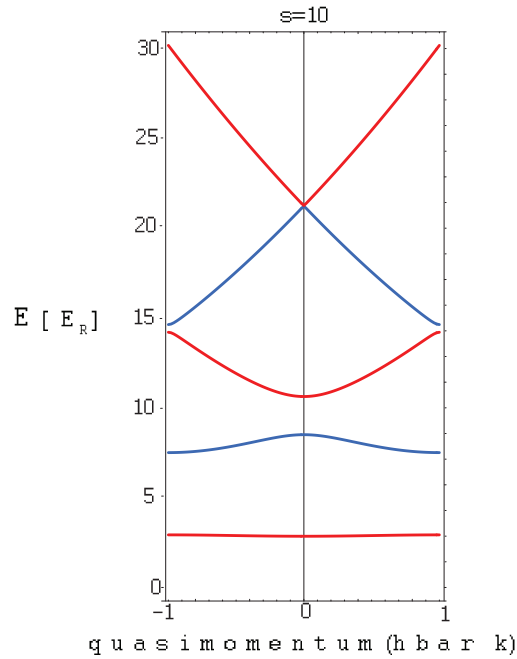
Figure 3.2: Band structure for a 10 E_R deep lattice formed from counterpropagating beams so that $d = \lambda/2$. Energy is given in units of E_R, the single photon recoil energy; quasimomentum is in units of $\hbar k$ with the edges of the bands at ± 1
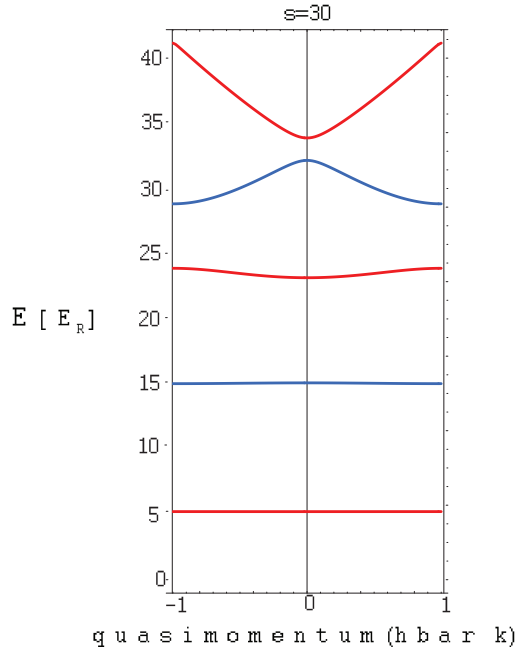
Figure 3.3: Band structure for a 30 E_R deep lattice formed from counterpropagating beams so that $d = \lambda/2$. Energy is given in units of E_R, the single photon recoil energy; quasimomentum is in units of $\hbar k$ with the edges of the bands at ± 1

overall confinement (which jointly can create energy offsets between wells) leads to a possible breaking of translational symmetry so that the single-particle q is in general no longer a good quantum number. The mechanism for this breaking of symmetry is explained as follows. For a deep 1D lattice, one can think of a Bloch state as a chain of harmonic oscillator eigenstates each centered on a well, with the phase difference between neighboring wells $\phi = dq/\hbar$. If the local chemical potential within a well, which is the sum of the local mean-field energy and the local energy offset due to external confinement, were to vary from well to well, then the phase differences between neighboring wells would change over time. By definition, this means that the quasimomentum would change, meaning that it is not a good quantum number.

Usually the atom-atom interactions and energy offsets are small compared to

the eigenenergies of the uniform, non-interacting Hamiltonian H_0, and so the band structure of H_0 is a good approximation to that of the full Hamiltonian (including interactions and inhomogeneity). Nevertheless, the differences need to be kept fully in mind and are quite relevant when we consider time scales for "mapping" bands (described below).

3.5   BEC Diffraction

A Bose-Einstein condensate is diffracted when an optical lattice is applied to it suddenly with respect to all time scales, it is allowed to evolve in the lattice for some duration t_{evolve}, and then the lattice is removed, again suddenly with respect to all time scales. The phenomenon of matter-wave diffraction can be understood very simply in the context of Bloch band theory. Ignoring atom-atom interactions and the overall external confinement, we calculate as follows.

$$\psi_{\text{BEC}}(t = t_{\text{evolve}}) = e^{i\frac{H_0}{\hbar}t}\psi_{\text{BEC}}(t = 0). \tag{3.38}$$

Using H_0 as written in matrix form following Eq. (3.35) in the plane wave basis, we can express $\psi_{\text{BEC}}(t = 0)$ as a single plane wave state $e^{i\kappa x} = |\kappa >$ where $\kappa = 0$ and use H_0 with $q = 0$ *as long as $\psi_{\text{BEC}}(t = 0)$ is spatially large compared to the lattice constant d* (i.e. $\psi_{\text{BEC}}(t = 0)$ extends over many lattice constants). If not, $\psi_{\text{BEC}}(t = 0)$ must be Fourier decomposed into a collection of plane wave states $e^{i\kappa x}$ and each plane wave component evolved separately with the Hamiltonian $H_0^{(q)}$ parameterized by the correct $q = \hbar j$ where $j = \kappa \mod 2\kappa_{\text{L}}$ and χ is the integer part

of $\kappa/2\kappa_{\mathrm{L}}$.

$$\psi_{\mathrm{BEC}}(t = t_{\mathrm{evolve}}) = \sum_{\chi} \sum_{q} e^{i \frac{H_0^{(q)}}{\hbar} t} |\chi, q\rangle . \tag{3.39}$$

Usually, $\psi_{\mathrm{BEC}}(t = 0)$ is spatially much larger than d and so the inner sum reduces to a single term $|q = 0\rangle$. (For an adiabatically loaded condensate, the outer sum also reduces to a single term, $|\chi = 0\rangle$.) The result of this calculation is a set of plane wave states separated by $2\hbar\kappa_{\mathrm{L}}$. For t_{evolve} less than the Raman-Nath time as discussed in Chap. 7, the plane wave weights are given by Bessel functions of the first kind.

3.6 Time Scales, Ground States and Adiabaticity Issues

For a particular energy band of a deep lattice, the time scale for *intraband* dynamics is set by the width of that band. Examples of the dynamics being referred to include spreading of the wave packet and tunneling. The lattice tunneling time in the bottom band is equal to $\hbar/J$ where $J = \frac{1}{4}(\epsilon_{0,\hbar k} - \epsilon_{0,0})$. For *interband* dynamics, the time scale is set by the energy differences between the states in the different bands. Obviously, there is a strong q-dependence to this interband timescale to the extent that the bands of interest are not flat.

We often require that a system remain in its ground state during the course of a change in the Hamiltonian. The general expression of this requirement is the *adiabaticity criterion*:

$$\left\langle \mathrm{e}|\dot{H}|\mathrm{g} \right\rangle \ll \frac{(E_{\mathrm{e}} - E_{\mathrm{g}})^2}{\hbar}, \tag{3.40}$$

46

where H is the total Hamiltonian, E is the energy of a state, and g, e refer to the ground and excited states. As an example, consider a BEC composed of non-interacting ^{87}Rb atoms trapped in a box potential. If a 1D optical lattice is applied to the BEC and one wishes to remain always in the absolute ground state, then the time scale for applying the optical lattice must be much greater than all other relevant time scales in the problem. The easiest time scale to be adiabatic with respect to (because it is so short) is that for band excitation at the center of the Brillouin zone in which evaluation of the adiabaticity criterion between the bottom and first band at $q = 0$ leads to [33]

$$\frac{ds}{dt} \ll 32\sqrt{2}\frac{E_\mathrm{R}}{\hbar}, \tag{3.41}$$

where s is the lattice depth in E_R and $E_\mathrm{e} - E_\mathrm{g}$ is set equal to $4E_\mathrm{R}$ because this is the minimum $q = 0$ energy difference between the two bands at $t = 0$. After $t = 0$ the energy difference increases and so the adiabaticity criterion is more easily met. However, away from $q = 0$ the energy difference decreases and so it is more difficult to be adiabatic. At the band edge $(q = \hbar k)$, it is impossible to be adiabatic at the instant the lattice is first applied and so band excitation in the form of Bragg scattering always occurs.

Now consider the BEC to be initially confined in an overall harmonic trap with average confining frequency $\bar{\omega} = (\omega_x \omega_y \omega_z)^{1/3}$. If the condensate is at rest with respect to the lattice as its depth is changing (we are at the center of the band), the most stringent adiabaticity criterion (for shallow lattices) is normally with respect

to the overall harmonic trap energy $\hbar\bar{\omega}$ (the smallest energy in the problem). Since $\bar{\omega}/2\pi$ can often be as small as 10 Hz, the timescale of adiabatic optical lattice ramps is often on the order of hundreds of milliseconds. Note that for very deep lattices, the tunneling energy J can be less than $\hbar\bar{\omega}$ and then this energy sets an even more stringent criterion for adiabaticity. An example where this would be relevant would be a shifting of the magnetic trap with the atoms already in a deep optical lattice.

The above adiabaticity examples are all for non-interacting systems. In the presence of *weak* atom-atom interactions, a condition for atoms to remain in the total ground state of a system while a lattice is being created or modified, is that they be given sufficient time to redistribute themselves between wells so that the local chemical potential does not vary from site to site. Again, this is a requirement in the weakly interacting regime where the tunneling energy J is much greater than the on-site interaction energy U (the local interaction energy bewteen two atoms). (If a system is already in the strongly interacting regime, where $U \gg J$, time scales can be much faster as discussed below.)

The timescale to be adiabatic with respect to weak atom-atom interactions is set by the mean field energy which in 3D is equal to $U_{\mathrm{int}} = \frac{4\pi\hbar^2 a}{m}n$ (Eq. (3.29)). For shallow lattices, this energy is typically intermediate between $\hbar\bar{\omega}$ and J. As the lattice depth increases, J decreases while U_{int} increases. At some point they cross each other and U_{int} becomes the second highest energy in the problem (after the band excitation energy which is $\simeq \hbar\omega_{\mathrm{L}}$. Depending on the total number of atoms N in the condensate and the strength of the confinement, U_{int}/h is typically in the range of 100 Hz to a few kHz.

Adiabaticity issues are very complicated and there are many unresolved problems currently under investigation. To give a feel for some of the issues being discussed, consider the following. The adiabaticity criterion given in Eq. (3.40) is misleading when considering system changes while in the Mott insulator state. Extremely fast Hamiltonian changes can occur while remaining fully in the ground state because the new ground state (the one for the new, changed Hamiltonian) is so close (in Hilbert space) to the old one, that non-adiabaticity, which occurs, is not really a problem.

The following subsection describes an process in which the time scale associated with U_{int} (as well as J) is very relevant.

3.6.1   Band Mapping

As mentioned above, the calculated band structure for a Hamiltonian describing non-interacting atoms in a homogeneous infinite lattice, H_0, is often a good approximation to the band structure for the true Hamiltonian which includes atom-atom interactions and external confinement [147]. This is especially true for 3D red-detuned lattices where these two effects nearly balance each other [148]. In general, however, these band structures are different.

Consider an experiment in which we adiabatically apply an optical lattice to an initially harmonically-trapped BEC. At the conclusion of the ramp, the system is still in the ground state of the many-body Hamiltonian. For weak atom-atom interactions, the band structure and eigenstates for the new Hamiltonian which includes

49

the mean-field interactions, H_{MF}, can be calculated [147]. In this new mean-field Bloch basis, the system is in the $n_{\mathrm{MF}} = 0$ (bottom) band at $q_{\mathrm{MF}} = 0$. It is not at $n = 0$ and $q = 0$ for the uniform, non-interacting Hamiltonian H_0. In fact, in general the projection of a mean-field Bloch state onto the single-particle Bloch basis will result in an occupation of *all* the states. Usually, however, the two bases are sufficiently similar (because interactions are weak) that a $|n_{\mathrm{MF}}, q_{\mathrm{MF}}\rangle$ Bloch state projects meaningfully onto only a small interval centered at the corresponding $|n, q\rangle$ single-particle Bloch state. For instance, the $|n_{\mathrm{MF}}, q_{\mathrm{MF}} = 0, 0\rangle$ mean-field ground state would project onto a small centered interval in the bottom band of the spectrum of H_0.

If we wish to know the projection of the H_{MF} ground state onto the single-particle Bloch basis, the lattice must be turned off in a time scale that is fast compared to $\hbar/U_{\mathrm{int}}$ (and $\hbar/J$) but slow compared to the interband separation. (This is not always possible.) The reason it must be slow compared to the interband separation is that we wish to adiabatically "map" each single-particle quasimomentum state onto its corresponding plane wave state (i.e. not diffract the wavefunction). Thus, the single-particle band structure must be smoothly transformed into the free particle dispersion relation. Following this "band mapping", and after a suitably long time-of-flight for the atoms, the spatial distribution reflects the momentum distribution within the single-particle band [46]. A limitation of this technique is that mean field effects during expansion blur the narrowest widths visible as does the initial size of the condensate, if one does not have a sufficiently long time of flight, which is often the case. If the condition on band excitation is violated, multiple

copies of the mapped band are created.

Chapter 4

The NIST Rubidium-87 Bose-Einstein Condensate Apparatus

This chapter covers the nuts and bolts of the NIST ^{87}Rb Bose-Einstein condensate apparatus, in which I will concentrate on the parts I was most involved with during its reconstruction in 2004. When the experiment was moved from Building 221 to Building 216 in the NIST AML (Advanced Measurement Laboratory), although we did not break the ultra-high vacuum or alter the main Ioffe-Pritchard magnetic trap, we took the opportunity to design and build a new system for creating and delivering the laser light to the atoms. In addition, changes were made to the oven region of the experiment. As the sole graduate student working on the experiment, I believe there is substantial benefit in documenting and describing as much of the hardware as is reasonably possible in this thesis for use by those who will continue to use the apparatus.

The ^{87}Rb BEC apparatus is composed of several subsystems. In order to perform the experiments described in this thesis, the subsystems must work together in concert. This chapter will describe the hardware aspects of the vacuum system, Zeeman slower magnetics, magneto-optical trap magnetics, slowing/trapping/cooling lasers, Ioffe-Pritchard trap, magnet cooling/dummy load/interlock system, and optical lattice laser system.

4.1 The Vacuum System

The vacuum system is built on a 12 inch thick non-magnetic (TMC 304 stainless steel) optical table and, as shown in Figure 4.1, encompasses a high vacuum (HV) region for the atom oven source and an ultra-high vacuum (UHV) region with good optical access where the experiments take place in a glass cell. The HV and UHV regions are connected by a differential pumping tube which also serves as a conduit for the atomic beam. We now describe the two vacuum regions.

4.1.1 HV Oven Chamber Region

The HV region contains the ^{87}Rb oven and is pumped by a 125 l/s ion pump (Varian VacIon Plus 150 Ion Starcell, MidiVac controller) with a non-evaporable getter insert (SAES CapaciTorr D 400-2). The HV manifold consists of a 14-port multi-CF (conflat) spherical square chamber (Kimball Physics) to which is attached the ^{87}Rb oven and the 125 l/s ion pump/getter. A Bayard-Alpert nude ion gauge (Granville-Phillips Series 274) attached to one arm of a six-way 2-3/4 inch CF cross on the opposite side of the ion pump from the oven normally reads approximately 3 10^{-10} Torr (Granville Phillips 307 controller). This reading is probably lower than the actual pressure in the oven region due to the low conductance between the ion gauge and the oven. The current leads for the getter insert occupy one arm of the cross. We use another arm as a pump-out port during periodic ion pump bakes (Varian all-metal valve 9515027).
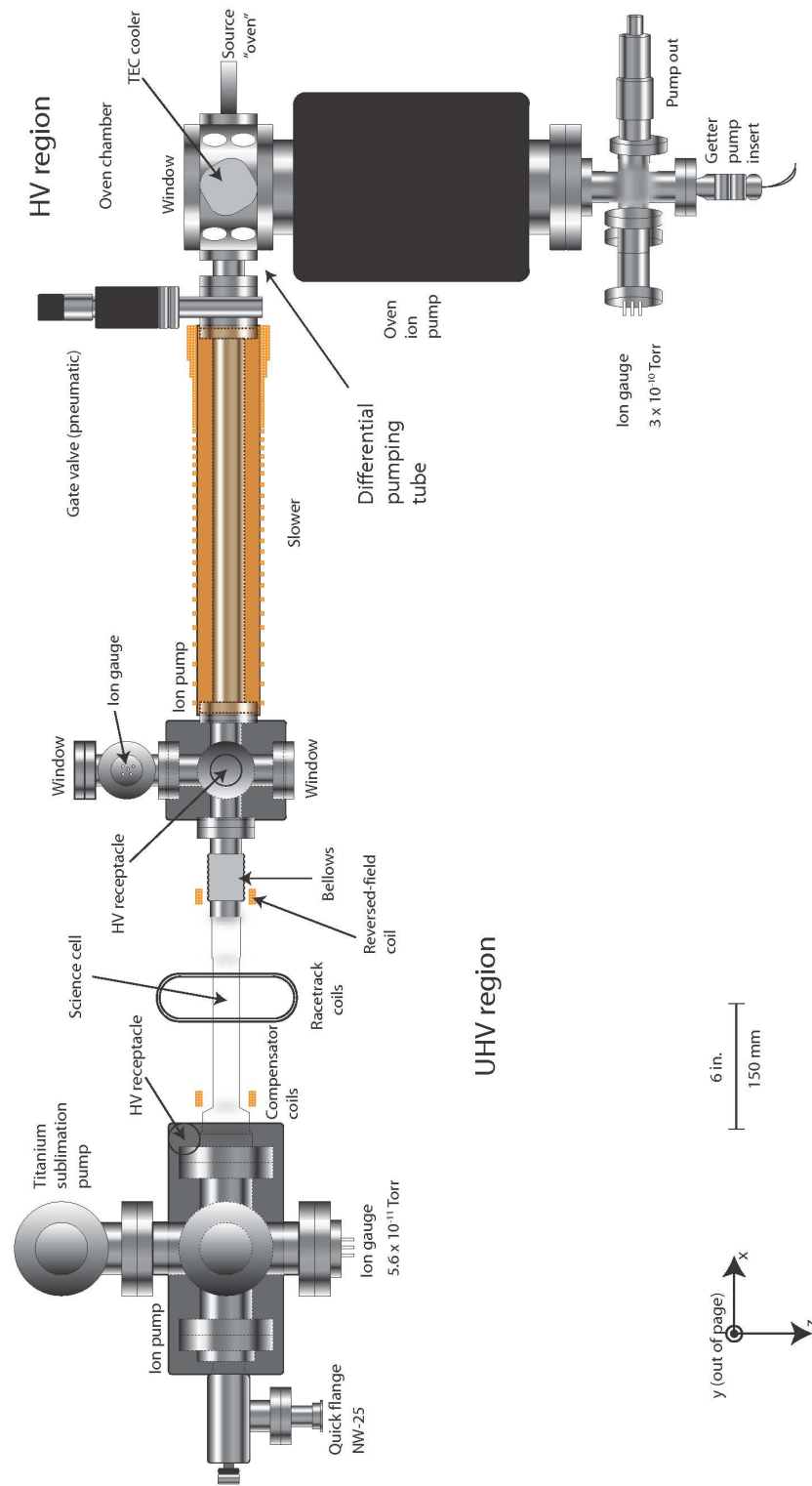
Figure 4.1: Layout of ^{87}Rb BEC apparatus vacuum system (view from above).

54

The ^{87}Rb Oven

The ^{87}Rb oven has had several incarnations. Currently, it is simply a crushed ^{87}Rb glass ampoule within a copper pinch-off tube (Duniway Stockroom) with an aluminum annulus insert in front of it which by itself probably provides very little beam collimation. During operation, the back of the oven is kept at approximately 135°C (nichrome heating wire/Omega temperature controller) while the front is cooled with chilled water to 55°F. Beyond the oven and within the HV oven chamber is a mechanical shutter (Uniblitz) attached to the differential pumping tube which blocks and unblocks the atomic beam. The shutter aperture plus the bore hole in a copper block cooled by a thermo-electric cooler provide additional collimation for the atomic beam effusing out of the oven. The differential pumping tube is a copper pinch-off tube mounted on a 2-3/4 inch CF flange (Duniway Stockroom). Its dimensions are 0.3 inch inner diameter and 2.0 inch length.

In an attempt to improve the performance of the source, we have bench tested a source that uses glass capillary arrays (Burle Industries). Based on theoretical models [145], we have experimented with a variety of glass capillary pore diameters, lengths, and densities. We have tried both leaded and soda glass heated to temperatures in the range of 135°C to 195°C. The result of these experiments is that the glass has always disintegrated at some point while being heated in the presence of the ^{87}Rb. We have heard anecdotally that pure SiO_2 is the only type of glass that can withstand alkali chemistry in this temperature range, but have not been able to test this assertion because, as far as we know, there are no longer any manufac-

turers of SiO_2 glass capillary arrays. These bench tests have so far not led to any modifications of the oven design on the apparatus.

Our final attempt to improve beam collimation will occur in late 2006 using a copper test oven on the bench. I designed and built a beam collimator consisting of a bundled array of 200 stainless steel tubes (McMaster-Carr) housed within a copper pinch-off tube. Each tube is 12 mm long with an inner diameter of 300 μm (40:1 aspect ratio). Since both the tube length and inner diameter are less than the calculated approximate 1 cm mean free path of the ^{87}Rb atoms (at the estimated temperature and pressure a few cm from the ampoule), this steel tube array should significantly improve beam collimation [145].

4.1.2   UHV Science Cell Region

The UHV region is pumped by two ion pumps, of capacity 20 l/s and 50 l/s (Varian VacIon Plus 20 Ion Starcell, Varian VacIon Plus 55 Ion Starcell, MidiVac controller). In addition, a water-cooled titanium sublimation pump (Varian) is connected to the UHV manifold. The UHV region includes the Pyrex science cell with a five-way 2-3/4 inch CF cross connected by a bellows at one end, and a 4-1/2 inch CF tee at the other end. The science cell was made by Jack Fuller (NIST glass shops) by frit sealing together 3.3 mm thick pieces of uncoated Pyrex glass which was then glass-blown by Jeff Anderson (NIST glass shops) onto the glass/metal CF piece (probably MDC). Also connected to the five-way cross are the 2-3/4 inch nipple for the Zeeman slower, the 20 l/s ion pump, and a 2-3/4 inch CF tee (which

has a window and a nude ion gauge). At the oven end of the Zeeman slower, there is a pneumatically-actuated 2-3/4 inch metal gate valve (MDC GV-1500M-P) which automatically closes if the pressure exceeds a setpoint, and then a very short 2-3/4 inch nipple (holding the differential pumping tube) connected to the oven chamber.

On the side of the science cell away from the Zeeman slower a 4-1/2 inch CF tee is connected to the cell. On top of the 4-1/2 inch CF tee is a six-way 4-1/2 inch CF cross which extends up vertically. The top arm of this cross connects to the 50 l/s ion pump. The four remaining arms contain a 2-3/4 inch pump-out valve (MDC, 1-1/2 inch diameter all-metal connected with a zero-length adapter), a 4-1/2 inch CF vertical elbow on top of which is the titanium sublimation pump, and a nude ion gauge. The pressure in the UHV region reads in the mid 10^{-11} Torr range.

Relocation of the UHV System

As a testament to the robustness of the UHV system, the entire UHV assembly was removed from an optical table, transported under ultra-high vacuum (approximately 1.0 x 10^{-10} Torr) from the old NIST physics Building 221 to the new space in Building 216 of the AML, and then repositioned on the new optical table. Figure 4.2 shows a group of extremely nervous physicists nearing the end of that harrowing journey.

We believe that a very small temporary leak may have occurred during the relocation, requiring a rebake of the UHV region. (It could also have been a virtual leak associated with turning on and off the ion pumps.) Although the Pyrex
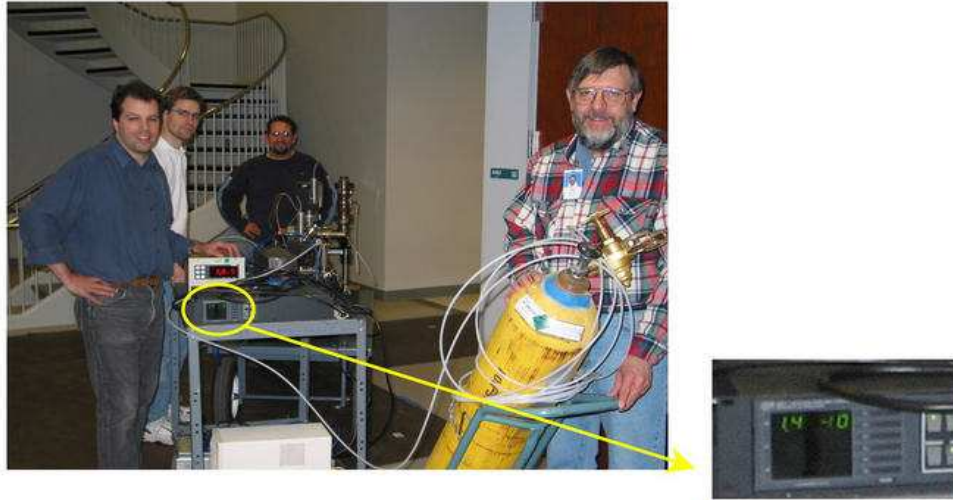
Figure 4.2: Transporting the ^{87}Rb BEC UHV chamber from Bldg. 221 to Bldg. 216. Ken O'Hara, Chad Fertig, Johnny Huckans, and Bill Phillips (the man with the beard) sometime during early spring 2004.

science cell and stainless steel are bakeable to 450ºC, the epoxy used to set the Ioffe-Pritchard magnets around the cell can be heated safely only to approximately 90ºC before it starts to soften. Steve Rolston and I performed an "easy-bake" by blowing 90ºC Glocoil-heated air for almost a week into an aluminum foil tent surrounding the UHV assembly. This procedure restored our pressure to the mid 10^{-11} Torr range.

4.2   Zeeman Slower and Magneto-Optical Trap Magnetics

To load the magneto-optical trap (MOT), we Zeeman-slow a large number of atoms to below the MOT capture velocity. The calculated magnitude of the mag-

netic field generated by the Zeeman slower as a function of distance down its axis is shown in Figure 4.3. This plot was generated by Chad Fertig by making dimensional measurements of the slower helix and then calculating the field in Mathematica using the Biot-Savart law with the currents we employ in the laboratory which are (40A, -51A) for the (slower, reverse slower). Based on this field profile and the slower laser detuning (approximately 150 MHz) below the F=2 to F'=3 transition, we slow atoms with initial velocities less than approximately 200 m/s (using a value of 100 G for the point where atoms fall onto the curve). At an oven temperature of 400K, the atomic velocity distribution is centered at approximately 200 m/s. At the end of the slower, atoms decouple from the field to be captured by the MOT at a velocity of a few m/s.
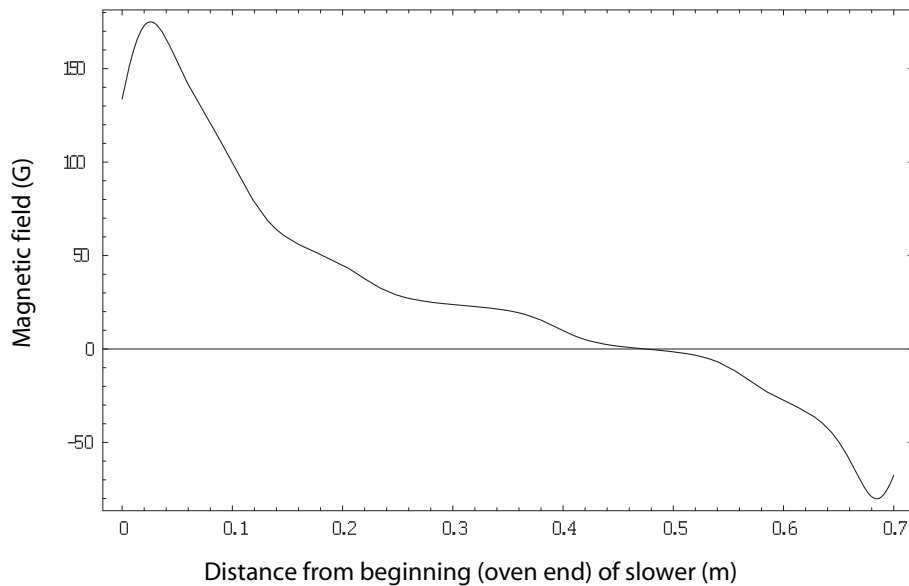
Figure 4.3: Calculated magnitude of the magnetic field along the NIST ^{87}Rb slower and reverse slower. The field direction is along the axis of the slower and reverse slower.

Because the magnetic field of the Zeeman slower does not follow a square

root profile $B(z) = B_{\mathrm{b}} + B_{\mathrm{o}}\sqrt{1 - (z/z_0)}$ [25], the deceleration of the atoms is not constant. Over the length of the slower, the average deceleration is approximately 10^5 m/s^2 which is roughly 60% of the maximum achievable deceleration, $\hbar k\gamma/2m$. The Zeeman slower is constructed of insulated hollow square copper tubing wound around and epoxy-potted onto a phenolic cylindrical form. The copper tubing is cooled with chilled water and protected by an interlock system (described in a later section of this chapter).

The MOT magnet is composed of two parallel, co-axial approximately square air-cooled coils (20 turns each) powered by separate bipolar supplies (Kepco). The coils are separated by a distance roughly equal to their diameters (approximately 8 cm). When equal current flows in parallel (quasi-Helmholtz), a measured magnetic field of 1.35 G/A in the $\hat{y}$ direction is created. When equal current flows in opposition, measured magnetic field gradients of 0.86 G/Acm in the $\hat{y}$ direction, 0.38 G/Acm in the $\hat{x}$ direction, and 0.47 G/Acm in the $\hat{z}$ direction are created. This asymmetry in the $\hat{x}$ and $\hat{z}$ direction field gradients is due to the MOT coils not being exactly square. The ability to control the MOT coils separately allows us to control the gradient and constant offset separately which is useful for other experiments in the Ioffe-Pritchard trap. During MOT loading, we run 16.6 A in the upper coil and -15 A in the lower coil. At the end of the MOT, molasses, and optical pumping stage, we typically have an approximately 5 mm cloud of a few 10^9 atoms in the F=1 ground hyperfine state at a temperature of approximately 40 μK as determined by time-of-flight measurements followed by absorption imaging [1].

4.3   Slowing and Trapping/Cooling Lasers

On a separate table from the main apparatus, are three commercial diode lasers used to slow, cool, trap, and probe the atoms. Figure 4.4 shows the layout of these lasers and associated optics on the table. The optical powers indicated at various locations in this figure are approximate. A New Focus Vortex 6013 master (7 mW, Littman) external cavity diode laser (ECDL) is locked using standard saturated absorption spectroscopy between the $F = 2$ hyperfine ground state and the $F' = 2, 3$ crossover of the $5^2P_{3/2}$ upper state. This light is then distributed via optical fiber to beat-note lock two other diode lasers: a Toptica DLX 110 (400 mW, distributed feedback, Littrow) used for the $F = 2$ to $F' = 3$ cycling transition in the slower, MOT, and imaging probe; and a Toptica DL 100 (150 mW, ECDL, Littrow) used for the $F = 1$ to $F' = 2$ repumping [26] of the atoms that have fallen out of the cycling transition in the slower and MOT.

The locking of the cycling transition laser, which is used both for the MOT and for the slower (with different shifts from AOMs), is achieved by beating its light against that of the master on a fast photodiode (Hamamatsu). The approximately 100 MHz beat signal is frequency divided down and compared to a voltage-controlled frequency source (voltage sent from the computer). The error signal is fed back to the current input on the cycling laser. The locking of the repump laser is achieved also by beating its light against that of the master on an integrated photodiode/amplifier contained within a National Semiconductor Lab Buddy and then sending the RF beat frequency into the arms of an RF Mach-Zehnder interferometer, one arm of
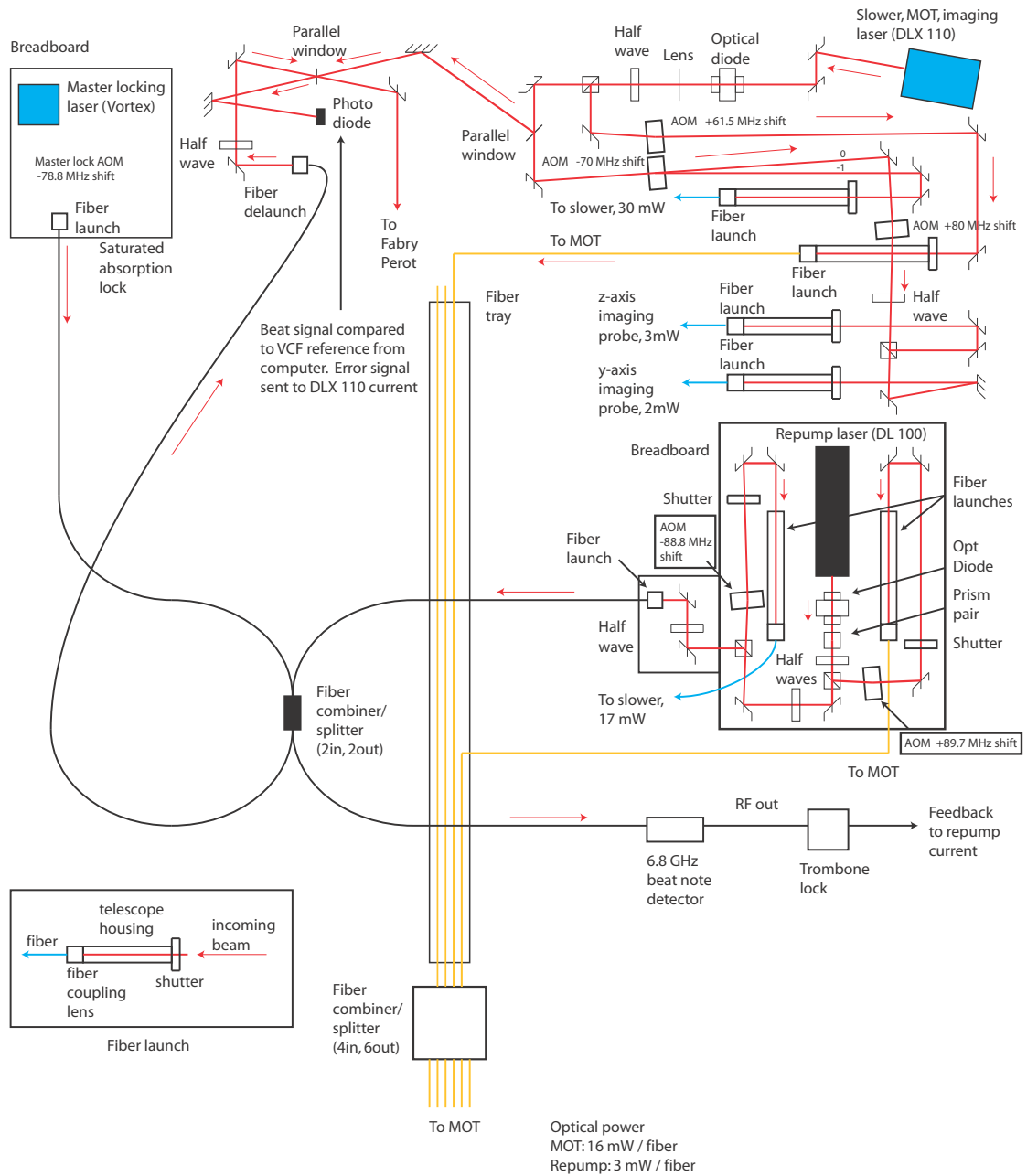
Figure 4.4: Layout of lasers on a separate table from the main apparatus for slowing, cooling, trapping and absorption imaging the atoms. The master laser (7 mW Vortex) is locked using standard saturated absorption spectroscopy. Its light is then used as a reference to beat-note lock the cycling and repump lasers.

which has a phase delay from a 6.8 GHz trombone [146]. The error signal is fed back to the current input of the repump laser. Diagrams of the various laser frequency shifts obtained as a result of the locking and acousto-optical modulators are shown in Figures 4.5 and 4.6. The frequencies shown in Figure 4.6 are not the frequencies seen by the atoms.
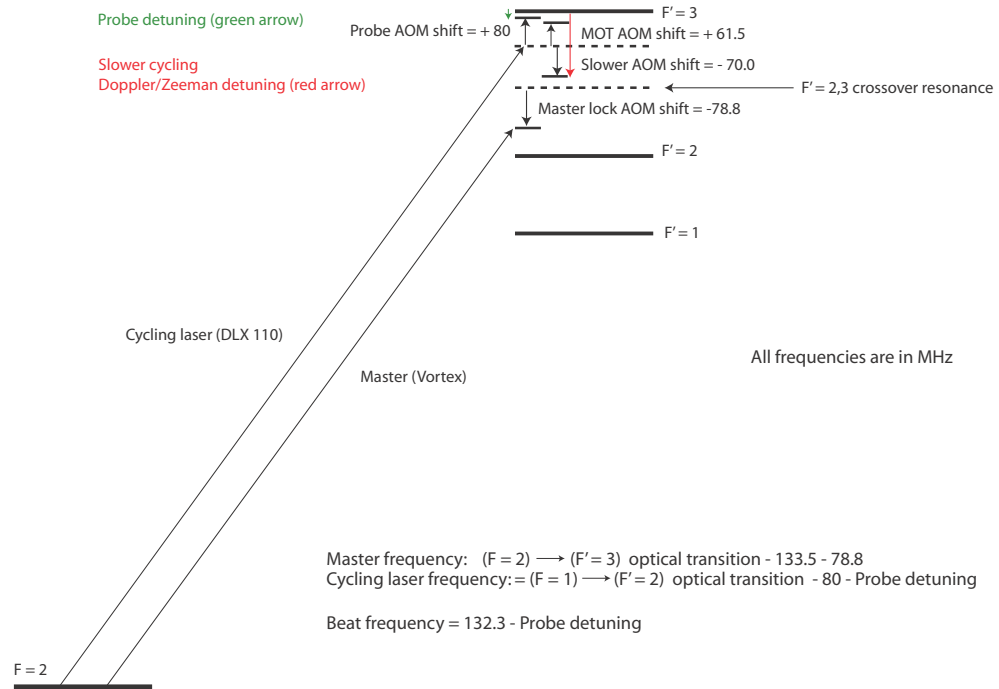
Figure 4.5: Frequencies of the master and cycling laser.

Light from the cycling and repump lasers for the MOT is launched into 2 of the 4 inputs of a 4-input/6-output polarization-maintaining fiber combiner/splitter (Canadian Instrumentation & Research, Ltd.) and then brought over to the experiment table. Using optical fibers to deliver light to the experiment has enabled us to decouple the generation and locking of the trapping laser light from the rest of the experiment. Thus any changes we make to the optics near these lasers do not require us to make changes to the optics near the experiment. This has obviated

F′ = 3

133.5

F′ = 2,3 crossover resonance

Master lock AOM shift = -78.8

F′ = 2

MOT repump detuning (green arrow)

MOT repump AOM shift = + 89.7

Slower repump
Doppler/Zeeman detuning (red arrow)

Slower repump AOM shift = - 88.8

F′ = 1

Master (Vortex)

All frequencies are in MHz

Repump (DL 100)

Master frequency: (F = 2) ⟶ (F′ = 3) optical transition - 133.5 - 78.8
Repump frequency: = (F = 1) ⟶ (F′ = 2) optical transition - 89.7 - MOT repump detuning

Beat frequency = 6690.3 - MOT repump detuning

F = 2

6834.7

F = 1

Figure 4.6: Frequencies of the master and repump laser.

a lot of extremely time-consuming and tedious beam alignment (which we used to perform in the old setup). In addition, having the trapping lasers on a different table than the vacuum chamber (where we normally are working, i.e. dropping Allen wrenches) allows the lasers to stay locked longer.

The MOT cycling and repump light is combined within the fiber combiner/ splitter. The six outputs feed six beam expanders/circular polarizers (designed by Ken O'Hara). The light from each expander reflects off an oval, gold, AR-coated mirror mounted on a mechanical flipper (Newport) which snaps out of the way to provide optical access when the MOT stage is finished. The slower and slower repump light is separately fiber launched and delaunched, without using a fiber combiner/splitter. After delaunch, the slower and repump light is combined

using a polarizing beamsplitter cube. Incidentally, in a zero-crossing slower (which is what we have) the slower repump light is normally tuned to work in the zero crossing region to prevent huge cycling losses due to atom disorientation. This was Chad Fertig's original design intent when he built the repump locking system. Experimentally, however, we have tuned our slower repump light to give us the largest possible MOT and the resultant frequency is *not* tuned to the zero crossing region (taking into account the velocity of the atoms). We surmise that our slower repump light is also important in the region between the oven and the beginning of the slower.

4.4   The Ioffe-Pritchard Trap

Magnetic trapping of neutral atoms is due to the Zeeman interaction between the magnetic moment $\vec{\mu}$ of the atom with an external magnetic field $\vec{B}(\vec{r})$. An atom in an inhomogeneous field experiences a force. The energy of an atom with magnetic moment $\vec{\mu}$ is

$$E_{\mathrm{zm}} = -\vec{\mu} \cdot \vec{B}(\vec{r}),$$
(4.1)

where $\vec{\mu} = m_F g_F \mu_{\mathrm{B}} \vec{F}/\hbar$. Here, m_F is the hyperfine magnetic quantum number, g_F is the hyperfine Landé g-factor, μ_{B} is the Bohr magneton, and $\vec{F}$ is the total angular momentum of the atom. From this expression, we see that atoms with positive magnetic moment are driven to regions of higher field (high field seekers) and those with negative magnetic moment are driven to low fields (low field seekers). Because it is impossible to create a magnetic field with a local maximum (in regions

65

where there are no electrical currents) [139], the only states trappable by magnetic field alone are those with negative magnetic moment. For ^{87}Rb, the relevant states are $|F = 1, m_F = -1\rangle, |F = 2, m_F = 1\rangle, |F = 2, m_F = 2\rangle$, and $|F = 2, m_F = 0\rangle$. (The $|F = 2, m_F = 0\rangle$ state is trappable due to the quadratic Zeeman effect.) For this thesis, experiments were done with ^{87}Rb atoms in the $|F = 1, m_F = -1\rangle$ state.

If the atom remains in the same quantum state relative to the instantaneous direction of the magnetic field, then the potential felt by the atom is simply proportional to the magnitude of the external magnetic field. However, a moving atom experiences a time-varying magnetic field which can induce transitions to untrapped states. If the rate of change of the magnetic field is comparable to or larger than the transition frequencies between the magnetic sublevels (of order $\mu_B|\vec{B}|$), then substantial "Majorana" spin-flip losses can occur. This puts a lower limit on the local magnetic field minimum which we can allow in our trap. An estimate of this minimum field can be obtained using the Landau-Zener parameter Γ_{lz} [140, 141]. While crossing the local minimum, the atomic magnetic moment will adiabatically follow the local direction of the magnetic field (and remain trapped), if:

$$\Gamma_{lz} = \frac{(g_F \mu_B B_{min})^2}{\hbar m_F g_F \mu_B \alpha v_T} \gg 1, \tag{4.2}$$

where B_{min} is the magnitude of the local field minimum, α is the gradient of the magnetic field in the vicinity of the local minimum and $v_T = \sqrt{8k_B T/\pi M}$ is the thermal velocity of the atom. We do not expect our magnetic trap to have atoms hotter than 1mK and so we can suppress Majorana losses on a single pass to the

10^{-5} level if $B_{\min} \geq 0.3$ G [144]. For this calculation we use $\alpha = 500$ G/cm and a transition probability of $e^{-\Gamma_{lz}}$. Observe that although high energy atoms have greater v_T than low energy atoms, this does not on average result in more Majorana loss. The reason is that the high energy atoms also have high angular momentum which tends to keep most of them away from the trap center.
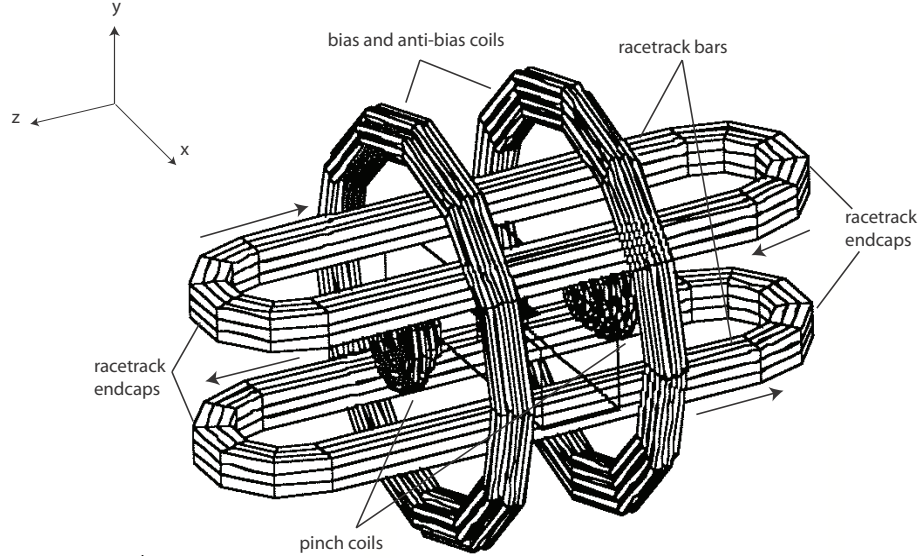
Figure 4.7: The Ioffe-Pritchard trap geometry. The racetrack bars produce a linear quadrupole field for radial confinement in the xy-plane with current directions indicated by the arrows. The pinch coils provide confinement along the z-axis. The field from the anti-bias coils counters the pinch field along $\hat{z}$ bringing the total field down to the 1 G level in the vicinity of the origin. The bias coils vary the radial gradient.

We create a magnetic field with a local minimum above zero based on the very successful Ioffe-Pritchard design [142]. As shown in Figure 4.7, the major components of the Ioffe-Pritchard (IP) trap are a double racetrack creating radial confinement in the xy-plane, two large coaxial (z-axis) bias coils in a nearly Helmholtz configuration to vary the radial confinement, and two small coaxial (z-axis) pinch coils (with two large, nearly Helmholtz antibias coils in current series but with

67

opposing direction) with a separation much larger then their radius to provide confinement in the $\hat{z}$ direction. The Ioffe-Pritchard trap can be viewed as a magnetic bottle. Because of the large currents used, the IP trap is continuously cooled by water flowing through the hollow-core copper tubing used to form the traps.

The magnetic field of the IP trap is the sum of the fields of the individual magnets which comprise it: the pinch, antibias, and bias coils, and the racetrack.

$$\vec{B}_{\text{IP}} = \vec{B}_{\text{p}} + \vec{B}_{\text{ab}} + \vec{B}_{\text{b}} + \vec{B}_{\text{rt}}. \tag{4.3}$$

We now describe the individual components.

4.4.1   Pinch/Antibias/Bias Coils

The currents in the pinch coils flow in the same direction; however, since the coil separation is much larger than the coil radius (i.e., *not* a true Helmholtz configuration), a magnetic field minimum is created in the vicinity of the midpoint between the coils. The magnetic field along the z-axis created by the pinch coils points in the $\hat{z}$ direction and is a positive quadratic (centered at the trap minimum) plus a spatially constant offset (also pointing in the $\hat{z}$ direction). A pair of large, nearly Helmholtz antibias coils (approximately coplanar and concentric with the pinch coils) are wound in series with (but opposing) the pinch coils to create a negative field along $\hat{z}$ which very nearly (but not totally, in order to avoid Majorana losses) cancels out the constant part of the pinch coil field.

The bias coils are also nearly Helmholtz. They are wound on top of the

antibias coils with current running opposite to the antibias coils. The magnetic field is dominated by a spatially constant term which points in the $\hat{z}$ direction (in the same direction as the pinch field). The purpose of the bias field is to allow us to vary the confinement in the radial direction provided by the racetrack. The bias field is orthogonal to the racetrack field, and the total field (vector sum of the two) has a magnitude whose curvature in the radial direction is bias field-dependent. The field from the pinch/antibias coils must be added to the bias field in calculating this confinement.

The pinch, anti-bias, and bias fields can be expressed exactly (for idealized coils) using eliptic integral solutions for the individual coils. The general solution for the magnetic field from a pair of coaxial coils with current flowing in the same direction is [143]:

$$
\begin{aligned}
\vec{B}_{00} &= \frac{\hat{x}G_0 x}{R\sqrt{x^2+y^2}}\left[\frac{\gamma_1}{Q_1}\left(E(k_1)\frac{1+\alpha^2+\beta_1^2}{Q_1^2-4\alpha}-K(k_1)\right)+\frac{\gamma_2}{Q_2}\left(E(k_2)\frac{1+\alpha^2+\beta_2^2}{Q_2^2-4\alpha}-K(k_2)\right)\right] \\
&+ \frac{\hat{y}G_0 y}{R\sqrt{x^2+y^2}}\left[\frac{\gamma_1}{Q_1}\left(E(k_1)\frac{1+\alpha^2+\beta_1^2}{Q_1^2-4\alpha}-K(k_1)\right)+\frac{\gamma_2}{Q_2}\left(E(k_2)\frac{1+\alpha^2+\beta_2^2}{Q_2^2-4\alpha}-K(k_2)\right)\right] \\
&+ \frac{\hat{z}G_0}{R}\left[\frac{1}{Q_1}\left(E(k_1)\frac{1-\alpha^2-\beta_1^2}{Q_1^2-4\alpha}+K(k_1)\right)+\frac{1}{Q_2}\left(E(k_2)\frac{1-\alpha^2-\beta_2^2}{Q_2^2-4\alpha}+K(k_2)\right)\right], \quad (4.4)
\end{aligned}
$$

where the following are defined.

$$
G_0 = \frac{\mu_0 nI}{2\pi} \quad (\mu_0 = \text{magnetic constant}, \; n = \text{number of turns}, \; I = \text{current})
$$

$$
R = \text{coil radius}
$$

$$
L = \text{distance between coils}
$$

$$\gamma_{1,2} = \frac{z \pm L/2}{\sqrt{x^2 + y^2}}$$

$$\alpha = \sqrt{x^2 + y^2}/R$$

$$\beta_{1,2} = z/R$$

$$Q_{1,2} = \sqrt{(1+\alpha)^2 + \beta_{1,2}^2}$$

$$k_{1,2} = \sqrt{4\alpha/Q_{1,2}^2}$$

$$E = \text{complete elliptic integral of the first kind}$$

$$K = \text{complete elliptic integral of the second kind.}$$

Using these exact solutions for the coils, we plot on Figure 4.8 the magnitude of the magnetic field along the z-axis at three stages in the creation of our ^{87}Rb BEC. Stage 1 is the state of the IP trap when the atoms are transferred from the MOT to the trap. Stage 2 is the "tight" trap achieved after compression (in which we increase the current in the coils and reduce the bias current to zero). RF evaporation is performed in this "tight" trap. After evaporation, stage 3 is the expanded trap at which point we transfer the atoms into an optical lattice.

4.4.2 Racetrack Magnet

As the name implies, the racetrack magnet looks like two oblong parallel racetracks, one above the other. In cross-section, the four long sides are at the corners of a square. Because the current runs in alternating directions as one goes around the square, the magnetic field is quadrupolar in the radial (xy) plane. When the field from the racetrack is added to the combined field from the bias, pinch, and

Atom transfer from MOT to IP trap

RF evaporation of atoms

Atom transfer from IP trap to optical lattice
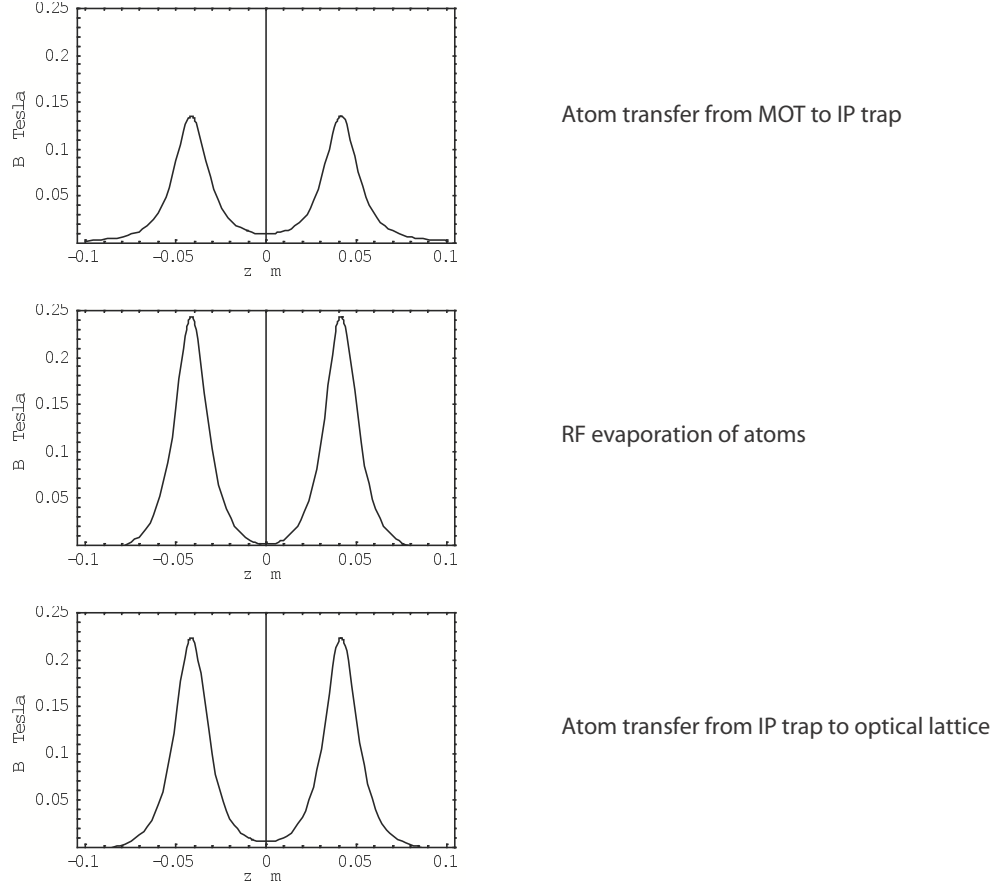
Figure 4.8: Magnitude of the magnetic field of the Ioffe-Pritchard trap along the $\hat{z}$ direction. The pinch coils create a magnetic field minimum for confinement along the $\hat{z}$ direction. This field is reduced by the antibias coils to the 1 G level in the vicinity of the origin. The bias coils independently vary the magnitude of the field at the bottom of the potential (trap bottom) and the radial gradient.

antibias coils, the total field points predominately in the $\hat{z}$ direction, however with a magnitude that is radially-dependent. Thus, we obtain variable radial confinement while keeping the quantization axis very nearly constant (in the $\hat{z}$ direction). (When the field from the bias coils is zero and $I_{\mathrm{rt}} = 540$ amps, the remnant field from the pinch/antibias coils (at $I_{\mathrm{p,ab}} = 580$ amps) is sufficient to not tilt the quantization axis more than .01 radian as long as the radial displacement $\rho \leq 13\mu$m.)

We model the racetrack magnet as four infinite bars and two endcap half-loop

"coils" with current flowing in opposite directions. The exact expression [143] for this model is

$$
\begin{aligned}
\vec{B}_{\text{rt}} &= \hat{x}G_0\bigg[\frac{-y+\frac{d}{2}}{\displaystyle\sum_{i=x,y}(i-\frac{d}{2})^2} + \frac{y+\frac{d}{2}}{\displaystyle\sum_{i=x,-y}(i-\frac{d}{2})^2} + \frac{-y-\frac{d}{2}}{\displaystyle\sum_{i=-x,-y}(i-\frac{d}{2})^2} + \frac{y-\frac{d}{2}}{\displaystyle\sum_{i=-x,y}(i-\frac{d}{2})^2} \\
&\quad + \frac{sx}{R\sqrt{x^2+y^2}}\bigg[\frac{\gamma_1}{Q_1}\Big(E(k_1)\frac{1+\alpha^2+\beta_1^2}{Q_1^2-4\alpha}-K(k_1)\Big) - \frac{\gamma_2}{Q_2}\Big(E(k_2)\frac{1+\alpha^2+\beta_2^2}{Q_2^2-4\alpha}-K(k_2)\Big)\bigg]\bigg] \\
&\quad + \hat{y}G_0\bigg[\frac{x-\frac{d}{2}}{\displaystyle\sum_{i=x,y}(i-\frac{d}{2})^2} + \frac{-x+\frac{d}{2}}{\displaystyle\sum_{i=x,-y}(i-\frac{d}{2})^2} + \frac{+x+\frac{d}{2}}{\displaystyle\sum_{i=-x,-y}(i-\frac{d}{2})^2} + \frac{-x-\frac{d}{2}}{\displaystyle\sum_{i=-x,y}(i-\frac{d}{2})^2} \\
&\quad + \frac{sy}{R\sqrt{x^2+y^2}}\bigg[\frac{\gamma_1}{Q_1}\Big(E(k_1)\frac{1+\alpha^2+\beta_1^2}{Q_1^2-4\alpha}-K(k_1)\Big) - \frac{\gamma_2}{Q_2}\Big(E(k_2)\frac{1+\alpha^2+\beta_2^2}{Q_2^2-4\alpha}-K(k_2)\Big)\bigg]\bigg] \\
&\quad + \frac{\hat{z}sG_0}{R}\bigg[\frac{1}{Q_1}\Big(E(k_1)\frac{1-\alpha^2-\beta_1^2}{Q_1^2-4\alpha}+K(k_1)\Big) - \frac{1}{Q_2}\Big(E(k_2)\frac{1-\alpha^2-\beta_2^2}{Q_2^2-4\alpha}+K(k_2)\Big)\bigg], (4.5)
\end{aligned}
$$

where, in addition to the previous definitions given for the coils, d is the distance between adjacent Ioffe bars, L (the distance between the endcap coils) is the length of a Ioffe bar, and R (the endcap coil radius) is $d/2$. A scale factor $s \approx 0.5$ is used to account for the incompleteness of the endcap coils.

Figure 4.9 depicts 2D slices of the IP trap field during the evaporation stage. The first panel depicts the magnetic field in the xy-plane at $z = 0$. The second panel depicts the magnetic field in the xz-plane at $y = 0$ ignoring the effect of the endcap coils. The third panel depicts the xz-plane field including the effect of the endcap coils showing a shift of the trap minimum in the $\hat{z}$ direction.
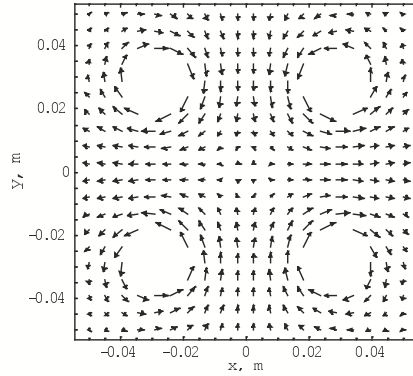
2D linear quadrupole field created by racetrack
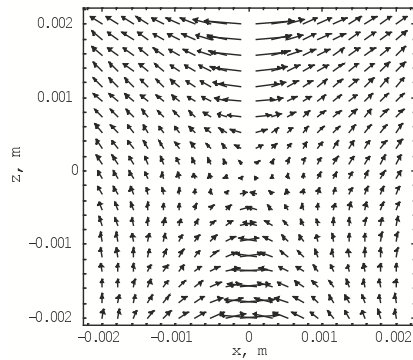
2D field in xz plane ignoring racetrack endcaps
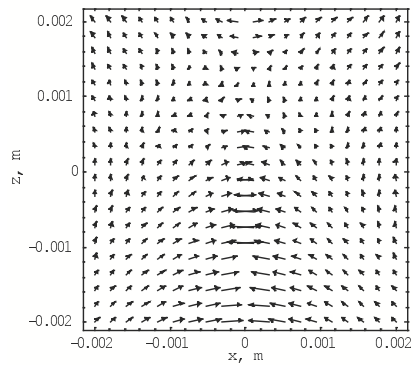
2D field in xz plane including racetrack endcaps

Figure 4.9: Top panel: linear quadrupolar field in the xy-plane created by racetrack. Middle panel: xz-plane magnetic field ignoring the effect of the racetrack endcaps. Bottom panel: xz-plane magnetic field including the effect of the racetrack endcaps.

73

4.4.3   Ioffe-Pritchard Trapping Frequencies

In the vicinity of the IP trap minimum, we can express the IP trapping frequencies as follows:

$$f_{z,\rho} = \frac{1}{2\pi}\sqrt{\frac{\nabla^2_{z,\rho}E_{\text{zm}}}{M}}, \tag{4.6}$$

where M is the mass of the ^{87}Rb atom. As discussed above, as long as the atom adiabatically follows the local magnetic field, E_{zm} is proportional to $|\vec{B}_{\text{IP}}|$. Because the IP trap is very nearly axially-symmetric, it is convenient to express $|\vec{B}_{\text{IP}}|$ as follows:

$$|\vec{B}_{\text{IP}}| = \sqrt{|\vec{B}_{\text{IP,z}}(z)|^2 + |\vec{B}_{\text{IP},\rho}(\rho)|^2}, \tag{4.7}$$

where, for small displacements from the trap minimum,

$$B_{\text{IP,z}} = B_{\text{p,z}}(z) + B_{\text{ab,z}}(z) + B_{\text{b,z}}(z) + B_{\text{rt,caps,z}}(z).$$

$$B_{\text{IP},\rho}(\rho) = B_{\text{rt,bars},\rho}(\rho) + B_{\text{rt,caps},\rho}(\rho). \tag{4.8}$$

For small displacements from the trap minimum, $|B_{\text{IP,z}}| \gg |B_{\text{IP},\rho}|$, and so we can express $|\vec{B}_{\text{IP}}|$ as

$$|\vec{B}_{\text{IP}}| = |B_{\text{IP,z}}| + \frac{|B_{\text{IP},\rho}|^2}{2|B_{\text{IP,z}})|}, \tag{4.9}$$

which gives us the following expressions for the trapping frequencies at the trap minimum.

$$f_z = \frac{1}{2\pi}\sqrt{\frac{m_F g_F \mu_{\text{B}}}{M}}\sqrt{\frac{\partial^2 |B_{\text{p,z}}|}{\partial z^2}}.$$

$$f_\rho = \frac{1}{2\pi}\sqrt{\frac{m_F g_F \mu_{\mathrm{B}}}{M|\vec{B}_{\mathrm{IP}}(\vec{z})|}}\left[\frac{\partial|B_{\mathrm{rt,bars,}\rho}|}{\partial\rho} + \frac{\partial|B_{\mathrm{rt,caps,}\rho}|}{\partial\rho}\right]. \tag{4.10}$$

In the expression for f_z we have ignored the contributions of $B_{\mathrm{ab,z}}$ and $B_{\mathrm{b,z}}$ because these terms are nearly constant in the vicinity of the trap minimum (nearly Helmholtz coils). The effect of $B_{\mathrm{rt,caps,z}}$ is a linear gradient which adds nothing to f_z; it does however shift the location of the trap minimum along z. The effect of $B_{\mathrm{rt,caps,}\rho}$ is a very slight breaking of the axial symmetry of the IP trap (an effect which we typically ignore). With these simplifications, we provide expressions for $\partial^2|B_{\mathrm{p,z}}|/\partial z^2$, $|B_{\mathrm{IP,z}}|$, and $\partial|B_{\mathrm{rt,bars,}\rho}|/\partial\rho$ in the vicinity of the local trap minimum in order to evaluate f_z and f_ρ.

$$\frac{\partial^2|B_{\mathrm{p,z}}|}{\partial z^2} = \frac{\mu_0 n_{\mathrm{p}} I_{\mathrm{p}}}{2}\left[\frac{-3R_{\mathrm{p}}^2}{(R_{\mathrm{p}}^2+(L_{\mathrm{p}}/2)^2)^{5/2}} + \frac{15R_{\mathrm{p}}^2(L_{\mathrm{p}}/2)^2}{(R_{\mathrm{p}}^2+(L_{\mathrm{p}}/2)^2)^{7/2}}\right.$$
$$+ \left.\frac{-3R_{\mathrm{p}}^2}{(R_{\mathrm{p}}^2+(L_{\mathrm{p}}/2)^2)^{5/2}} + \frac{15R_{\mathrm{p}}^2(L_{\mathrm{p}}/2)^2}{(R_{\mathrm{p}}^2+(L_{\mathrm{p}}/2)^2)^{7/2}}\right]$$
$$|B_{\mathrm{IP,z}}| = \frac{\mu_0 n_{\mathrm{p}} I_{\mathrm{p}}}{2}\left[\frac{R_{\mathrm{p}}^2}{(R_{\mathrm{p}}^2+(L_{\mathrm{p}}/2)^2)^{3/2}} + \frac{R_{\mathrm{p}}^2}{(R_{\mathrm{p}}^2+(L_{\mathrm{p}}/2)^2)^{3/2}}\right]$$
$$- \frac{\mu_0 n_{\mathrm{ab}} I_{\mathrm{ab}}}{2}\left[\frac{R_{\mathrm{ab}}^2}{(R_{\mathrm{ab}}^2+(L_{\mathrm{ab}}/2)^2)^{3/2}} + \frac{R_{\mathrm{ab}}^2}{(R_{\mathrm{ab}}^2+(L_{\mathrm{ab}}/2)^2)^{3/2}}\right]$$
$$+ \frac{\mu_0 n_{\mathrm{b}} I_{\mathrm{b}}}{2}\left[\frac{R_{\mathrm{b}}^2}{(R_{\mathrm{b}}^2+(L_{\mathrm{b}}/2)^2)^{3/2}} + \frac{R_{\mathrm{b}}^2}{(R_{\mathrm{b}}^2+(L_{\mathrm{b}}/2)^2)^{3/2}}\right]$$
$$\frac{\partial|B_{\mathrm{rt,bars,}\rho}|}{\partial\rho} = \frac{4\mu_0 n_{\mathrm{rt}} I_{\mathrm{rt}}}{\pi d_{\mathrm{rt}}^2}, \tag{4.11}$$

where we have ignored the $B_{\mathrm{rt,caps,z}}$ term in $B_{\mathrm{IP,z}}$ because it is very small (though not exactly zero at the trap minimum because of the z shift of the trap minimum).

As explained above, the shift of the trap minimum along $\hat{z}$ is due to $B_{\mathrm{rt,caps,z}}$ which creates a linear gradient along z. Along the z-axis, we have the following

expression for $\partial |B_{\text{rt,caps,z}}|/\partial z$.

$$\frac{\partial |B_{\text{rt,caps,z}}|}{\partial z} = \frac{\mu_0 n_{\text{rt}} I_{\text{rt}}/2}{2} \left[\frac{-3 L_{\text{rt}} R_{\text{rt}}^2}{(R_{\text{rt}}^2 + (L_{\text{rt}}/2)^2)^{5/2}} \right]. \tag{4.12}$$

We have divided I_{rt} by two to account for the missing vertical sections of the endcap coils. The shift in the local field minimum is

$$z_{\text{shift}} = -\frac{\partial |\vec{B}_{\text{rt,caps}}(\vec{z})|}{\partial z} \Big/ \frac{\partial^2 |\vec{B}_{\text{p}}(\vec{z})|}{\partial z^2}. \tag{4.13}$$

For the three stages described above (trap loading, trap evaporation, lattice loading), Table 4.1 summarizes the currents used in the IP trap components, the trap frequencies, and Zeeman energies at the bottom of the trap. Table 4.2 provides physical data for the Ioffe-Pritchard trap. Finally, we make mention of a "fine bias" coil which is nearly Helmholtz along the z-axis used for trimming purposes.

Stage	Pinch/ Antibias	Bias	Racetrack	f_ρ	f_z	Trap Bottom
Trap load	300 A	100 A	252 A	10.7 Hz	6.3 Hz	64.56 MHz
Evaporation	580 A	0 A	540 A	125 Hz	8.7 Hz	2.16 MHz
Lattice load	520 A	53 A	425 A	24 Hz	8.2 Hz	35.56 MHz

Table 4.1: Calculated Ioffe-Pritchard magnetic trap currents, confinement frequencies, and Zeeman energies at the trap bottom. These were determined by measuring various trap parameters (oscillation frequencies, positional shifts, and trap bottom) at a range of currents to determine coefficients in a Taylor series expansion of the magnetic fields.

Variable	Pinch coils	Antibias coils	Bias coils	Racetrack bars and "coils"
n	10 turns	3 turns	9 turns	9 turns
R	1.4 cm	9.0 cm	8.0 cm	3 cm (endcap coil radius)
d				5.7 cm (bar separation)
L	8.3 cm	9.5 cm	9.4 cm	23 cm

Table 4.2: Ioffe-Pritchard magnetic trap physical data. These are mean values of measured quantities (i.e. *not* filamentary values).

4.4.4 Magnetic Trap Cooling, Power Supplies, Dummy Loads and Interlock System

The IP trap is continuously cooled by chilled water flowing through the hollow-core copper tubing. The process chilled (55^oF) water originates from the Advanced Measurement Laboratory (AML) filtered, closed-loop circulating system. The AML water pumps have variable frequency drives and are capable of delivering up to 85 psig on the supply side. NIST operates at a supply pressure of approximately 40 psig which we then boost to approximately 110 psi for the experiment. We connect to the AML water system in the adjacent service corridor and bring it into the lab overhead using heavy-duty, high-pressure (1000 psi) mine-spray hose (Alfagomma MSHA 1C-152/6, $1\frac{3}{8}$ inch OD). The hose feeds an aluminum 10-port discharge manifold (on the floor beside the optical table) which splits the water for the various uses. The water returns from the experiment into another 10-port manifold and goes overhead back to the service corridor via the mine-spray hose. The AML return water is always 20 psig below its supply and thus is normally about 20 psig. Thus, with our (Teel) booster pump, we drop 90 psig across the experiment. Table 4.3 summarizes the uses of the discharge and intake manifold ports.

Discharge Port	Use	Valved?	Flow Meter	Elec Conn
1	Bias		104L110 (.06-.6 gpm)	
2	Ti-Sub Pump	yes		
3	——			
4	Racetrack			+
5	Slower/Oven	yes	104L110 (.06-.6 gpm)	
6	——			
7	Pressure gauge			
8	——			
9	Reverse slower	yes	100C110 (.1-1.0 gpm)	
10	Pinch/Antibias		100C110 (.8-6.0 gpm)	
Intake Port	Use	Valved?	Flow Meter	Elec Conn
1	Bias			+
2	——			
3	Bias			-
4	Ti-Sub Pump			
5	Racetrack			-
6	Reverse Slower			
7	Slower/Oven			
8	Pinch/Antibias	yes		
9	Pinch/Antibias			+
10	Pinch/Antibias			-

Table 4.3: Cooling water discharge and intake manifold port uses. Where an electrical connection is made at a port, its polarity is noted.

We generate electrical current for the IP trap using a single Sorensen DHP 15-660 (15V, 660A) supply for the pinch coils, two Sorensen DHP 10-660 (10V, 660A) supplies in series (one in voltage control and one in current control mode) for the racetrack (although this will become a single supply in late 2006), and a single Agilent 6571A (8V, 220A) for the bias coils. The Sorensens are switching supplies and are rated at 10 mVrms ripple, +/- 0.05% stability, and 2 ms transient response. The Agilent is rated at 650 μVrms and 200 mArms ripple, 0.02% + 69 mA (8 hour) stability, and <900 μs transient response. Current from the supplies is under analog voltage control via the rear panel 25-pin J1 connector for the Sorensens and the

rear panel 7-pin analog connector for the Agilent. The Sorensen J1 connectors allow remote turn on/off (TTL between pins #14 and #2) which we use as part of the interlock system. The Agilent is integrated into the interlock system via a small Pomona box called the "kick box" for historical reasons. The interlock system is explained in detail below.

Current from the supplies is carried to the magnets and "dummy" loads (described below) by 4/0 AWG (0.13 ohm/km), highly flexible welding cable (Carol Super V Vu-tron). Cable ends are soldered into large copper lugs. At the magnet connections, the lugs are high-temperature (silver) soldered onto 1/2 inch diameter copper rods which are then "swage-loked" into brass welding tees which serve as the electrical/water junctions. Our attention to these connection details resulted in much lower total voltage drops compared to the first incarnation of this experiment where we did not solder.

During final RF-evaporation, when we compress the IP trap by increasing the current in the pinch/antibias/racetracks and sending the bias current to 0, the Sorensen supplies switch from having been in constant voltage mode to constant current mode. This is accomplished by setting the current limit (on the supply front panel) to a value that we know is the correct IP current and then sending an analog signal to the J1 corresponding to a current higher than this value. We have found that this procedure results in quieter current.

To prevent the IP power supplies from going to their voltage limits and yet still being able to apply and remove a large magnetic field in approximately 250 μsec, we built three "dummy" loads (one each) for the pinch/antibias, bias, and racetrack

magnets. Figure 4.10 displays a dummy load schematic. During an experiment, when we command current into or out of the IP trap, the supplies only see a change in the load inductances; TTL signals simply shunt the currents back and forth between the magnets and the dummy loads. Voltage drops in the dummy loads occur across stainless steel tubing bent into configurations which attempt to minimize the creation of magnetic fields. This tubing is internally water-cooled. We use Powerex CM1200 IGBTs and Powerex BG1A gate driver boards which are mounted on water-cooled copper plates to switch the current between the magnets and dummy loads. Varistors are used across each magnet and dummy load to clamp the maximum voltage due to inductive kicks. Six-port discharge and intake aluminum manifolds are used for chilled water management.

An interlock system monitors the temperatures of the dummy load stainless steel tubing for the bias, pinch/antibias, and racetrack magnets, and the water flowrates in the bias coils, racetrack, slower/oven brightwall, reverse slower and pinch/antibias coils. Should any of the temperatures in the dummy load tubing exceed a selectable setpoint or should the water flowrate go below a point defined by the particular flowmeter on a manifold discharge port, the Agilent and Sorensen power supplies will cease providing current. We use Proteus Industries celcon/polysulfone flowmeters which can withstand up to 100 psi at $55^o F$. The particular model used for a water port (including its acceptable flow rate range) is contained in Table 4.3. A diagram of the overall interlock system (including a schematic of the "kick box") is shown in Figure 4.11.
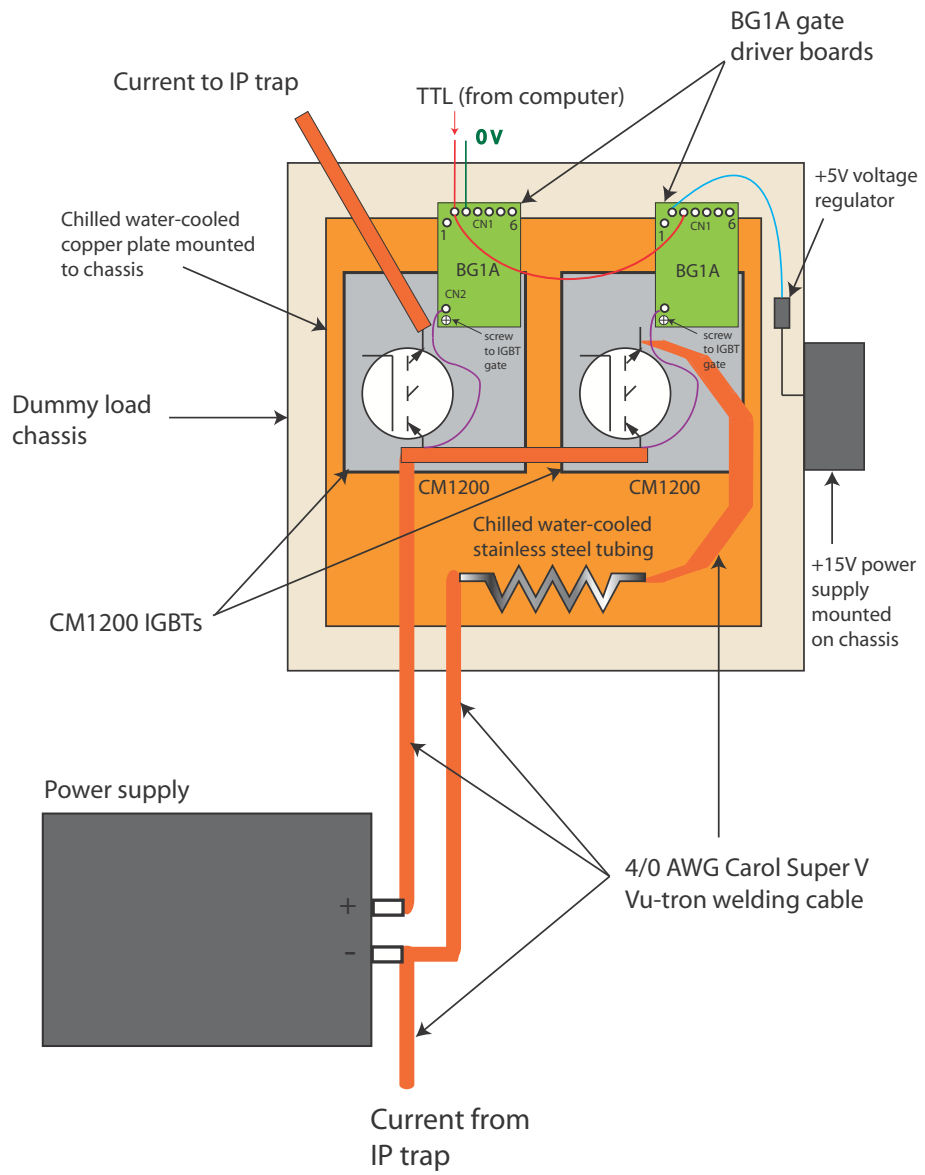
Figure 4.10: Dummy load schematic.
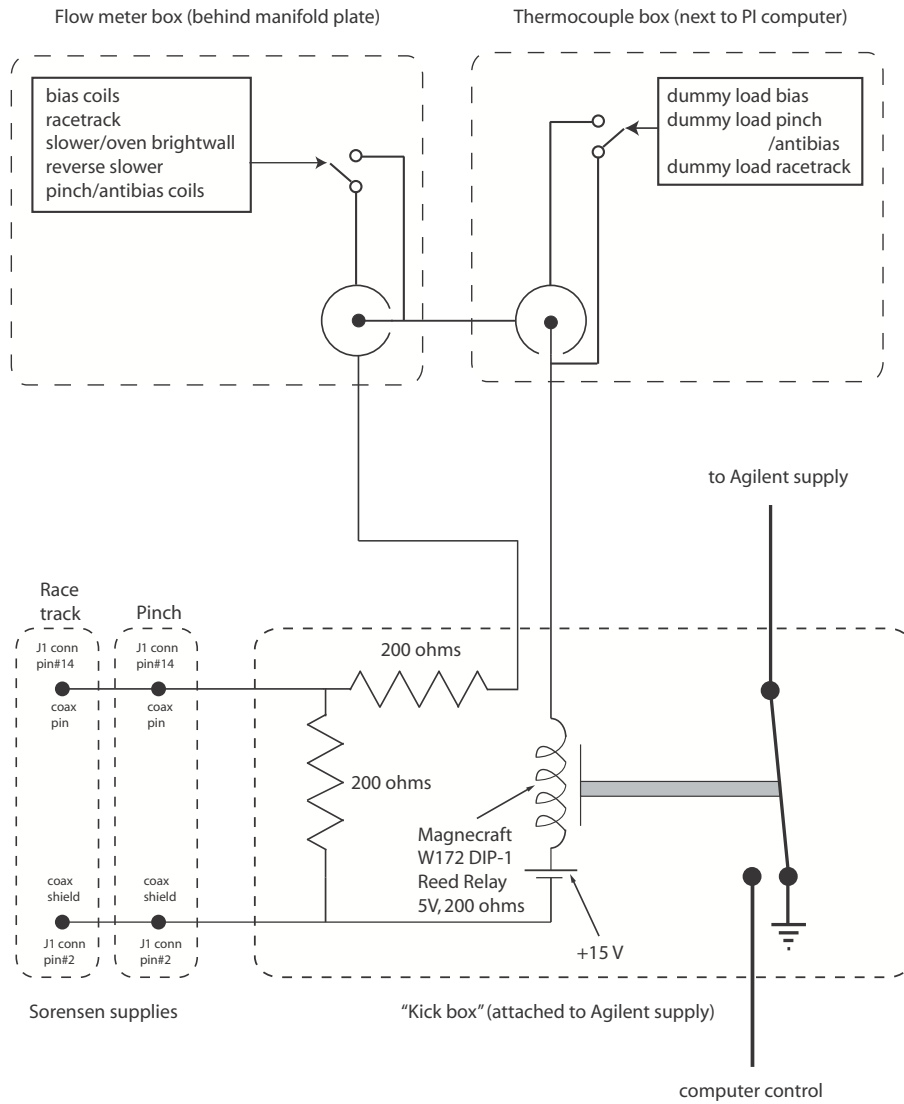
Figure 4.11: The interlock system including the very important "kick box" which powers the entire interlock system and controls the signal to the Agilent supply. The voltage drop across the 200 ohm resistor enables the Sorensen power supplies by providing the proper voltage across pins #2 and #14.

4.5 Titanium-Sapphire Laser for Optical Lattices

We employ a 1.5 W Coherent MBR-110 Titanium-Sapphire (titanium-doped sapphire) laser pumped by a 10 W frequency-doubled Nd:YVO$_4$ (neodymium-doped yttrium vanadate) Coherent Verdi V10 laser to generate the light for our optical lattices. The Ti:Sapph uses a birefringent filter and Brewster plates to coarse tune its wavelength. A thin etalon is used for fine-tuning and single-mode operation. Light transmission through the etalon is locked to the laser frequency to prevent mode-hopping while the laser is being fine-tuned. The Ti:Sapph dithers this thin etalon at approximately 90 kHz in order to generate an error signal, which unfortunately puts amplitude modulation on the laser light within a frequency range (90 kHz and higher harmonics) which is very important in many of our experiments. In speaking with company representatives, we have learned of the following methods to minimize this modulation amplitude. This information is *not* contained in any of the MBR-110 manuals.

Remove the cover of the main electronics box. Then, using a photodiode and oscilloscope to see the light coming out of the laser, turn the PR-16 potentiometer within the electronics box to reduce the amplitude modulation on the oscilloscope. Turning PR-16 in this direction has the effect of reducing the drive voltage to the etalon which loosens the lock (i.e. reduces the etalon scan range). Thus, although the amplitude modulation can be reduced, it cannot be entirely removed. According to Coherent, the 1 V pk-pk etalon signal recommended by the manual, can be reduced to approximately 100 mV pk-pk. The 180 kHz first harmonic noise (because

the laser is locking to a maximum in the light transmission through the etalon) can be minimized by playing with the PR-6 potentiometer which adjusts the gain of the "noise eater" circuit.
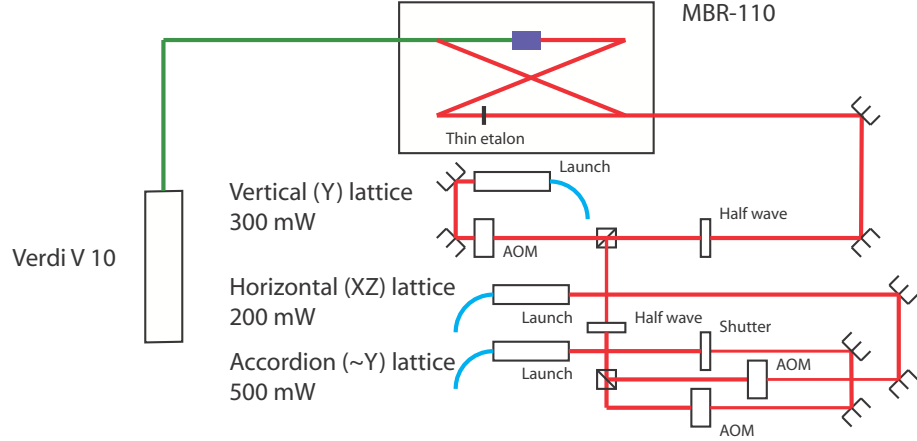
Figure 4.12: Layout Ti:Sapph laser system for optical lattices.

Figure 4.12 depicts the way in which we split the Ti:Sapph light for the various optical lattices. The powers indicated are purely nominal and are often varied depending on the requirements of the particular experiment being conducted. For all five experiments described in this thesis, the light from the Ti:Sapph was red-detuned (relative to both the D1 and D2 transitions at 795 nm and 780 nm, respectively) to 810 nm, linearly polarized at the atoms, and contained within an approximately Gaussian beam with a minimum waist w_0 of approximately 200μm located at the atom cloud. After being split into multiple beams and passed through acousto-optical modulators, the laser light for three of the experiments described in this thesis (those using the "accordion lattice" as described in Chaps. 7 and 8 and the 2D vibrational decay experiment described in Chap. 9 and in the Appendices) was launched into a single-mode, polarization-maintaining fiber and thus was spa-

tially filtered to be very nearly TEM$_{00}$ before being directed onto the atoms. The other two experiments (described in Chap. 9 and the Appendices) did not have the light brought to the atoms via a fiber and thus there was no spatial filtering after the laser.

For the quasi-1D BEC experiments described in Chap. 9 and the Appendices, a 2D optical lattice was created by intersecting two independent retro-reflected 1D lattices at an angle of 80° in the horizontal plane. The light polarization was also in the horizontal plane. The independent 1D lattices were detuned from each other by 5 MHz for one experiment and 6 MHz for the other. In either case, these detunings created a very fast time-modulation of the cross term in the expression for the light intensity (see Eq. (3.22)) relative to ω_L and thus the atoms were not able to kinetically respond to the cross term. For the dipole damping experiment described in Chap. 9 and the Appendices, a third independent (perturbing) retro-reflected 1D optical lattice was created. This lattice was also linearly polarized and since it was approximately vertical, its polarization could not be orthogonal to both of the horizontal lattices. Thus, it was also detuned by 6 MHz from one of the lattices and 12 MHz from the other. The detunings and intensities of all the lattices were controlled by acousto-optical modulators/RF generators (Intra-Action).

For the 2D lattice experiments described in Chap. 9 and the Appendices, each independent 1D retro-reflected optical lattice was generated by focussing an approximately collimated beam from the Ti:Sapph laser to an approximate 200μm waist at the BEC, after which the light was nearly re-collimated by a lens which placed a much larger (imaginary) waist slightly behind an adjustable retro-reflecting

mirror. The reason, the retro-reflecting mirror was slightly in advance of the second waist was to compensate for the loss of light intensity due to passage through the glass cell and lenses and reflection off of the retro mirror. Thus, the beam waist at the atoms on the retro path was slightly smaller than the waist on the incoming path.

The implementation of the 1D accordion lattice is carefully described in Chap. 5. Unlike the optical lattices used for the three-body and dipole damping experiments, this 1D lattice was not generated by retroreflecting a beam. Instead, after the beam came out of the fiber, it was split into two beams that were then recombined on the atoms. The two beams were not counterpropagating at the atoms; in fact they were often very nearly copropagating—the angle of their intersection was variable. For this reason, the polarization of these two beams was necessarily perpendicular to the plane they defined in order to minimize the dependence of the lattice depth on their intersection angle.

As with the trapping lasers, we now fiber-launch all light from the Ti:Sapph laser for delivery to the science cell. Although this method reduces the total power available for our experiments due to unavoidable launching and delaunching inefficiencies, it has considerably reduced the time we spend aligning laser beams. All of us in the laboratory have become quite expert in maximizing the light power into a fiber.

Chapter 5

A 1D Optical Lattice with Dynamically-variable Periodicity

Optical lattices are normally created with fixed periodicity. The usual arrangement for a 1D lattice is a retro-reflected laser beam with the lattice constant d equal to $\lambda/2$ where λ is the wavelength of the laser light used to create the optical lattice. Much larger values of d are obtained if the two beams forming the 1D lattice intersect at a small angle. Assuming that the two beams are of equal intensity, and neglecting beam profiles in the directions perpendicular to their axes of propagation,

$$U \;\; = \;\; \frac{U_L}{2}[\cos(\vec{k_1} \cdot \vec{r} - \omega t) + \cos(\vec{k_2} \cdot \vec{r} - \omega t)]^2, \tag{5.1}$$

where U_L is the two-beam lattice depth and the rest of the notation is borrowed from Chap. 3. This expression also assumes linear, parallel polarization and a two-level atom. Multiplying out the right hand side we obtain,

$$\begin{aligned} U \;\; = \;\; & \frac{U_L}{2}[\cos^2(\vec{k_1} \cdot \vec{r} - \omega t) + \cos^2(\vec{k_2} \cdot \vec{r} - \omega t) \\ & + \;\; \cos((\vec{k_1} + \vec{k_2}) \cdot \vec{r} - 2\omega t) + \cos((\vec{k_1} - \vec{k_2}) \cdot \vec{r})]. \end{aligned} \tag{5.2}$$

Taking the time average of the right hand side to get the average potential, we obtain

$$U = \frac{U_L}{2}[1 + \cos((\vec{k_1} - \vec{k_2}) \cdot \vec{r})]. \tag{5.3}$$

If $|\vec{k_1}| = |\vec{k_2}| = k$, then $\vec{k_1} - \vec{k_2} = 2k \sin \frac{\theta}{2} \hat{x}$ where $\hat{x}$ is in the direction perpendicular to the line bisecting the angle θ made by the intersecting laser beams. Choosing $\vec{r}$ to lie in this direction and defining it as our lattice axis, we have

$$U = U_L \cos^2(kx \sin \frac{\theta}{2}). \tag{5.4}$$

The lattice constant is therefore $\lambda/(2 \sin \frac{\theta}{2})$. Note that if $\theta = \pi$, the formula reproduces the standard result for counterpropagating beams, $d = \lambda/2$.

To dynamically change the lattice constant, a method is needed to change the laser beam intersection angle while keeping the intersection point fixed in space. A conceptual design which accomplishes this is depicted in Figure 5.1. The basic idea is to image a point on a rotating mirror through two different paths to another point in space (the location of the BEC). Laser light is introduced into the device by a single mode optical fiber. Coming out of the fiber, the light first passes through a half-wave plate so that the light may be polarized as desired (normally linear, s-polarization). The fiber lens creates a waist at a galvanometer-mounted mirror. Specifically, the beam waist is placed at a central mirror location as close as possible to a point along the rotation axis, to minimally displace the reflected beam when the galvanometer is rotated. Rotation of the galvanometer causes the reflected beam to

scan across a lens located one focal length f away from the galvanometer mirror. Because the mirror is at f and the waist is at the mirror, the beam emerges parallel to the optical axis for all entrance points.
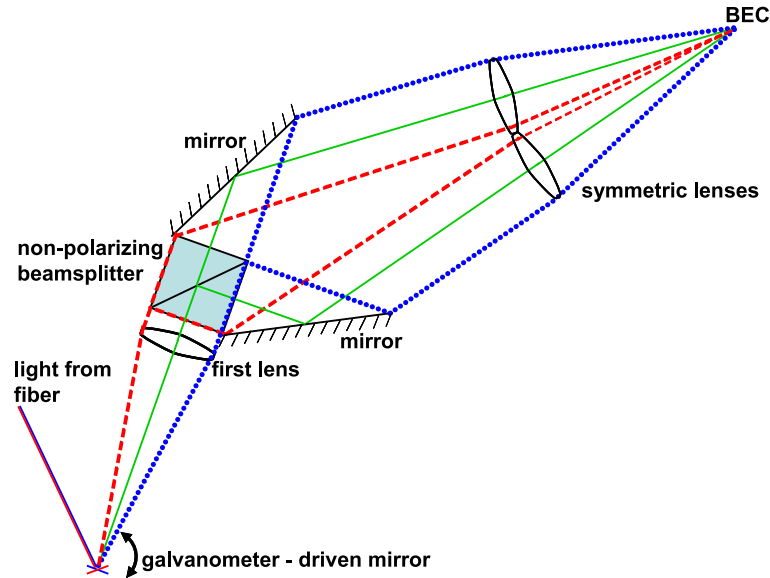
Figure 5.1: Accordion optical lattice schematic.

The beam then enters a non-polarizing beamsplitter cube. As the galvanometer is rotated, the beam scans across the face of the cube. The reflected and transmitted beams exit the cube at points that are symmetric with respect to the diagonal axis. Reflecting off two symmetrically located mirrors, they enter individual lenses which are oriented so that their focal points coincide. Thus, the two coherent beams intersect at an angle dictated by the galvanometer and the position of the intersection does not change. Since the distance between the first lens and the second set of lenses is twice the lens focal length, the beam waist at the galvanometer mirror is placed at the point of intersection (the BEC). I wish to thank Trey Porto for the very original design of this device.
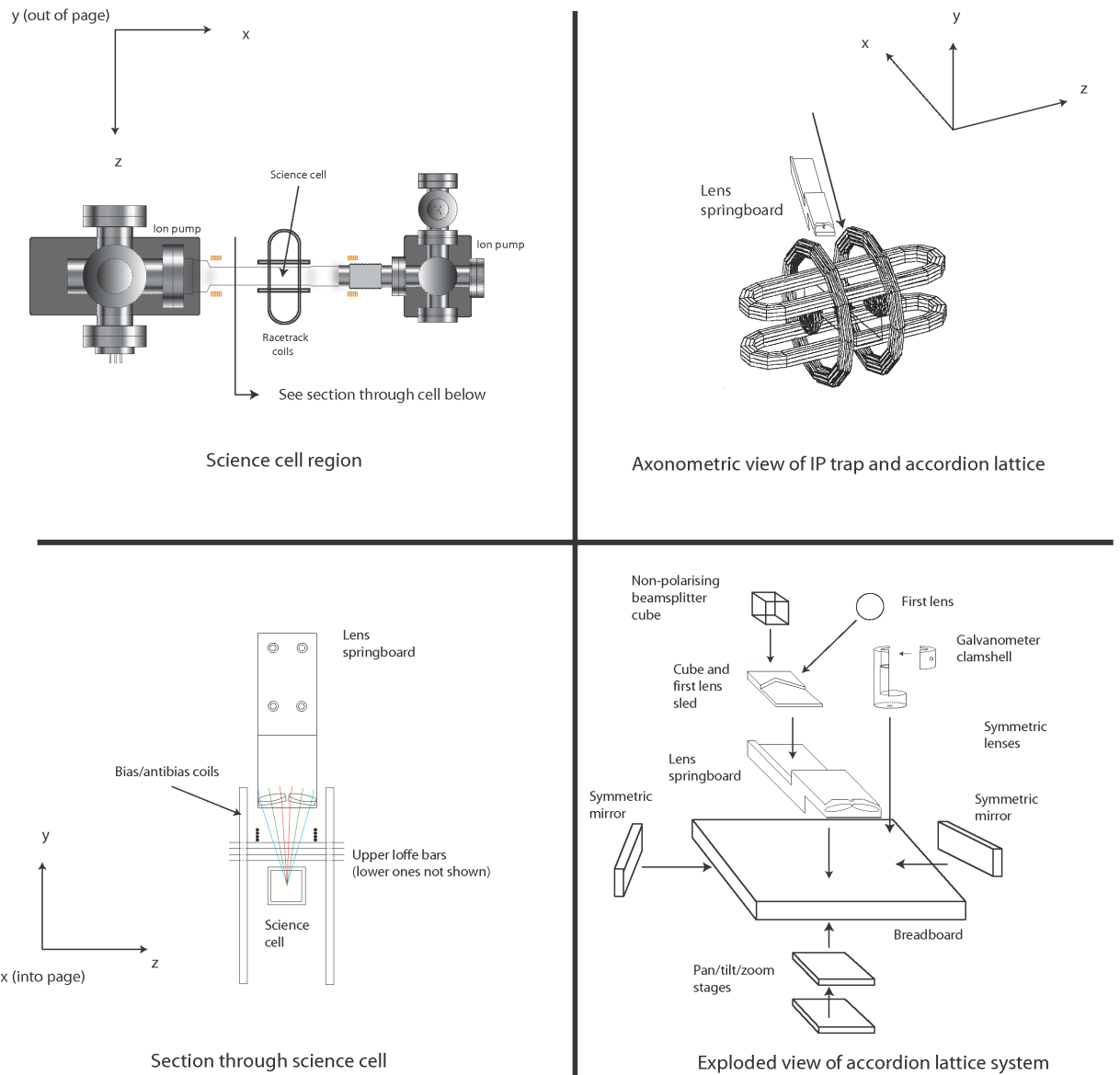
Figure 5.2: Orientation of the accordion lattice breadboard with respect to the ^{87}Rb BEC apparatus and overview of the breadboard design.

5.1.1 Orientation with Respect to ^{87}Rb BEC Apparatus

It was decided early on in the design of the accordion lattice that due to mechanical and optical access issues, the axis of the accordion lattice should be

along the z-axis of the ^{87}Rb BEC apparatus as shown in Figure 5.2. The minimum lattice periodicity is set by the maximum angle between the intersecting beams and mechanical/optical access limits this maximum angle. As shown in Figure 5.3, for their full scanning ranges the two beams forming the lattice must always pass through the top of the glass science cell and hit the condensate within the cell.
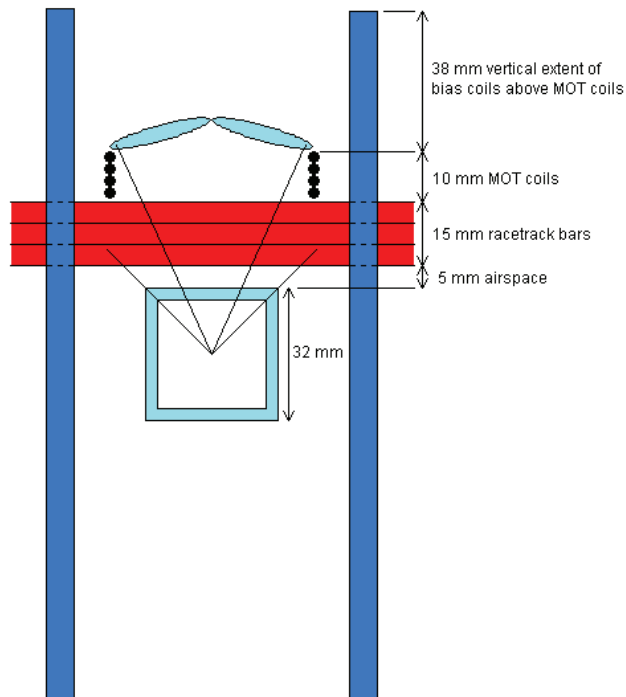
Figure 5.3: Section through experimental glass cell.

The cell is square in cross section and assuming that the condensate is created at the exact center of the cell (which incidentally we discovered was not exactly true when we reassembled the apparatus in 2004), the maximum intersection angle could in principle be as large as $\pi/2$. Other practical issues such as the distance between the bias coils, the height of the cell, and the limited availability of low f-number

lenses ultimately limited the maximum intersection angle (in this implementation) to roughly 0.7 radians yielding a practical minimum periodicity of approximately 3λ. Although a smaller minimum periodicity could have been achieved by separating the lenses, this would have also reduced the maximum periodicity. In the end, for us it was the lenses that set the limit on the minimum periodicity.

5.1.2   Lens Aberrations

One of the major challenges in physically implementing this device was to keep the intersection point of the beams fixed in space as the galvanometer rotated. In order to do this, it was important to minimize the relevant aberrations of the three lenses. For fixed wavelength lattice beams, chromatic aberrations are irrelevant. Of the monochromatic aberrations (which up to third order are spherical aberration, coma, astigmatism, Petzval field curvature, and distortion) [93], we focussed on spherical aberration. We were able to safely ignore coma and astigmatism because all rays were engineered to be meridional (in the plane containing the optical axis and the point where the ray intersects the lens). Petzval field curvature and distortion were not addressed because an extended object was not being imaged. This left spherical aberration, and specifically longitudinal spherical aberration (L·SA) because we wanted our system to minimize focal point displacement along the optical axis as a function of the distance of the paraxial ray from the optical axis as shown in Figure 5.4. It is important that the axis of symmetry of the 1D lattice remain fixed in space relative to the atom cloud as its periodicity changes.
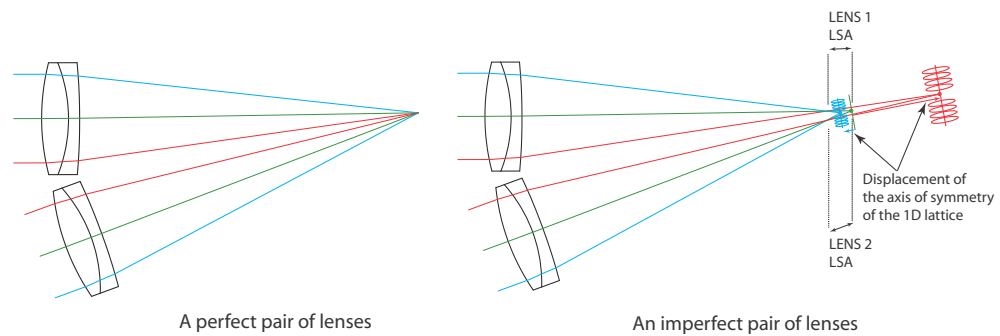
Figure 5.4: The effect of longitudinal spherical aberration and misalignment on the accordion lattice. The outer blue rays form a set of pancakes closer to the lenses than the nominal focal point indicated by the green line. The inner red rays form a set of pancakes farther from the focal point. Depending on the alignment, the displacement of the place where the beams intersect can be larger then the longitudinal spherical aberration. We minimize this during final alignment.

Detailed Specifications:

Paraxial Focal Length (f): 80.0 ± 1.6
Wavefront Distortion: < λ/5 at 830 nm
Design Wavelength (λ): 830.0 nm
f_b: 75.6 mm
F-Number: 3.200
B: 76.0 mm
D: 22.50
Diameter: 25.00 +0/−0.15 mm
Center Thickness (t_c): 8.50 ± 0.25 mm
Edge Thickness (t_e): 6.4 mm
Material: SK 11 and SF 5
Surface Quality: 60-40 scratch and dig
Cement: Ultraviolet-cured polyester
Centration: 4 arc minutes
Edges: Ground
Coating: /077 HEBBAR, 750-1100 nm

Figure 5.5: The Melles Griot 06 LAI 009 precision achromatic doublet used in the accordion lattice.
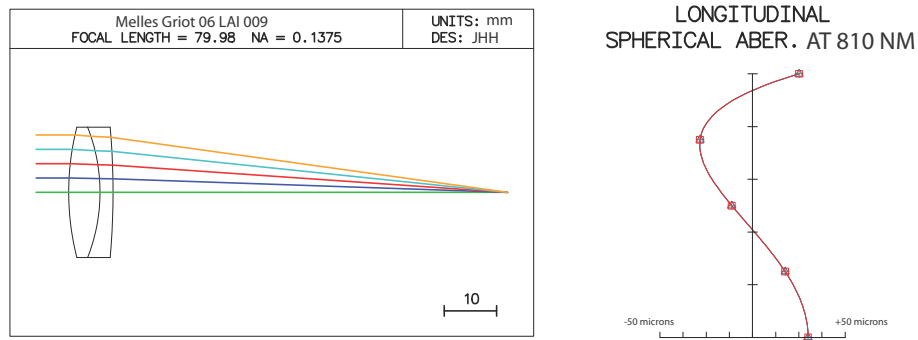
Figure 5.6: Longitudinal spherical aberration of the 06 LAI 009 as reported by OSLO (see text). The abscissa of the graph on the right is the longitudinal aberration (distance from the image surface to the intersection of the ray with the optical axis). Positive LSA corresponds to an intersection closer to the lens. The ordinate of the graph is the fractional pupil coordinate, ranging from 0 to 1, where 0 corresponds to a ray going through the center of the lens and 1 is for a ray going through the lens at a distance from the center equal to 0.9 of the lens radius as indicated by the yellow ray in the left panel.

The three lenses used in the accordion lattice are all the same Model 06 LAI 009 precision achromatic doublets made by Melles Griot [101] as shown in Figure 5.5. This lens is a synthetic polyester-cemented Fraunhofer doublet composed of a crown double-convex lens in intimate contact with a concave-nearly planar flint lens. The lens diameter is 25 mm and nominal focal length is 80 mm. A high-efficiency, broadband anti-reflection (/077 HEBBAR 750-1100 nm) coating was applied by the manufacturer which resulted in reflectance and absorption coefficients less than .01 at the wavelengths of interest. This model was chosen with the help of the computer program OSLO Light Edition 6.1 [100] which is a program for optics design and has access to a large database of commercially available lenses from various manufacturers. By first limiting the selection based on the physical constraints of the experiment, a set of lenses which minimized longitudinal spherical aberration was selected through a process of trial and error. The range of longitudinal spherical

94

aberration predicted by OSLO at 810 nm was -30 micrometers to +30 micrometers up to a pupil coordinate of 1 as shown in Figure 5.6. Negative and positive L·SA correspond to the focal point being behind and in front of the paraxial focal point, respectively.

5.1.3 Construction of Accordion Lattice Breadboard

We now describe the mechanical parts of the accordion lattice breadboard used to hold the optics. All of the optics required to overlap the two lens foci for the full galvanometer rotational range are contained on this breadboard and light is brought to the breadboard with an optical fiber. This decoupled the accordion lattice alignment procedure from the alignment procedure to put the joint focal point on the BEC. We stacked two low-profile stages (Newport) underneath the breadboard base to permit alignment of the entire breadboard to bring the joint focal point onto the BEC. We custom-designed many of these parts because of BEC apparatus space limitations and accordion lattice component fragility. Some parts were machined by me and others by Duane Enderle in the Radiation Physics building. Figure 5.2 gives an exploded overview of nearly all of these small parts and how they fit together.

The two lenses closest to the atom cloud were cut by Jack Fuller of the NIST glass shops as shown on Figure 5.7 so that only a central 9.8 mm section remained. This enabled the lenses to be glued down directly onto a flat surface and thus brought closely together. It also removed unused parts of the lenses for improved optical access of other beams, such as the vertical MOT beams. Details of the

hardware created to support and adjust the locations of the three lenses and beam-splitting cube is shown on Figure 5.8. The two symmetric lenses are supported by and epoxied to the end of an aluminum "springboard." A milled area here assists in the positioning of the lenses. The cube is cradled by the milled area of (and epoxied onto) an aluminum "sled." The sled also is tapped to receive the holder for the third lens which is uncut. The sled was slid along the slot in the springboard for final alignment and then "dogged" down. The springboard and sled were bolted onto a 1/2 in. thick tapped aluminum breadboard cut to 6 in. x 6 in. The 25 mm x 61 mm x 14 mm symmetric gold coated mirrors were cut by the NIST glass shops (Jack Fuller) from a single 75 mm x 75 mm x 14 mm mirror slab from Melles Griot (02 MFG 007). These mirrors were epoxied onto mirror holders which were then bolted to the breadboard.

9.8 mm
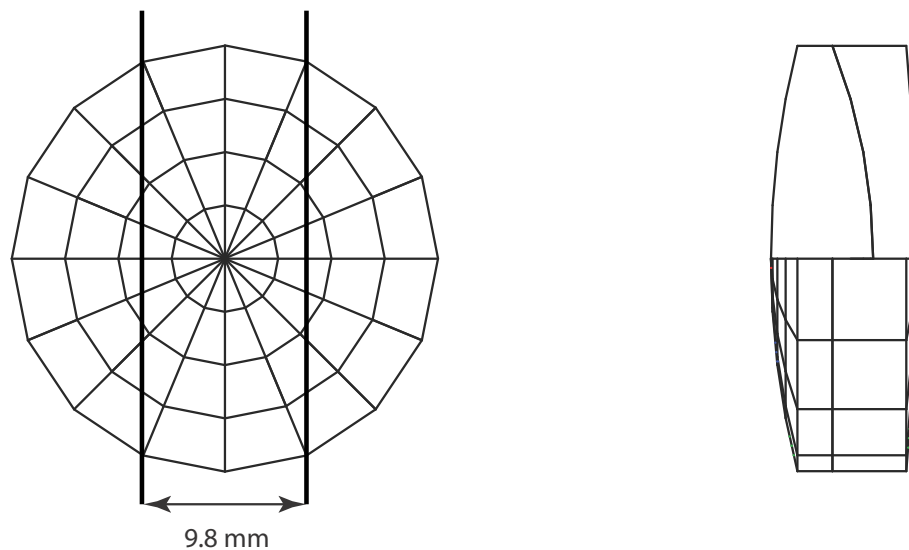
Figure 5.7: Locations of the cuts to the 06 LAI 009 precision achromatic doublet.

The galvanometer needed to be held firmly because it is a moving part. The manufacturer advised us against fastening around its base and the shaft could not

6.4
Springboard
13.0
8.3
88.9
26
8.9
1.6
25.4
7.3
38.1
50.8

tapped
4.7
57.2
2.0
44.5
Sled
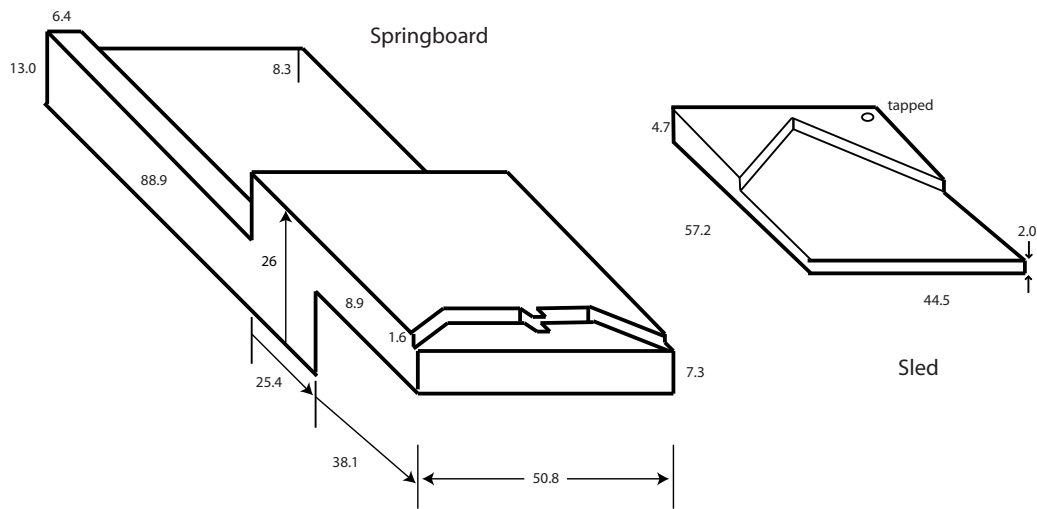
6.7 dia. hole goes completely through (8.3 deep)
9.9 dia. hole (counterbore) goes down 6.7

152.4
12.7
6.7
9.9
12.7
50.8
25.4
50.8
6.4
88.9

45°
25.4
3.2
8.7
Springboard
25.4
3.2
63.5

PLAN

tapped
4.0
45°
9.3
THICKNESS
HERE = 2.0
Sled
44.5
12.7
19.1
45°
THICKNESS
HERE = 4.7
57.2
PLAN
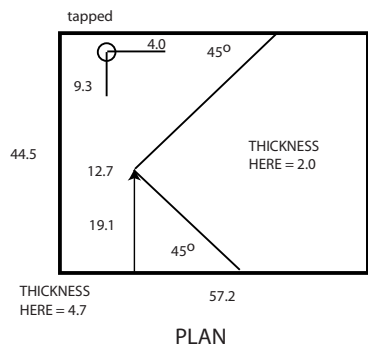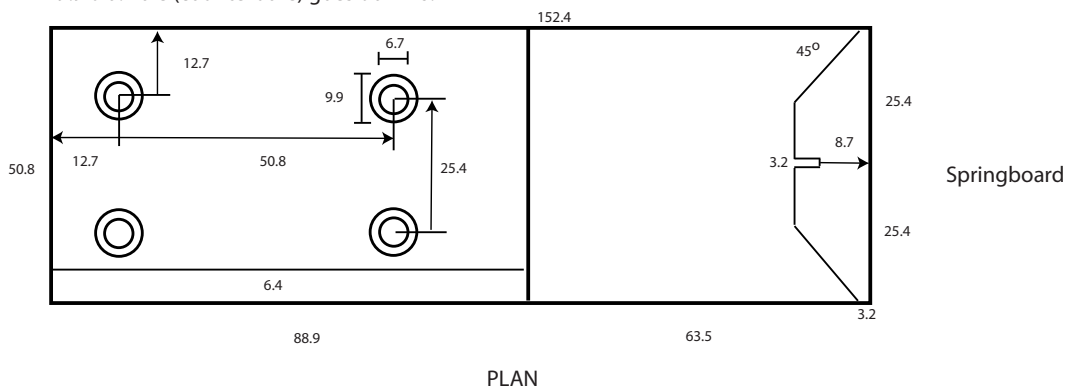
MATERIAL: ALUMINUM
all dimensions in mm
TOLERANCE: .05 mm (2 mil)

Figure 5.8: Springboard and sled hardware to support and align lens and cube.

97

be clamped too tightly because of the possibility of bearing seizure. As shown on Figure 5.9, we designed and built a small aluminum "clamshell" jig to hold the shaft housing, spreading the force over a large surface area while permitting frictional heat from shaft rotation to be dissipated.

All dimensions in mm.
Material: Aluminum
Tolerance for upper bore hole: .025 mm (1 mil)
All other tolerances: .125 mm. (5 mil)
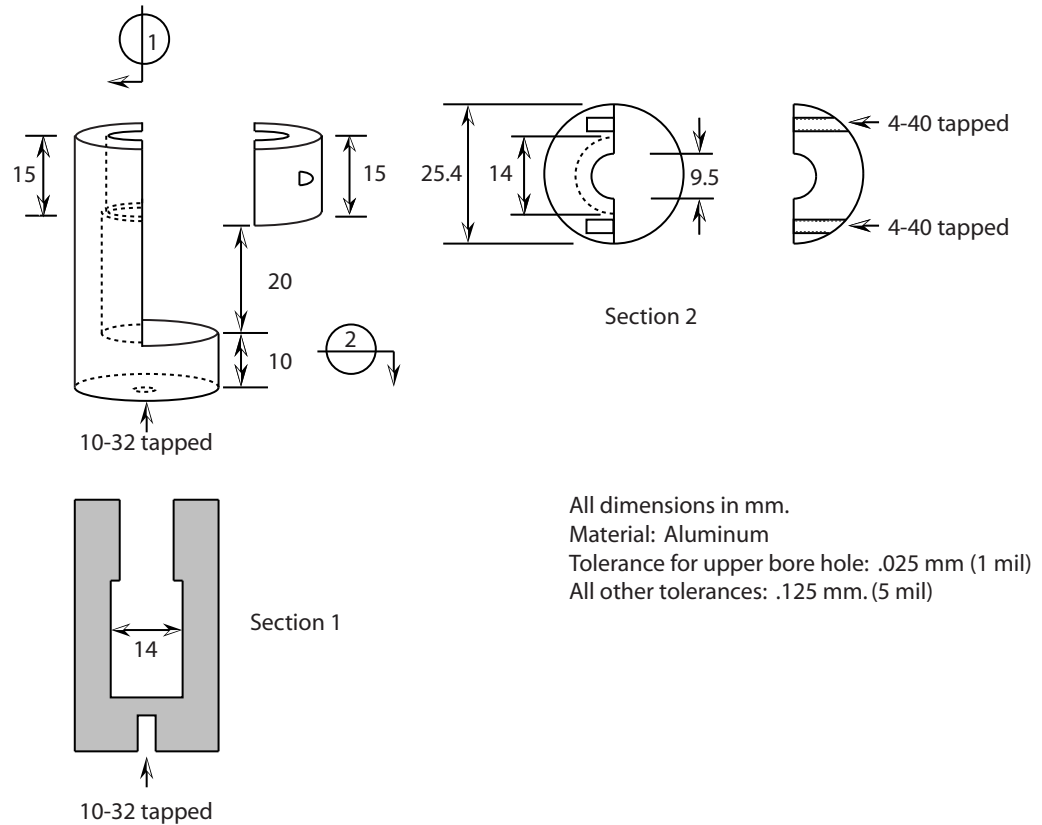
Figure 5.9: Clamshell hardware to hold the galvanometer.

The optical fiber patchcord which brings the light into the accordion lattice was made by OZ Optics Ltd. It was supplied with all connectors and focussing optics. The 8 m long, polarization-maintaining fiber has a 5 μm diameter core, 125 μm diameter cladding, and 3 mm OD Kevlar-reinforced PVC jacket. The fiber was cut angle-flat with NTT/FC connectors. Back reflection was less than -40 dB. Held by a 33 mm OD flange, the focussing lens was a 3mm diameter asphere with a 2.7

mm focal length arranged to create a 190 μm waist at 150 mm working distance. The half-wave plate which we installed after the fiber lens was, unfortunately, not zero-order, requiring adjustment when the laser wavelength is changed. We intend to rectify this deficiency in late 2006.

5.1.4   Accordion Beam Alignment on Breadboard

We oriented the two final symmetric lenses so as to approximately overlap their focal points. Then adjusting the symmetric mirrors, we minimized the displacement of the intersection point of the two outgoing beams as the incoming beams were scanned across the lenses. This was accomplished on the bench with a piece of Pyrex glass (that was identical to that used in the construction of the cell in the experiment) inserted in the paths of the beams to account for the deviation due to the glass cell in the actual experiment. A CCD array was placed at the BEC location and in planes perpendicular to the bisector of the two beams forward of and behind the BEC location. The center of the each beam was determined using a two-dimensional gaussian fit. Figure 5.10 depicts the measured beam intersections after final alignment.

5.2   Analysis of Heating in the Accordion Lattice

The galvanometer which controls the rotation of the first mirror is a VM500 made by GSI Lumonics (now GSI Group, Inc.) [99]. It is a closed loop (capacitor pick-up) servo-actuated limited-rotation motor. It allows the 4mm clear aperture
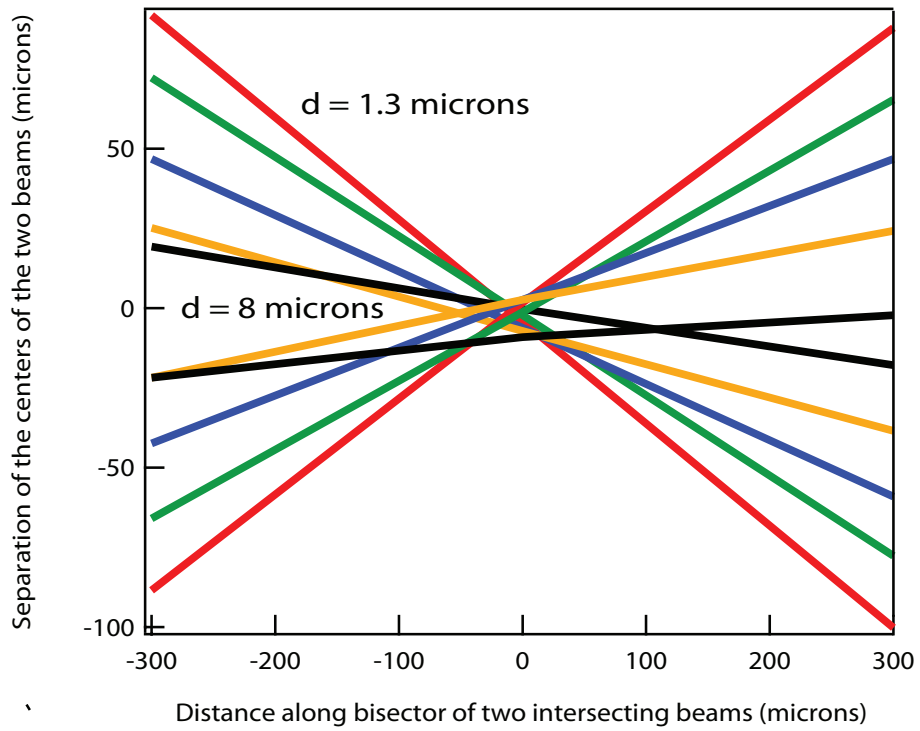
Figure 5.10: Final alignment of the accordion lattice. The red beams give a lattice periodicity of 1.3 μm and the black beams give a periodicity of approximately 8 μm. The intersection point of the black beams is displaced slightly more than 100 μm from the intersection points of most of the other beam pairs.

gold mirror to rotate approximately +/- 1 radian with a -3 dB bandwidth of 3500 Hz. A concern in the development of our device was the amount of lattice periodicity, d, fluctuation generated by galvanometer dither. Lattice periodicity variation causes fluctuation of the harmonic frequency, f_o, of the array of sinusoidal optical traps because $f_o = 2\sqrt{s}E_R 2d/h\lambda$ where s is the lattice depth in single photon recoil energy units, E_R. This heats the atoms parametrically, causing them to leave the ground state. This is the situation at the center of the intersection of the beams. Away from the center, in addition to parametric excitation, lattice periodicity fluctuation causes translational noise.

5.2.1   Parametric Heating

The energy, $E(t)$, of a parametrically-heated cloud in a harmonic trap increases exponentially in time with a rate constant given by [98]

$$\frac{\dot{E}}{E(t)} = \Gamma = \pi^2 f_o^2 S_\epsilon(2f_o), \tag{5.5}$$

where $f_o = \omega_o/2\pi$ is the optical trap oscillation frequency and $S_\epsilon(2f_o)$ is the one-sided (frequency analyzed only up to the Nyquist frequency) power spectral density of the fractional fluctuation in the spring constant $(M\omega_o^2)$ of the optical trap measured at twice the optical trap frequency. For a deep optical lattice, the relationship between the trap frequency and galvanometer rotation angle $\phi = \theta/2$ is

$$f_o = 2\sqrt{s}\frac{E_R}{h}\sin\phi, \tag{5.6}$$

where E_R is the single photon recoil energy ($h^2/(2m\lambda^2)$), s is the lattice depth in units of E_R, and $\phi=0$ corresponds to the angle giving an infinite lattice constant. The relationship between the fractional fluctuation in the trap spring constant and the galvanometer dither, $\delta\phi$, is

$$\frac{\delta(\frac{1}{2}M\omega_o^2)}{\frac{1}{2}M\omega_o^2} = 2\delta\phi\cot\phi. \tag{5.7}$$

Using these two relationships, we find that the heating rate constant at the center of the beam intersection is

$$\Gamma = 16\pi^2 s(\frac{E_R}{h})^2 S_\phi(2f_o)\cos^2\phi, \tag{5.8}$$

where $S_\phi(2f_o)$ is the one-sided power spectral density of the angular fluctuation of the galvanometer measured at twice the trap frequency.

5.2.2 Translational Heating

For a harmonic trap, translational noise caused by lattice constant fluctuation results in heating that is independent of the energy of the trapped particle [98]. A characteristic time, τ_x, may be defined [98] which is the time it takes to double the initial trap energy $\tau_x = \langle E(0)\rangle / \langle\dot{E}\rangle$:

$$\tau_x = \frac{\langle x^2\rangle}{\pi^2 f_o^2 S_x(f_o)}, \tag{5.9}$$

where $\langle x^2 \rangle$ is the initial mean-square displacement of an atom in a trap and $S_x(f_o)$ is the one-sided power spectral density of the trap position fluctuation measured at the trap frequency. The relationship between the trap position fluctuation and the galvanometer dither is

$$\delta x = \frac{\lambda n \cot \phi}{2 \sin \phi} \delta \phi, \tag{5.10}$$

where n is the number of lattice sites away from the intersection point center that the lattice site of interest is located. Using this expression and Eq. (5.9) and assuming the ground state so that $\langle x^2 \rangle = \hbar/4\pi M f_o$, we obtain:

$$\tau_x^{-1} = 8\pi^4 n^2 S_\phi(f_o) (\frac{E_R}{h})^2 s^{3/2} \Big[\zeta - \frac{1}{\zeta} \Big], \tag{5.11}$$

where $\zeta = 2d/\lambda$ is the lattice scale factor. Notice that by definition s and E_R are not changed by lattice constant variation. Therefore, for a fixed laser wavelength and intensity, the only dependence τ_x has on the optical trap oscillation frequency is contained in $S_\phi(2f_o)$ Also observe that, because of the $\zeta - 1/\zeta$ factor, Eq. (5.11) predicts that no translational heating occurs for counterpropagating beams. This is expected, since we have derived a translational heating expression due to angular noise.

5.2.3   VM500 Dither Noise

We measured the rotational dither noise of the VM500 galvanometer by looking at its reflected light past a razor blade onto a photodiode and obtained a power
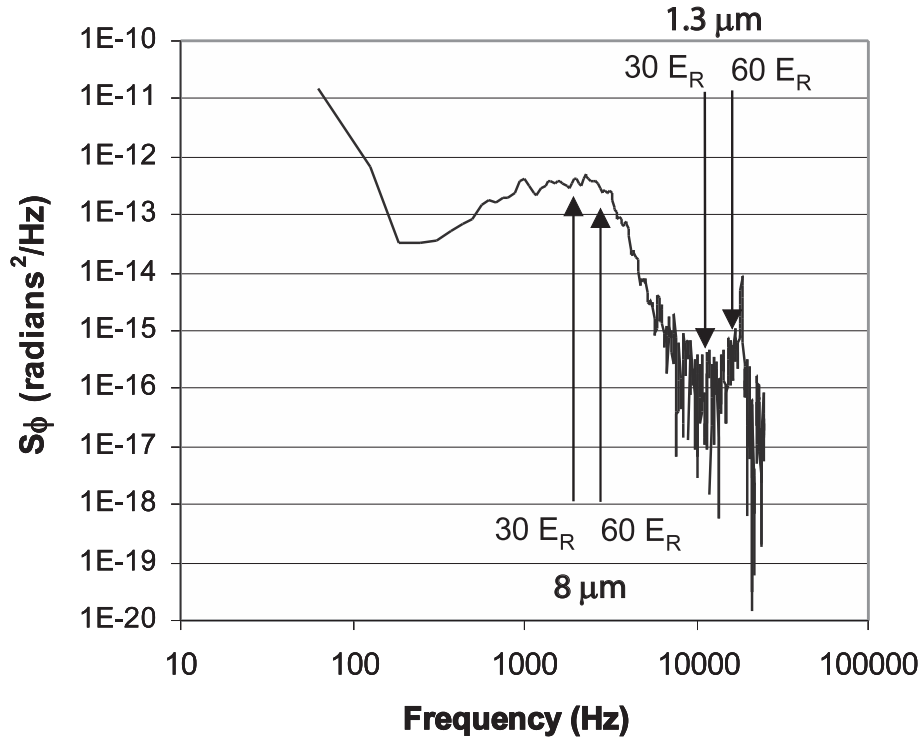
Figure 5.11: VM500 galvanometer dither noise with no applied voltage.

spectrum with a very broad peak centered at 2 kHz and a slightly narrower dip centered at 10 kHz as shown in Figure 5.11. (I was able to convert the measured photodiode noise into rotational dither noise by first measuring the photodiode response from a known small angular modulation signal. I also verified that laser light amplitude noise was not a contributor to the noise I measured.) The dither was measured with no voltage applied to the control circuitry. The peak at 2 kHz was approximately 40 dB higher than the dip at 10 kHz. Using the power spectrum in Figure 5.11, for a 30 E_R deep lattice at $d = 1.3$ μm, the characteristic times for parametric and translational heating would be approximately 3000 sec and 60 sec, respectively, assuming excitation from the ground state. At the same lattice depth at $d = 8$ μm, the characteristic times would be approximately 300 sec and 100 msec.

For these calculations, we set n equal to 4 and 20 for the $d = 8$ μm and $d = 1.3$ μm configurations, respectively.

5.2.4 Power Supply and Signal Generator Noise

Sobered by these results, we attempted to track down the source of the VM500 dither noise. We suspected the supply powering the galvanometer feedback/control circuitry might be one source of the noise. This was a linear (non-switching) Sola/Hevi-Duty SLD15-3030-15 capable of delivering 3 A at ±15 V. We switched to an array of lantern batteries which had problems delivering sufficient current. We considered trying an automobile or marine battery, but instead borrowed a dual DC supply (Topward 6302D) from the NIST Tweezers laboratory which reduced dither noise overall by several dB again by looking at the light past a razor blade onto a photodiode.

Next, we looked carefully at the noise on the signal voltage from the generators used to send commands to the VM500 feedback/control circuitry. Although this was not a contributor to the previously measured noise because there was no signal, we wanted to know if the signal generator noise would be a limiting factor (preventing us from performing long duration experiments) during normal use of the accordion lattice (when voltages were applied). We examined two or three SRS DS345 signal generators and two or three Agilent 33250A signal generators from our laboratory and were surprised at what we found. First of all, the SRS DS345 is quieter than the Agilent 33250A at any frequency up to a few kHz as long as it is commanding

0 V in offset or arbitrary waveform mode. (Offset mode means that the generator outputs a constant voltage offset selected by the user with no additional waveform. Arbitrary waveform mode means that there is no offset voltage and a constant voltage is created by programming an appropriate constant waveform which is then executed by the generator.) However, (presumably due to noise in a gain stage), noise from the SRS DS345 increases rapidly when it commands non-zero voltages. At 1 V, its noise increases 20-30 dB, depending on whether it is in offset or arbitrary mode (arbitrary mode is higher). In contrast, noise from the Agilent 33250A does not increase when it commands non-zero voltages. At 1 V, it is on average quieter than the SRS DS345, however with a very pronounced 60 Hz overtone spectrum.
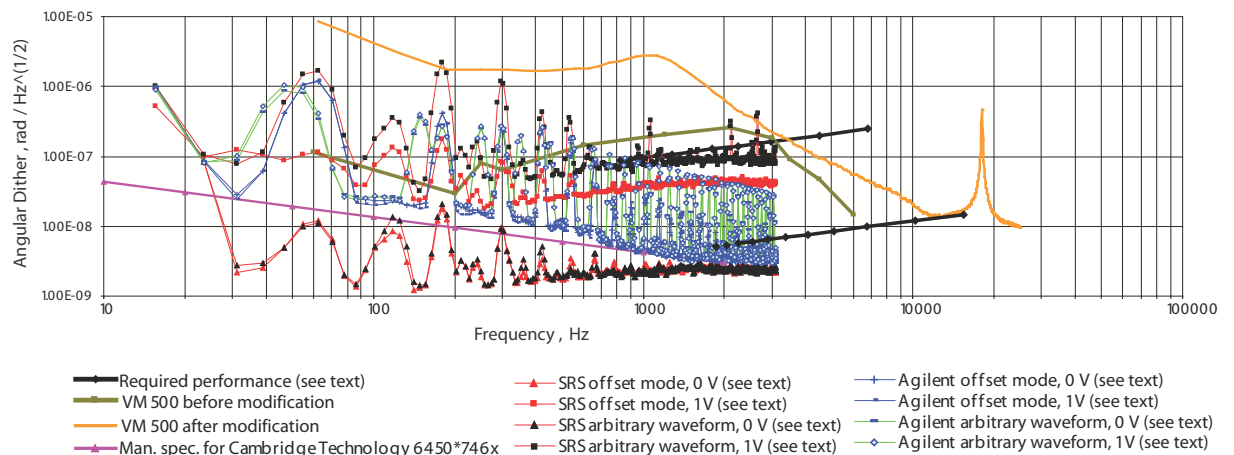
Figure 5.12: A comparison of dither noises. Black curves are example not-to-exceed specifications for translational noise. Voltage noise from signal generators has been converted into angular noise.

To see if the signal generator noise is a limiting factor, we plot various curves in Figure 5.12 which we now describe. All of the signal generator voltage noise data are converted into corresponding dither noise and compared to the measured

VM500 galvanometer dither noise. This conversion was done by using the previously measured flat voltage/angle transfer function up to the 3kHz galvanometer corner frequency. The measured VM500 dither noise is for before (greenish-brown) and after (pumpkin) factory-specified modifications were made to the feedback electronics in an attempt to quiet it. (It is apparent that these modifications increased the noise.) Depending on the frequency, the signal generators could or could not be contributing a major part of the noise. Also shown in this figure are example required performance curves. The upper black curve is for $\tau_x^{-1} = 0.2$ s^{-1}, $s = 10$ E_{R} and $n = 2$. The lower black curve is for $\tau_x^{-1} = 0.2$ s^{-1}, $s = 50$ E_{R} and $n = 10$. The frequency domain of each curve corresponds to the full range of lattice periodicities given by the frequency and lattice depth. The choice of $\tau_x^{-1} = 0.2$ s^{-1} is a good estimate of the longest experiments (≈ 5 s) we may wish to conduct. As is expected, the translational noise specification curve shifts depending on the optical lattice depth and the number of lattice sites n away from the center an atom is. Finally, a noise specification for the quietest galvanometer commercially available, the Cambridge Technology 6450 (*746x option) is plotted for comparison.

5.3   Motional Adiabaticity

Another important issue is maintaining adiabaticity while dynamically changing the lattice constant. We theoretically investigate this problem from the standpoint of a single particle. Our goal is to change d continuously without excitation from the ground vibrational level to higher levels. For our analysis, we assume the

deep lattice limit. In this situation, we ignore tunnelling and interactions, and restrict our attention to a single lattice site of the optical lattice. Accordingly, the eigenvalues are labelled by a single index which corresponds to the band index of the full lattice.

To model the dynamics of a single well undergoing expansion or contraction, we employ an adiabatic basis set [102]. The wave function Ψ is expanded as follows,

$$\Psi(t) = \sum_j a_j(t) \exp^{-\frac{i}{\hbar}\int_0^t E_j(t')dt'} |j(t)\rangle, \tag{5.12}$$

where $|j(t)\rangle$ is the instantaneous basis vector with eigenvalue $E_j(t)$ corresponding to the single-well size at some point in time, $d(t)$. This ansatz is inserted into the Schrödinger equation and solved for the coefficients. The dynamics is then computed from the coupled set of equations,

$$\dot{a}_i = \sum_{j \neq i} a_j(t) \frac{\langle i(t)|\dot{H}|j(t)\rangle}{E_i(t) - E_j(t)} \exp^{i(\alpha_j(t) - \alpha_i(t))}, \tag{5.13}$$

where the coefficient $\alpha_j(t) = -\frac{1}{\hbar}\int_0^t E_j(t')dt'$ is defined to simplify the notation.

It has been verified [103] that a reduced basis set consisting of the first two terms is a good approximation to the problem if the expansion (or contraction) time is longer than the optical trap oscillation period. For the central cell in the lattice, which does not translate during expansion (or contraction), the ground and second excited state is a good basis. For all other cells, the coefficient for the first excited

state is much larger than that for the second excited state which we can therefore ignore. Furthermore, if the stretching takes place sufficiently slowly, then we can set $a_0 = 1$ and

$$a_1(t) = \int_0^t \frac{\left\langle 1(t')|\dot{H}|0(t')\right\rangle}{E_1(t') - E_0(t')} \exp^{i(\alpha_0(t') - \alpha_1(t'))} dt' \tag{5.14}$$

We have solved Eq. (5.14) analytically (except for a final numerical integration) by substituting a quadratic potential for the actual sinusoidal potential. Since we are only considering the ground and first excited states in the deep lattice limit, this is a reasonable approximation. Figure 5.13 depicts the final value of $a_1^* a_1$ at the approximate edge of the cloud after an exponential lattice compression from 8 μm to 1.3 μm for compression durations of 200 msec to 500 msec. The trap oscillation frequency evolution was $\omega(t) = \omega_0 e^{\gamma t}$ where ω_0 is the initial trap frequency and γ is chosen so that ω is equal to the final trap frequency at the end of the ramp. For example, in Figure 5.13, a ramp duration of 200 msec gives $\gamma = 9.2$ sec^{-1}. For this calculation, a lattice depth of $30 E_R$ was assumed, giving $\omega_0 = 12000$ rad/sec. Note that the rapid small-scale variations from a straight line are due to a sampling of the high frequency portion of the transition probability that oscillates at the trap oscillation frequency. Since this calculation was performed near the edge of the cloud (n=10), it is close to a worst-case assessment. Lattice sites closer to the center of the atomic cloud would translate less and thus result in less band excitation. Nevertheless, it is clear from this analysis that lattice compressions and expansions will likely require hundreds of milliseconds in order to maintain high fidelity.
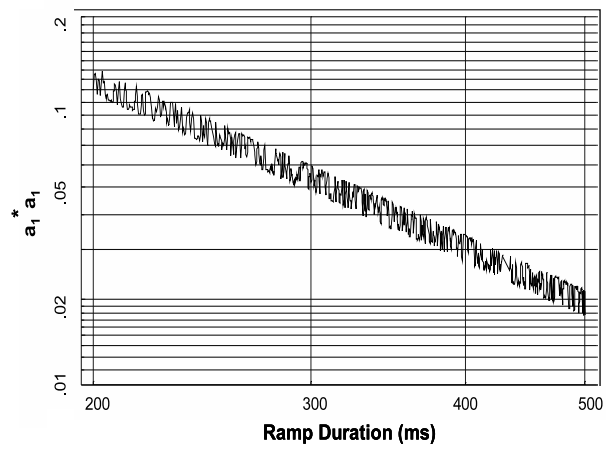
Figure 5.13: First band excitation versus exponential compression duration for a constant lattice depth of 30 E_R. For all ramps, the starting frequency was 12 000 rad/sec and the ending frequency was 75 000 rad/sec corresponding to starting and ending lattice spacings of 8 μm and 1.3 μm, respectively.

Chapter 6

Periodicity Calibration of the Accordion Lattice

The spatial periodicity d of a 1D optical lattice formed by two laser beams intersecting at an angle θ is equal to $\lambda/[2\sin(\theta/2)]$, where λ is the wavelength of the laser light. This fact can be easily confirmed by performing a BEC diffraction experiment. As shown in Figure 6.1, following the diffraction of the BEC, if there is a sufficiently long time-of-flight t_{TOF} to be in the far field (where the separation between orders is large compared to the cloud size of the individual orders), then the momentum components (orders) of the BEC produced by the optical lattice will have time to separate from each other and this minimum separation distance D between the orders (ignoring the effect of atom-atom interactions during expansion) is simply related to the lattice periodicity by

$$D = \frac{2\hbar k \sin(\theta/2)}{M} t_{\text{TOF}} = \frac{2\hbar \kappa_{\text{L}}}{M} t_{\text{TOF}} = \frac{h}{Md} t_{\text{TOF}}, \qquad (6.1)$$

where k and κ_{L} are the magnitudes of the single photon wavevector and half the reciprocal lattice vector, respectively, and M is the mass of the atom (in our case ^{87}Rb). Another method to determine d is by mapping the Bloch bands as described in Sec. 3.6. In this case the total width of a Brillouin zone also equals ht_{TOF}/Md.

These methods work well as long as the *lattice* recoil energy E_{L} as defined in Eq. (3.27) is much larger than the peak mean-field energy U_{int} at the center of the
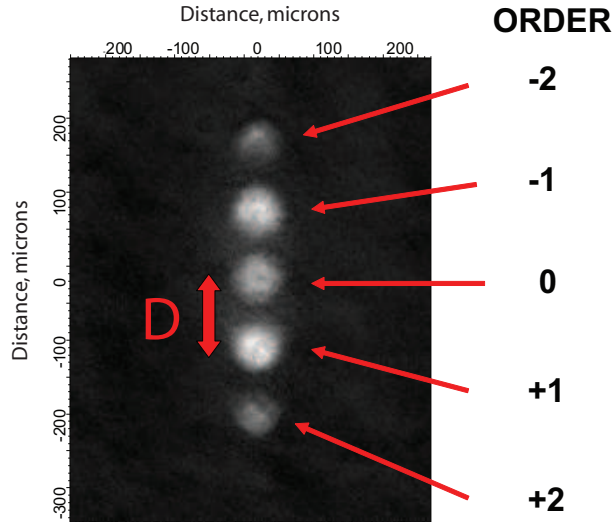
Figure 6.1: Matter wave diffraction. A BEC of approximately 200 000 ^{87}Rb atoms is pulsed by a 30 E_{R} deep optical lattice with lattice constant $d = 1.3\mu$m for $t_{\mathrm{pulse}} = 8\mu$s and then expands freely for $t_{\mathrm{TOF}} = 27$ ms.

central lattice site at the time of release of the BEC. If this is not the case, then for the diffraction experiment two complications occur. First, inter-order atom-atom interactions alter D resulting in erroneous d values. Second, if $E_{\mathrm{L}} < U_{\mathrm{int}}$, the orders (which can be viewed as copies of the original BEC separated in momentum space by the reciprocal lattice vector) will individually expand during the time-of-flight faster then they are separating from each other, and thus it will not be possible to even determine D from the far field diffraction since one is never in the far field. This is because the expansion of a BEC during time-of-flight is created by the fact that mean-field energy is converted to kinetic energy, when all confining potentials are removed [45].

These issues affected the calibration of the accordion lattice at long periodicities where $E_{\mathrm{L}} \not> U_{\mathrm{int}}$. As opposed to simply calculating the lattice periodicity based on what we believed the angle of intersection of the two beams to be, we wanted to

calibrate the lattice periodicity in-situ using diffraction. If we had decided to determine the accordion lattice periodicities by directly measuring the beam intersection angles, we would have had to determine angles to better than 0.001 radian precision (at $d = 3$ μm) to achieve the precision of the superlattice experiment described below. This would have required, for example, measuring 1 mm center-to-center laser beam separations at a distance of 1 m where the beams have a $1/e^2$ full waist of 5 mm which, although possible, would have been difficult. Additionally, we would have had to take into account the effect of the glass cell in the experiment with an ersatz piece of glass which would have led to some additional uncertainty. Finally, the required angular precision increases inverse quadratically with the beam intersection angle to the point where we would have needed 80 μrad precision at the smallest angles (longest periodicities), which would have been hopeless.

Thus, we began by diffracting the BEC and measuring D after a time of flight of the atoms. However, as the beam intersection angle was reduced and d correspondingly increased, it soon became impossible to measure D because the orders were no longer well separated, as shown in Figure 6.2. They increasingly overlapped and began to interfere with one another. This order interference became the ultimate effect by which we were finally able to calibrate the accordion lattice for long periodicities.

This chapter describes the three techniques used for the accordion lattice calibration and describes an intriguing method which could be further developed to make very precise measurements of U_{int} (or at least the part of U_{int} which is responsible for incrementally separating orders).
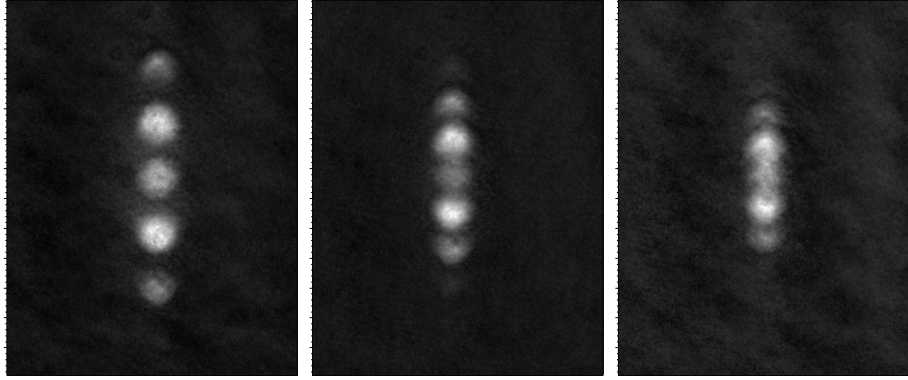
Figure 6.2: The same BEC diffraction experiment described in Figure 6.1 is performed for different lattice periodicities, d. As d increases from 1.3μm, 2.2μm, to 2.5μm (left to right), the BEC orders increasingly overlap.

6.1 BEC Far-field Diffraction in the Accordion Lattice

The initial diffraction experiment to determine the lattice periodicity as a function of voltage applied to the accordion lattice galvanometer proceeded as follows. A BEC of approximately 200 000 ^{87}Rb atoms was produced in the tight magnetic trap (axial and radial trapping frequencies of 8.7 Hz and 125 Hz, respectively). The BEC was adiabatically expanded to the weak magnetic trap (axial and radial trapping frequencies of 8.2 Hz and 24 Hz, respectively). The galvanometer feedback/control circuit was then commanded a constant voltage from the computer which rotated the accordion mirror to a fixed position. Laser light at $\lambda = 810.345$ nm (in air) from the Ti:Sapph laser was abruptly applied to the atoms at the full lattice depth of approximately 30 E_{R} and held constant for 8μs. At the end of the 8μs, the lattice and IP trap were extinguished (total time for the current to leave the IP trap was approximately 250 μs). Following a 27.1 ms time of flight, the falling and expanding

114

cloud of atoms was absorption imaged along the vertical axis at 6x magnification with $F = 2 \rightarrow F' = 3$ resonant light.

The preceding process was repeated 100 times, each time with a different voltage applied to the galvanometer control circuit. The scan began at 1.2 volts and ended at -1.0 volts with a constant step size of 0.022 volts corresponding to 2.7 mrad constant step size (1% periodicity increments at smallest periodicities and 5% increments at largest periodicities). The images obtained after each time of flight appeared similar to those in Figures 6.1 and 6.2. We performed triple 1D Gaussian fits on each image to extract average values of D, the distance between the +1, 0, and -1 orders. Another fitting gave us D values based on the distances between the 0th order and the $\pm 2^{\text{nd}}$ orders. From these values of D, we calculated the lattice periodicity as a function of the galvanometer voltage using Eq. (6.1). The results are presented with an overall fitting function $d = (\lambda/2)/\sin(\text{B} + \text{C} * V_{\text{galvo}})$ in Figure 6.3.

The D values extracted from the +1, 0, -1 order fitting procedure showed significantly more scatter as the galvanometer voltage was reduced below 0 volts for two main reasons. The first reason was simply that the fitting procedure became increasingly difficult as the orders increasingly overlapped. The second reason was that as the lattice periodicity grew larger, the measurement became increasingly dependent on N, the total number of atoms in the condensate. Thus noise in N was translated into noise in D as follows. The greater the N, the greater the mean-field energy U_{int} at the moment the condensate is released, and thus the greater the incremental separation between the orders due to this part of the energy of

115
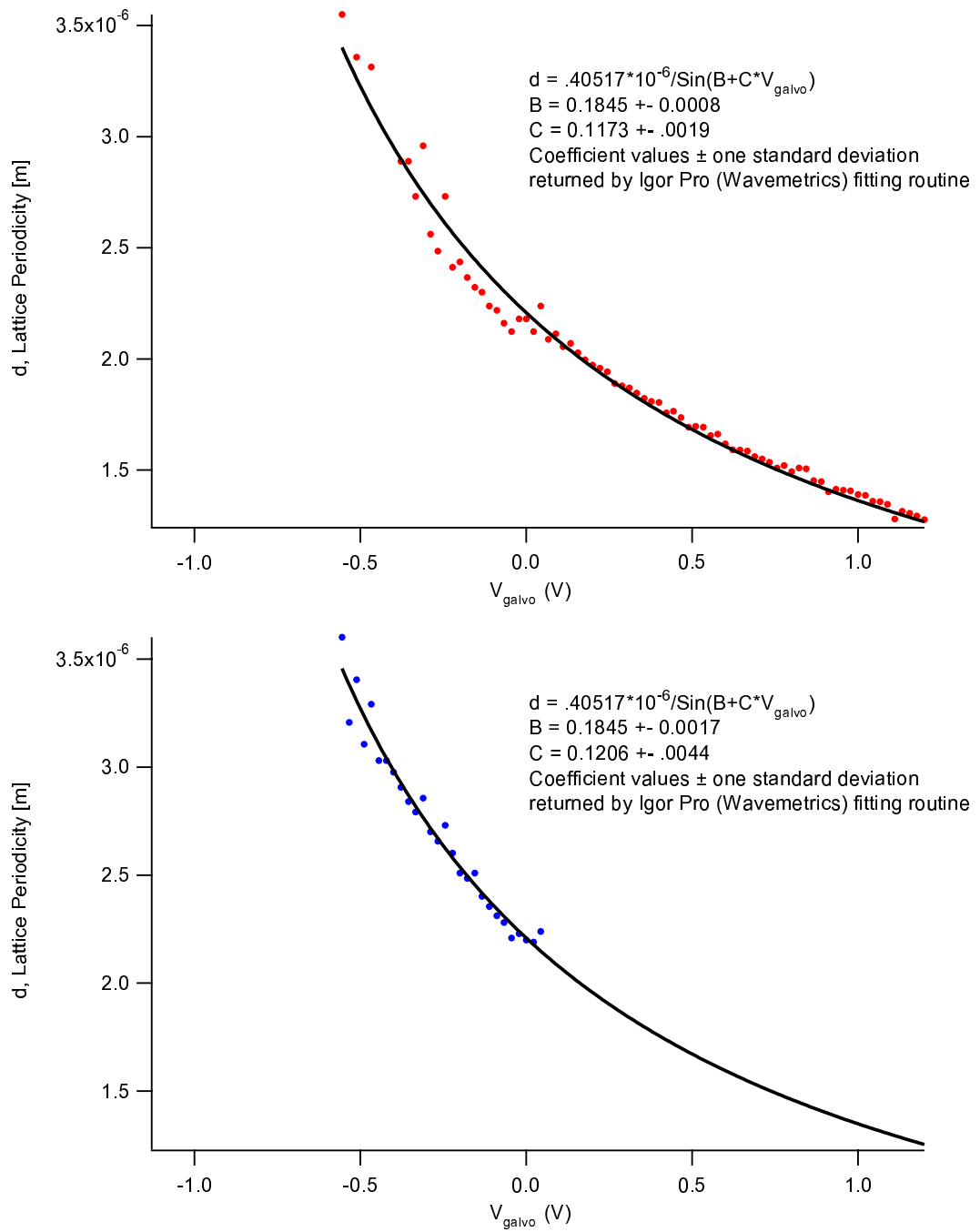
Figure 6.3: Lattice periodicity as a function of accordion lattice galvanometer voltage. Top graph is from a fitting of the 0th order and the $\pm 1^{st}$ orders. Bottom graph is for the 0th order and the $\pm 2^{nd}$ orders.

the atoms. Based on this line of reasoning, at a given $E_{\rm L}$, the largest (and most accurate) periodicities would be calculated when N was smallest. This was indeed the case as the red points for negative voltage above the fitting curve in the upper graph of Figure 6.3 all corresponded to small N experiments.

We expect this effect to be smaller if we look at the distances between the $0^{\rm th}$ order and the $\pm 2^{\rm nd}$ orders because assuming an approximately constant mean-field energy impulse, it represents a smaller fraction of the momentum imparted by the lattice. As shown in the lower graph of Figure 6.3, there is slightly less scatter in the data. The technique of looking at order separations was still ultimately limited by the inability to resolve the orders for reasonable values of N. This caused us to explore alternative procedures to calibrate the accordion lattice which will now be described.

6.2 Loading a BEC into a Superlattice

We decided to use a second 1D lattice whose lattice constant was known with very high precision [149] as a reference for the accordion lattice. This second 1D optical lattice had a fixed periodicity of $\lambda/\sqrt{2}$ and was nearly parallel to and super-imposed on the accordion lattice similar to an earlier NIST experiment [104]. The misalignment between the axes of the two optical lattices comprising the superlat-tice was approximately 30 mrad and so the projection of one on the other was better than 0.999. Since the two lattices were at laser frequencies differing by several MHz,

the total light shift potential seen by the atoms was simply

$$U_L(z) = s_1 E_\mathrm{R} \sin^2\left(\frac{\pi z}{d_1}\right) + s_2 E_\mathrm{R} \sin^2\left(\frac{\pi z}{d_2}\right), \qquad (6.2)$$

where s_1, d_1, s_2, d_2 were the depths and periodicities of the two lattices.

A superlattice potential has a primitive cell periodicity equal to the least common multiple (assuming there is one) of the two underlying periodicities as shown in Figure 6.4. If we load a condensate adiabatically with respect to band excitation into a superlattice potential and then snap the lattice off, the resultant diffraction pattern reveals the primitive cell periodicity. (A diabatic lattice loading and snap off might also reveal the primitive cell periodicity.) There is still a mean-field energy contribution to the kinetic energy of the atoms in the diffraction pattern, and thus we are not able to determine the absolute periodicity of the superlattice knowing only D (for the superlattice) and t_TOF. However, since we know one of the underlying lattice periodicities, we can infer the periodicity of the unknown (accordion) lattice by scanning the accordion lattice periodicity finely across its full range and looking for features in the spectrum of spatial frequencies if the diffraction patterns where the two periodicities are rationally related. We expect these features to look like local minima in the spatial frequency spectrum because frequencies on either side of a diffraction frequency resulting from rationally related lattice periodicities come from primitive lattices with larger periodicities which yield diffraction patterns with higher spatial frequencies.. The experiment proceeded as follows. A BEC of approximately 200 000 ^{87}Rb atoms was produced in the same manner as described
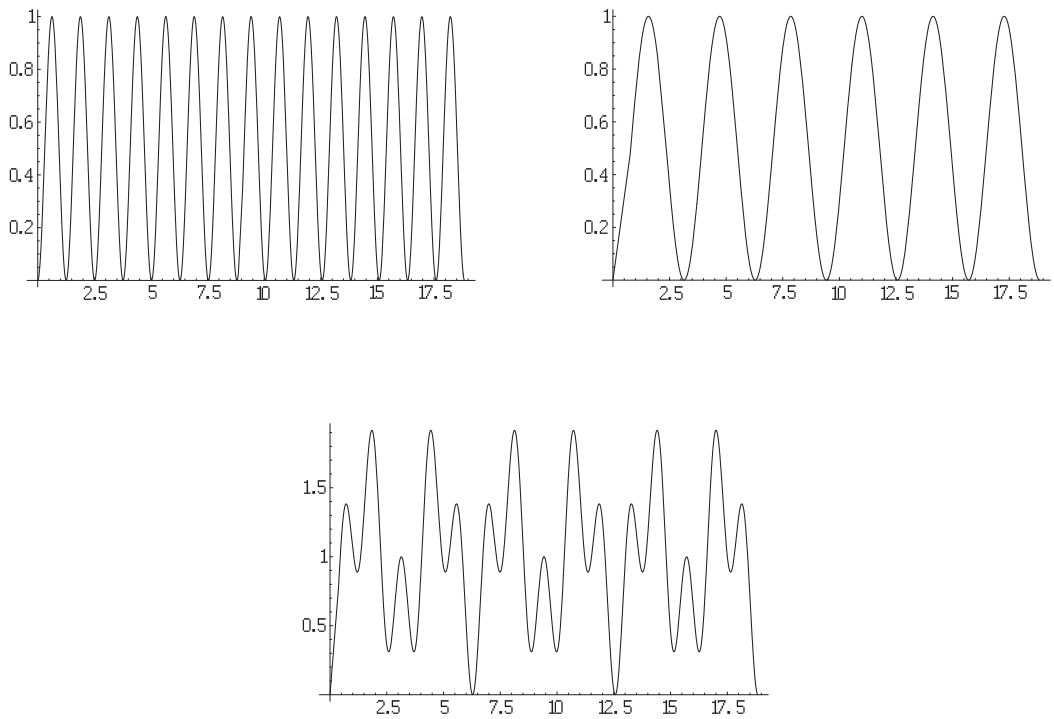
Figure 6.4: Creation of superlattice by summing two independent lattices. The ratio of the periodicities of these two independent lattices is $\frac{5}{2}$. The superlattice has a periodicity equal to the least common multiple of the periodicities of the two independent lattices—in this case 5 times the period of the smallest lattice.

in the previous section. A constant voltage was applied to the galvanometer control circuit to rotate the accordion mirror to a fixed position. Laser light at $\lambda = 810.345$ nm (in air) from the Ti:Sapph laser was applied over 400 μs with a time constant τ of 50 μs ($e^{t/\tau}$) to load the condensate in the superlattice. The individual lattices each had an approximate depth of 30 E_{R}. At the end of the 400 μs period, the lattice was extinguished and the magnetic trap turned off. Following a 27.1 ms time of flight, the atomic cloud was absorption imaged along the vertical axis at 6x magnification with $F = 2 \rightarrow F' = 3$ resonant light. Note that the 400 μs turn-on time satisfied the adiabaticity criterion (Eq. 3.40) by a factor of 7 for the fixed periodicity $\lambda/\sqrt{2}$ lattice and by a lesser (and variable) amount for the accordion lattice.

As before, the galvanometer was scanned beginning at 1.2 volts and ending at -1.0 volts with a constant step size of 0.022 volts. A central slice was taken from each diffraction image and all 100 slices were stacked side by side as shown in the top panel of Figure 6.5. The middle panel of this figure is the 1D Fourier transform of all 100 slices, again stacked side by side. The bottom panel is a blow-up of the bottom third of the middle panel.

The arrows along the horizontal axis in the middle panel of Figure 6.5 indicate the locations of several local minima in the spectrum of spatial frequencies of the diffraction patterns. It is important to use Figure 6.3 as a guide in interpreting this information. For instance, there is a very obvious local minimum at a galvanometer voltage of 0.60 volts. Consulting Figure 6.3, we see that this voltage (according to the fitting function) would correspond to an accordion lattice periodicity of 1.6 μm which is 2.8 times the periodicity of the fixed $\lambda/\sqrt{2}$ lattice. However, this ratio
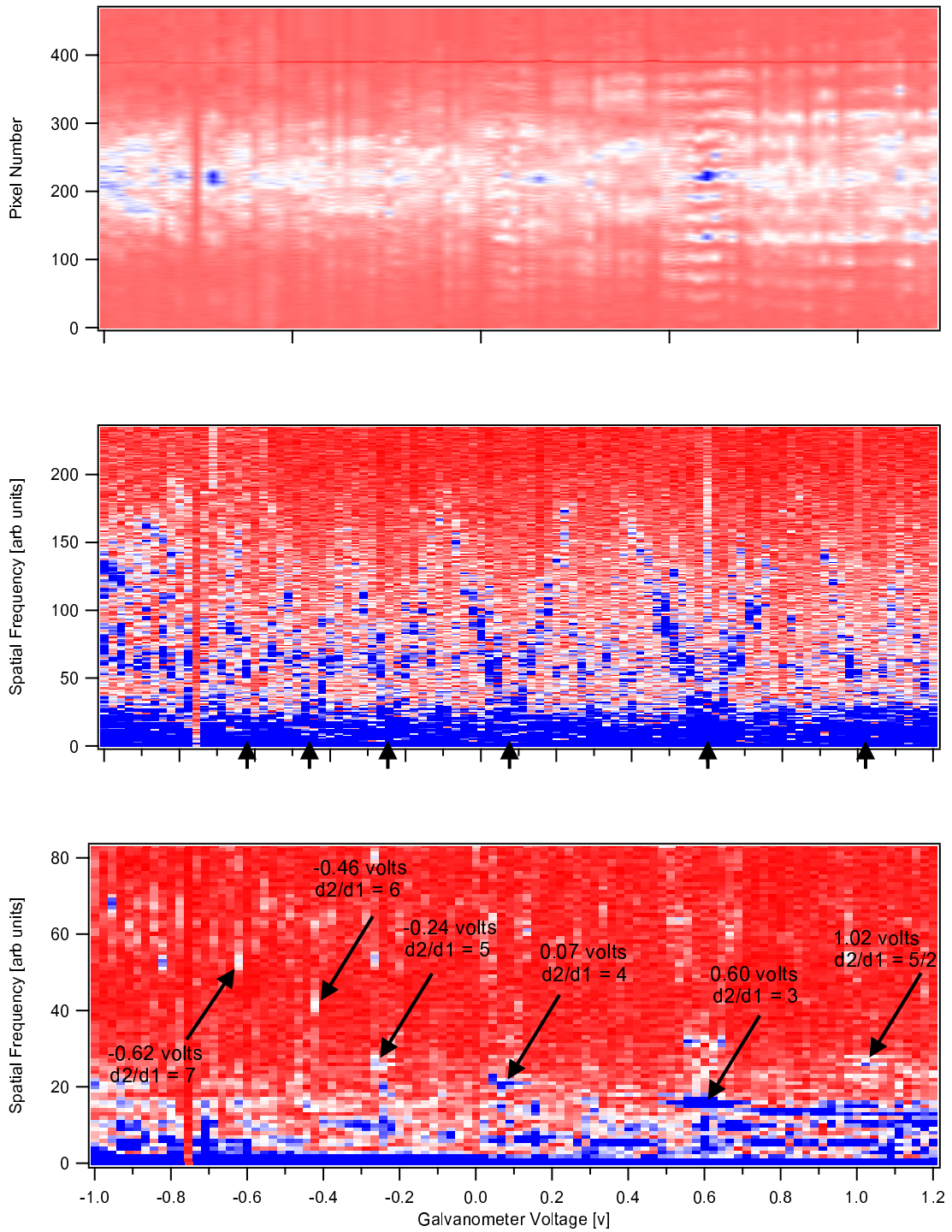
Figure 6.5: Top: BEC diffraction from a 1D superlattice after band-adiabatic loading. Middle: Array of 1D Fourier transform magnitudes of diffraction patterns. Bottom: Lower third of middle panel (with different look-up table). Blue (red) is large (small) signal

of 2.8 cannot possibly correspond to a local minimum because it is very close to a ratio of 3 which would have a lower spatial frequency. Thus, we can assume that the true ratio of the periodicities of the two lattices at 0.60 volts is actually 3 and that the incorrect ratio of 2.8 resulted from the mean-field distortions discussed in Sec. 6.1. Identical lines of reasoning allow us to locate five other local minima and identify each one with its proper lattice period ratio as shown in the bottom panel of Figure 6.5. For the experiment we performed, it was difficult to glean any information below a galvanometer voltage of -0.60 volts based on a visual inspection of the transforms.

The six data points from Figure 6.5 are plotted in Figure 6.6 along with the data from Figure 6.3 for comparison. As can be seen, the superlattice diffraction data predicts larger lattice periodicities than the accordion lattice far-field diffraction data, which is expected since the superlattice diffraction data is interpreted in a way that is insensitive to the mean-field energy. Within its range of usefulness, this superlattice technique measures d significantly more accurately than that described in the previous section since it is based on a fixed reference lattice whose periodicity is known very precisely to calibrate the accordion lattice.

6.2.1 Measurement of Mean-Field Energy

The differences in the periodicities predicted by the two techniques can be used to estimate the amount of mean-field energy at the instant of condensate re-
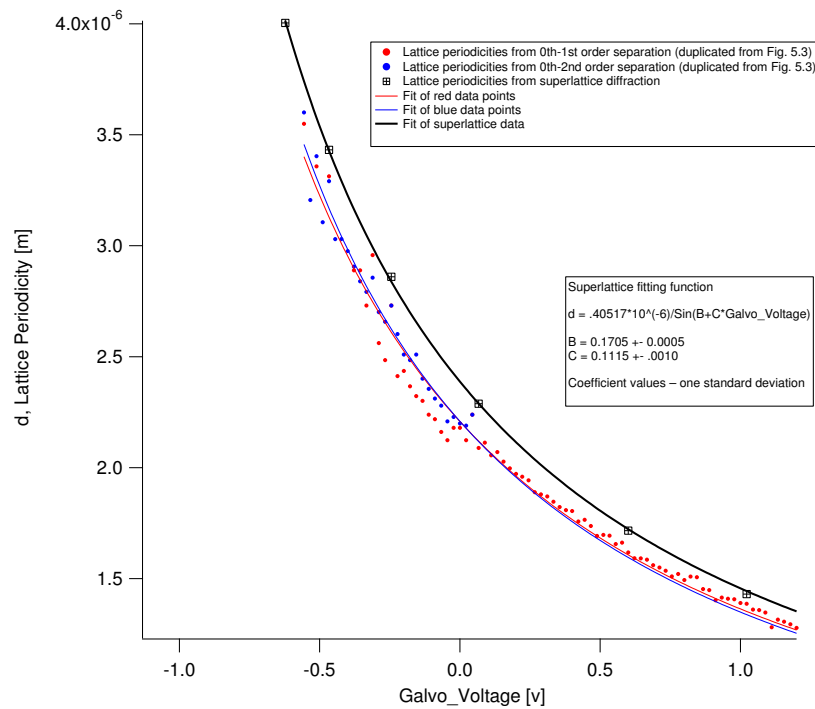
Figure 6.6: Lattice periodicity as a function of accordion lattice galvanometer voltage determined from two techniques. Red and blue data points (duplicated from Figure 6.3) are determined by diffraction from the accordion lattice only. Black boxes are determined from superlattice diffraction. The linearity between the applied voltage and the angle of the galvanometer is better than 0.9992 (as specified by the manufacturer).

lease that goes into causing the orders to separate, U_{sep}.

$$U_{\text{sep}} = \frac{M}{2}\left[\left(1 - \frac{d_{\text{single}}}{d_{\text{super}}}\right)2v_{\text{L}}\right]^2, \tag{6.3}$$

where d_{single} and d_{super} are the calculated periodicities from the single and superlattice diffraction techniques and $v_{\text{L}} = \hbar\kappa_{\text{L}}/M = h/2Md$ is the *lattice* recoil velocity, consistent with the way we have defined E_{L} in this thesis. Remarkably, from the data in Figure 6.6, we are able to measure U_{sep} energies of about 1 Hz (50 pK) (and less) at lattice periodicities of 3 μm (and greater), based on the observed $d_{\text{single}}/d_{\text{super}} \approx 0.92$. Even at the relatively shorter lattice periodicities of 1.3 μm, we measure a U_{sep} of only about 4 Hz (250 pK).

It is interesting that $d_{\text{single}}/d_{\text{super}}$ is nearly constant over the range we measured it. A possible explanation is that, in the inter-order interference regime (explained below), faster separating orders (smaller period lattices) are more likely during their flights to be at distances from the center where the overall BEC density gradient is higher and thus they obtain a higher mean-field impulse (which if it were proportional to their momentum from the lattice would yield a constant $d_{\text{single}}/d_{\text{super}}$). If we were to extrapolate the data (assume that $d_{\text{single}}/d_{\text{super}}$ remains 0.92) to a $d = \lambda/2$ lattice, using Eq. (6.3) we would obtain $U_{\text{sep}} \approx 80$ Hz (4 nK). Since the total mean-field energy per atom is about 120 Hz (6 nK), this would mean that about 2/3 of the total mean-field energy would go into order separation for the $\lambda/2$ lattice. This extrapolated $U_{\text{sep}}/U_{\text{int}}$ ratio of 2/3 is the same as the ratio which was calculated for

an earlier NIST experiment at $\lambda/2$ in which there were only two separating orders [45]. Our data indicates that this fraction decreases in proportion to the decrease in recoil velocity while more and more of the mean-field energy goes into expanding the orders self-similarly. The fact that the ratio decreases as v_{L} decreases makes intuitive sense because the approximation that the orders do not deform as they separate which was used to derive the 2/3 ratio in [45] is increasingly less valid as v_{L} decreases. Since the distortion of each order is primarily a self-similar expansion, it is understandable that it would reduce the energy for order separation.

It is possible that there is a systematic error in t_{TOF} for the single lattice diffraction experiment which could partially account for $d_{\mathrm{single}}/d_{\mathrm{super}} \neq 1$ (perhaps an AOM switch delay). Although we do not have a precise value for this uncertainty, we are fairly confident that it is less than 1% based on oscilloscope observations and thus cannot account for the discrepancy. Another source of uncertainty is related to the fineness of the accordion lattice scan. However, the resolution of the accordion lattice scan in the superlattice experiment corresponded to an uncertainty in d_{super} of only 2% at 3 μm and less at the smaller periodicities which therefore also precludes this as an explanation. (Furthermore, this type of uncertainty is random and not systematic.)

The superlattice experiment did not give us information at the longest periodicities; however it seems that it could have in principle. The initial loading time would have been longer to remain band-adiabatic and the scan would likely have been finer, repeated several times and averaged. Instead, however, we developed a different technique which made use of interference between overlapping orders.

6.3 Interference Between Diffraction Orders

Figure 6.2 shows how changing the lattice periodicity can affect the diffraction of a BEC. What is not captured in this triptych is the effect on the diffraction pattern when the average mean-field energy per atom before time-of-flight is greater than the lattice recoil energy. In this case, the rate of expansion of the orders is greater than the rate of order separation and consequently there is significant spatial-overlapping of the orders for all times of flight. Figure 6.7 shows an absorption image of a diffracted BEC where the initial average mean-field energy per atom was about 120 Hz and the lattice recoil energy was about 6 Hz corresponding to a lattice periodicity of 9.3 μm. This pattern resulted from a $t_{\text{pulse}} = 100$ μs diffraction pulse followed by a 27.1 ms time of flight. The size of each order after mean-field expansion is about 50 μm and the distance between the centers of neighboring orders in the absence of mean-field effects would have been about 12 μm. Thus, there is significant overlapping of neighboring orders. Notice also the very visible fringing along the diffraction axis.

The bottom half of Figure 6.7 depicts a slice through the top image along the blue cursor line. This cursor position was chosen because it gave the best overall fringe contrast. The average fringe separation y between the two vertical black lines is 13.4 μm. (Average fringe separations are slightly smaller in the vicinity of the center of the cross-section possibly indicating smaller mean-field impulses for the inner orders.) When we first obtained images such as these, we thought that the fringing might be due to the matter-wave Talbot effect wherein an image of the

optical lattice was being reformed periodically in time with periodicity fixed to the initial spatial periodicity of the lattice.

This idea was soon laid to rest by experiments such as that summarized in the top half of Figure 6.8. In this experiment, the galvanometer was commanded a fixed voltage of -1.1 volts which corresponded to a very nominal $d = 10$ μm lattice periodicity. A deep lattice then pulsed each BEC the same 100 μs and we varied the time of flight with 500 μs resolution. Here we show slices through diffraction images following increasingly longer times of flight. Thus, shot-by-shot, we have created a space-time picture of the expansion of a single BEC starting from 4 ms after release until 27 msec after it. The bottom half of Figure 6.8 depicts the Fourier transform of each slice in the top half of the figure. The most obvious feature in the bottom image is the strong signal of a decreasing spatial frequency as the time of flight is increased. This signal is not consistent with a Talbot effect interpretation, but rather with a continuously expanding diffraction pattern. It is possible that the spatial frequency signal of 100 units at a $t_{TOF} = 15.5$ ms is related to the Talbot effect, but highly unlikely because this signal would imply a lattice periodicity of about 13 μm (which is significantly more than our best estimates of the maximum periodicity achievable with the accordion lattice). We do not have an explanation for the obvious spatial periodicity gradient of the time-of-flight image (Figure 6.8, top panel) for late times of flight.

The fact that the data in Figure 6.8 seems to be described by an expanding diffraction pattern motivated us to develop an appropriate model describing the physics. Fortunately, we had just heard about the work of the group in Tübingen
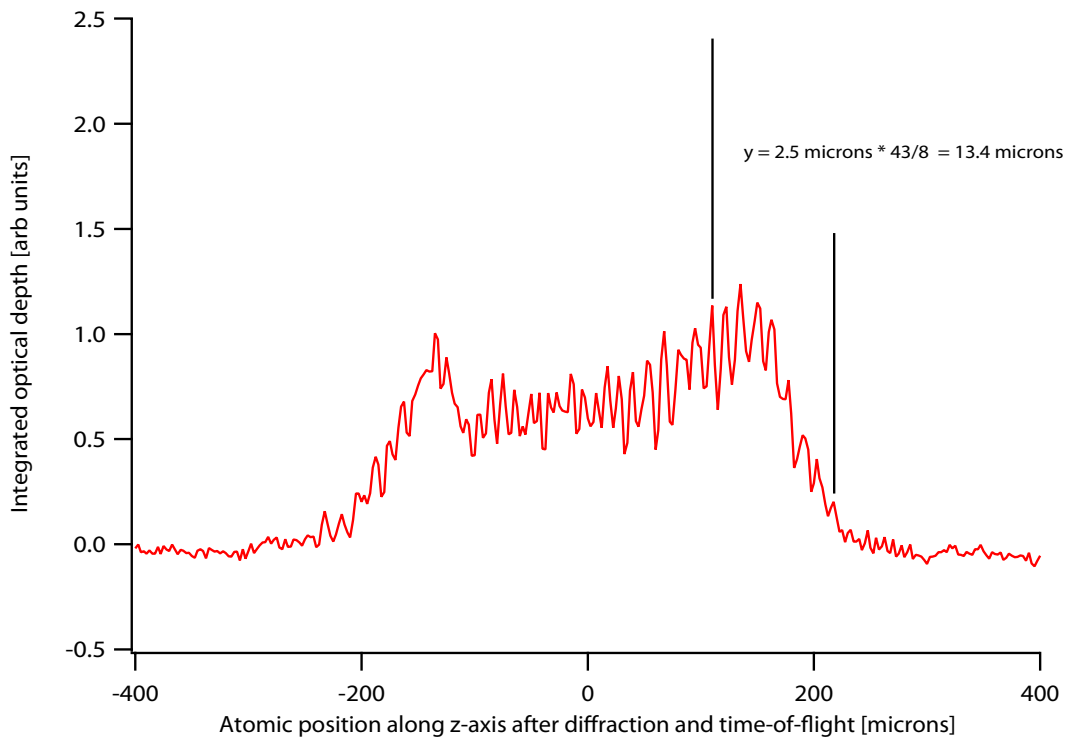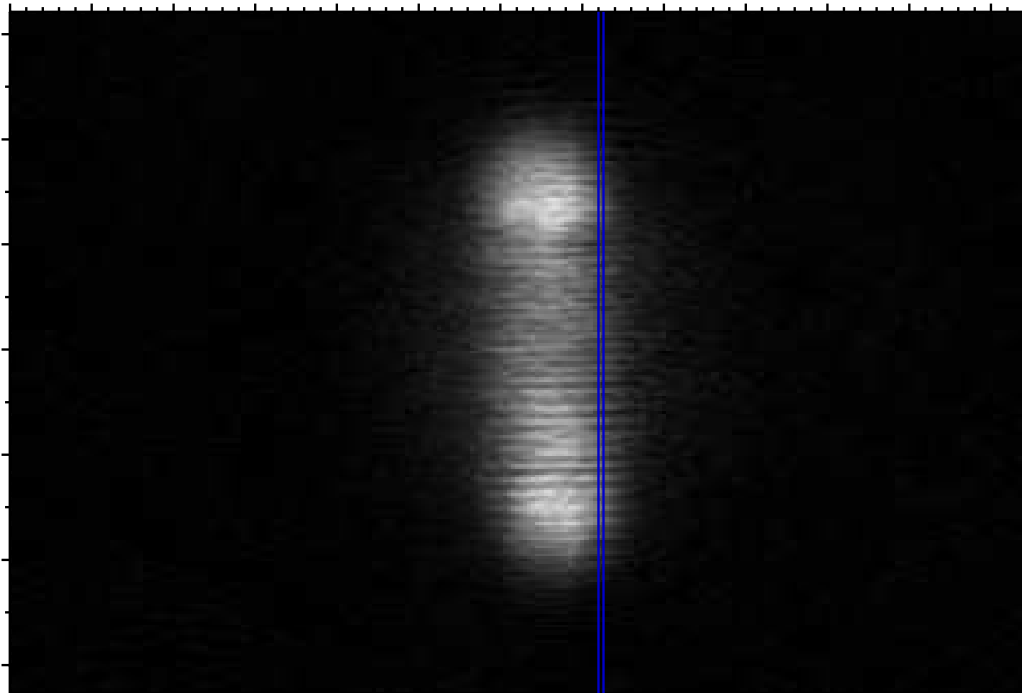
Figure 6.7: Top panel: Interference of many overlapping orders of a diffracted BEC. Bottom panel: Cross-section through the top figure along the blue cursor
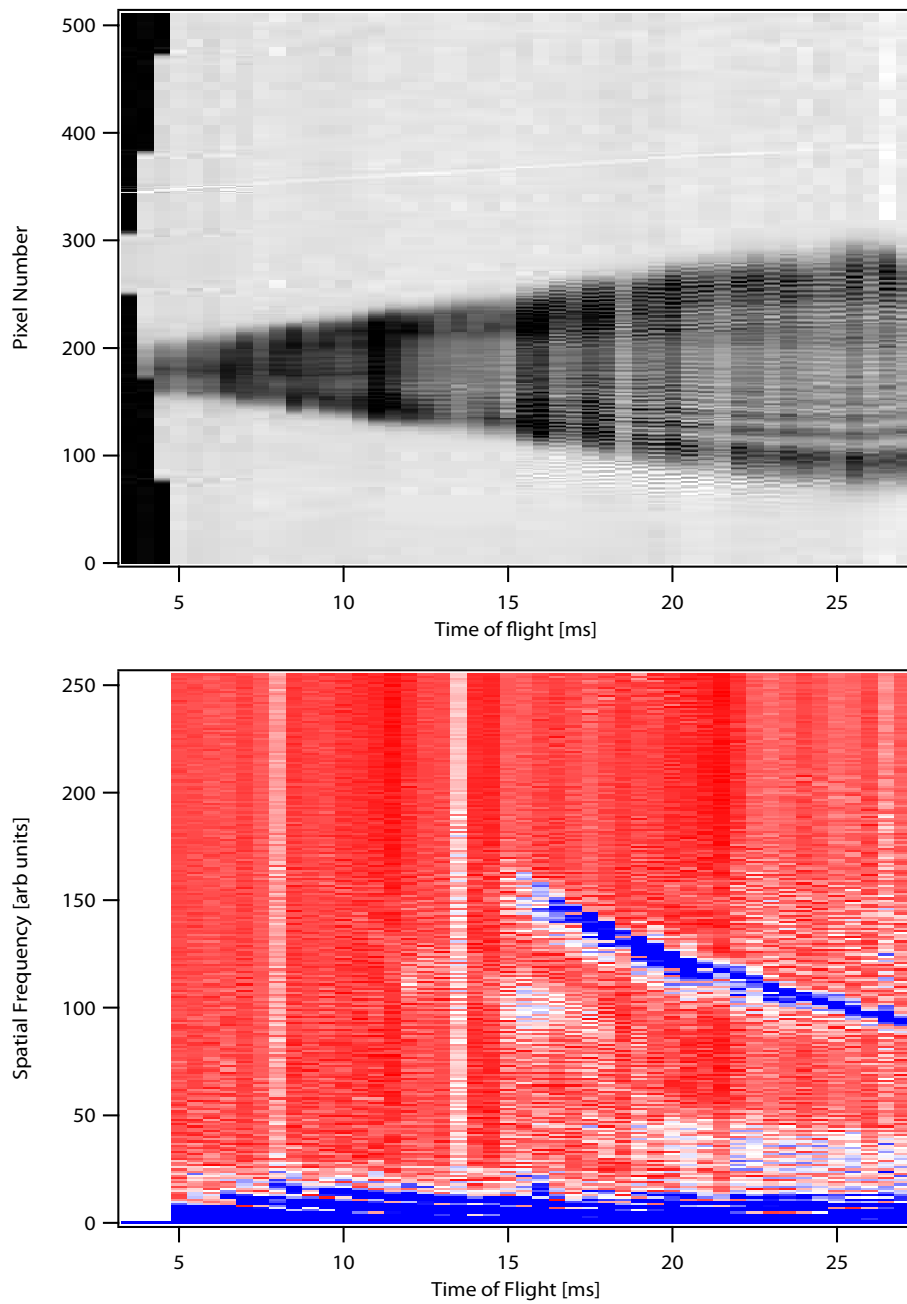
Figure 6.8: Top panel: Time of flight expansion following BEC diffraction and inter-order interference. Bottom panel: Time series of 1D spatial Fourier transforms.

[44] and were able to adapt their analysis to this measurement. In their experiment, they diffracted a ^{87}Rb BEC from a 4 μm periodic potential and used the interferences between the overlapping orders to prove that they had coherence. Their experiment was also in the regime where the mean-field energy dominated over the lattice recoil energy. The diffraction in their experiment was in the Raman-Nath regime (explained in Chap. 7) and this is the case for the data in Figure 6.8 as well. For this situation, the interference between overlapping diffraction orders arises from the coherent superposition of the wavefunctions of the individual orders,

$$\Psi_n(z) = \sqrt{n(z - n\Delta z)} J_n(S) e^{i[\alpha(z - n\Delta z)^2 - n\pi/2 + 2n\kappa_{\mathrm{L}}(z - n\Delta z) + \phi_n^{\mathrm{tof}}]}, \qquad (6.4)$$

where $n(z)$ is the BEC number density, Δz is the center-to-center separation between neighboring orders after time of flight, $J_n(S)$ are Bessel functions of the first kind as a function of the phase modulation index $S = U t_{\mathrm{pulse}}/\hbar$ (U is the lattice depth), α is the curvature of the parabolic phase profile of the BEC, κ_{L} is half the reciprocal lattice vector, and ϕ_n^{tof} is the phase accumulated by an order during time-of-flight. The mean-field impulse during time-of-flight is contained in the ϕ_n^{tof} term. We make two simplifying assumptions at this point. First, we assume that an order only overlaps its two nearest neighbors and that they overlap perfectly. Second, we assume that all $J_n(S)$ are equal. These assumptions do not significantly affect our determination of the spatial frequencies of the interferences.

We evaluate $\left|\Psi_{-1} + \Psi_0 + \Psi_{-1}\right|^2$ and find that there are two spatial frequencies. One is a fundamental at $2\kappa_{\mathrm{L}} - \nabla\phi_1^{\mathrm{tof}}$ and the other is the first harmonic at $4\kappa_{\mathrm{L}} - $

$2\nabla\phi_1^{\mathrm{tof}}$. In calculating this, we assumed that $\phi_0^{\mathrm{tof}} = 0$ and that the time-of-flight gradients in the $\pm 1^{\mathrm{st}}$ orders are equal and opposite. Thus, the problem is symmetric and only two frequencies are expected. The fundamental frequency is due to the interference between the 0th order and either the $+1^{\mathrm{st}}$ order or the -1st order. The harmonic is due to the interference between the $+1^{\mathrm{st}}$ order and the -1st order. The phase gradient piece in each frequency is proportional to the incremental velocity of an order caused by the initial mean-field repulsion. As before, it has the effect of making the lattice period look smaller.

Armed with this understanding, we then performed a final diffraction scan of the accordion lattice between 0 and -1.1 volts with a step size of 0.01 volts. For this run, t_{pulse} was a constant 100 μs and t_{TOF} was a constant 27.1 ms. As before, a section is taken through each interference pattern and then the sections are stacked sequentially according to the accordion galvanometer voltage. This data is shown in the top half of Figure 6.9; the bottom half shows the corresponding 1D Fourier transforms.

The wiggles in the top graph indicate that the extent of the envelope of the orders varies depending on the lattice periodicity and depth. These effects do not influence the determination of the lattice constant. (However, it is an interesting observation that led to the experiment described in Chap. 7.) The apparent harmonic spacing between the curves in the bottom graph can be interpreted as the result of a very small mean-field contribution to the order separation. (We should point out that it could also support the conjecture in Sec. 6.2.1 that $d_{\mathrm{single}}/d_{\mathrm{super}}$ might remain constant.) Either way, it is in contrast to the idea in Sec. 6.1 that the $\pm 2^{\mathrm{nd}}$

orders were pushed out less by mean-field than the $\pm 1^{\text{st}}$ orders. This discrepancy may be related to being in different diffraction regimes (inter-order interference vs. far-field) but we are not sure. The most plausible explanation for the harmonic spacing is the smallness of the mean-field contribution to the inter-order separation.

Finally, we collect together all data from the three calibration techniques for comparison in Figure 6.10. The two fit curves are for the superlattice diffraction technique, and the inter-order interference technique. They predict lattice constants that differ by 9% in the long periodicity limit and 3% in the short limit. The fit to the combined data from both techniques is shown within the box on Figure 6.10. A strong justification for the combined calibration can be seen in the beyond Raman-Nath diffraction experiment described in Chap. 7.
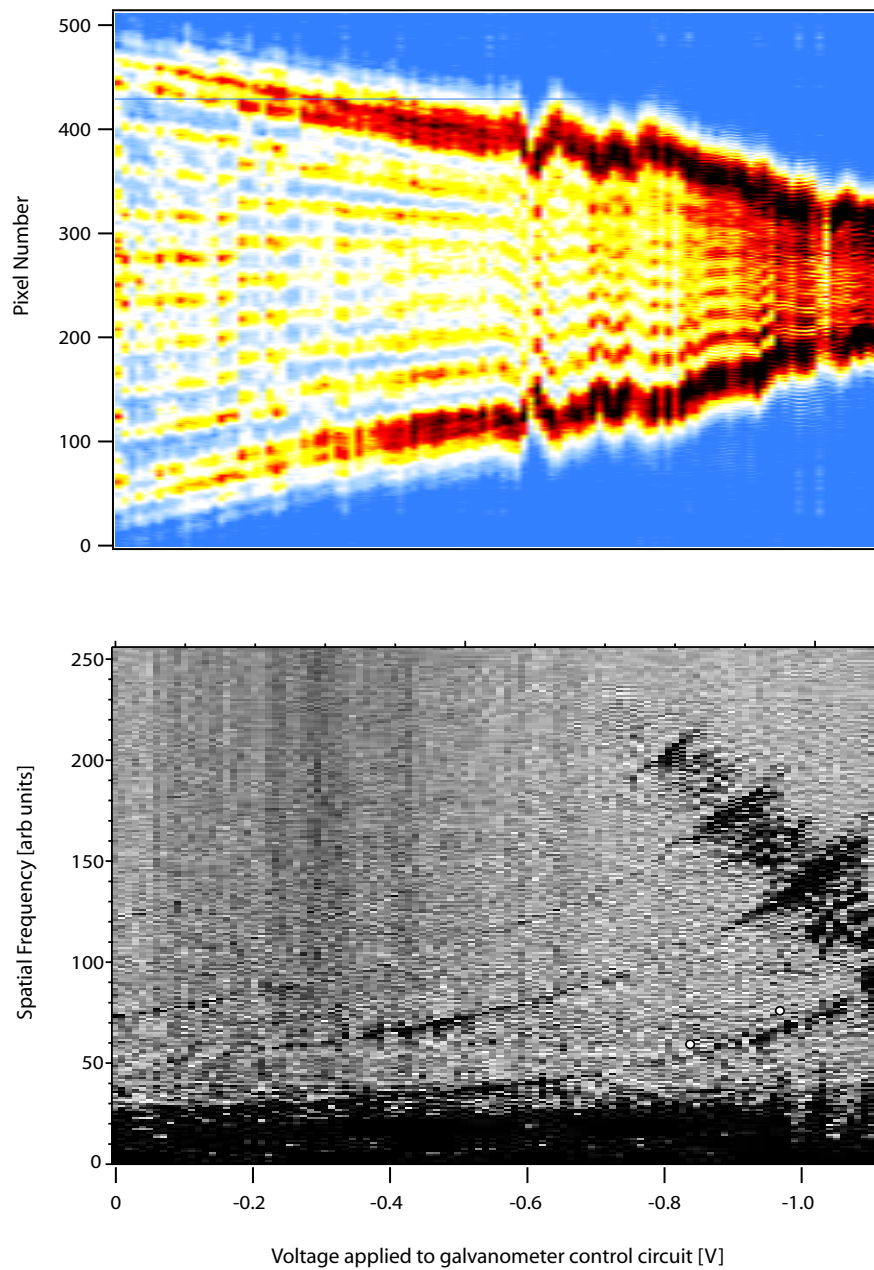
Figure 6.9: Top panel: Diffraction patterns as a function of the voltage applied to the accordion lattice. Small periodicity is on the left and large is on the right. Diffraction goes from far field to inter-order interference. Bottom panel: Stacked 1D Fourier transforms of the periodicity scan.
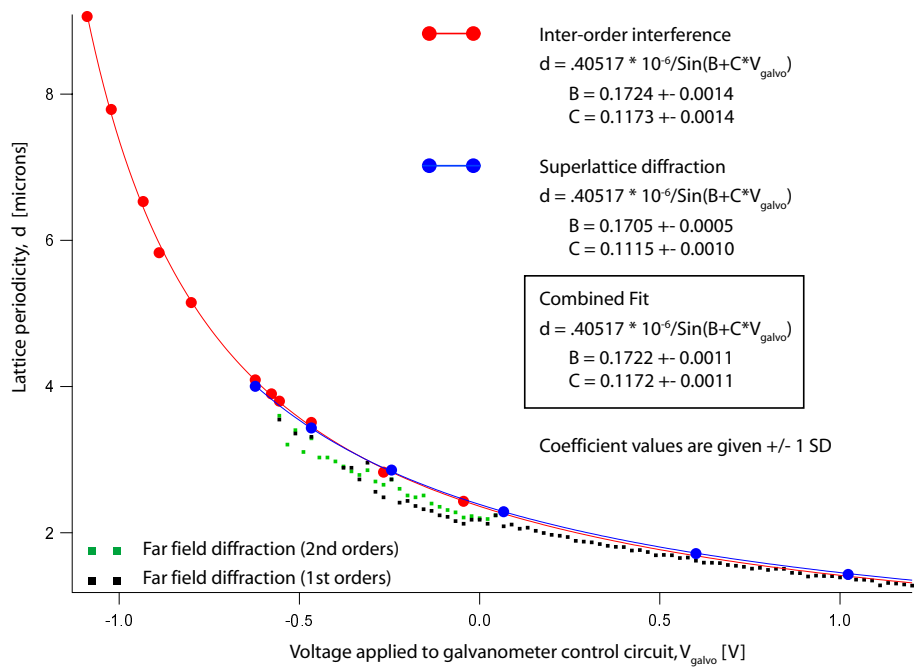
Figure 6.10: Data from three techniques to calibrate the accordion lattice with independent fits and one combined fit for the superlattice and inter-order interference techniques. All fitting was done by Igor 4.0 (Wavemetrics). The combined fit is confirmed by the experiment described in the next chapter.

Chapter 7

Long Periodicity Diffraction Beyond Raman Nath

7.1 Introduction

Modern atom optics experiments, in particular the diffraction of atoms by standing waves of light [90, 92, 94] provide a dramatic demonstration of the wave nature of atoms. The advent of ultra-cold and Bose-condensed atoms, with their extremely narrow momentum distribution, has made well-resolved diffraction components [95] a commonplace feature of atomic physics. Most such experiments have been in a regime where the light shift potential of the diffracting standing wave has relatively few bound states (bands) or produces relatively few diffraction orders. Under such conditions, the wave nature of the atoms is essential for describing the behavior of the system. By contrast, when the optical potential has many bound states the quantum system can exhibit strongly classical behavior, described by classical trajectories. This regime has been theoretically investigated both from a quantum [62, 73] and classical [79] standpoint. In 1994, Janicke and Wilkens calculated the long time diffraction of cold atoms in which they predicted a dramatic collapse and revival (see Figure 7.1) of the short time diffraction pattern [73]. Here, for the first time we present an experimental realization of this sort of pattern in the limit of many bound states. We investigate this regime by applying a deep standing wave as a pulse to a Bose-Einstein condensate (BEC) creating an optical potential

(with many bound states) at a range of lattice periodicities, and measuring the time evolution of the momentum distribution.
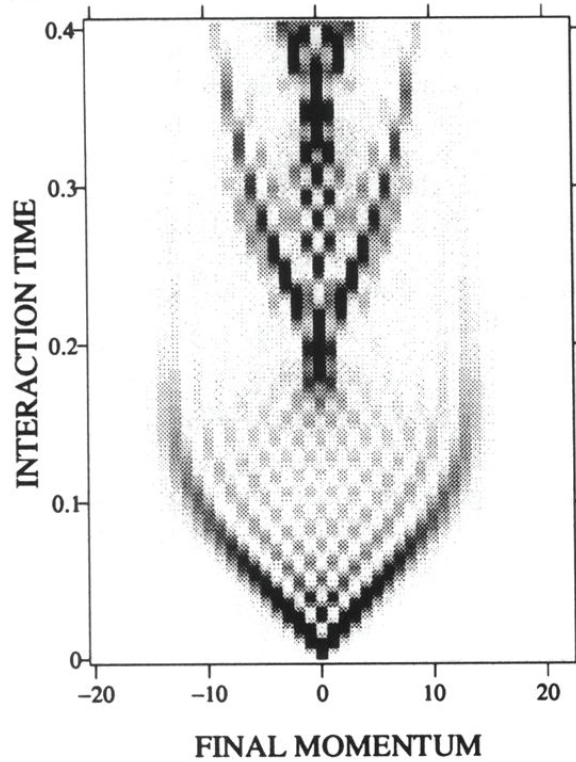
Figure 7.1: Final momentum distribution (in units of quasimomentum) of atoms in a magneto-optical field as a function of interaction time (in units of $\hbar$ divided by the lattice recoil energy). The lattice is applied as a stepfunction to the atoms. Figure courtesy of Janicke and Wilkens.

A classical trajectory approach to the motion of atoms in an optical standing wave has been used in some early experiments [32, 96, 97] to describe channelling and focussing. These experiments used thermal beams of atoms and measured the atomic position distribution within the standing wave. Another experiment used an optical standing wave to diffract cold atoms from a MOT, observing a collapse of the diffraction pattern, but not a clear revival [91]. Our experiments extend the earlier experiments by starting with a BEC having an extremely narrow momentum

distribution and by measuring the time-evolution of the momentum distribution for a range of lattice periodicities. We compare our results to the predictions of a quantum mechanical simulation and find excellent agreement. We also employ a classical model which captures the essential features and provides important physical insight into the evolution of the momentum distribution. In addition, we examine in detail the consequences of the anharmonicity of the potential which leads us to the mathematical physics of caustics [79].

7.2 Experiment

In our experiment, we create a one-dimensional (1D) optical lattice formed by two intersecting laser beams. Each beam has an electric field, in the plane-wave approximation, given by $\vec{E}(\vec{r}, t) = \hat{e} E_0 e^{i(\vec{k} \cdot \vec{r} - \omega t)} + c.c.$. The total field amplitude is given by

$$\vec{E}(\vec{r}, t) = 4 E_0 \hat{e} \cos(\frac{\vec{k_1} + \vec{k_2}}{2} \cdot \vec{r} - \omega t) \cos(\frac{\vec{k_1} - \vec{k_2}}{2} \cdot \vec{r}) \tag{7.1}$$

where $\vec{k_1}$ and $\vec{k_2}$ are the wavevectors of the two beams and ω is the frequency. This electric field creates an optical lattice potential for the atoms given by

$$U(z) = U_0 \cos^2(\kappa_{\mathrm{L}} z) \tag{7.2}$$

137

where $U_0 = \hbar\Omega_0^2/\delta$ and $\kappa_{\mathrm{L}} = |\vec{k}_1 - \vec{k}_2|/2 = \pi/d$ is one-half of the magnitude of the reciprocal lattice vector. We vary κ_{L} by changing the angle between $\vec{k}_1$ and $\vec{k}_2$. Here d is the lattice constant, Ω_0 is the on-resonance single beam Rabi frequency, and δ is the detuning between the frequency of the laser light and the resonant atomic transition. The direction $\hat{z}$ is parallel to $\vec{k}_1 - \vec{k}_2$. The detuning $\delta \gg \Omega_0, \Gamma$ where Γ is the natural linewidth of the atomic transition so that we can ignore spontaneous emission and not saturate the transition. Also, $\delta \ll \omega_o$ where ω_o is the atomic transition frequency so that the rotating wave approximation is valid.

Our experimental apparatus for producing a BEC was described in Chap. 4 and was also described in an early paper [104]. For the present experiment, we typically achieve a nearly pure BEC with $N_{\mathrm{tot}} = 0.4 - 1.4 \times 10^5$ atoms in the $(F, m_{\mathrm{F}}) = (1, -1)$ hyperfine state of ^{87}Rb. We use a Ioffe-Pritchard trap with an oscillation frequency of $\nu_{\mathrm{z}} = 8.2$ Hz in the weak direction and $\nu_{\mathrm{x}}, \nu_{\mathrm{y}} = 24$ Hz or 33 Hz in the tight directions depending on the experiment. The atoms are then loaded into optical lattices at four different lattice periodicities. Before loading, for the 1.8 μm lattice, the average number of atoms was 1.2×10^5 with a peak density of 2.9×10^{13} cm^{-3}. For the 3.5 μm lattice, the average number was 1.4×10^5 with a peak density of 3.1×10^{13} cm^{-3}. For the 6.5 μm lattice, the average number was 3.7×10^4 with a peak density of 2.4×10^{13} cm^{-3}. For the 9.3 μm lattice, the average number was 4.7×10^4 with a peak density of 2.6×10^{13} cm^{-3}.

The lattice beams derive from a Ti:Sapphire laser operating at $\lambda = 810.3$ nm (detuned below both $5S \rightarrow 5P$ transitions at 795 nm and 780 nm). At the BEC, the $1/e^2$ radius of each beam is ≈ 200 μm. The lattice is turned on abruptly to a nominal

depth of 30 E_R and held constant for a variable time t_hold. Here the single photon recoil energy $E_\mathrm{R} = \hbar^2 k^2 / 2M$ where M is the mass and $k = 2\pi/\lambda$ is the magnitude of the photon wavevector. After t_hold we release the atoms by suddenly turning off the lattice and magnetic trap. The atoms expand ballistically for 20.2 ms and the resulting spatial distribution of atoms (in the limit that atom-atom interactions can be ignored), corresponds to the momentum distribution at the instance of release. We record the spatial distribution of the atoms using resonant absorption imaging. Figure 7.2 shows a series of such images as a function of t_hold at four different lattice periodicities. The result is a picture of the evolving momentum distribution for each lattice periodicity in striking similarity to the initial figure by Janicke and Wilkens.

7.3 Results

Figure 7.2a depicts the measured momentum distribution of a BEC pulsed by a lattice of periodicity 1.8 μm as a function of time. We see that the width of the momentum distribution initially grows linearly with time. In addition, the distribution is characterized by a momentum dicretization at $2\hbar\kappa_\mathrm{L}$ as expected. These early-time measurements are consistent with diffraction predictions using the Raman-Nath approximation. Simply stated, ignoring the kinetic energy term in the Hamiltonian (during application of the pulse) constitutes the Raman-Nath approximation. This implicitly means that the density of atoms is unchanged during the diffraction on the length scale of the lattice periodicity. This can be interpreted physically in two ways. In the first way, no substantial population of atoms moves a distance of order
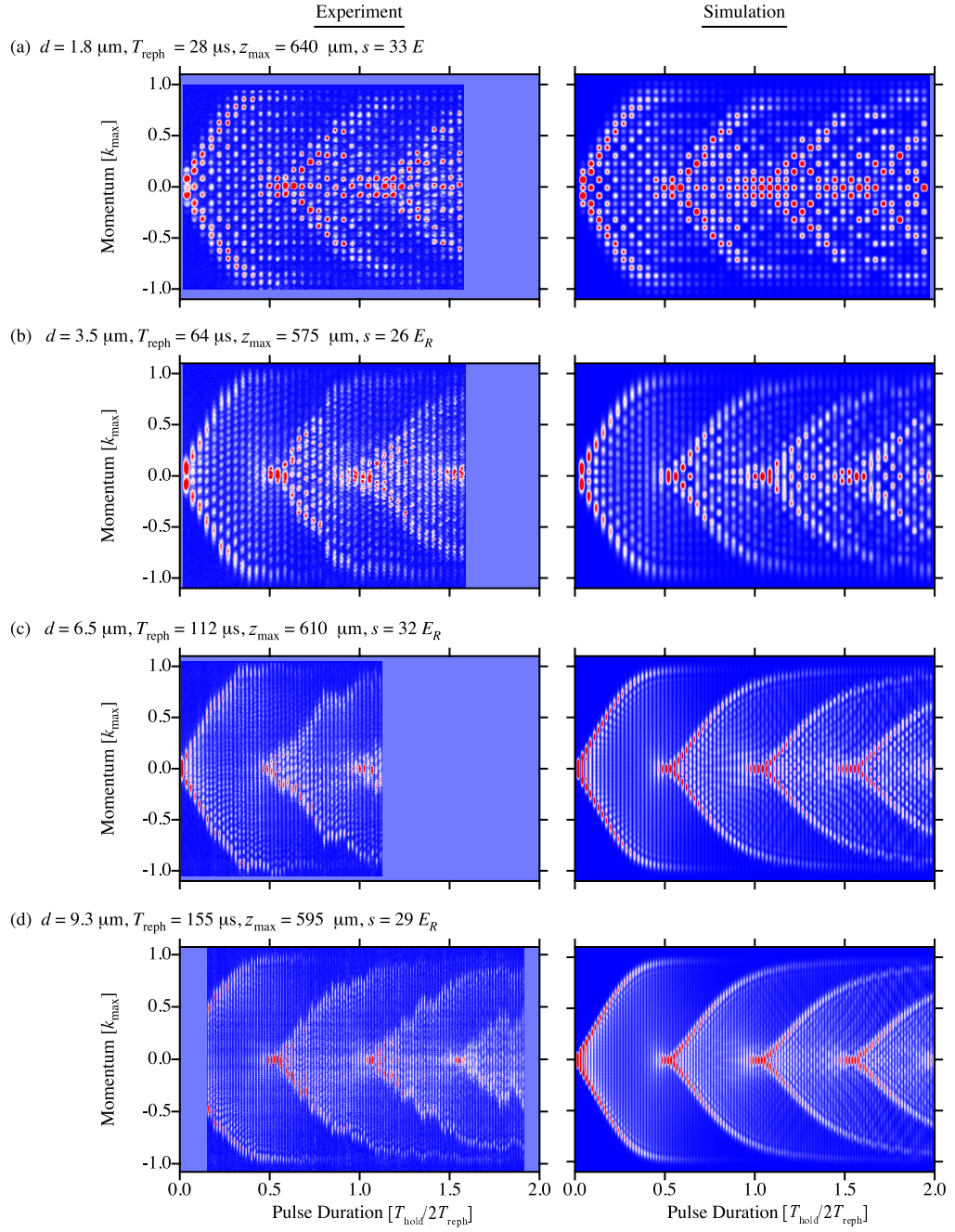
Figure 7.2: Evolution of the momentum distribution at four different lattice periodicities: $d = 1.8$ μm, 3.5 μm, 6.5 μm, and 9.3 μm. The Thomas-Fermi radius in the lattice direction ranged from 26 μm to 29 μm. In the transverse directions the radius ranged from 6 μm to 10 μm.

140

d. Alternately, applying our classical intuition, an atom will have time to oscillate much less than a quarter period in a nearly harmonic potential. The Raman-Nath approximation is valid when the time that the atom spends interacting with the optical lattice, t_{hold}, is much less than

$$t_{\text{RN}} = \frac{\hbar}{\sqrt{s_{\text{L}}} E_{\text{L}}} \qquad (7.3)$$

where s_{L} is the optical lattice depth expressed in units of the lattice recoil energy, $E_{\text{L}} = \hbar^2 \kappa_{\text{L}}^2 / 2M$. In this approximation, the evolution of the atomic population within each order n is given by $J_{\text{n}}^2(U_0 t_{\text{hold}}/\hbar)$ where the J_{n} are Bessel functions of the first kind.

It is evident from Figure 7.2a, that as t_{hold} (the pulse duration) increases beyond t_{RN} (which is $\sim 2T_{\text{reph}}/\pi$), the momentum distribution width first saturates to an amplitude corresponding to an atomic velocity of 32 mm/s. This velocity corresponds to a kinetic energy given by the depth of the well. The momentum distribution then suddenly collapses with a large fraction of the population returning to the lowest orders. The suddenness of this collapse is by no means an obvious result, but can be understood, as we will see below, in a classical model. The collapse is not total inasmuch as there remains a sizable occupation of the higher momentum orders at the collapse point. Beyond the collapse, the momentum distribution revives and the process approximately repeats. This recurring nature of the momentum evolution cannot be predicted within the Raman-Nath approximation.

The point in time when the collapse occurs can be predicted on the basis

of the lattice depth and periodicity. The depth U_0 is inferred from the maximum momentum $k_{\mathrm{max}} = z_{\mathrm{max}} M / t_{\mathrm{TOF}} \hbar$ where z_{max} is the maximum amplitude of the diffraction pattern after time of flight (see Figure 7.2). The depth U_0 can be used along with the lattice periodicity d to predict a collapse/revival time (approximately half the harmonic oscillator period from Eq. (3.26)). This predicted revival time agrees to within a few percent of the measured rephase time T_{reph}. Since T_{reph} agrees so well with the calculated collapse/revival time, this validates the lattice periodicity calibration we performed in Chap. 6.

Figures 7.2b-d depict the same process for increasingly long periodicity lattices. The character of each is similar; however, there are differences which we shall discuss later. (For example, there are interferences between overlapping orders which do not occur for the smaller periodicity lattice in Figure 7.2a.) Figure 7.2 also depicts the results of numerical quantum simulations of our experiment. The Hamiltonian used in this simulation included mean-field interactions as given by the time-dependent Gross-Pitaevskii (GP) equation. Although measurable (see Chap. 6 and section 7.7) the role of interactions is not significant in these simulations. We modeled the full problem by assuming that the wavefunction solution dimensionally factorizes giving us an effective 1D atom-atom interaction strength, $g_{\mathrm{1D}} = 4g_{\mathrm{3D}}/3\pi R_{\mathrm{x}} R_{\mathrm{y}}$ where $g_{\mathrm{3D}} = 4\pi\hbar^2 a/M$ is the 3D interaction strength, R_{x} and R_{y} are the Thomas-Fermi radii in the directions perpendicular to the lattice, and a is the s-wave scattering length of ^{87}Rb. We find good agreement between these simulations and our experimental data.

7.4   Quantum Mechanical Interpretation of Results

In the deep lattice limit, the number of bound states (bands) in a sinusoidal potential scales as the square root of its depth s_L, expressed in units of the lattice recoil energy, E_L. Since the lattice recoil energy scales quadratically with κ_L, the number of bound states in an optical lattice grows linearly with the lattice periodicity at fixed total depth. An optical lattice with a depth of 30 E_R (single photon recoil energy) formed by two counter-propagating beams has a depth of 30 E_L and approximately four bound states. However, the same 30 E_R lattice formed by two beams intersecting at 87 mrad create a lattice with a periodicity of 9.3 μm, a depth of 15800 E_L and approximately 80 bound states. This proliferation of bound states quickly pushes the system toward the classical limit in which atom diffraction corresponds to a change in the initial atom velocity distribution as a result of time spent in the periodic potential.

To better understand the data, the top panel of Figure 7.3 shows the projection of an infinite 1D condensate onto the eigenfunctions (Bloch states) of a 1D sinusoidal potential of depth 30 E_R with the relevant lattice constants of $d = 1.8, 3.5, 6.5,$ and 9.3 μm. (For reference, the projection for a standard retro-reflected lattice with a periodicity of $\lambda/2 = .405$ μm is also given.) Only even Bloch states are occupied since the wavefunction is symmetric. The bottom panel of Figure 7.3 shows the calculated energy differences between consecutive even states divide by twice the harmonic frequency $\omega_{ho} = 2\sqrt{s_L}E_L/\hbar$. As expected, the non-harmonic character of the spectrum means that there is no single time at which the system

Lattice depth = 30 E_R
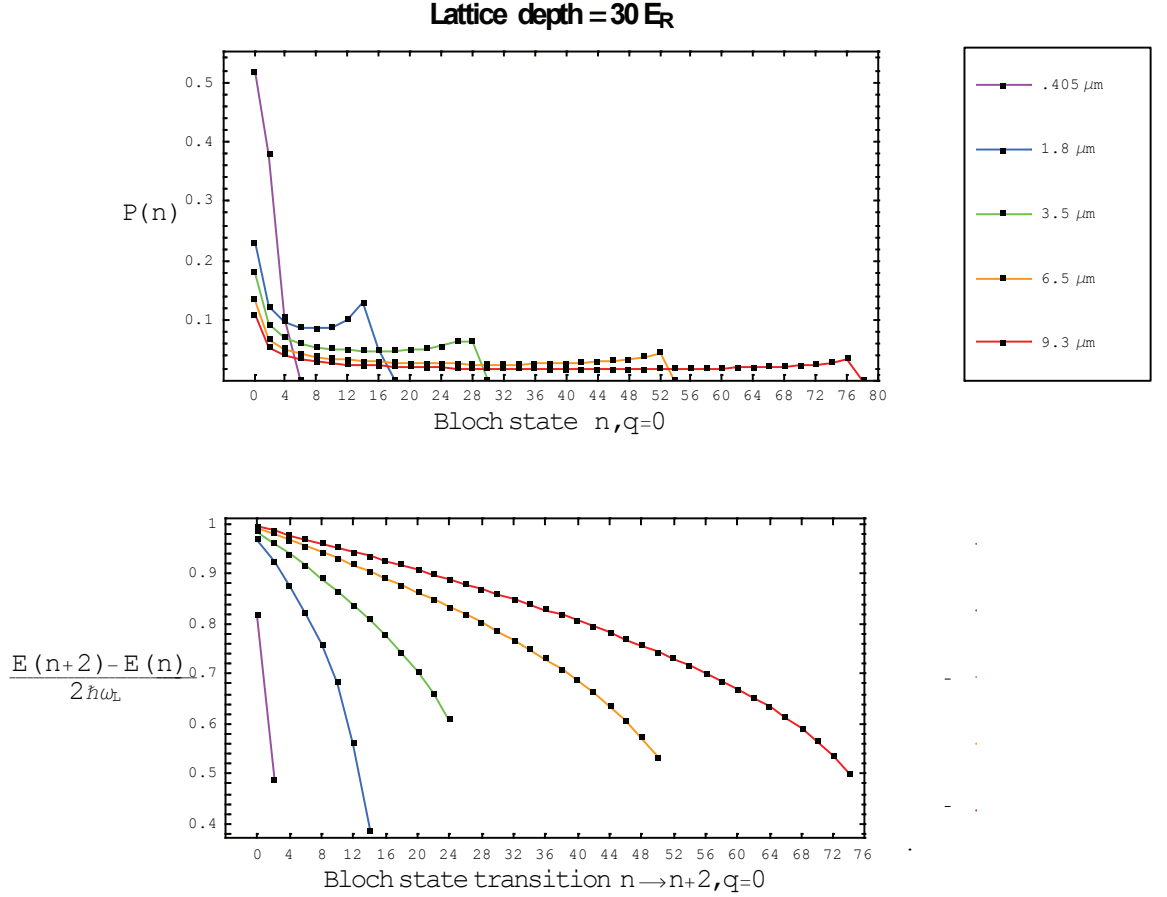
Figure 7.3: Top Panel: Bloch state decomposition of a homogeneous BEC diabatically loaded into a 30 E_R lattice (overlap integral of an infinite, constant density condensate with the Mathieu functions) with periodicities of .405 μm ($\lambda/2$), 1.8 μm, 3.5 μm, 6.5 μm, and 9.3 μm. Bottom panel: Eigenenergy separations between neighboring occupied Bloch states divided by the breathing mode energy (twice the harmonic energy).

perfectly rephases. Nevertheless, as we will see, over half of the population rephases within a fairly narrow time window at the first rephasing time. For example, for the counterpropagating lattice 90% of the population rephases at exactly the same time. For the 1.8 μm lattice, 55% rephases within a window that is $\approx 1/10$ the time to the start of the rephasing. We define T_{reph} as the inverse of the frequency difference between the ground and first even excited state. Notice from the eigenenergy spectra that T_{reph} is slightly longer than π/ω_{ho}. For the lattice periodicities examined in our

144

experiments, the bottom panel indicates that $1.0 < T_{\text{reph}}\omega_{\text{ho}}/\pi < 1.03$ whereas for a 30 E_{R} deep, retro-reflected optical lattice $T_{\text{reph}}\omega_{\text{ho}}/\pi \approx 1.22$.
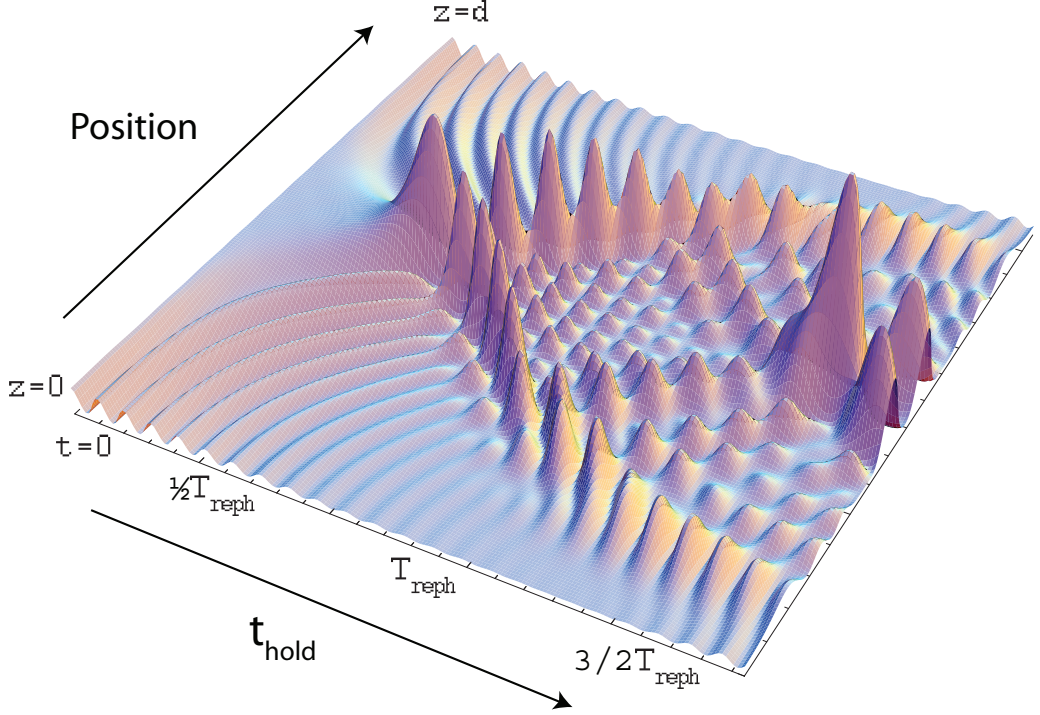
Figure 7.4: Position space evolution of the magnitude squared of the condensate wavefunction within a single well of an optical lattice with periodicity d of 1.8 μm and depth of 30 E_{R}. Positions $z = 0, d$ correspond to the lips of the well. The condensate is large compared to d; each initial Bloch state is at $q = 0$ (with no spread). At $t_{\text{hold}} = T_{\text{reph}}/2$ and $3T_{\text{reph}}/2$ there is a large increase in density at the center of the well when the atoms have maximum momentum.

Next consider the evolution of the system in position space. Starting with a flat wavefunction across all the wells, the probability flows to the center of each well. Flow velocity increases to a maximum roughly concurrent with the advent of a large peak in the wavefunction at the center of each well at approximately 1/4 the harmonic period. This is followed by flow away from each center at a decreasing

velocity until near zero velocity is reached where the process starts again. Figure 7.4 shows the evolution of the wavefunction in a single well for a $d = 1.8$ μm lattice. When the lattice is snapped off, the entire wavefunction across all of the wells is projected onto the plane wave basis which is the proper eigenbasis for free expansion during time of flight.

7.5   Classical Interpretation of Results

Many aspects of this quantum mechanical system can be understood classically (in some cases quantitatively). In the classical limit, the recurrence of the diffraction pattern beyond the Raman-Nath regime is equivalent to the motion of a particle in a single well of a sinusoidal potential. In this picture, each atom has zero velocity initially and has position drawn from the initial probability distribution $|\Psi(x, t = 0)|^2$; each atom must eventually reach a turning point where its velocity returns to zero. Since the potential is sinusoidal, the motion of an atom is increasingly harmonic the smaller its amplitude of oscillation (in the absence of atom-atom interactions). In contrast, the larger the amplitude, the more anharmonic the motion and the longer the time to the eventual turning point. Figure 7.5 displays the trajectories of a classical particle in a sinusoidal potential for a range of initial displacements from the bottom of the well. The shortest periods correspond to particles starting very near the bottom.

The position solution to this classical problem was applied to acousto-optical diffraction experiments by Lucas and Biquard in 1932 [70]. Later, both the po-

sition and momentum solutions were applied to acousto-optical diffraction theory by Nomoto in 1951 [71, 72]. Berry has expanded upon this work [82] as well as the theoretical work by C. V. Raman and N. S. N. Nath [74–77] dealing with the diffraction of light by ultrasonic waves.
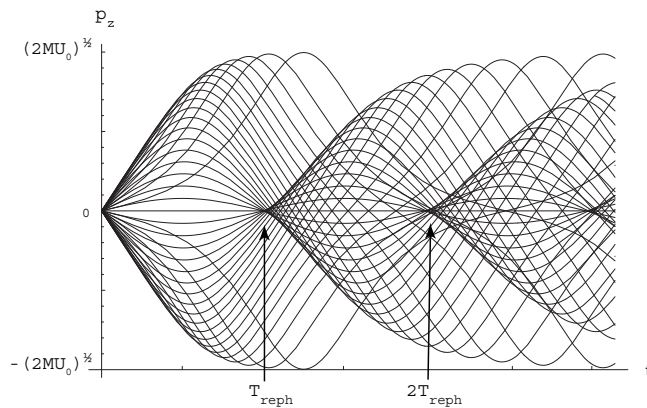
Figure 7.5: Inverse elliptic integral solutions to the motion of a classical particle in a sinusoidal potential. Each curve corresponds to a particle starting with zero velocity at some point on the potential. The shortest period is for a particle starting close to the bottom of a well. The longest period is for a particle starting near the top.

Substantial insight can be gained from this classical picture. For example, the asymmetric character of the recurrence is explained by plotting the results of the classical calculations in a single-well phase space portrait [79] as shown in Figure 7.6. At the instant that the lattice is snapped on, the atoms in one well are evenly distributed in space from one peak to the other, all at $P = 0$. As time passes, the distribution rotates clockwise about the origin; however, reflecting the non-harmonic nature of the potential, not at a single rotational frequency. The farther the point from the origin, the slower its rotation (the end points of the distribution are stationary). The projection of this evolving distribution onto the P axis is the classical analog of our measured momentum distribution. The horizontal tangents

147
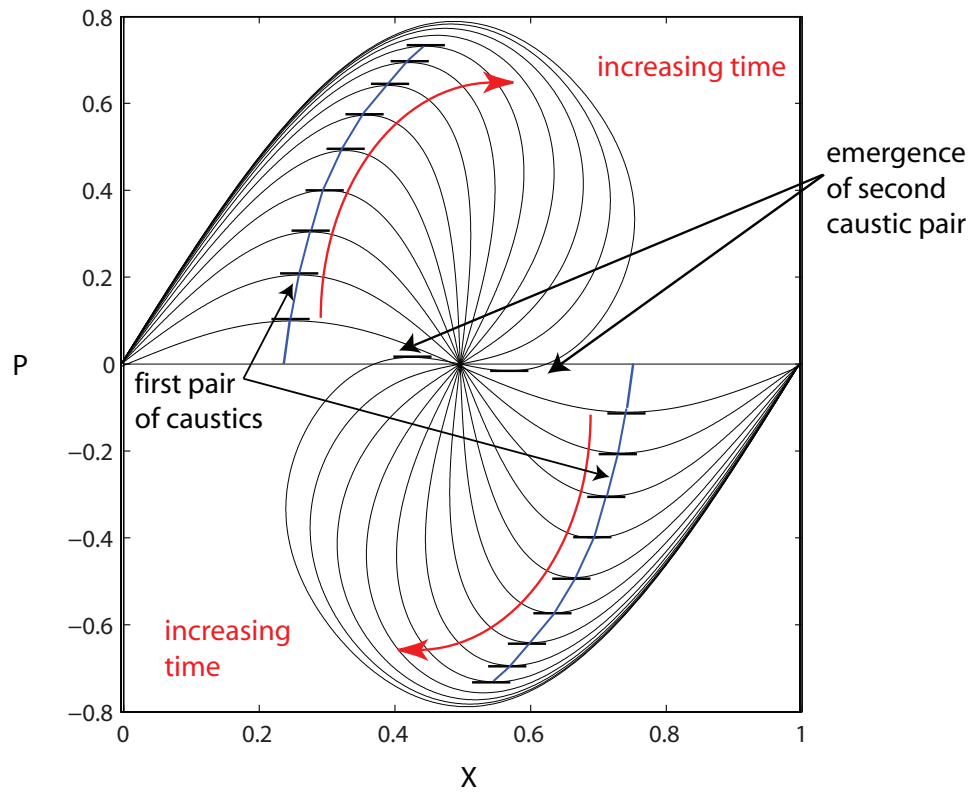
Figure 7.6: Characteristic evolution of a classical uniform distribution of atoms in a single well of a sinusoidal potential. The atoms are initially all at $P = 0$ when the potential is first turned on. Positions $X = 0$ and $X = 1$ are at the peaks on either side of a single well. Position $X = 0.5$ is the center of the well. The evolution is characterized by fixed points at the boundaries and a segment rotating at the harmonic frequency in the $X = 0.5$ limit. Between these points, the distribution is stretched like taffy.

to the evolving distribution project most intensely onto the P axis. The locus of these tangent points is referred to as a caustic. As the distribution approaches the first turning point, the horizontal tangents are far from $P = 0$; there is no focussed signal near $P = 0$. However, at the instant that the central part of the distribution goes through the turning point, another pair of caustics emerges from $P = 0$ and starts to travel away from the X axis. This is the reason for the asymmetry in the momentum evolution; the evolution would only be symmetric for a perfectly harmonic potential.

7.6   The Connection to Optical Catastrophe Theory

In catastrophe theory [84–86], the caustics we describe are called folds and cusps. The folds are the symmetric caustic pairs travelling away from $P = 0$. The cusps are the vertices where two fold caustics join. Catastrophe theory has been applied with much success to the field of optics by Berry [81]. There, the origin of each caustic can be intuitively explained using the ray theory of light. Geometrical optical caustics are structurally stable singularities connected to phenomena such as lens focal points, rainbows, and the shimmering light structures reflected from water surfaces. Corresponding caustics emerge in the wave theory of light. Each geometrical ray caustic becomes "decorated" with interferences and the resulting pattern is known as a "diffraction catastrophe" [89]. Figure 7.7 shows a geometrical ray cusp caustic and its corresponding diffraction cusp caustic with its characteristic distorted interior array structure [83]. While these are generic representations of

cusp caustics, they could represent, for example, ultrasonic diffraction of light with the light propagation direction as the abscissa, a transverse direction as the ordinate, and the color as the intensity of the light. As far as we know, our data represents the first evidence of fold and cusp diffraction catastrophes in matter wave diffraction. In addition, the sequence from Figure 7.2a-d, shows the nature of the transition from a (quantum) diffraction situation to a (classical) situation. As pointed out by Berry and O'Dell [79, 80], caustics eventually dominate the classical distribution in momentum space for long-time evolution in a sinusoidal potential. One is therefore able to calculate ergodic averages using them as a basis.
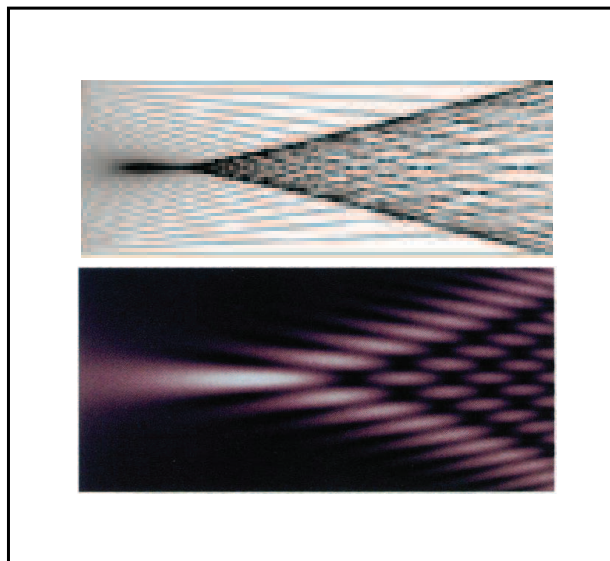
Figure 7.7: Top panel: The classical cusp caustic based on ray theory. Bottom panel: The corresponding diffraction cusp (Pearcey function) caustic (courtesy of M. V. Berry). The banding in the top ray picture is an artifact, while that in the bottom wave picture, is real.

Diffraction catastrophes constitute a class of special functions that are outside of the standard hypergeometric functions (e.g. Bessel, Hermite, Laguerre, Legendre,

Mathieu, etc.) [88]. The diffraction catastrophe for the fold caustic is an Airy function (not the function describing Fraunhofer diffraction) and for the cusp it is the Pearcey function [87].

7.7 The Role of Atom-atom Interactions

We now turn to a discussion of the effects of atom-atom interactions on the previous analysis. Counterintuitively, the importance of atom-atom interactions grows as the lattice periodicity increases for two reasons: (1) the lattice recoil energy decreases quadratically with $\kappa_{\rm L}$ allowing atoms to interact for longer times; (2) for a fixed total number of condensate atoms, the number of atoms per well increases as $1/\kappa_{\rm L}$ while its ground state width $a_{\rm ho} = \sqrt{\hbar/m\omega_{\rm ho}}$ grows only as $\sqrt{1/\kappa_{\rm L}}$. Our GP simulations indicate that the atoms become compressed during the evolution and at $t_{\rm hold} = T_{\rm reph}/2$ the bulk of the wavefunction in a single well occupies a width slightly *less* than $a_{\rm ho}$. Thus, using the ground state wavefunction at $t_{\rm hold} = T_{\rm reph}/2$ is probably a conservative estimate for calculating the (brief) maximum density. Using this, the maximum ground state atom density and consequently the maximum mean-field energy $E_{\rm int}^{\rm max}$ increases as $\sqrt{1/\kappa_{\rm L}}$.

When $t_{\rm hold}$ is equal to an odd multiple of $T_{\rm reph}/2$, the mean-field energy reaches a maximum $E_{\rm int}^{\rm max}$ at the center of each well. For each lattice periodicity and number of atoms in the BEC in our experiment, we calculate $E_{\rm int}^{\rm max} \approx g_{\rm 1D}N_{\rm cp}|\Psi_{\rm ho}|^2$, where $N_{\rm cp}$ is the number of atoms in the central pancake and $\Psi_{\rm ho}$ is the harmonic oscillator ground state. Table 7.1 shows these results and for comparison the recoil energy

Energy (Hz)	1.8μm	3.5μm	6.5μm	9.3μm
$E_{\mathrm{int}}^{\mathrm{max}}$	570	860	680	920
E_{L}	178	47	13	7
$2\hbar\omega_{\mathrm{ho}}$	17250	8880	4780	3340
$E_{\mathrm{kin}}^{\mathrm{max}}$	105000	105000	105000	105000

Table 7.1: Maximum interaction energy, lattice recoil energy, monopole oscillation energy, and maximum kinetic energy for the various periodicity 30 E_{R} lattices in our experiment.

(E_{L}), the breathing mode energy $(2\hbar\omega_{\mathrm{ho}})$, and the maximum kinetic energy $E_{\mathrm{kin}}^{\mathrm{max}}$ for each lattice periodicity.

Because of the insight gained by plotting the results of our classical evolution calculations in a phase space portrait, we performed these classical calculations again, but this time including atom-atom interactions as a mean-field repulsive energy proportional to the (time-dependent) local atomic density. In the classical calculation, we modeled the force on an atom as $F = \cos 2\pi x + A[N(x) - N(x+\delta x)]$ where the first term is due to the lattice, and the second term is from the mean field repulsion. A is proportional to the strength of the atom-atom interaction and $N(x)$ is the number of atoms within a bin at x. Since the purpose of this calculation was to identify the potential qualitative effects of interactions, we purposely did *not* attempt to calibrate the strength of the interaction used in this calculation to correspond to the actual s-wave scattering length of ^{87}Rb. The simulation was performed by calculating the classical distribution trajectory without interactions, coarse-grain averaging to obtain a new density profile which added an effective potential to the original sinusoidal potential, and then iterating.

Figure 7.8 depicts the classical evolution of the distribution of atom positions
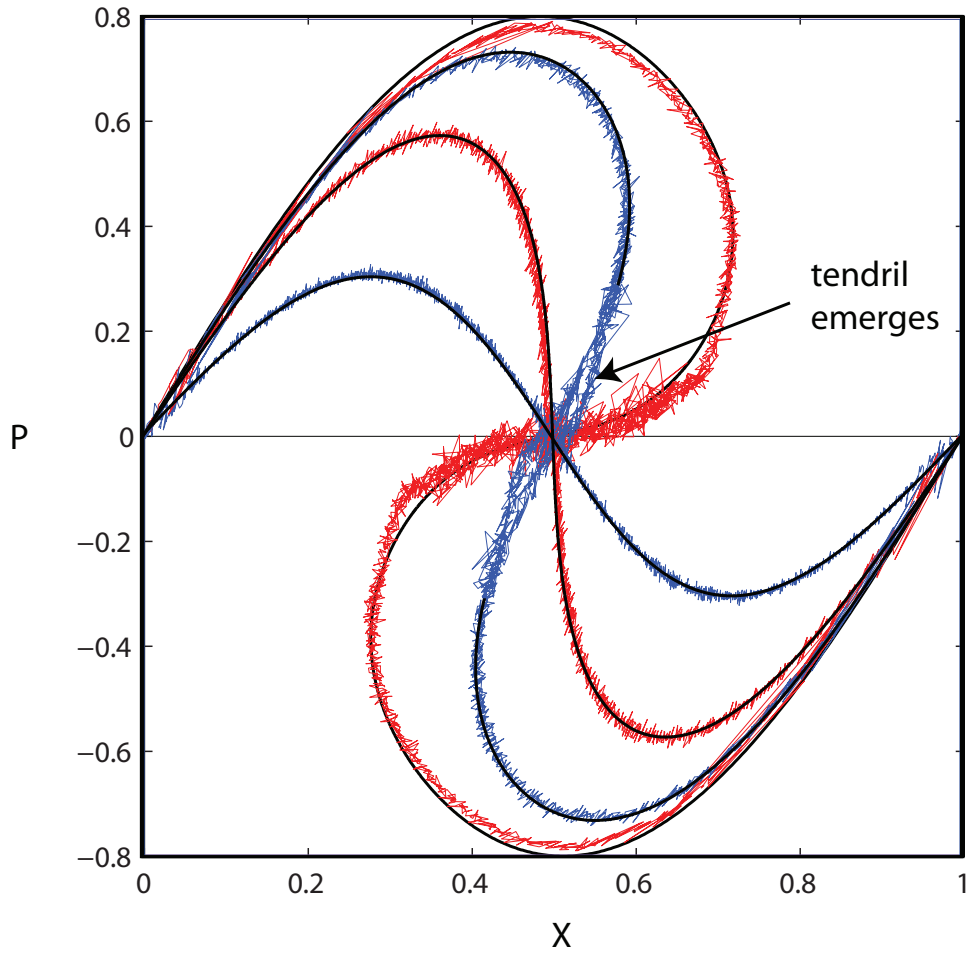
Figure 7.8: The calculated evolution of the classical distribution of atoms including atom-atom interactions (fuzzy colored curves where the fuzziness is likely due to the graininess of the simulation). The increase in density near the center of the well at $t_{\mathrm{hold}} = T_{\mathrm{reph}}/2$ creates a mean-field barrier slowing atoms which have yet to arrive at the center of the well and accelerating atoms which are just past the barrier. For reference, the evolution without interactions is shown in black.

and velocities approaching T_{reph}. With sufficient mean-field interaction, near the center of the well, velocity class bifurcations emerge. For the calculation, the mean-field interaction strength was approximately two orders of magnitude larger than it was in our experiment (where the lattice depth was $\sim 10^5$ Hz, the initial maximum interaction energy, before interaction with the lattice, was $\sim 10^2$ Hz). The physical picture is that the temporary increase in density at the center of the well at $t_{\mathrm{hold}} = T_{\mathrm{reph}}/2$ creates a mean field bump slowing atoms which have yet to arrive at the center of the well and accelerating atoms which are just past the barrier. Berry has called similar phase space portrait structures "tendril" distortions [80]. We have examined our data carefully for the possible presence of caustics associated with these bifurcations, but unfortunately do not see them. We are optimistic that a BEC with a larger atom number in a large periodicity lattice would reveal these secondary caustics. For our 9.3 μm lattice, the average total condensate number was only $N_{\mathrm{tot}} \approx 5 \times 10^4$ which could have been much higher.

Although we do not observe the direct effect of atom-atom interactions during their evolution in the lattice, we believe we have observed an indirect effect of atom-atom interactions which we now discuss. (We *did* see atom-atom interactions in the work described in Chap. 6, however, these were time-of-flight interaction effects and not due to anything that happened while the atoms were in the lattice.) We have calculated the 1D spatial Fourier transform at each time step t_{hold} in the 1.8 μm lattice. (The real space picture from Figure 7.2a is duplicated in the top panel of Figure 7.9.) The dominant signal is a nearly constant spatial frequency centered at 25 (arbitrary units) corresponding to the average order separation as
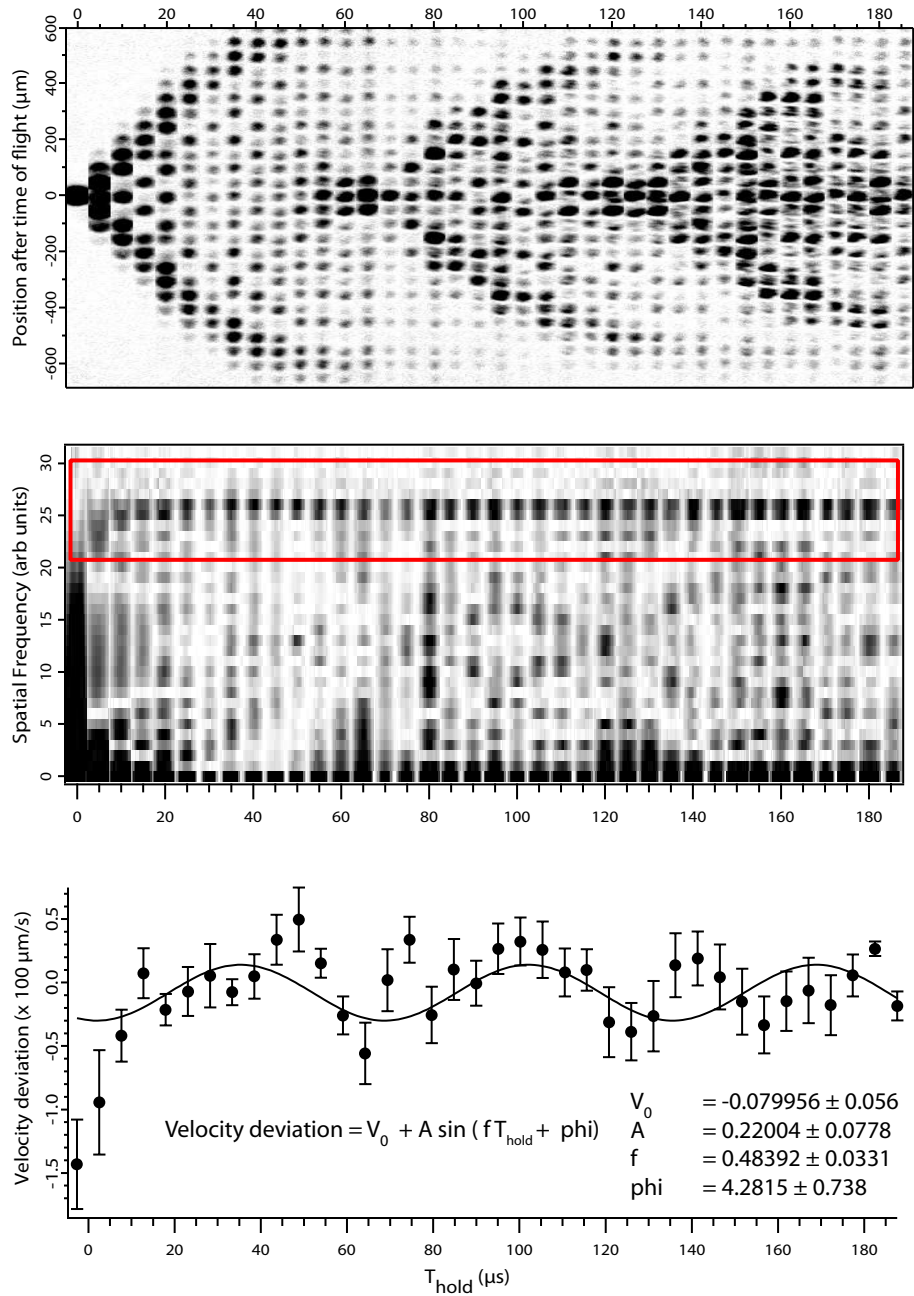
Figure 7.9: Top panel: BEC diffraction in a 1.8 μm lattice. Middle panel: 1D spatial Fourier transform of the diffraction focussed on the frequency corresponding to the average neighboring order separation. Bottom panel: Wobble in the average order separation possibly caused by the shape of the condensate wavefunction at the diffraction endpoint and its effect on atom-atom interactions during subsequent time of flight.

shown in the middle panel of Figure 7.9. While not visible at the scale of the middle panel, by taking the centroid of the Fourier transform within the red rectangle we have detected a slight wobble in this frequency as shown in the bottom panel of Figure 7.8 corresponding to atomic velocity deviations on the order of 50 μm/s. When fit to a sine using Igor Pro, the extracted wobble frequency is approximately equal to the recurrence rate of the diffraction oscillations. In the fit, all parameters: the amplitude, offset, frequency, and phase were free with fitting uncertainties indicated in the figure. The extracted phase is such that the average order separation after time of flight is slightly larger when the atoms emerge from the lattice with a roughly constant density profile (most similar to the original BEC profile before being subjected to the optical lattice). The order separation is smallest when the atoms exit the lattice peaked at the center of the wells. A possible interpretation of this result is that when the atoms emerge with an approximately flat density profile (at a rephasing time), there is little subsequent diffraction and thus the orders are pushed by the full condensate at the beginning of the time of flight. In contrast, when the atoms leave the lattice starting from a peaked spatial distribution, there is maximal subsequent diffraction and so very soon there are few atoms at the cloud center during early times-of-flight to push orders out.

7.8   Conclusion

We measured the theoretically predicted [73] collapse and revival of the short time diffraction pattern of a BEC pulsed by a 1D optical lattice. Because of the long

lattice periodicities, bound states proliferated and various classical hallmarks were observed in the long-time momentum evolution of the wavefunction. We compared our results to the predictions of the time-dependent GP equation and employed a classical model which captured most of the essential features while providing important physical insight. We carefully examined the consequences of the anharmonicity of the potential and recognized the emergence of ultra-cold atom-diffraction caustics. Finally, we found evidence for a slight effect of atom-atom interactions during the time of flight possibly due to the state of the wavefunction at the diffraction endpoint.

Chapter 8

Observation of Temperature-Dependent Spatial Phase Fluctuations

Near the Berezinskii-Kosterlitz-Thouless Transition in a Trapped 2D

Degenerate Bose Gas

8.1 Introduction

The type of order a Bose system has is affected by its dimensionality. In a 3D system at low temperatures, long range order is common; however, in a homogeneous 2D system with a continuous symmetry, thermal fluctuations destroy long range order at any finite temperature [106, 107]. Thus, as stated in Chapter 1, a homogeneous 2D system cannot Bose-condense above $T = 0$. Instead, a homogeneous 2D system undergoes a phase transition at a finite critical temperature above which it is normal and below which it is a superfluid. The theory of Berezinskii and of Kosterlitz and Thouless (BKT) [14–17] relates this transition to the development of geometrical order in the form of vortex-antivortex pairs (a pair of vortices with opposite rotation). Below the transition, the vortex-antivortex pairs are bound and at the transition the pairs begin to separate. Slightly above the transition, the proliferation of these unbound vortices and anti-vortices drives the system into the normal state.

Unlike the typical finite-temperature phase transition, the BKT transition

has no spontaneous symmetry breaking and creation of a spatially uniform order parameter. Instead, there is only quasi-uniformity below the transition and the spatial correlations in the order parameter decay algebraically. Above the transition, the quasi-uniformity cannot be maintained and the correlations decay exponentially. This description relates to a host of 2D phenomena including superfluidity in 2D ^{4}He [108, 109], spin-polarized hydrogen on 2D surfaces [110], spin ordering in $CuGeO_3$ [111], orientational ordering of CF_3Br monolayers physisorbed on graphite [112], and surface roughening in Pt(110)-(1x2) [113].

Such theories of many-body physics can be tested using harmonically-trapped Bose gases. As discussed in Chapter 1, one can create reduced dimensional systems of harmonically-trapped atomic Bose gases by imposing very tight confinement in one or two directions. In the case of tight confinement in one direction, quantum-degenerate 2D Bose gases have been produced both in single pancake traps and in multiple 2D pancakes at the nodes of a 1D optical lattice [114–122]. Recent experiments at ENS in Paris [124, 126] have examined the interference between 2D pancakes and extracted phase information indicating the occurrence of the BKT transition. They also revealed the presence of single and multiple isolated vortices. These experiments are interesting because they shed light on the debate [105, 127–132] as to whether an interacting trapped Bose gas undergoes an ordinary Bose-Einstein or a BKT transition. One result of these experiments was that the BKT transition occurs in the trapped system, however as a finite-width crossover instead of a sharp transition, presumably due to finite-size effects [133]. Recognizing all of the uncertainties that we will discuss, the results of our experiment are also consis-

tent with a finite-width BKT transition. In addition, our results are consistent with a recent theoretical prediction by Holzmann, Baym, Blaizot, and Laloë [131] which predicts a significantly reduced jump in the power-law behavior of correlations, and places the BKT transition temperature T_{BKT} for a finite, trapped system slightly below the calculated BEC transition temperature T_{BEC} for an ideal, trapped 2D gas. Finally, our results extend to temperatures lower than the predicted BKT transition temperature, thus providing information about superfluid densities and the nature of phase fluctuations approaching $T = 0$.

8.2 Experiment

The overview of our experiment (see Fig. 8.1) is as follows. We create a very small number of independent 2D pancakes of atoms by applying a deep 1D optical lattice to a 3D BEC. In the tight direction ($\hat{z}$) each pancake is well described by a single particle harmonic oscillator in the ground state. In the weak directions ($\hat{x}$ and $\hat{y}$), each pancake is described by the 2D Gross-Pitaevskii equation. The process of creating the initial 3D condensate and subsequent 2D pancakes results in a variable amount of heat being deposited into the system. While we do not know for certain the source of this variability, our best guess is that it is due to small uncontrolled position and velocity fluctuations during the creation process. After creating the pancakes, we suddenly turn off all confining potentials and allow the pancakes to expand into each other. We then absorption-image the atoms after a time of flight t_{TOF} and extract relative phase information in the $\hat{x}$ direction. Note
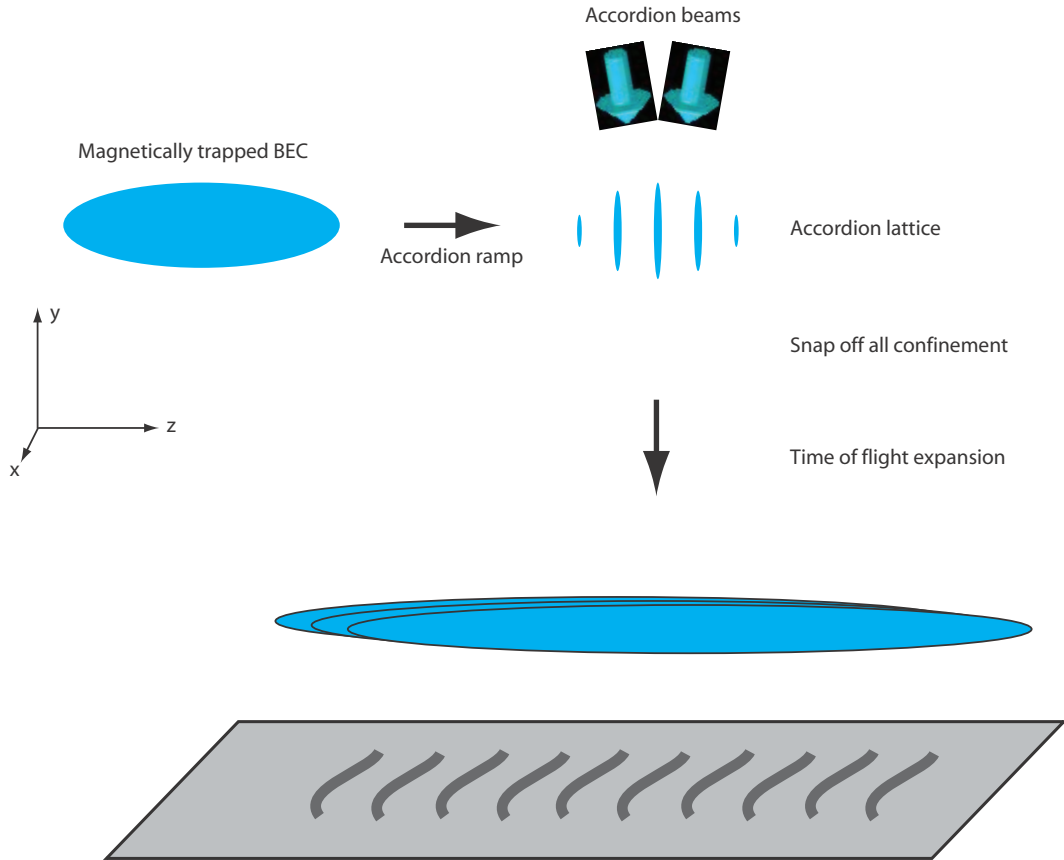
Figure 8.1: A 3D magnetically trapped BEC is subdivided into a very small number of independent 2D Bose gases by the accordion optical lattice set at $d = 8.4\ \mu$m. The original BEC of approximately 8.5×10^3 ^{87}Rb atoms is now three or four 2D Bose gas pancakes (sometimes with very small "satellites" on the ends) with the largest pancakes containing approximately 3.0×10^3 atoms. At the conclusion of the optical lattice ramp of 200 ms, we suddenly extinguish the light and turn off the magnetic trap. The pancakes expand mainly in the $\hat{z}$ direction for 30.2 ms and overlap . We absorption-image the interference pattern onto our CCD camera using resonant laser light.

that the absorption-imaging process destroys the cloud of atoms. Phase variations in the $\hat{y}$ direction are automatically integrated by the absorption imaging. We calculate a first order correlation function in the $\hat{x}$ direction and extract an exponent characterizing the decay of the correlation function with the integration length L_x in the $\hat{x}$ direction. Our experiment is very similar to the ENS experiment. Differences include the fact that we do not limit to two pancakes and we do not control the temperature of the atoms. Further differences will be pointed out as we continue.

We produce a 3D magnetically trapped ^{87}Rb BEC with $8.5(20) \times 10^3$ atoms in the $|F = 1, m_F = -1\rangle$ state [54]. We then apply a 1D optical lattice with a periodicity of $d = 8.4(4)\mu$m nearly along the $\hat{y}$ direction to split the BEC into three or four main pancakes (often with two additional very small satellite pancakes) reaching the 2D regime. The lattice potential is ramped up slowly over 200 ms in order to be adiabatic with respect to mean-field interactions and vibrational excitations. At full laser power, the lattice depth is $s = 30(3)$ expressed in units of $E_R = h^2/2M\lambda^2$ where $\lambda = 810.3$nm is the wavelength of the laser light and $M = 1.443 \times 10^{-25}$kg is the mass of the ^{87}Rb atom. The harmonic oscillator length in the $\hat{z}$ direction is 240(20) nm. Assuming a symmetric splitting of the BEC, when there are three main pancakes, the central pancake has $3.1(7) \times 10^3$ atoms with a chemical potential $\mu = 3.3(3) \times 10^2$Hz; the resulting peak 2D density is $2.7(3) \times 10^9$cm^{-2}. The calculated 2D Thomas-Fermi radii are $R_x = 7.0(6)\mu$m and $R_y = 10.9(8)\mu$m. When there are four main pancakes, the two central pancakes each have $3.0(7) \times 10^3$ atoms with a chemical potential $\mu = 3.2(3) \times 10^2$Hz; the resulting peak 2D density is $2.6(3) \times 10^9$cm^{-2}. The 2D Thomas-Fermi radii are

$R_x = 6.9(6)\mu$m and $R_y = 10.9(8)\mu$m. The above uncertainties are predominately due to shot-to-shot variations in the number of atoms in the original condensate.
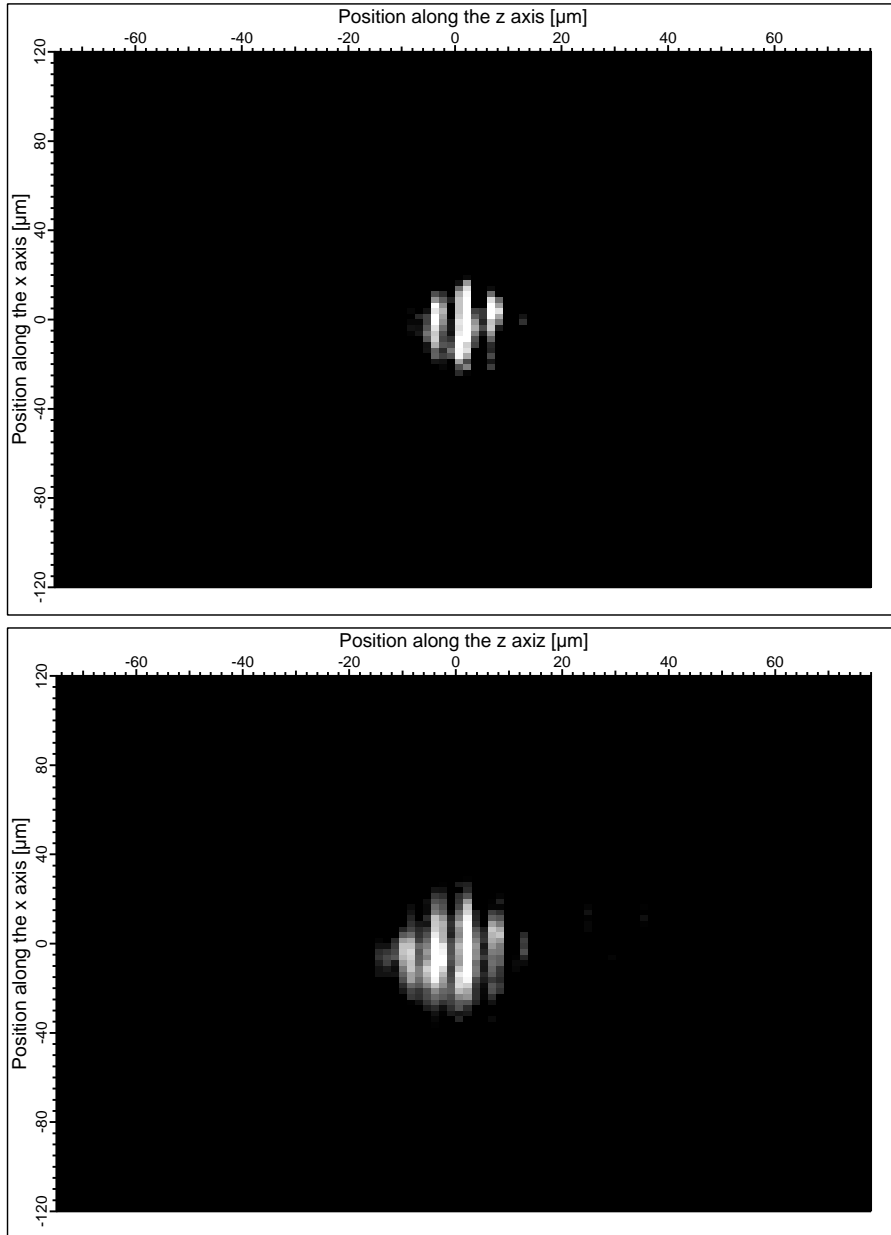
Figure 8.2: Typical in-situ images of the 2D BEC pancakes just prior to expansion.

The harmonic frequency in the $\hat{z}$ direction is 1900(100) Hz which is much larger than the chemical potential of the atoms in the pancakes which means that each pancake is a 2D system. Tunnelling between the pancakes is negligible on the time

scale of the experiment (the tunneling time for the ground state is in excess of 10^{90}s [125]). In fact, motion in the $\hat{z}$ direction is frozen out during the ramp when the lattice is less than 1 E_R deep. The radial oscillation frequencies are $\omega_x/2\pi =42(1)$ Hz and $\omega_y/2\pi =24(1)$ Hz. The number of pancakes was confirmed by in-situ imaging as shown in Fig. 8.2. As mentioned, we often observe five or six pancakes in our images, however in these instances the outer two satellite pancakes are always very small (typically less than 5% of the total number of atoms).

At the conclusion of the lattice ramp to make the pancakes, we suddenly turn off all confinement of the atoms. The pancakes expand for 30.2 ms predominately in the $\hat{z}$ direction and increasingly overlap to create a 3D matter wave interference pattern. We absorption image the expanding cloud with resonant laser light directed in the $\hat{y}$ direction and record the projected image on our Princeton Instruments CCD camera as shown in Fig. 8.3. We then take a 1D spatial Fourier transform along $\hat{z}$ of the recorded interference pattern for each x position. We obtain a magnitude $m(x)$ and phase $\phi(x)$ (Fig. 8.3b) at the fundamental spatial frequency for strips in the $\hat{z}$ direction at each x position (which is one pixel wide). The phase $\phi(x)$ is determined using a bandwidth equal to 0.025 of the fundamental frequency whose FWHM is typically approximately 0.04 of the fundamental frequency. Although the phase itself is arbitrary, its variation with x is nevertheless significant. Almost immediately we notice that some of the images have more phase variation from strip to strip than others (Fig. 8.3c), a fact that is reflected in the $\phi(x)$ curves (Fig. 8.3d). In fact, some of the images have a very clear phase discontinuity where $\phi(x)$ suddenly jumps by approximately π as shown in Fig. 8.3e and 8.3f.

These images have the appearance of a zipper with interference fringes displaced from each other on either side of a dislocation line. Note that the jump shown is close to π, but not exactly, because in addition to the phase discontinuity, this type of image still has the more gentle phase variations as seen in Fig. 8.3d. Zipper images are consistent with interference between pancakes in which one pancake has an isolated vortex [132]. A possible interpretation is that they indicate proximity to the Berezinskii-Kosterlitz-Thouless transition [126]. Well below the transition (on the superfluid side), the vortex-antivortex pairs are still bound, whereas far above the transition (on the normal side), the proliferation of unbound pairs makes the chance of observing a single vortex or antivortex unlikely.

To determine the temperature of each cloud after time of flight, we perform multiple fits on each image. We first fit a bimodal distribution to the integrated average of the central 80% (in the $\hat{z}$ direction) of the image profile in the $\hat{x}$ direction. The bimodal distribution is a Thomas-Fermi function for the central core and a Gaussian in the wings. (The fact that we have assumed a central Tomas-Fermi profile after time-of-flight is justified if the expansion of the cloud follows Castin-Dum [34].) The quality of these fits is in general quite good with example fits shown in Fig. 8.4. To verify the robustness of each fit, we varied the width of the profile from 80% to 160% and then to 320%. We also tried fits where the central Thomas-Fermi region of the cloud was ignored and only a fit to the wings was performed. These fitting modifications resulted in 10-20% variations in the extracted temperature which we report as uncertainties. In the ENS experiment, temperature was not determined by fitting to the time-of-flight images; instead, the
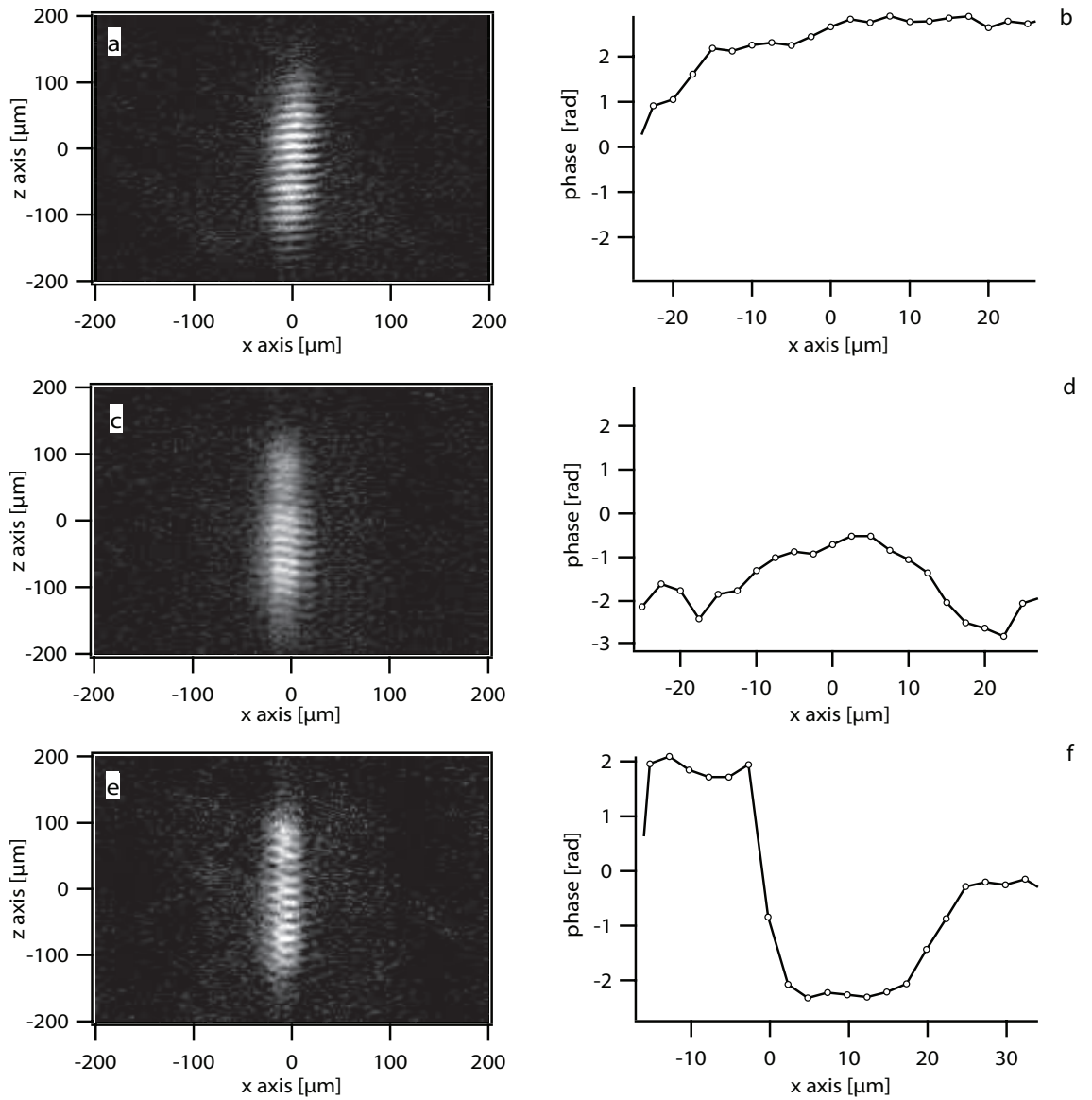
Figure 8.3: Left images: Examples of the interference between the 2D BECs projected onto the xy-plane of our CCD camera. Note the 90° rotation of these images relative to Fig. 8.2. Right images: Phase of the 1D spatial Fourier transform along $\hat{z}$ of the interference pattern for each x position. The phase is at the fundamental frequency of the interference pattern. For four pancakes, this interference phase mainly reflects the relative spatial phase between the central two pancakes. For three pancakes, it represents the relative spatial phase between the outer pancakes.

maximum fringe constrast was determined for each image and this was assumed to be an indicator of the temperature. For comparison, we also determine the maximum fringe contrast C_0 obtained by fitting the interference pattern in the $\hat{z}$ direction within a strip 30 μm wide with the function $A \exp(-\frac{(z-z_0)^2}{\sigma^2})[1 - C_0 \cos(kz - \chi(z))]$. Here $k = Md/\hbar t_{\text{TOF}}$ and $\chi(z)$ is the phase. In Fig. 8.5 we plot $1 - C_0$ against the temperature for each image. For our experiment (with more than two pancakes), the contrast C_0 is not well correlated with the temperature and thus we do not use it as a substitute for the temperature.
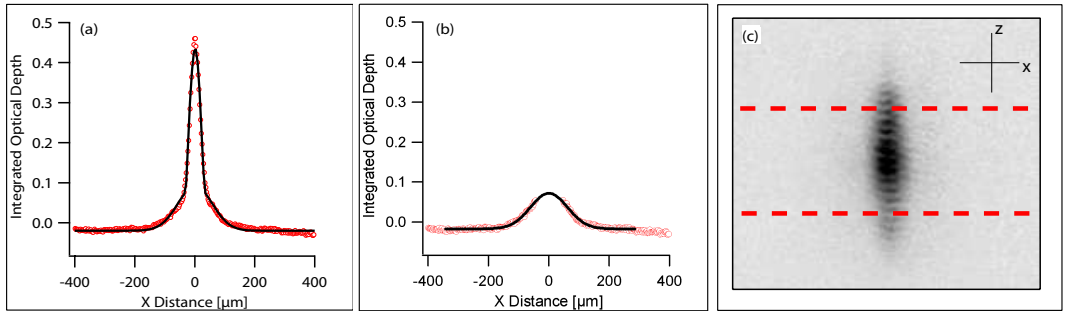
Figure 8.4: Cross sections (a) and (b) of a time-of-flight absorption image (c) of the expanded atom cloud. The solid black line in (a) is a bimodal fit which is Thomas-Fermi in the central region and Gaussian in the wings. In (b), a Gaussian is fit to the wings only. The dashed lines in the absorption image indicate the width of the integrated region used to obtain the cross section (which is the central 80% in the $\hat{z}$ direction). The temperature extracted from (a) is 35 nK and from (b) is 42 nK. Differences such as these are included in the reported temperature uncertainties.

The central contrast was the thermometer used in the ENS experiment [126] because with only two interfering sources one expects unity contrast at zero temperature. The contrast in the interference between N equal amplitude individually-coherent sources with random phases which change from shot-to-shot averaged over many experiments is reduced by a factor of $\sqrt{N-1}$ [120, 137, 138]. The reduction factor is slightly less when the source amplitudes follow a Thomas-Fermi distribu-

167
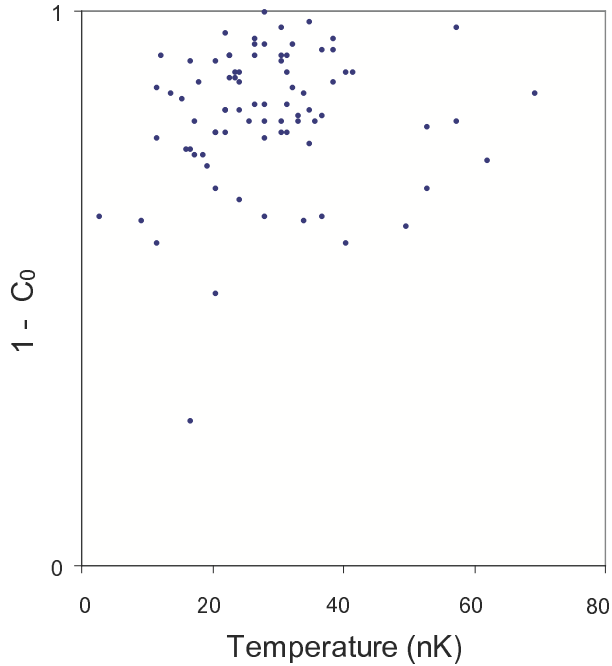
Figure 8.5: Temperature, as measured from the Gaussian wings of the time-of-flight distribution, of the cloud after time of flight vs. $1 - C_0$, the maximum fringe constrast. Because of the weak correlation between the temperature and the contrast, we do not use the contrast as a substitute for the temperature in our experiment.

tion [137, 138]. For our experiment, we therefore would expect an average contrast (over many experiments) of 0.6 to 0.7 if there were no thermal atoms. Because of random variations of the phases of the pancakes, we would expect the contrast to vary from shot to shot, a variation that has nothing to do with temperature. Since our imaging system resolves down to approximately 4 μm (based on the loss of the Fourier transform signal in Chapter 6 when the near-field diffraction fringe separation reached the resolution) and the fringe spacing is $ht_{\mathrm{TOF}}/Md = 16$ μm, we attribute our lower average contrast to the presence of thermal atoms. Based on the extracted temperatures and 2D trapped BEC theory, we calculate a variable thermal population between a few percent of the total number of atoms and almost all of the atoms, based on the temperatures extracted from the bimodal fitting.

8.3 Analysis

At this point we wish to glean as much quantitative information as possible from the interference data. This has been considered from an experimental point of view in Ref. [126] and a theoretical point of view in Ref. [135]. We generally follow the experimental and theoretical procedures in Refs. [126, 135] except as noted below. The coherence of the system can be extracted from g_1, the first order correlation function.

$$g_1(\vec{r}, \vec{r'}) = \langle \psi^*(\vec{r}) \psi(\vec{r'}) \rangle, \qquad (8.1)$$

where $\psi(\vec{r})$ is the field operator at location $\vec{r}$. By measuring the two-field correlation function of the interfering spatially overlapped 2D condensates, we obtain relative spatial phase correlation properties of the initial 2D clouds before expansion [134]. With two pancakes [126], the interference intensity correlations give the relative phase correlations between the two pancakes. When there are three pancakes and the atom number distribution is symmetric (the outer pancakes have approximately the same number), the interference intensity correlations reveal the relative phase correlation between the outer two pancakes. This is plainly true if one examines the first harmonic of the Fourier spectrum of the interference pattern which corresponds to interference between the outer pancakes; however, it is also true if one examines the fundamental frequency of the interference pattern (which corresponds to the sum of the interferences between the two pairs of neighbors).

In order to understand this, we cast the problem into the more familiar one of a three-slit interference pattern with arbitrary phases on the sources. Consider three point sources separated by a distance d in the $\hat{z}$ direction. These represent the central and two outer pancakes at some point (x, y). Now imagine that we are in a frame moving at v_{ref} with respect to these sources, so that the atoms appear to have a de Broglie wavelength $\lambda = h/Mv_{\mathrm{ref}}$. The sources are released at time $t = 0$ and at $t = t_{\mathrm{TOF}}$ we determine the interference pattern produced by those sources on a virtual screen a distance $L = v_{\mathrm{ref}}t_{\mathrm{TOF}}$ away from the original source position. We take $L \gg d^2/\lambda$, in order to be in the far field, which is equivalent to $t_{\mathrm{TOF}} \gg d^2M/h$, the condition for well-separated interference orders. (Note that this condition is independent of v_{ref}, as it must be.)

The amplitude on the screen of Fig. 8.6, at some angle ϕ corresponding to a
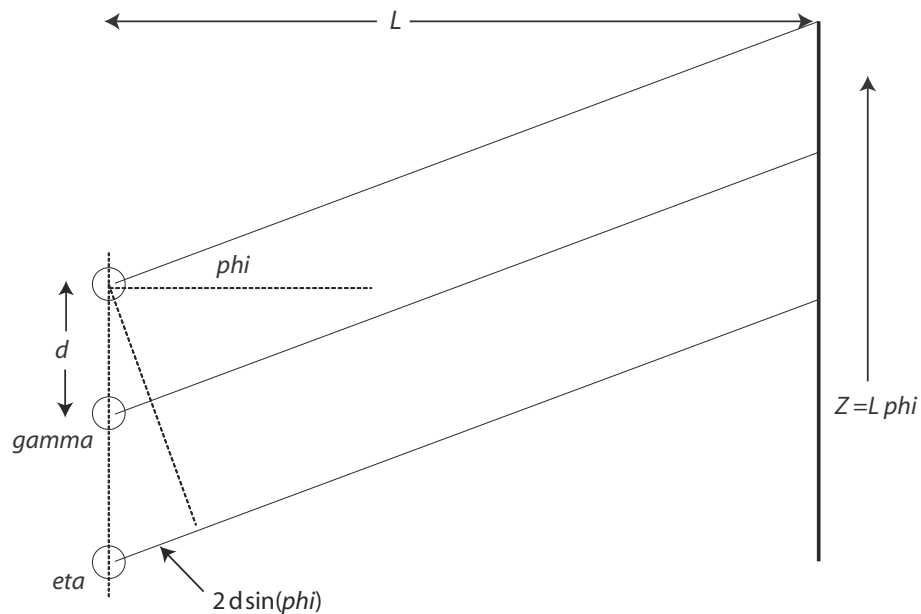
Figure 8.6: The interference of three 2D Bose gases is modelled as a three-source interference pattern on a virtual screen with arbitrary phases on the sources.

170

position z, is the sum of the amplitudes from the three sources. Taking the central source amplitude to be unity, and the outer amplitudes to be f, and the phase of the upper source to be zero, the phase of the central source to be γ, and the phase of the lower source to be η, we have

$$A = f + \exp^{i(\frac{2\pi d \sin \phi}{\lambda} + \gamma)} + f \exp^{i(\frac{4\pi d \sin \phi}{\lambda} + \eta)}. \tag{8.2}$$

Taking $\phi \ll 1$ (without loss of generality, since v_{ref} can be arbitrarily large) we have

$$A = f + \cos(2\pi d\phi/\lambda + \gamma) + f \cos(4\pi d\phi/\lambda + \eta) + i(\sin(2\pi d\phi/\lambda + \gamma) + f \sin 4\pi d\phi/\lambda + \eta). \tag{8.3}$$

But $2\pi d\phi/\lambda$ is also $zdM/t_{\text{TOF}}\hbar$ which we define now as θ, which is simply the z coordinate of the interference pattern expressed in units of the fundamental period of the interference pattern divided by 2π. Thus,

$$A = f + \cos(\theta + \gamma) + f \cos(2\theta + 2\delta) + i(\sin \theta + \gamma + f \sin(2\theta + 2\delta)), \tag{8.4}$$

where we have defined $\eta = 2\delta$.

The observed intensity is the absolute square of this amplitude:

$$I = [f + \cos(\theta + \gamma) + f \cos(2\theta + 2\delta)]^2 + [\sin(\theta + \gamma) + f \sin(2\theta + 2\delta)]^2. \tag{8.5}$$

We now Fourier transform the interference intensity I at the fundamental (where

the conjugate variable is unity).

$$\int_0^{2\pi} d\theta \cos\theta \left[\; (f + \cos(\theta + \gamma) + f\cos(2\theta + 2\delta))^2 \right.$$
$$\left. + \; (\sin(\theta + \gamma) + f\sin(2\theta + 2\delta))^2 \right] = 4\pi f \cos(\gamma - \delta)\cos\delta, \quad (8.6)$$

$$\int_0^{2\pi} d\theta \sin\theta \left[\; (f + \cos(\theta + \gamma) + f\cos(2\theta + 2\delta))^2 \right.$$
$$\left. + \; (\sin(\theta + \gamma) + f\sin(2\theta + 2\delta))^2 \right] = 4\pi f \cos(\gamma - \delta)\sin\delta. \quad (8.7)$$

The phase of the transform is the arctan of the ratio of the sin integral to the cos integral.

$$\phi(x) = \arctan \frac{4\pi f \cos(\gamma(x) - \delta(x))\sin\delta(x)}{4\pi f \cos(\gamma(x) - \delta(x))\cos\delta(x)} = \delta(x). \quad (8.8)$$

Thus, based on our symmetry assumptions, the dependence on γ is gone at the fundamental, leaving only the dependence on δ, half the phase difference between the outer clouds. However, information about the phase of the central cloud has not totally vanished; it is encoded in the relative magnitudes of the fundamental and the first harmonic in the interference intensity (which we do not include in our correlation analysis described below). With four symmetric pancakes dominated by a central pair, phase information at the interference fundamental is dominated by the relative spatial phase between the central pancake pair which can be demonstrated

172

in a similar way. For pancake distributions intermediate to the symmetric three and symmetric four pancake situations, the analysis is not as simple, which complicates the determination of phase correlations.

A method to analyze correlation data in which the correlations are partially integrated over lengths in the $\hat{x}$ and $\hat{y}$ directions has been developed by Polkovnikov, Altman, and Demler [135]. In their paper, they derive an expression for $\langle |A_Q|^2 \rangle$ the quantum observable corresponding to the intensity of the interference fringes in arbitrary dimension. In 2D the expression is

$$\left\langle |A_Q|^2 \right\rangle \sim L_x L_y \int_0^{L_x} dx \int_0^{L_y} dy \left\langle a^\dagger(x,y) a(0,0) \right\rangle^2, \qquad (8.9)$$

where a and $a^\dagger$ are the Bose creation and annihilation operators and L_x and L_y are the integration lengths in the $\hat{x}$ and $\hat{y}$ directions. We have adapted their expression by performing the integration with a fixed L_y (corresponding to the automatic integration performed by our absorption-imaging), a variable L_x, and substituting an expression for the integrand [135] which reflects the algebraic character of the off-diagonal correlations:

$$\left\langle a^\dagger(\mathbf{r}) a(\mathbf{0}) \right\rangle \sim (\frac{\xi_h}{r})^\alpha, \qquad (8.10)$$

where ξ_h is the 2D healing length. The exponent α for a 2D Bose system below the BKT transition is given by $\alpha = M k_B T / 2\pi n_s(T) \hbar^2$ and for weakly interacting

bosons at temperatures well below T_{BKT}, the superfluid density $n_s(T)$ equals the 2D atom number density [135]. However, at T_{BKT} the superfluid density equals a universal value $4/\lambda_{\text{th}}^2$ where λ_{th} is the thermal de Broglie wavelength [108]. Thus, α takes on a universal value of 0.25 at T_{BKT}. Performing the integral in Eq. (8.9), we find the following scaling for $\langle |A_Q|^2 \rangle$.

$$\left\langle |A_Q|^2 \right\rangle \sim (L_y L_x)^{2-\alpha^*}, \tag{8.11}$$

where the experimentally measured α^* is functionally related to the BKT α exponent as shown in Fig. 8.7. We establish this relationship by performing the integral for $\langle |A_Q|^2 \rangle$ with $L_y \sim 4L_x$ which corresponds to the approximately 80 μm Thomas-Fermi time-of-flight diameter in the $\hat{y}$ imaging direction and the approximate 20 μm distance in the $\hat{x}$ direction over which we integrate. This relationship is valid for the ratio of L_y to L_x in our experiment. The relationship is close to that found in the $L_y \gg L_x$ limit and is therefore fairly accurate for integrations performed in the $\hat{x}$ direction up to L_x. Beyond L_x (where we do not integrate) the relationship gradually changes to that found in the limit of $L_y \ll L_x$ [126, 135].

We use boxcar functions for the condensate density (constant within the integration ranges and zero outside of them) in place of the actual profiles of the cloud in the $\hat{x}$ and $\hat{y}$ directions. The integral was also calculated using an ellipse for the condensate profile in the $\hat{y}$ and $\hat{x}$ directions and gave very similar results.

The connection between $g_1(\vec{r}, \vec{r}')$ and $\langle |A_Q|^2 \rangle$ is as follows [126].
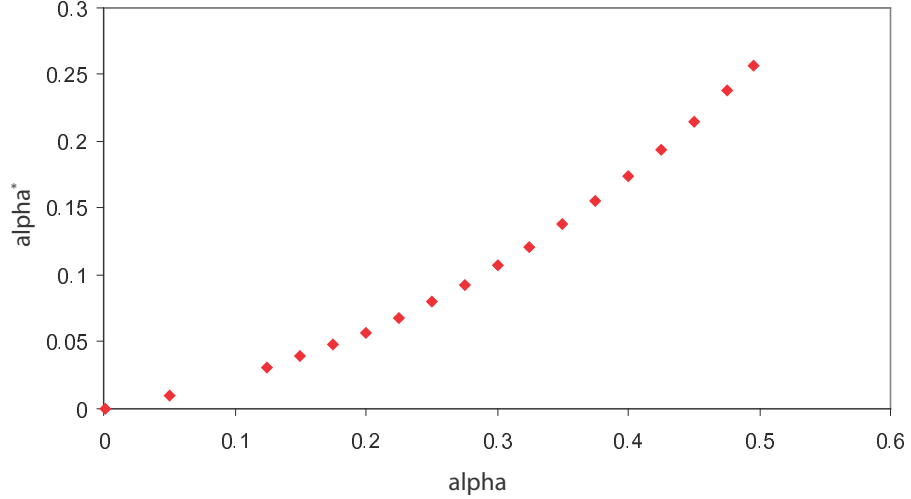
Figure 8.7: The expected relationship between the BKT α exponent and our experimentally measured α^* exponent taking into account the ratio between the integration lengths in the $\hat{x}$ and $\hat{y}$ directions. The condensate density profile is assumed constant over the integration ranges.

$$\frac{1}{L_x} \int_0^{L_x} dx [g_1(\vec{r}, \vec{r}')]^2 \propto \frac{\left\langle |A_Q^2| \right\rangle}{L_x^2} \propto \left(\frac{1}{L_x}\right)^{\alpha^*}. \tag{8.12}$$

Now, analogous to the ENS experiment, we may define an integrated phase of the Fourier transform of the interference pattern at the fundamental $\mathcal{F}(L_x)$ as a function of the integration length L_x in the $\hat{x}$ direction

$$\mathcal{F}(L_x) = \frac{1}{L_x} \left| \int_{-L_x/2}^{L_x/2} dx \exp^{i\phi(x)} \right|, \tag{8.13}$$

which, when averaged over many shots, should decay with the following functional form when there is 2D algebraic decay of the off-diagonal correlations in the bosonic field.

$$\left\langle \mathcal{F}^2(L_x) \right\rangle \propto \frac{1}{L_x} \int_0^{L_x} dx [g_1(\vec{r}, \vec{r}')]^2 \propto \left(\frac{1}{L_x}\right)^{\alpha^*}. \tag{8.14}$$

175

Thus, the 2D correlation properties can be characterized by the exponent α^* which we may extract from our measured interference images.

8.4   Results

Similarly to the ENS experiment, in calculating the $\langle \mathcal{F}^2(L_x) \rangle$ curves, we restrict the range over which we integrate each shot and perform fits to the central part of the interference pattern along x where the magnitude of the Fourier transform $m(x)$ at the fundamental is at least approximately 50% of its maximum value except for occasional isolated points. This distance is approximately 20 μm. Fig. 8.8 shows the logarithm of $\langle \mathcal{F}^2(L_x) \rangle$ as a function of the logarithm of L_x (divided by 5 μm), the integration length in the $\hat{x}$ direction for the specified average temperature of the shots making up the group. Linear fits of the log-log plots are also shown for each graph. To help compare the graphs, we normalize each to $\ln[\langle \mathcal{F}^2(0) \rangle] = 1$ and superimpose them in Fig. 8.9.

The final graph in Fig. 8.10 depicts the measured exponent α^* as a function of temperature. The reported uncertainty in the temperature is dominated by the individual temperature fit uncertainties. For α^*, the reported uncertainty is the standard deviation reported by the fitting program (Igor Pro) used to make the linear fits of the log-log graphs in Fig. 8.8.

Also shown in the graph as horizontal dashed lines are the values of the BKT exponent $\alpha = 0.25$ and $\alpha = 0.50$ corresponding to the α^* values. The agreement
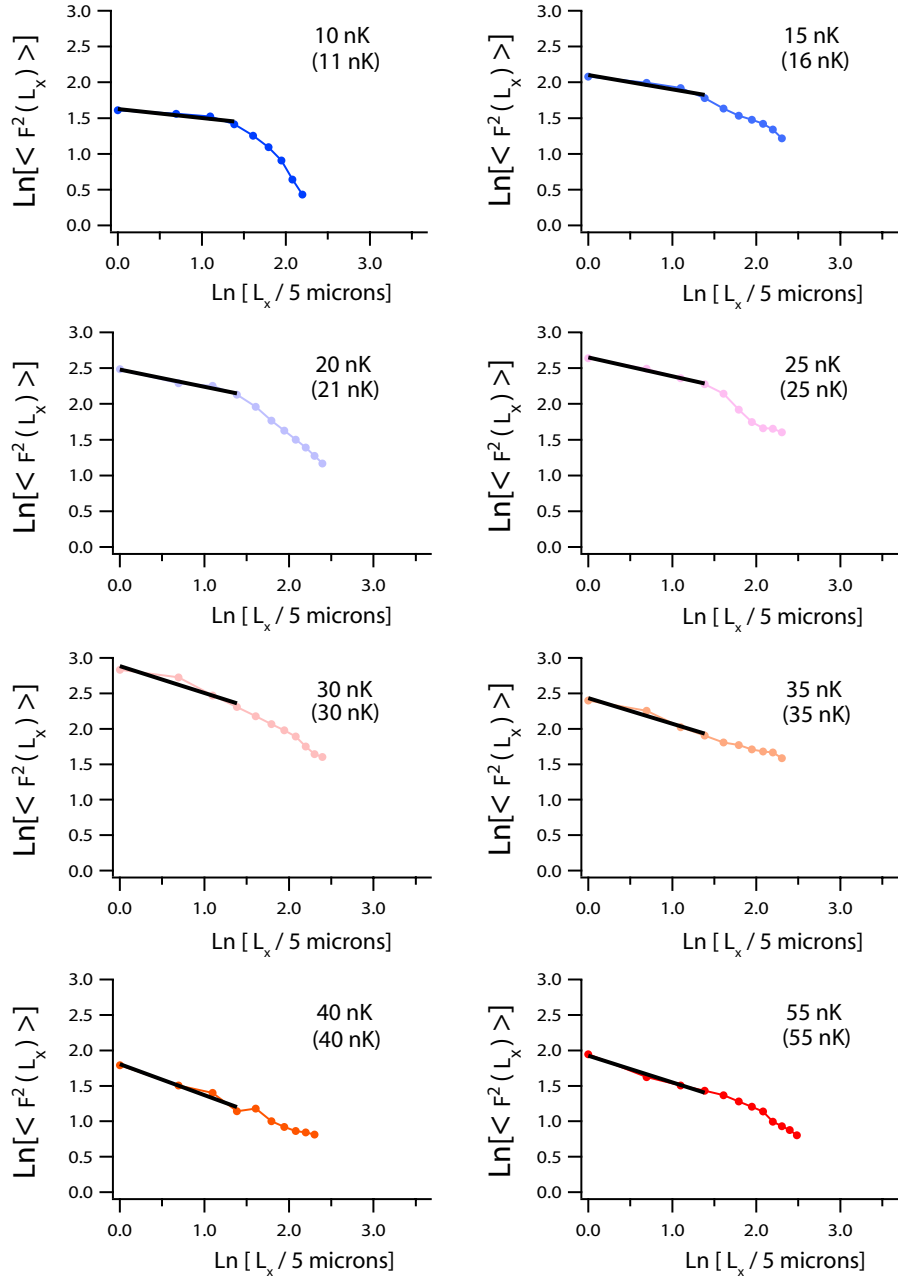
Figure 8.8: The logarithm of $\langle \mathcal{F}^2(L_x) \rangle$ versus the logarithm of $L_x/5\mu$m, the integration length for shots grouped by measured temperature. The top temperature in each graph is the center of the bin, whereas the bottom temperature (in parentheses) is the average of the measured temperatures within the bin. The Thomas-Fermi diameter is 50 μm corresponding to $\ln[50\ \mu$m$/5\ \mu$m$] = 2.3$.
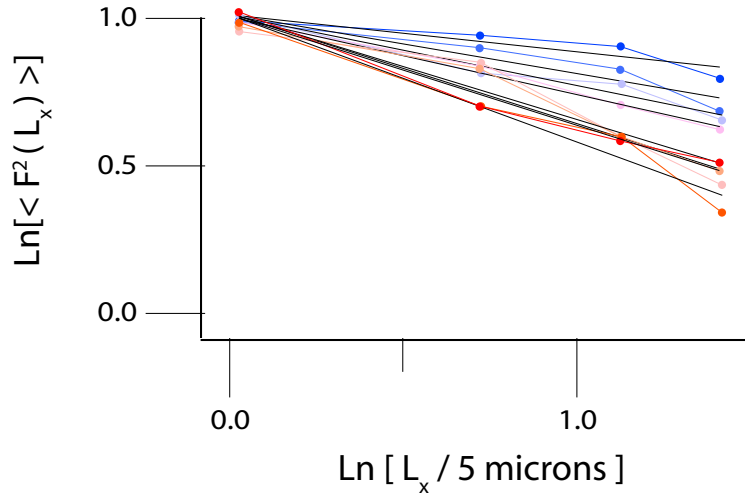
Figure 8.9: Each graph in Fig. 8.8 is normalized to $\ln[\langle \mathcal{F}^2(0)\rangle] = 1$ and superimposed.

between α and α^* at 0.50 is due to the fact that the decay of the correlations changes from algebraic below the BKT transition as given by Eq. (8.10) to exponential above the transition. Using a decaying exponential as an integrand, we obtain $\alpha^* = 0.50$ for any L_x and L_y. This part of the physics is not incorporated into the analysis which establishes the relationship between α and α^* as shown in Fig. 8.7.

Also shown in the graph as a vertical dashed line is the calculated BEC transition temperature T_{BEC} for a 2D trapped ideal Bose gas corresponding to our experimental parameters. The uncertainty in this predicted temperature (mainly due to our original BEC number uncertainty) is indicated by the salmon-colored band. As another vertical dashed line, we indicate a recent theoretical prediction [131] for the BKT transition temperature T_{BKT} for a trapped Bose gas. This prediction is $T_{\text{BKT}} = T_{\text{BEC}}(1 - 3\nu \log^2 \nu/\pi^2)$ where ν is the ratio of the s-wave scattering length to the harmonic oscillator size in the frozen direction. The uncertainty is given by the green band (also due to atom number uncertainty). The tan and green bands
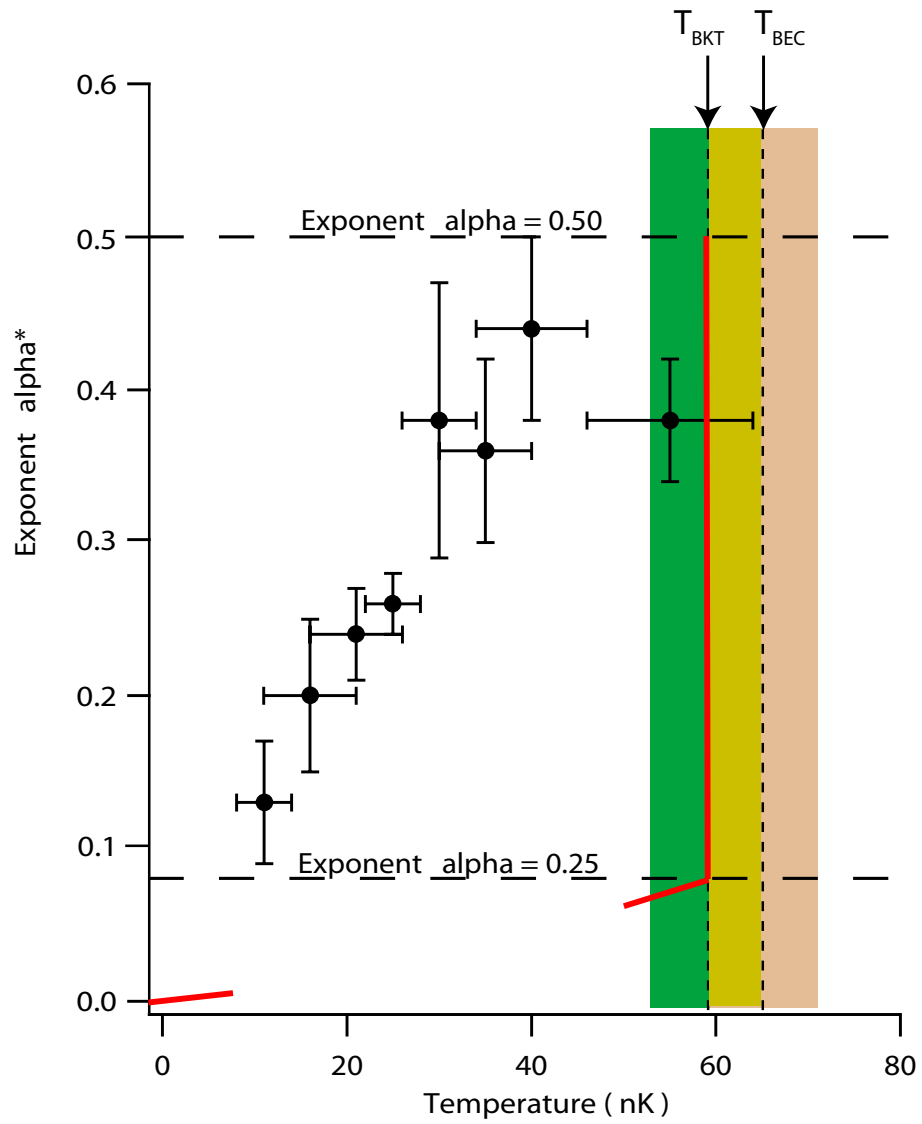
Figure 8.10: The extracted average α^* exponent as a function of the average temperature of the shots.

overlap as indicated by the mustard-colored band.

The red curves in Fig. 8.10 indicate the theoretically-predicted behavior of the BKT α exponent (translated into α^*), which is $\alpha = Mk_{\mathrm{B}}T/2\pi n_s(T)\hbar^2$ where $n_s(T)$ is the 2D superfluid density as a function of temperature T. At $T = 0$, $n_s(0)$ is simply equal to the particle density (unity superfluid fraction) which we use to draw the small red segment near the origin. As T approaches T_{BKT}, $n_s(T)$ is renormalized by fluctuations, and at the transition takes on the value $n_s(T_{\mathrm{BKT}}) = 2Mk_{\mathrm{B}}T_{\mathrm{BKT}}/\pi\hbar^2 = 4/\lambda_{\mathrm{th}}^2(T_{\mathrm{BKT}})$ where λ_{th} is the thermal de Broglie wavelength [108] (thereby giving α the universal value of 0.25 at the transition). Using this value for $n_s(T_{\mathrm{BKT}})$ (which for our experimental parameters gives a superfluid fraction of approximately 0.2), we draw the small red segment approaching $\alpha = 0.25$. At $\alpha = 0.25$, theory predicts a discontinuous jump in α to 0.50 for a homogeneous system [135, 136] as the system goes normal (non-superfluid).

8.5   Discussion

We do not see a jump in α^* near T_{BKT} (see the red curve in Fig. 8.10) as has been observed in condensed matter systems such as 2D ^{4}He systems [108, 109]. Instead, we see a monotonic, nearly linear increase in α^* from an extrapolated value of 0 at $T = 0$ to a value of approximately 0.50 at $T = T_{\mathrm{BKT}}$. There are several possible reasons for this lack of a jump in α^*. Probably the two most important reasons are: 1) the assumption that three pancakes have a symmetric population distribution and that four pancakes are overwhelmingly dominated by the two in the

center may not be sufficiently valid, and 2) it is not clear that a discontinuous jump is expected for a finite-size system [133]. In fact, Ref. [131] predicts that the jump of the superfluid mass at the transition is proportional to ν (where ν is the ratio of the s-wave scattering length to the harmonic oscillator size in the frozen direction), and is thus highly suppressed compared with that in a homogeneous system. This reason was also cited by the ENS group as a possible explanation for the smoothness of the transition which they measured.

Although we state that the variation in the population distribution within the pancakes might contribute to the measured absence of a jump in α^*, it is not clear that, *on average*, this variability would cause the measured value of α^* to be always higher than in the case of two pancakes. In fact, it may be the case that with a sufficiently large number of shots, the result with three or four pancakes would average to the result with only two pancakes. If this were true, then we would conclude that the smoothness of the measured transition is predominately due to finite-size effects. We intend to further investigate this issue.

Assuming that a measured power law exponent, α^*, less than 0.50 means we are not in the thermal regime, our results are consistent with the theoretical prediction by Holzmann, Baym, Blaizot and Laloë [131] which places the transition temperature T_{BKT} for a finite, trapped system slightly below the calculated BEC transition temperature T_{BEC} for an ideal, trapped 2D gas. This is an important result which could not be established by the ENS group because they did not extract temperatures from their measured data. Although, given our uncertainties, we would have to conclude that our data would also be consistent with a predicted

transition temperature significantly higher than the result, our data would contradict a predicted transition temperature significantly lower.

As previously stated, we occasionally observe nearly π phase dislocations (zippers) in our images. These occur in approximately 5% of our data. It has been suggested that the proliferation of these zippers may be a signature of being near T_{BKT} [126]. In future experiments, we will attempt to image these vortices along the lattice axis as opposed to from the side. This should allow us to make contact with the spatial origins, arrangements, and movements of the vortices.

Chapter 9

Summary of Published Experiments

This chapter is a summary of experiments performed over the course of my graduate studies in the ^{87}Rb BEC laboratory whose results have already been published in peer-reviewed journals. There seems little point in completely rewriting these already well-polished (or, what we in the Laser Cooling group call "tortured") papers. In addition, since I was not the lead experimentalist in these investigations, including them in this dissertation on the same footing as the experiments described in Chaps. 6, 7 and 8 (in which I was the principal investigator) would be misleading. Instead, I have chosen to provide short summaries of each experiment in this chapter with copies of the published papers in the Appendices.

9.1 Observation of Reduced Three-Body Recombination in a Correlated 1D Degenerate Bose Gas

In this experiment, we investigate the correlation properties of a 1D interacting Bose gas. In 1D, atom-atom interactions dominate as the atomic density decreases. This is unlike the situation in 3D where atom-atom interactions decrease in importance as the density decreases. In 2D, the interaction energy is independent of the density. These results can be understood in the homogeneous case by expressing the ratio of the mean-field interaction energy to the kinetic energy per atom in

terms of the 1D, 2D, or 3D atomic densities. A single parameter $\gamma \equiv Mg/2n_{1D}\hbar^2$, where g is the s-wave interaction strength and n_{1D} is the 1D atomic density, entirely characterizes a homogeneous 1D gas with repulsive short range interactions. As γ increases, interactions increasingly dominate and it becomes energetically favorable for the gas to be correlated. For $\gamma \gg 1$, we enter the Tonks-Girardeau regime [8, 9] where the many-body ground state becomes highly correlated in order to minimize the interaction energy and the bosons become impenetrable, behaving like fermions. The second and higher-order local correlation functions g_i vanish [10] at small inter-atomic separation, meaning that no more than one particle can be found at a given position.

We adiabatically load a 3D magnetically-trapped BEC into a deep 2D optical lattice creating an array of independent 1D tubes. We measure the three-body recombination rate for the BEC in the magnetic trap and for the BEC loaded into the optical lattice. The recombination rate coefficient is a factor of seven smaller in the lattice, which we interpret as a corresponding factor of seven reduction in the local (3D) third-order correlation function g_3. For our experiment in which we have an array of 1D tubes, we calculate a median value of 0.45 for γ which is in the regime intermediate between that of an uncorrelated gas where $\gamma \ll 1$ and the highly correlated Tonks-Girardeau gas where $\gamma \gg 1$. At the time that we wrote the paper, there was no calculation of $g_3(\gamma)$ in this regime; however, there is an expression for $g_2(\gamma)$ in this regime and we use the approximate expression $g_3 = (g_2)^3$ which is expected to be nearly exact in the mean field regime and for $\gamma \gg 1$ exceeds the exact g_3 by a factor of 2 [11]. We find that our inferred reduction

in g_3 based on the measured three-body recombination suppression is consistent with this approximation, within experimental uncertainty.

9.2   Strongly Inhibited Transport of a Degenerate 1D Bose Gas in a Lattice

This experiment studies the inhibition of transport in a 1D Bose gas in the presence of a 1D optical lattice along the 1D axis. Transport of the 1D gas is established by setting up dipole oscillations of the entire gas in a combined harmonic and optical lattice potential. The degree of inhibition is quantified by modelling the center of mass of the 1D gas as a classical, damped simple harmonic oscillator and extracting a damping coefficient. We observe significant damping for very shallow 1D lattices (0.25 photon recoil energies) and dramatic increases in the damping with increasing lattice depth. The damping becomes so strong that the 1D gas is immobile for times an order of magnitude longer than the single-particle tunneling time.

As with the three-body recombination experiment, we create an array of independent 1D tubes by loading a 3D BEC into a deep 2D optical lattice. We then corrugate the tubes by adiabatically applying an axial 1D lattice. We excite dipole oscillations of the center of mass of the atoms in all of the tubes by suddenly applying a linear magnetic field gradient, thus displacing the total harmonic trap (but not the lattice) 3 μm. One quarter dipole period later, the maximum velocities correspond to quasimomenta less than the band structure inflection point (where

the effective mass changes sign) up to a 8 E_R deep 1D lattice, which rules out an explanation for the damping based on a single-particle dynamical instability. If we do not create the array of 1D tubes, but simply establish dipole oscillations of a 3D BEC in the same combined harmonic and 1D optical lattice, then we do not see the damping. This tells us that the damping has something to do with the reduced dimensionality and/or the density variations caused by the presence of the tubes.

This experiment has generated theoretical interest [150–155] and various explanations have been put forth to explain the unexpected results. The common thread to all of the theoretical explanations is the role of quantum fluctuations which are more pronounced in 1D than in 2D and 3D. Where the explanations seem to diverge is in describing specifically how the fluctuations cause the inhibited transport. Some explanations emphasize the role of quantum depletion [150–152] as a source of "friction" for the atoms still in the condensate. Other explanations focus on the ability of the system to "tunnel" to the dynamical instability point because of the fluctuations [155]. As of this writing, there is no general consensus.

9.3   Collisional De-excitation in a Quasi-2D Degenerate Bose Gas

Here, we probe in detail the collisional decay of a quasi-2D degenerate Bose gas. The gas is quasi-2D in the sense that although motion is restricted in one direction, atom-atom interactions take place in 3D. We start by creating a stack of 2D pancakes and Raman-exciting quantized vibrational motion in the (initially frozen) direction normal to the pancakes. The Raman transitions between the vibrational levels are

driven by a pair of nearly counterpropagating laser beams. Following the excitation, we measure the rates of collisional decay from the discrete spectrum of excited vibrational states. The measured decay rates are suppressed due to the reduced dimensionality, in analogy to inhibited spontaneous emission.

Following each decay event, the released vibrational energy (which can be thought of as an internal-state energy-quantum) is transformed into the kinetic energy of back-to-back atoms travelling out in (weak) directions normal to the tight (initially frozen) direction. Because of the well-defined energies of de-excitation and the randomness of the outgoing directions, the images after time-of-flight appear as a set of well-defined concentric rings in the 2D plane with radii corresponding to vibrational energy level differences. These images provide us accurate information on the numbers of atoms participating in individual, allowed decay channels. Images taken in one of the weak directions following band-mapping (band-mapping is explained in Chap. 3) permit us to identify the final vibrational states. The experimental results consist of measured decay rates which are compared to calculated decay rates based on a Fermi's golden rule treatment. We find good agreement between our experimental results and the results of the calculations.

Because the atom-atom interaction preceding the decay is well described by a delta-function potential, decay channels are restricted to those whose matrix element (containing two entering particle wavefunctions and two exiting particle wavefunctions) is an overall even function. We observe this decay channel restriction in our experimental data. In addition to being an important demonstration of inhibited decay due to the reduced dimensionality, this experiment represents a novel single-shot

187

spectrographic technique, potentially useful for other investigations.

Chapter 10

Conclusion

10.1 Summary of the Dissertation

In addition to its obvious purpose of documenting what I have accomplished as a University of Maryland graduate student at NIST, it is hoped that this dissertation will serve several other important functions. I believe that a good dissertation helps to advance the state of knowledge *and* is a useful how-to manual. It is also nice if it reads like an engrossing novel where you cannot stop turning the pages. With this in mind, like many Ph.D. students before me have done, I feel I now have license to stretch out a bit and add a touch of drama and human elements to the recapitulation of the dissertation.

Chap. 1 began at a level understandable to anyone who has had a course in statistical mechanics and knows what a boson is. Thus, hopefully even an armchair physicist will have an inkling about the general topic of this dissertation. Chap. 1 ended with a table (Table 1.1) that I have wanted hanging on my wall over the years. Table 1.1 summarizes succinctly (if possible) various expressions for the degeneracy temperatures and ground state occupations in 1D, 2D, and 3D for the cases of the ideal Bose gas, the weakly interacting Bose gas, and the harmonically-trapped Bose gas. If I ever see this table hanging on a wall in anyone's laboratory or office in the future, I will consider this thesis a success (and demand royalties :-)).

Chaps. 2, 3, and especially 4 were written keeping foremost in mind my bewilderment when I began working in the ^{87}Rb laboratory in 2002. I remember thinking then how great it would be if I could read someone's thesis describing the ^{87}Rb experimental hardware from soup to nuts. In addition, I wanted written descriptions and brief theoretical backgrounds on the specialized experimental techniques (such as lattice pulsing and band-mapping) that everyone in the lab was talking about. Alas, it could not be so since the apparatus was then less than one year old and I was the first graduate student to work on it. (I'm sure I drove Trey Porto and postdocs Bruno Laburthe Tolra, Ken O'Hara, and Chad Fertig insane with my incessant questions.) So, for the future graduate students and postdocs entering the ^{87}Rb laboratory, part of this thesis is my gift to you with apologies for not covering everything.

Chaps. 5 and 6 comprised a couplet, an ode really, to the practical genius of Trey Porto. Although I put together the accordion lattice and calibrated it, the idea for the lattice sprang from his head (with contributions from Bruno Laburthe Tolra). Like the later double-well lattice (not described in this thesis) that he (with Poul Jessen) dreamt up, this device bears his distinct signature. Trey is a clever physicist and I am eternally grateful for his bequest of the design of the accordion lattice to me. Chap. 5 is an extremely thorough description of the design and construction of the accordion lattice as well as an analysis of atomic ground state excitation due to rotational noise and lattice compression/stretching. Chap. 6 describes the painstaking process of calibrating the accordion lattice. I was assisted during this crucial stage by Bruno Laburthe Tolra and Ian Spielman. Ian deserves special thanks for

helping to turn a rather pedestrian procedure (calibrating a tool) into an exciting proto-experiment involving two lattices with commensurate/incommensurate periodicities.

The way in which the beyond-Raman-Nath diffraction experiment described in Chap. 7 unfolded deserves a story. When I first saw the saturation of the diffraction order envelope amplitude, its sudden collapse and subsequent revival, I was mystified. I could make no sense of it. (Even a certain Nobel prize-winning physicist did not have an explanation for what was going on.) I felt like the blind man feeling the elephant until I finally scanned far out in lattice pulse duration, sequenced the diffraction data by pulse duration and saw the organizing principle of the order envelope executing a strange asymmetric oscillation. I remember Carl Williams looking at the data and asking "What's the fish?" (The lunch lady said the same thing.) (See Figure 7.1) I had suspected an oscillation of some sort months earlier while staring at a single diffraction image and noticing its similarity to a highly-excited harmonic oscillator. A few weeks later, I was flabbergasted when I saw a theory paper from 1994 by Janicke and Wilkens with the same "fish" patterns in their figures. I ran down to the lab in great excitement and showed the paper to Marco Anderlini who said something like "Now you have it Johnny!"

At this point, everything fell into place with the exception of an intuitive understanding of the asymmetry of the envelope oscillations. For achieving insight into the reason for this asymmetry based on a phase space portrait, I want to especially thank Vincent Boyer for very helpful discussions. I remember the joy of sharing this insight with Trey who had been challenging me to come up with

an explanation. Once I explained it to him, he immediately gave the proper name (caustics) to the features I was trying to describe to him. Imagine my surprise when I discovered a few weeks later that M. V. Berry had also thought about this anharmonic oscillator asymmetry in the context of geometrical optics and had developed the same phase space portrait explanation involving caustics. Now that everything is pretty well understood, it all seems rather simple; but this is how it always is.

The story behind Chap. 8 is also interesting. It started with a group meeting in which I described some strange diagonal interference patterns I had observed while trying to align the accordion lattice. After the meeting, Ennio Arimondo button-holed me and told me what he thought these patterns were. I had a vague idea of what he was talking about because I remembered discussing the ENS experiment a few weeks earlier with Marco. Of course, I had heard of the Kosterlitz-Thouless transition, but I did not know much about it. So, while Ennio fed me a steady diet of theory papers, I performed various calculations to see if I was in the proper regime to be seeing KT vortices. I also consulted with my old condensed matter professor, Ted Einstein at Maryland to learn more about the KT transition in condensed matter systems. I read the early 2D superfluid ^{4}He papers by my Cornell advanced lab instructor, John Reppy. This was an intense period of learning for me. When I got back to the lab, I changed some of the experimental parameters (ramp duration, snap-off time, and lattice periodicities). Almost immediately, the data started looking better. I remember getting a beautiful zipper diffraction pattern at the exact instant that Bill happened to walk into the lab. This felt good.

192

My investigation into (Berezinskii-)Kosterlitz-Thouless physics using a BEC with the accordion lattice represents the scientific high point of my graduate school career and I am delighted to incorporate it in my thesis. I am deeply indebted to Ennio for his early insights and correct interpretation of the preliminary data. He was the spark plug behind my effort and I appreciated our valuable discussions as well as his overall encouragement.

Chap. 9 describes three very significant experiments, two of which were performed quite early in my graduate school career. I know that I was very lucky to have had the opportunity to essentially "cut my AMO experimental teeth" on such important experiments. Thanks Bill and Trey.

And now for a forward look...

10.2   The Challenges and Opportunities Ahead

As stated in Chap. 1 my thesis is about the physics of dilute gaseous BECs confined to lower dimensions by optical lattices. In looking to the future, I have focussed on condensed matter-analog experiments using a new optical lattice knob hitherto unused by researchers in the field, namely the ability to dynamically vary the periodicity of an optical lattice while keeping ultra-cold atoms in the ground state in situ. I was in the midst of these motional adiabaticity investigations, attempting to quiet the rotational dither noise, when a series of unfortunate events led to a failure of the accordion lattice. Sadly, my graduate school career may end before I am able to rectify this problem, let alone complete the motional adiabaticity study

and thus fully exploit one of the truly novel features of the accordion lattice. This, then, represents an immediate challenge for me (or someone after me) following the completion of this dissertation.

Luckily, even without motional adiabaticity proof-of-principle, the accordion lattice offers several unique advantages. The ability to rapidly vary the lattice constant *between* shots permits a rapid exploration of experimental space. For instance, it is unlikely that I would have been able to find the best location to perform the BKT experiment described in Chap. 8 without the accordion lattice. Also, the superlattice experiment described in Chap. 6 as part of the periodicity calibration could never have been done without the accordion lattice. A similar superlattice experiment should (and probably will) be performed in the future focussing on commensurate/incommensurate phase transitions [156, 157].

Taking a more expansive view of the field, as stated in Chap. 3 we are now at the point where important, unsettled questions in condensed matter physics may be answered using ultracold neutral atoms in optical lattices. More work is needed on the nature of the 2D Berezinskii-Kosterlitz-Thouless transition in trapped systems and its relationship to the transition in a homogeneous system.

Expanding our view even further to degenerate Fermi systems, it is hoped that experiments which will be performed shortly [158] will tell us whether high T_c superconductivity is contained within the Hubbard model. I am excited to begin a postdoc position in a laboratory that will attempt to answer this very fundamental question with potentially significant practical repercussions. Competition with other laboratories will likely be quite fierce.

The combination of BECs and optical lattices has enabled the exploration of fundamental quantum mechanical issues using systems that are accessible and highly flexible. "Thank you Bill" for helping to create an exhilarating and dynamic sub-field of AMO physics. Your enthusiasm, persistence, and never-ending curiosity have enabled the creation of now two generations of laser-coolers and atom-trappers.

Appendix A

Observation of Reduced Three-Body Recombination in a Correlated 1D Degenerate Bose Gas

Observation of Reduced Three-Body Recombination in a Correlated 1D Degenerate Bose Gas

B. Laburthe Tolra,* K. M. O'Hara, J. H. Huckans, W. D. Phillips, S. L. Rolston,† and J. V. Porto

National Institute of Standards and Technology, Gaithersburg, Maryland 20899, USA
(Received 7 November 2003; published 10 May 2004)

We investigate the correlation properties of a one-dimensional interacting Bose gas by loading a magnetically trapped ^{87}Rb Bose-Einstein condensate (BEC) into a deep two-dimensional optical lattice. We measure the three-body recombination rate for both the BEC in the magnetic trap and the BEC loaded into the optical lattice. The recombination rate coefficient is a factor of 7 smaller in the lattice, which we interpret as a reduction in the local three-body correlation function in the 1D case. This is a signature of correlation intermediate between that of the uncorrelated, phase coherent, 1D, mean-field regime and the strongly correlated Tonks-Girardeau regime.

The majority of experiments with quantum degenerate gases have been performed in the weakly interacting limit, on Bose-Einstein condensates (BECs) characterized by long-range phase coherence and well described by the mean-field Gross-Pitaevskii (GP) equation [1]. While the success of the GP equation in accounting for many experimental results has been spectacular, it has also led to the search for physics beyond mean-field theory. As in condensed matter physics, there is now great interest in highly correlated systems, where mean-field approaches are inapplicable and a (second) quantization of the atom field is required. Progress toward such correlated systems includes the recent observation of number squeezed states [2] and the Mott-insulator transition [3] in BECs loaded into optical lattices, and the use of Feshbach resonances to increase interactions between atoms [4]. Here we present evidence of strong correlations in a 1D degenerate Bose gas as reflected in a reduction of three-body recombination.

The role of fluctuations and correlations in Bose gases increases with reduced dimension. In homogeneous systems, BEC is possible only in 3D. In 2D, a Kosterlitz-Thouless transition occurs, and in 1D there is no finite temperature transition [5]. By contrast, BEC is possible in 1D, 2D, and 3D for trapped systems [6]. Trapped 1D systems with δ-function repulsive interactions are particularly interesting, in that for high density the ground state is a condensate, while in the low density limit the ground state is a highly correlated state known as a Tonks gas [7]. This ground state is an example of "fermionization," where the repulsive interactions mimic the Pauli exclusion principle. Indeed, the low energy excitation spectrum is identical to that of noninteracting fermions, and the many-body wave function of the Bose gas is equal to the absolute value of the fermionic wave function [8].

For such a 1D Bose gas, the degree of correlation depends on the ratio between two energies: the repulsive energy of uncorrelated atoms at a given density, $E_{\rm unc} =$ gn_{1D}, and the quantum kinetic energy needed to correlate particles by localizing them with respect to each other on the order of the mean interparticle distance d, $E_{\rm cor} = \hbar^2/2md^2$. Here, g is the strength of the δ-function interaction, m is the atomic mass, and $n_{1D} = 1/d$ is the 1D density. A single parameter $\gamma \equiv E_{\rm unc}/4E_{\rm cor} = mg/2n_{1D}\hbar^2$ entirely characterizes a homogeneous 1D gas with repulsive short range interactions. For $\gamma \gg 1$, it is energetically favorable for the gas to be correlated. The exact eigenstate solutions [7] and correlation functions [9] have been calculated for arbitrary values of γ. Recently, these results have been extended to harmonically trapped gases, addressing, e.g., the excitation spectrum [10], the shape of the trapped gas [11], and the single-particle correlation function [9].

The many-body ground state has two limiting forms. In the Tonks-Girardeau (TG) regime, where $\gamma \gg 1$, the ground state becomes correlated in order to minimize the interaction energy and the bosons become impenetrable, behaving like fermions as described in [8]. The second and higher-order local correlation functions g_i vanish [12], meaning that no more than one particle can be found at a given position. On the other hand, in the mean-field (MF) regime when $\gamma \ll 1$, the GP equation describes the system well. In this regime the healing length, $l_h = \hbar/\sqrt{mgn_{1D}}$, is much larger than the mean interparticle distance. Note the counterintuitive result that the system reaches the correlated regime for *low* 1D densities, contrary to the 3D case where $n_{3D}a_s^3 = (\gamma/2\pi)^3 \gg 1$ corresponds to the correlated regime. (Here a_s is the zero-energy 3D scattering length [13], and γ is the appropriate energy ratio in 3D.)

To probe correlations we measure three-body recombination rates (proportional to the local third-order correlation function g_3) of 1D gases produced in a 2D optical lattice. This technique was used in Ref. [14] to demonstrate that there is a reduction of g_3 in a 3D BEC by a factor of 6 compared to a thermal gas. We observe a further reduction of three-body recombination in a

1D gas compared to the 3D BEC situation. Even though $\gamma \simeq 0.5$ for our system, which is far from the TG regime, this is a signature that the correlations are significant due to the fermionization of the particles.

We realize a 1D gas by confining a 3D gas sufficiently tightly in two directions that the radial confinement energy $\hbar\omega_\perp$ is much larger than all other relevant energies in the system: $k_B T$, the axial trapping energy $\hbar\omega_z$, and the chemical potential. Reference [15] has recently produced a 1D Bose gas using similar techniques. Since a_s is much smaller than $a_\perp = \sqrt{\hbar/m\omega_\perp}$ ($a_s/a_\perp \simeq 0.1$ in our system), the atom-atom interaction strength is largely determined by a_s, with only a small correction due to confinement [16,17]: $a_{\mathrm{eff}} = a_s/(1 - 1.46 a_s/\sqrt{2} a_\perp)$. There is no excitation in the radial direction and by integrating over the radial coordinates, one can show [16] that the system is formally equivalent to a true 1D gas with interaction strength $g = 4\hbar^2 a_{\mathrm{eff}}/m a_\perp^2$, so that $\gamma = 2 a_{\mathrm{eff}}/(n_{1D} a_\perp^2)$. The 3D density is related to the effective 1D density by $n_{1D} = 1/d = \pi a_\perp^2 n_{3D}$.

Our approach is to load a BEC into the ground state of a deep 2D optical lattice so that the BEC is divided into an array of independent 1D quantum gases, each tubular lattice site acting as a highly anisotropic trap. Our experimental apparatus has been described elsewhere [18]. We achieve BEC with up to $N_0 = 5 \times 10^5$ atoms in the $(F, m_F) = (1, -1)$ hyperfine state of ^{87}Rb (for which $a_s = 5.313$ nm [13]). An Ioffe-Pritchard trap confines the atoms with initial "tight" trap frequencies of $\nu_x = \nu_z = 210$ Hz, and $\nu_y = 8.2$ Hz, giving a peak atomic density of up to 3×10^{14} cm^{-3}. Before applying the optical lattice, we adiabatically lower ν_x and ν_z to a "weak" trap frequency of 28 Hz (keeping ν_y fixed), resulting in peak densities of $\sim 5 \times 10^{13}$ cm^{-3}.

We create a 2D optical lattice from two independent, retroreflected 1D lattices which lie in the xy plane and intersect at an angle of 80°. The independent 1D lattices are detuned from each other by 5 MHz. All beams derive from a Ti:sapphire laser operating at $\lambda = 810.08$ nm (detuned below both $5S \rightarrow 5P$ transitions at 795 and 780 nm), and the polarizations of the lattice beams are in the xy plane. Each 1D lattice is measured [19] to be $29(1)$ E_R deep (where $E_R = h^2/2m\lambda^2$) [20]. At each lattice site the ground state of the radial motion is well approximated by a Gaussian wave function with $a_\perp = 58.5(5)$ nm corresponding to an effective $\omega_\perp/2\pi = 33.8(6)$ kHz. By observing dipole oscillations following a sudden, brief displacement of the trap center, we measure the axial frequency along the tubes to be $\omega_z/2\pi = 55.9(6)$ Hz. This frequency results from the combined effect of the magnetic trap and the dipole potential of the lattice beams along the tubes. To load the atoms into the lattice, the laser light is increased over 200 ms with an approximately half Gaussian shape (rms width 70 ms), which is adiabatic with respect to all vibrational excitations. We estimate that the interaction-free tunneling time from one lattice site to the next for a 29 E_R lat-

tice is $\simeq 150$ ms. Although this is shorter than the time of the experiment (up to 12 s), it corresponds to an energy much smaller than the interaction energy in the tubes and should not modify the local 1D correlation properties [21].

To measure the reduction of g_3 due to correlations, we observe the corresponding reduction in the three-body recombination rate coefficient. The local three-body recombination rate (in either 1D or 3D) is proportional to the cube of the local density. For ^{87}Rb, it is known that two-body losses [14,22], including photoassociation at 810 nm [23], are very small [24]. Our model, therefore, includes only one-body and three-body processes so that the total number of atoms N decays according to

$$\frac{dN}{dt} = -K_1 N - \int K_3^{1D} n_{3D}^3 dV. \tag{1}$$

We account for atomic redistribution during decay through the evolution of the density profile. Determination of the three-body recombination rate coefficient K_3^{1D} requires an accurate estimate of the density, which we ascertain from a measurement of the number of trapped atoms as a function of time, along with a determination of the size and shape of the atom cloud.

Figure 1 shows the total number of atoms as a function of time t in the lattice, obtained by absorption imaging 34 ms after release from the lattice and magnetic trap. We calibrate our absorption measurements by comparing the observed expansion of a released condensate to the known number-dependent expression for the expansion [25]. [The inferred absorption cross section agrees ($\sim 10\%$) with one calculated from the steady state Zeeman sublevel distribution resulting from optical pumping.] The number of atoms in the BEC fluctuates by less than 20% from shot to shot. We automate the experiment to produce a BEC every minute and each data point is typically an average of five measurements.
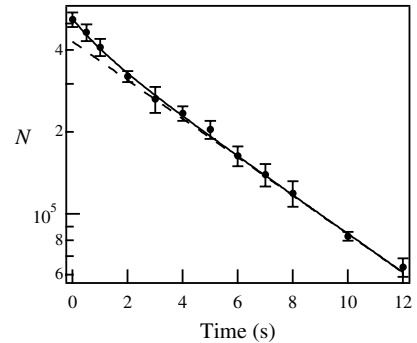

FIG. 1. Number of atoms as a function of time in the 2D lattice. The solid line is a fit to the decay as described in the text, and the dashed line is an extrapolation of the asymptotic one-body loss.

190401-2   190401-2

In order to minimize systematic effects due to long term thermal drift of the trap coils, we run current in the magnetic trap *after* the imaging such that the total time that the magnetic trap is on is the same for each measurement. While the atoms are in the lattice, we apply a radio frequency shield [22] tuned 500 kHz above the minimum of the trap to reduce heating without significantly increasing the loss of atoms trapped in the lattice.

We measure the size of the lattice-trapped cloud in the xy plane by phase contrast imaging. The initial column density distribution of the cloud is well described by an integrated Thomas-Fermi (TF) profile, with radii of $R_x = 13.1(5)$ μm and $R_y = 22.5(10)$ μm so that the observed number of atoms per tube at (x, y) is well described by $\mathcal{N}_{tube} = \mathcal{N}_{max}[1 - (x/R_x)^2 - (y/R_y)^2]^{3/2}$, where $\mathcal{N}_{max} = 5N_0\lambda^2/8\pi R_x R_y$ is the number of atoms in the central tube and $\lambda/2$ is the spacing of the tubes. Based on the initial total number and the measured sizes of the cloud, we determine $\mathcal{N}_{max} = 230(40)$. In the xz plane, we measure the size of the cloud using a different (absorption) imaging system. The initial xz density distribution is also described by a TF profile, of radii $R_x = 15(2)$ μm (in agreement with our phase contrast xy measurement) and $R_z = 17(2)$ μm. For our parameters, the atom distribution along the tubes (along z) is not expected to deviate significantly from a TF profile [11]; indeed R_z agrees with the 1D TF value calculated based on $\mathcal{N}_{max}$. We note that the peak density is $\sim 1 \times 10^{15}$ cm^{-3}, which would lead to rapid three-body loss in a 3D system.

We observe that the cloud slowly expands in the z direction over the course of the measurement: the cloud expands by 5 μm in 2 s while the R_x and R_y radii remain constant, consistent with a 1 kHz/s rate of energy increase along z. Spontaneous emission initially deposits a majority of the recoil energy into radial motion, but since $k_B T \ll \hbar\omega_\perp$, equilibration will eventually transfer essentially all the energy to axial motion. The observed axial heating rate lies between the limits set by full equilibration and no equilibration. This expansion reduces the density only modestly during the first 2 s, when most of the three-body decay occurs, and we account for it in our modeling of the decay.

To model the decay using Eq. (1), we assume an overall 3D TF density profile with Gaussian radial distributions within each tube. In addition, for simplicity of modeling we assume K_3^{1D} to be a constant (see below). With these approximations, Eq. (1) becomes

$$\frac{dN}{dt} = -K_1 N - \alpha(t)K_3^{1D}N^3, \qquad (2)$$

where $\alpha(t) = (25/896\pi^4)[\lambda^2/a_\perp^2 R_x R_y R_z(t)]^2$. The radii R_x and R_y are kept constant at their measured values, and $R_z(t)$ grows linearly in time at the measured rate of 2.5 μm/s. This differential equation has an analytic solution which gives the total number as a function of time, to which we fit the data of Fig. 1.

190401-3

With this analysis, we determine $K_3^{1D} = 1.2(7) \times 10^{-30}$ cm^6 s^{-1} and $K_1 = 0.16(2)$ s^{-1}. This result is relatively insensitive to the specific model used for atomic spatial redistribution during decay, and variations among realistic models fall within the quoted uncertainties. We attribute K_1 mainly to optical pumping to states other than the original $(1, -1)$ state, which are untrapped in the combined optical, magnetic, and gravitational potential. For the depth and detuning of our lattice, the majority of photon scattering events returns the atoms to the original $(1, -1)$ Zeeman sublevel and does not contribute to K_1. The calculated loss rate for a $29E_R$ lattice is 0.17 s^{-1}, in good agreement with our measured K_1.

To determine the reduction of three-body recombination in 1D, we must compare K_3^{1D} to K_3^{3D}. A comparison in the same apparatus reduces the uncertainty due to our 15% systematic number uncertainty. (The effect of this systematic uncertainty is not eliminated entirely because the power law dependence of dN/dt on N is different in 1D and 3D.) We therefore repeat our experiments in a tight magnetic trap in the absence of a lattice, similar to Refs. [14,22]. (But see [26].) For the $(1, -1)$ state, we measure [27] $K_3^{3D} = 8.3(20) \times 10^{-30}$ cm^6 s^{-1} (see Fig. 2), which is in agreement with the value of $5.8(1.9) \times 10^{-30}$ cm^6 s^{-1} measured in [14].

Comparing our measurements, we find that the ratio of the three-body decay coefficients in 1D and 3D is 0.14(9). This represents a factor of 7 reduction in g_3^{1D} over g_3^{3D}, a clear signature of correlations.

For comparison of the observed reduction in g_3 with theory, we calculate γ at the center of each tube. From the experimentally determined density distribution we find at $t = 0$ that $\gamma > 0.34$, with 80% of the atoms having $0.34 < \gamma < 0.65$, and median value $\gamma_m = 0.45$. We do not expect correlations to vary significantly over this range of γ [12], so the assumption of using a single average K_3^{1D} in the model should be reasonable.
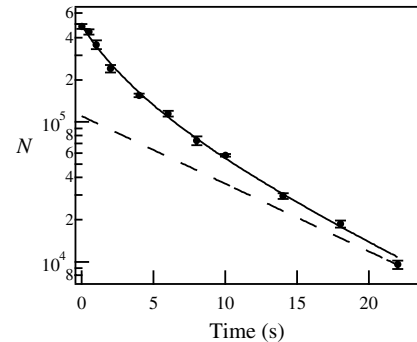

FIG. 2. Number as a function of time in the tight magnetic trap (no 2D lattice). The solid line is a fit to the decay [22], and the dashed line is an extrapolation of the asymptotic one-body loss.
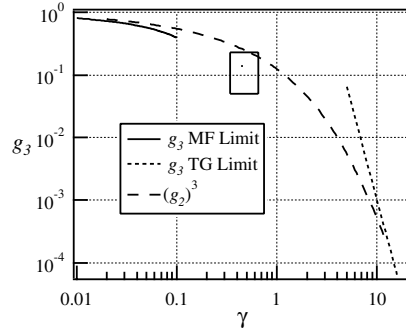
190401-3

FIG. 3.   Comparison of our results with theoretical calculations of the third-order correlation function g_3 vs γ. The solid and short-dashed lines represent the MF and TG limits of g_3 from [9], and the dashed line is an estimate [28] of $g_3 = (g_2)^3$, based on g_2 calculated in [12]. The measured suppression factor K_3^{1D}/K_3^{3D} is indicated by the box, where the height represents the measurement uncertainty and the width is the 0% to 80% range of γ for our system.

In Fig. 3 we compare the measured reduction in the three-body loss rate coefficient with theoretical estimates for g_3 in an interacting 1D gas at $T = 0$. Although there is currently no calculation of g_3, we plot the approximation $g_3 = (g_2)^3$, which is expected to be nearly exact in the MF regime and for $\gamma \gg 1$ exceeds the exact g_3 by a factor of 2 [28]. The value of g_2 used is that for a homogeneous system [12]. The value of g_2 is expected to be insensitive to T for $T \ll T_d \simeq \mathcal{N}_{max} \hbar \omega_z / k_B$ in this range of γ. From the measured values of $\mathcal{N}$ and ω_z we estimate the distribution of degeneracy temperatures, finding at $t = 0$ a peak value of ~ 13 kHz and a median value of ~ 9 kHz. While it is difficult to measure the temperature in our system, the measured size at $t = 0$ is consistent with zero-temperature TF theory and is certainly much less than $m \omega_z^2 R_z^2 / 2$, which during the first several seconds does not exceed ~ 6 kHz.

The reduction in K_3^{1D} relative to K_3^{3D} is a sensitive indicator of correlations and shows that we are beyond the mean-field regime, signifying the beginning of fermionization of bosons in 1D. Interestingly, collective oscillations in this parameter regime are well described by 1D mean-field theory, as verified by Ref. [15]. The fundamental effects of low dimensionality on the correlation properties of a quantum Bose gas are also of practical interest, given the interest in the physics of "atom lasers" loaded in waveguides. In addition, these experiments indicate that high density, strongly correlated 1D systems can be realized without fast decay due to three-body recombination.

*Permanent address: Laboratoire de Physique des Lasers (UMR 7538), Université Paris 13, Paris, France.
†Permanent address: Department of Physics, University of Maryland, College Park, MD 20742, USA.
[1] F. Dalfovo, S. Giorgini, L. P. Pitaevskii, and S. Stringari, Rev. Mod. Phys. **71**, 463 (1999).
[2] C. Orzel et al., Science **291**, 2386 (2001).
[3] M. Greiner et al., Nature (London) **415**, 39 (2002).
[4] J. L. Roberts et al., Phys. Rev. Lett. **86**, 4211 (2001).
[5] P. C. Hohenberg, Phys. Rev. **158**, 383 (1967); J. M. Kosterlitz and D. J. Thouless, J. Phys. C **6**, 1181 (1973).
[6] V. Bagnato and D. Kleppner, Phys. Rev. A **44**, 7439 (1991); W. Ketterle and N. J. van Druten, Phys. Rev. A **54**, 656 (1996).
[7] E. H. Lieb and W. Liniger, Phys. Rev. **130**, 1605 (1963); E. H. Lieb, ibid. **130**, 1616 (1963).
[8] M. Girardeau, J. Math. Phys. (N.Y.) **1**, 516 (1960); Phys. Rev. **139**, B500 (1965).
[9] D. M. Gangardt and G. V. Shlyapnikov, Phys. Rev. Lett. **90**, 010401 (2003).
[10] C. Menotti and S. Stringari, Phys. Rev. A **66**, 043610 (2002).
[11] V. Dunjko, V. Lorent, and M. Olshanii, Phys. Rev. Lett. **86**, 5413 (2001).
[12] K. V. Kheruntsyan, D. M. Gangardt, P. D. Drummond, and G. V. Shlyapnikov, Phys. Rev. Lett. **91**, 040403 (2003).
[13] E. G. M. van Kempen, S. J. J. M. F. Kokkelmans, D. J. Heinzen, and B. J. Verhaar, Phys. Rev. Lett. **88**, 093201 (2002).
[14] E. A. Burt et al., Phys. Rev. Lett. **79**, 337 (1997).
[15] H. Moritz, T. Stöferle, M. Köhl, and T. Esslinger, Phys. Rev. Lett. **91**, 250402 (2003).
[16] M. Olshanii, Phys. Rev. Lett. **81**, 938 (1998).
[17] E. L. Bolda, E. Tiesinga, and P. S. Julienne, Phys. Rev. A **68**, 032702 (2003).
[18] S. Peil et al., Phys. Rev. A **67**, 051603(R) (2003).
[19] We determine the lattice depth by observing the amplitude of diffraction orders following a brief application of the lattice to the BEC, as described in Yu. B. Ovchinnikov et al., Phys. Rev. Lett. **83**, 284 (1999).
[20] All uncertainties reported here are 1 standard deviation combined statistical and systematic uncertainties.
[21] P. Pedri and L. Santos, Phys. Rev. Lett. **91**, 110401 (2003).
[22] J. Söding et al., Appl. Phys. B **69**, 257 (1999).
[23] C. Williams (private communication).
[24] Even though correlations suppress three-body decay more than two-body decay, the upper limit for the two-body decay rate [14] is still negligible.
[25] Y. Castin and R. Dum, Phys. Rev. Lett. **77**, 5315 (1996).
[26] References [14,22] used $a_s = 5.45$ nm [E. Burt (private communication)] and 5.8 nm, respectively. Using the most recent $a_s = 5.313$ nm reduces their K_3 by 3% and 12%, respectively.
[27] We also measure the three-body rate for the $(2, 2)$ state, obtaining $K_3^{3D} = 1.5(3) \times 10^{-29}$ cm⁶/s, in agreement with the result $1.8(4) \times 10^{-29}$ cm⁶/s found in [22]. Our measurements in the $(2, 2)$ and $(1, -1)$ states yield a ratio of 1.8(6), confirming that K_3^{3D} is different for these states.
[28] G. V. Shlyapnikov (private communication).

Appendix B

Strongly Inhibited Transport of a Degenerate 1D Bose Gas in a Lattice

PHYSICAL REVIEW LETTERS

Strongly Inhibited Transport of a Degenerate 1D Bose Gas in a Lattice

C. D. Fertig,[1,2] K. M. O'Hara,[1,*] J. H. Huckans,[1,2] S. L. Rolston,[1,2] W. D. Phillips,[1,2] and J. V. Porto[1]

[1]*National Institute of Standards and Technology, Gaithersburg, Maryland 20899-8424, USA*
[2]*University of Maryland, College Park, Maryland 20742, USA*

We report the observation of strongly damped dipole oscillations of a quantum degenerate 1D atomic Bose gas in a combined harmonic and optical lattice potential. Damping is significant for very shallow axial lattices (0.25 photon recoil energies), and increases dramatically with increasing lattice depth, such that the gas becomes nearly immobile for times an order of magnitude longer than the single-particle tunneling time. Surprisingly, we see no broadening of the atomic quasimomentum distribution after damped motion. Recent theoretical work suggests that quantum fluctuations can strongly damp dipole oscillations of a 1D atomic Bose gas, providing a possible explanation for our observations.

The ability of highly degenerate quantum systems to sustain dissipationless flow is one of the most striking manifestations of quantum mechanics. However, transport in such systems can be dramatically modified by the presence of a relatively weak but rapidly spatially varying ("corrugated") potential along the transport axis. For example, the periodic potential of an optical lattice inhibits transport in a degenerate Fermi atomic gas [1–3], but not, in general, in a degenerate Bose gas [i.e., Bose-Einstein condensate (BEC)] [4,5]. However, under certain conditions, highly dissipative transport in a BEC in an optical lattice [6–8] can arise from nonlinear dynamical instabilities [9–11]. In low dimensional systems, of which 1D atomic gases [12–16] and superconducting nanowires [17] are important experimentally realized examples, a corrugated potential can cause dramatic changes in ground state and transport properties.

We study inhibited transport in a 1D Bose gas in the presence of an optical lattice along the 1D axis. In the absence of such a lattice, dipole oscillations are undamped [14], since it is a general result that the dipole mode of a harmonically confined gas is unaffected by two-body interactions (generalized Kohn's theorem) [18]. This result does not strictly hold for a combined harmonic and periodic potential; nevertheless, undamped oscillations have been observed in 3D BECs for small amplitudes and weak interactions [5,19].

In this Letter, we report a study of strongly damped dipole oscillations of a 1D Bose gas in a combined harmonic and periodic potential, under conditions for which undamped motion has been observed previously for 3D BECs. This striking difference between one dimension and three dimensions was recently reported qualitatively in Ref. [13]. Here we measure the damped motion as a function of axial lattice depth. Significant damping is induced by very shallow lattices, and in deeper lattices the motion is overdamped to the degree that the gas is nearly immobile for times an order of magnitude longer than the single-particle tunneling time. We emphasize, and discuss further below, that the inhibited transport is not due

to Bloch oscillations [4,20], where transport is frustrated by Bragg reflection at the Brillouin zone (BZ) boundary, as has been seen in previous experiments [1,2,7].

Our method to realize an ensemble of independent 1D Bose gases is similar to earlier work [12]. We produce a nearly pure ^{87}Rb condensate of $N = (0.8–1.6) \times 10^5$ atoms in the $|F = 1, m_F = -1\rangle$ state in a Ioffe-Pritchard magnetic trap ($\nu_x = \nu_z = 29$ Hz, $\nu_y = 8$ Hz). We next partition the BEC into an array of independent, vertical 1D "tubes" by adiabatically applying a transverse (in the xy plane) 2D confining lattice [12–16,21]. The confining lattice is ramped on during 200 ms to a depth of approximately $30E_R$ (where $E_R = h^2/2m\lambda^2$ is the photon recoil energy, and λ is the laser wavelength). The combined magnetic and optical potential results in approximately 5000 occupied tubes, each with an axial frequency of $\omega_0/2\pi \approx 60$ Hz. We observe a Thomas-Fermi density envelope in the combined magnetic and optical potential, and calculate [12] cloud radii of $r_x = 14(1)$ μm [22], $r_y = 20(1)$ μm, and $r_z = 10.6(5)$ μm for $N = 1.4 \times 10^5$. From this, we estimate a peak 1D density of $4.8(4) \times 10^4$ cm^{-1} in the central tube, and a peak 3D density of $4.7(4) \times 10^4$ cm^{-3}. Subsequently, we corrugate the tubes by adiabatically applying, over 20 ms, an axial (vertically along z) 1D lattice. The Rayleigh length of the axial lattice beams is large enough that they do not significantly modify the axial harmonic potential. All lattice beams derive from a single Ti:Sapphire laser operating at $\lambda = 810$ nm, far detuned from the atomic resonances at 780 and 795 nm. The pairs of lattice beams are detuned from each other by 6 MHz, making them effectively independent [23]. The final configuration consists of three independent standing waves, each formed from a pair of counterpropagating beams.

We excite dipole oscillations of the center of mass of the atoms in all the tubes by suddenly ($\lesssim 150$ μs) applying a linear magnetic field gradient, thus displacing the total harmonic trap (but not the lattice) axially by $z_0 \approx 3$ μm. This displacement is less than 30% of r_z and corresponds to approximately eight axial lattice sites [24]. The waists of the Gaussian transverse lattice beams

　　　120403-1　　　

202

($w_0 \approx 210 \; \mu$m) are much larger than both z_0 and the size of the trapped cloud.

The oscillation in the position of the atoms is too small for our imaging system to clearly resolve. We therefore observe oscillation in *velocity* by waiting a variable time t_w after the initial displacement, then suddenly turning off all trapping potentials (with time constants of $\approx 250 \; \mu$s and $\approx 150 \; \mu$s for the optical and magnetic potentials, respectively), and imaging the position z_{TOF} of the atoms after a time of flight (TOF) $t_{\mathrm{TOF}} = 18.4$ ms. The velocity of the atoms at t_w is found by simple kinematics, and is approximately given by $z_{\mathrm{TOF}}/t_{\mathrm{TOF}}$. The turn-off of the optical lattice is fast compared to the oscillation period, but slow enough to avoid diffraction of the atoms (i.e., adiabatic with respect to band excitations).

We observe damped dipole oscillations for axial lattice depths from $V = 0E_R$ to $2E_R$, as seen in Fig. 1. In the absence of an axial lattice, we observe oscillations (period $T = 15.4$ ms) consistent with no damping [Fig. 1(a)], indicating that tube-to-tube dephasing and trap anharmonicities are not significant on the time scale of our experiments. However, the oscillations are noticeably damped in a lattice only $0.25E_R$ deep. Such a shallow lattice modulates the atomic density by only 6%, and modifies the single-particle energy-quasimomentum dispersion relation $E(q)$ from that of a free particle around only the last few percent of the BZ. [We note here, and discuss further below, that the amplitude of motion is kept well within the quadratic part of $E(q)$ for shallow lattices.]

Beyond a lattice depth of $\approx 3E_R$ the motion is overdamped, and there are no oscillations. In this case, the atoms' velocity can be quite small, so we use a technique that maps the atoms' *position* in the trap to the cloud position after TOF. The experiment proceeds as before, except that after the trap is displaced by z_0, the atoms are allowed to relax toward their equilibrium position at $z = 0$ for a fixed time $t_w = 90$ ms. We then rapidly (with time

constant $\approx 250 \; \mu$s) turn off *only the axial lattice*. The remaining transverse lattice and magnetic potentials are left on for 3.75 ms (approximately a quarter period of undamped axial harmonic motion), then turned off simultaneously (as in the underdamped experiment). This converts the axial displacement $z(t_w)$ into a velocity, which we measure by TOF.

Figure 2(a) shows $z(t_w = 90$ ms$)$ as a function of axial lattice depth. For the shallowest lattices, this wait time is sufficient for the atoms to damp to the equilibrium position $z = 0$. For the deepest lattices, the motion is so overdamped that there is negligible motion during this time, and the position remains $z \approx z_0$. We note that, in the absence of damping, atoms would tunnel through the lattice to the equilibrium position in a time $(T/4)\sqrt{m^*/m}$, where m^* is the effective mass. This time is only 8 ms for noninteracting particles in a $10E_R$ lattice. A comparison can also be made to the tunneling time from the Mathieu function treatment of band structure, $4h/\Delta E = 15$ ms, where ΔE is the height of the band.

To quantify the damping, we model the motion as damped simple harmonic, $m^* \ddot{z} = -b\dot{z} - kz$, and extract a damping constant $b = b(V)$ for different axial lattice depths V. For underdamped motion, we simultaneously fit the oscillation data for eight depths to the expression
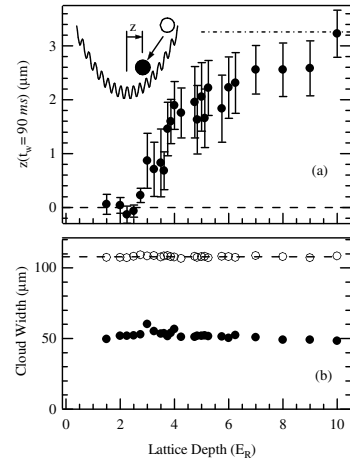
FIG. 2. Overdamped motion of a 1D Bose gas in an optical lattice. (a) Plot of the atoms' position 90 ms after shifting the trap, as a function of lattice depth. Inset depicts relaxation of the atoms toward equilibrium. Immediately after the trap is displaced to z_0, the atoms (open circle) begin to move toward equilibrium, reaching a displacement z from equilibrium after 90 ms (solid circle). Also shown is the initial position of the atoms (dash-dotted line). (b) The $1/e$ half-widths of Gaussian fits to axial TOF distributions (solid symbols), and the half-widths of square transverse TOF distributions (open symbols) resulting from a uniformly filled BZ (see text, and Fig. 4). Also shown (dashed line) is the BZ calculated from lattice parameters.
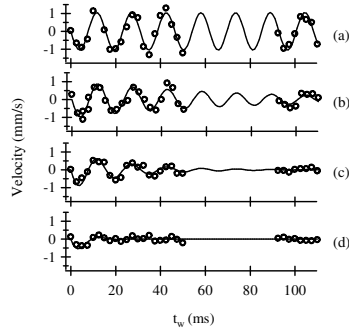

FIG. 1. Damped oscillations of a 1D Bose gas in an optical lattice. Shown are plots of velocity versus wait time t_w from $t_w = 0$ to 110 ms, and for axial lattice depths of (a) $0E_R$, (b) $0.25E_R$, (c) $0.50E_R$, and (d) $2.0E_R$, where E_R is the photon recoil energy (see text).

$$\dot{z}(t) = A \frac{k}{\omega m^*} e^{-bt/2m^*} \sin(\omega t),$$

where $\omega \equiv \sqrt{k/m^* - (b/2m^*)^2}$, and A and k are fit parameters common across all V. For overdamped motion, we determine $b = b(V)$ from the overdamped solution for $z(t_w)$, which in the limit of strong damping simplifies to

$$z(t_w) \approx z_0 \left(\frac{e^{-kt_w/b}}{1 - km^*/b^2} + \frac{e^{-bt_w/m^*}}{1 - b^2/km^*} \right),$$

where z_0 and k are inputs derived from measurements of undamped oscillations. In our analysis, we use a single-particle calculation of the effective mass m^* [26].

Figure 3 shows a plot of $b(V)/b_0$ versus lattice depth V, where $b_0 \equiv 2m\omega_0$ corresponds to critically damped harmonic motion for $\omega_0 \equiv \sqrt{k/m}$. We show data for both the underdamped and overdamped regimes, and note that the damping constant increases by at least a factor 1000 for a 30-fold increase in lattice depth.

The axial width of the cloud after TOF can provide information about the distribution of atomic quasimomenta in the lattice. The lattice turn-off time constant of 250 μs is long enough to avoid diffraction, but short enough to be nonadiabatic with respect to interwell tunneling and interactions. (Related experiments in 2D [21] and 3D [25] lattices support this conclusion.) In the absence of interactions, and neglecting the initial size of the cloud, the turn-off maps the single-particle quasimomentum distribution of atoms in the lattice to free-particle (i.e., plane-wave) momentum states that can be directly observed in TOF. In the presence of interactions, the mapping is complicated by mean-field repulsion during TOF. A variational calculation [27] indicates that mean-field repulsion is in fact the dominant contributor to the axial TOF width in our system. Therefore, the extracted TOF width greatly overestimates the width of a narrow initial quasimomentum distribution.
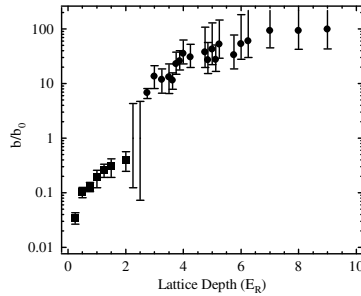

FIG. 3. Plot of the reduced damping constant b/b_0 for various depths V of the axial lattice, as determined using the underdamped (squares) and overdamped (circles) experimental techniques. Near critical damping ($V \approx 3E_R$), the analysis cannot distinguish between underdamped and overdamped motion, so only upper and lower bounds are shown at $V = 2.25$ and 2.50.

An example TOF image is shown in Fig. 4, together with cross-sectional profiles of the optical depth along the axial and transverse directions. The first BZ of the transverse lattice is uniformly filled, producing a uniform, square spatial distribution (in the xy plane) after TOF. Our imaging system views this square distribution along the diagonal in the xy plane, resulting in a triangular profile, from which we extract the width of the square [open symbols, Fig. 2(b)]. In the axial direction the distribution is narrower and reasonably well fit to a Gaussian, from which we extract the axial (along z) TOF $1/e$ half-width [solid symbols, Fig. 2(b)]. Even for the strongly overdamped data, the axial TOF width (which, we recall, overstates the width of narrow quasimomentum distributions) is much narrower than the BZ. This implies that the inhibition of transport is not due to effects related to Bloch oscillations of a filled BZ, as observed in Refs. [1,7]. Furthermore, we do not see a significant difference in TOF width between atoms that undergo damped harmonic motion and those that are unexcited but held for an equal time [28]. This is in stark contrast to earlier experiments on 3D BECs [6,8,11], where strong damping was accompanied by a pronounced broadening and fragmentation of the quasimomentum distribution.

Large amplitude dipole oscillations in a lattice can damp due to dynamical instabilities caused by particle interactions. For a 3D BEC moving in an optical lattice, such an instability point occurs at $q \gtrsim q_\pi/2$ ($q_\pi \equiv 2\pi/\lambda$ is the BZ boundary), where the dispersion relation has an inflection point, as predicted in [9,10] and observed in [6,8,11]. This effect is manifested as a large increase in the width of the quasimomentum distribution. Here, in contrast, we keep the maximum (single-particle) quasimomentum q_{max} of the oscillation small by limiting the initial energy of displacement $E(z_0) = m\omega_0^2 z_0^2/2$. For $V < 2E_R$, our choice of z_0 corresponds to $q_{max} \approx q_\pi/5$. For deeper lattices, our fixed z_0 corresponds to a larger q_{max}, but is always less than $q_\pi/2$ for $V < 9E_R$. (In a separate experiment, we excited oscillations in our system with twice the usual amplitude, and saw stronger damping that was ac-
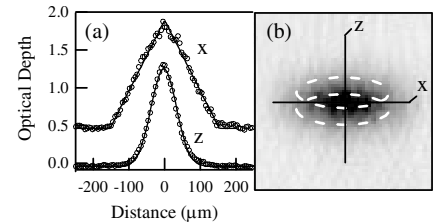

FIG. 4. Cross sections (a) of a TOF absorption image (b) of the expanded atom cloud. The plot of the transverse cross section (along x) is offset vertically by 0.5 units for clarity. The solid lines are Gaussian (triangular) fits to the axial (transverse) profiles, respectively. The dashed ovals in (b) indicate the peak-to-peak range of motion of undamped dipole oscillations.

companied by a broadening of the axial TOF width by nearly a factor of 2.)

For small amplitude dipole oscillations ($q_{max} \ll q_{\pi}/2$) of a 3D BEC in an optical lattice, the effect of the lattice is merely to increase the effective mass, leading to undamped motion at a lower frequency [5,19]. In the reduced dimensionality system of our 1D Bose gas, we have seen that the optical lattice has a qualitatively different effect. To highlight the difference between these two situations, we excited dipole oscillations in a 3D BEC (i.e., *no transverse confining lattice*) in a $4E_R$ axial lattice, and saw no damping. This is in contrast to the results of the same experiment in a 1D Bose gas (i.e., *with a transverse confining lattice*), shown in Fig. 3, where $b(V = 4E_R)/b_0 \approx 50$ corresponds to extremely overdamped motion.

After we performed these experiments, theoretical treatments appeared which suggested that zero-temperature quantum fluctuations can lead to substantial damping of transport in a 1D atomic Bose gas [29,30]. Our observations, including the significant damping in lattices too shallow to support a Mott-insulator phase [31], can be explained by the mechanisms of Refs. [29,30], but appear to be inconsistent with a mechanism involving incompressibility [13].

It is possible that there is a temperature dependence to the damping; unfortunately, we can derive little information on temperature from the TOF widths. Future experiments to investigate the temperature dependence could shed light on the relative importance of quantum and thermal fluctuations to dissipation, a question of interest in, for example, the development of ultrathin superconducting wires [17]. We also look forward to testing other explicit predictions of these theories, such as the dependence of damping on displacement and dimensionality. We note that the periodic potential of an optical lattice is free from defects, and that 1D atomic Bose gases are well isolated from the environment, yielding a relatively clean system in which to compare experiment with theory. The ability to continuously and dynamically vary the confining potentials makes optical lattice experiments attractive for future studies of superfluidity in low dimensional quantum systems.

*Current address: Department of Physics, Pennsylvania State University, University Park, PA 16802, USA.

[1] G. Modugno *et al.*, Phys. Rev. A **68**, 011601(R) (2003).
[2] L. Pezzè *et al.*, Phys. Rev. Lett. **93**, 120401 (2004).
[3] H. Ott *et al.*, Phys. Rev. Lett. **92**, 160601 (2004).
[4] O. Morsch *et al.*, Phys. Rev. Lett. **87**, 140402 (2001).
[5] F. S. Cataliotti *et al.*, Science **293**, 843 (2001).
[6] S. Burger *et al.*, Phys. Rev. Lett. **86**, 4447 (2001); B. Wu and Q. Niu, Phys. Rev. Lett. **89**, 088901 (2002); S. Burger *et al.*, *ibid.* **89**, 088902 (2002).
[7] F. Ferlaino *et al.*, Phys. Rev. A **66**, 011604(R) (2002).
[8] F. S. Cataliotti *et al.*, New J. Phys. **5**, 71 (2003).
[9] B. Wu and Q. Niu, Phys. Rev. A **64**, 061603 (2001).
[10] A. Smerzi, A. Trombettoni, P. G. Kevrekidis, and A. R. Bishop, Phys. Rev. Lett. **89**, 170402 (2002).
[11] L. Fallani *et al.*, Phys. Rev. Lett. **93**, 140406 (2004).
[12] B. L. Tolra *et al.*, Phys. Rev. Lett. **92**, 190401 (2004).
[13] T. Stöferle *et al.*, Phys. Rev. Lett. **92**, 130403 (2004).
[14] H. Moritz, T. Stöferle, M. Köhl, and T. Esslinger, Phys. Rev. Lett. **91**, 250402 (2003).
[15] B. Parades *et al.*, Nature (London) **429**, 277 (2004).
[16] T. Kinoshita, T. Wenger, and D. S. Weiss, Science **305**, 1125 (2004).
[17] A. Bezryadin, C. N. Lau, and M. Tinkham, Nature (London) **404**, 971 (2000).
[18] F. Dalfovo, S. Giorgini, L. Pitaevskii, and S. Stringari, Rev. Mod. Phys. **71**, 463 (1999).
[19] M. Krämer, L. Pitaevskii, and S. Stringari, Phys. Rev. Lett. **88**, 180404 (2002).
[20] M. BenDahan *et al.*, Phys. Rev. Lett. **76**, 4508 (1996).
[21] M. Greiner *et al.*, Phys. Rev. Lett. **87**, 160405 (2001).
[22] Error bars here and everywhere else represent the uncorrelated combination of 1 standard deviation statistical and systematic uncertainties (if any).
[23] S. L. Winoto, M. T. DePue, N. E. Bramall, and D. S. Weiss, Phys. Rev. A **59**, R19 (1999).
[24] For all lattice depths, the maximum site-to-site potential difference of 40 Hz is much less than both the on-site interaction energy and the tunneling energy, so that the transport studied in this work is fundamentally different from the excitations due to potential gradients reported in Ref. [25].
[25] M. Greiner *et al.*, Nature (London) **415**, 39 (2002).
[26] For overdamped motion, the extracted damping constants b depend very weakly on m^*/m. For underdamped motion, the shallowness of the axial lattice means corrections to m^* due to interactions should be small. Therefore we expect all extracted damping constants b to be insensitive to corrections to m^* due to interactions.
[27] A. M. Rey (private communication).
[28] During the ~ 100 ms in which we observe the cloud's motion, we observe a small growth in the width of the TOF image, at a rate that is independent of excitation or damping, consistent with heating due to spontaneous scattering of lattice photons.
[29] A. Polkovnikov and D.-W. Wang, Phys. Rev. Lett. **93**, 070401 (2004).
[30] J. Gea-Banacloche *et al.*, cond-mat/0410677.
[31] C. Kollath, U. Schollwöck, J. von Delft, and W. Zwerger, Phys. Rev. A **69**, 031601(R) (2004).

Appendix C

Collisional De-excitation in a Quasi-2D Degenerate Bose Gas

Collisional deexcitation in a quasi-two-dimensional degenerate bosonic gas

I. B. Spielman,[1,*] P. R. Johnson,[1] J. H. Huckans,[1,2] C. D. Fertig,[1,2,†] S. L. Rolston,[1,2] W. D. Phillips,[1,2] and J. V. Porto[1]

[1]*National Institute of Standards and Technology, Gaithersburg, Maryland 20899, USA*
[2]*University of Maryland, College Park, Maryland 20742, USA*
(Received 3 September 2005; published 15 February 2006)

We separate a Bose-Einstein condensate into an array of two-dimensional (2D) sheets and excite quantized vibrational motion in the direction normal to the sheets. The measured collisional decay rates are suppressed due to the reduced dimensionality, a matter wave analog to inhibited spontaneous emission. After decay, the large excitation energy is transferred to back-to-back outgoing atoms, imaged as rings in the 2D plane. The ring diameters correspond to vibrational energy level differences, and edge-on imaging allows identification of the final vibrational states.

Most quasi-2D quantum systems have been realized with electrons in semiconductors, where a 1D potential confines the electrons to the lowest quantized vibrational states in one direction, i.e., the energies in the 2D plane are much smaller than the vibrational level spacing. Recently it has become possible to confine degenerate atomic Bose gases to 2D [1,2] and investigate vibrational excitations in the tightly confined direction [3]. Trapped 2D atomic gases provide experimental opportunities unavailable in electron systems. For example, unlike semiconductors, the atomic system is nearly defect-free. Further, the dynamic control of the confining potential, coupled with an ability to image the atoms, enables the direct detection of the excited-state population and the momentum distribution. Quantized vibrational states are an ingredient in proposals to realize exotic states of matter, such as striped or super-solid phases [4–6], and are possible motional qubit states for quantum computation [7–9]. Stronger confinement (beyond that described herein) can also change the nature of collisions [10–12].

Here we study the vibrational relaxation of a quasi-2D Bose-Einstein condensate (BEC), where quantized motion in the tightly confined direction plays a role analogous to an internal degree of freedom. We transfer a large fraction of atoms into excited vibrational states, creating highly non-equilibrium atom populations. In this system, atom-atom collisions provide the only significant relaxation mechanism, transferring "internal" energy to 2D kinetic energy. We directly observe atom populations as outgoing rings (Fig. 1) representing distinct decay channels. The excited-state lifetimes are enhanced due to the reduction in the density of final scattering states, relative to scattering into a 3D continuum—analogous to suppressed spontaneous emission in a planar cavity [13]. Scattering in unconfined geometries has been studied, for example, in the context of cold coherent collisions between 3D BECs [14,15].

We create independent 2D sheets (or pancakes) of atoms by applying a deep 1D optical lattice to a 3D BEC. In the tight direction ($\hat{z}$) the system is well-described by a single-

particle 1D Schrödinger equation, yielding discrete vibrational levels labeled by an index n. Atoms, Raman-excited from the ground state $n=0$ to $n=1$ or 2, collide and decay. By imaging after a time of flight t_{TOF}, we identify the momentum and population of atoms in the various final vibrational states. We extract excited-state lifetimes from time sequences of these single-shot vibrational spectra.

We produce a magnetically trapped ^{87}Rb BEC with up to 2.5×10^5 atoms in the $|F=1, m_F=-1\rangle$ state [16]. The BEC is separated into a stack of about 80 pancakes by
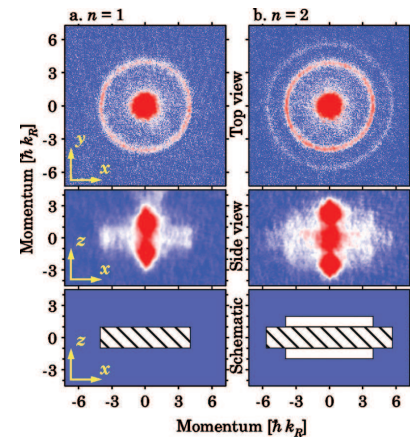
FIG. 1. (Color) Absorption images of vibrationally excited atoms after a 1 ms decay and subsequent TOF, with 60% initial population in the (a) $n=1$ and (b) $n=2$ vibrational levels. In the top views, outgoing rings ($t_{TOF}=7.1$ ms) correspond to different in-plane energies imparted to the atoms from various decay channels. Viewed from the side ($t_{TOF}=13.1$ ms) the vertical momentum distribution identifies the vibrational states. Here, the rings appear as rectangles, and the schematic of the side view shows the expected distributions from the dominant decay processes to $n=1$ (white rectangles) and $n=0$ (hatched rectangles). The uncollided fraction in the center of the image (not shown in the schematic) is distributed vertically in accordance with the remaining excited fraction.

*Electronic address: ian.spielman@nist.gov
†Present address: University of Georgia, Athens, GA 30602.

       020702-1

an optical lattice with period $d=410(1)$ nm [22] vertically aligned along $\hat{z}$ [23]. When in the ground vibrational state, the largest pancake has $N \approx 4.6(10) \times 10^3$ atoms with a chemical potential $\mu=1.6(2)$ kHz; the resulting peak 2D and 3D densities are $2.2(2) \times 10^9$ cm^{-2} and $2.9(3) \times 10^{14}$ cm^{-3}, respectively. The 2D Thomas-Fermi radii are $R_x=11.0(6)$ μm and $R_y=12.0(7)$ μm. In the combined magnetic and optical potential, the in-plane oscillation frequencies are $\omega_x/2\pi=55(1)$ Hz and $\omega_y/2\pi=50(1)$ Hz. The lattice is raised continuously from zero in 200 ms with an exponentially increasing ramp (50 ms time constant). This time scale is chosen to be adiabatic with respect to mean-field interactions and vibrational excitations. By pulsing the lattice and observing the resulting atom diffraction [17], we measure a lattice depth of $s=77(4)$, expressed in units of $E_R=h^2/8md^2=h \times 3.42(2)$ kHz. For a single well of the deep sinusoidal potential, the energy spacings are $E_{n+1}-E_n \simeq E_R[2\sqrt{s}-(n+1)]$ (these energies, which include the lowest-order anharmonic correction, are shifted at the 1% level by the interatomic interaction). The harmonic frequency is $\omega_z/2\pi=2E_R\sqrt{s}/h=60(1)$ kHz.

Raman transitions between vibrational levels [18] are driven by a pair of laser beams. The nearly counterpropagating Raman beams are oriented approximately along $\hat{z}$ [24], are detuned 82 GHz below the ^{87}Rb $D2$ transition, and have a relative detuning δ ranging from 50 to 120 kHz. A 1 ms Raman pulse excites a fraction f_n of the atom population to either $n=1$ or 2.

The anharmonicity of the potential allows us to selectively transfer populations between desired vibrational levels, provided the pulse duration t_p is long enough that its Fourier spread resolves the $\gtrsim E_R/h$ difference from unwanted transitions. t_p must also be shorter than the vibrational lifetime τ. For our experiment (where $\tau \gtrsim t_p \gtrsim \hbar/E_R$), we find that by detuning below Raman resonance and chirping 15 kHz through resonance in 1 ms, we controllably transfer up to 65% of the atoms to either $n=1$ or 2 (simulations indicate a maximum transfer of around 75% in this situation) with only ~5% population in unwanted states [25].

The vibrationally excited atoms are allowed to decay for variable hold times t_{hold} ranging from 10 μs to 10 ms; then the lattice is turned off in 200 μs. The magnetic trap is then turned off in ≈ 300 μs, and the atom cloud expands for t_{TOF} before absorption imaging. The resulting atomic distribution, which constitutes an average over the ~80 pancakes, is imaged along one of two axes: perpendicular to the pancakes (top view, along $\hat{z}$) and edge-on (side view, along $\hat{y}$).

The decay of a pair of atoms from initial vibrational states a and b to final states c and d (denoted $ab \rightarrow cd$) can be viewed as a 2D two-body inelastic collision process, where vibrational states in the confined direction play the role of internal states. The release of vibrational energy leads to back-to-back atom pairs with large momenta in the 2D plane. Figure 1 shows example TOF images from which we can infer the final momentum distribution. Image coordinates are in units of recoil momentum, $\hbar k_R=\pi\hbar/d$ [26], and the corresponding recoil velocity is $\hbar k_R/m=5.6$ mm/s. Each image pair [Figs. 1(a) and 1(b)] contains nearly full spectral information of an excited state and its decay paths.

TABLE I. Release energies (including the lowest-order anharmonic corrections) and matrix elements for the experimentally relevant decay paths and lattice depth $s=77$ (sorted in order of increasing decay energy). The energies denote the per atom difference between initial and final vibrational energies.

Ring	Decay path	E_f-E_i	I_{cd}^{ab}
Central ring	$11 \rightarrow 20$	$E_R/2$	0.0243
	$22 \rightarrow 31$	$E_R/2$	0.0257
	$22 \rightarrow 40$	$2E_R$	0.0007
Inner ring	$11 \rightarrow 00$	$\hbar\omega_z-E_R$	0.2202
	$22 \rightarrow 11$	$\hbar\omega_z-2E_R$	0.1556
	$22 \rightarrow 20$	$\hbar\omega_z-3E_R/2$	0.0020
	$20 \rightarrow 00$	$\hbar\omega_z-3E_R/2$	0.1128
Outer ring	$22 \rightarrow 00$	$2\hbar\omega_z-3E_R$	0.1075

The decay paths allowed by parity and conservation of energy are shown in Table I. For atoms excited to $n=1$, only two decay paths contribute. The high-energy process, $11 \rightarrow 00$, gives rise to the ring in Fig. 1(a) (top view), while the ring from the low-energy $11 \rightarrow 20$ process is not resolved from the central cloud. Each ring's radius corresponds to the atomic in-plane velocity and hence the per atom difference between initial and final vibrational energies. In Fig. 1(b), atoms excited to $n=2$ decay through several channels. The processes $22 \rightarrow 11$, $20 \rightarrow 00$, and $22 \rightarrow 20$ all contribute to the inner ring of Fig. 1(b), each with an energy of about $2E_R\sqrt{s}$ per atom. The outer ring results solely from the $22 \rightarrow 00$ decay process.

Figures 2(a) and 2(b) show the radial density of the atomic cloud after an angular integration of the data in Figs. 1(a) and 1(b), respectively. We extract the vibrational energy spacings by fitting the data to Lorentzians. We attribute the atom background between the peaks to secondary scattering involving outgoing atoms and include it in the fits as a linearly sloping baseline. The measured energies agree with
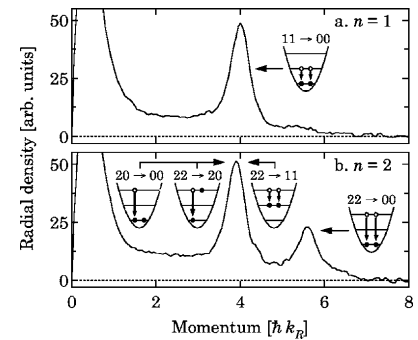

FIG. 2. Angular integrals of top view data. (a) From Fig. 1(a), the single ring gives rise to a peak located at $k=4.0(1)$ k_R. (b) The two rings in Fig. 1(b) yield two peaks at $k=3.9(1)k_R$ and $5.6(2)k_R$. The diagrams schematically illustrate the decay channels which contribute to each peak.

those expected from the known lattice depth, within our 4% experimental uncertainty. The branching ratio between the inner and outer rings estimated from Fig. 2 (ignoring the atom background) is 2.1(3). The value calculated from the matrix elements in Table I is 2.9(3) for an excited fraction $f_2 = 0.60(5)$.

The side view images in Figs. 1(a) and 1(b) complement the top view images by identifying the final vibrational states. The 200 μs lattice turn-off is adiabatic with respect to the 55 kHz vibrational frequency. As a result, the turn-off procedure maps quasimomentum states in the 1D lattice to the corresponding free-particle momentum states [19,20]. For example, atoms in the $n=1$ vibrational state reside in the second Brillouin zone (BZ), and are mapped to a continuum of momentum states k_z where $k_R < |k_z| < 2k_R$ [27].

Figure 1(a) shows atoms which were initially excited into $n=1$. In the side view, the atom cloud's extent along $\hat{z}$ reflects the mapping of quasimomentum to momentum, and the extent in the horizontal direction reflects the final in-plane momentum. The ring in the top view appears as a rectangle in the side view [schematically illustrated by the hatched rectangle in Fig. 1(a)]. The dense, vertically aligned double-lobed structure at the center of the side view image is largely due to atoms which have not decayed and remain in the $n=1$ state (second BZ). Figure 1(b) depicts atoms initially in $n=2$. The process $22 \rightarrow 00$ gives rise to atoms in the first BZ [hatched rectangle in Fig. 1(b)], while $22 \rightarrow 11$ leads to atoms in the second BZ [white rectangles in Fig. 1(b)]. Note that the vertical central structure is taller since it contains atoms remaining in $n=2$ (third BZ).

We calculate short-time two-body branching ratios and decay rates in a single pancake using Fermi's golden rule. Due to the extreme anisotropy of our potential, the initial condensate wave functions can be approximated as a product of single-particle wave functions, $\Psi_i(x,y,z) \approx \psi(x,y)\varphi_{n_i}(z)$. Here $\psi(x,y)$ satisfies an effective 2D Gross-Pitaevskii equation [10] for $n=0$ atoms in the Thomas-Fermi limit; we assume $\psi(x,y)$ remains unchanged during the short duration of the experiment. The $\varphi_{n_i}(z)$ solve the Schrödinger equation for the 1D lattice potential and are nearly harmonic-oscillator wave functions with an extent $\sigma_z = \sqrt{\hbar/m\omega_z}$. The final states $\Psi_f(x,y,z) = \exp[-i(k_x x + k_y y)]\varphi_{n_f}(z)$ are free particles in x and y, which is justified since $\omega_z \gg \omega_{x,y}$. The rate for the scattering process $ab \rightarrow cd$ is $\Gamma_{cd}^{ab} N_a N_b$, with atom populations N_a and N_b, and

$$\Gamma_{cd}^{ab} = 2\pi a_s^2 \omega_z I_{cd}^{ab} \int dx dy |\psi(x,y)|^4, \tag{1}$$

where $I_{cd}^{ab} = 2\pi |\sigma_z \int dz \varphi_a(z)\varphi_b(z)\varphi_c(z)\varphi_d(z)|^2$ is dimensionless (see Table I), and $a_s = 5.3$ nm is the s-wave scattering length [21,28]. Parity considerations make $I_{cd}^{ab} = 0$ when $a+b+c+d$ is odd. The total rate is a sum over energetically allowed final states c and d.

For atoms excited to $n=1$, the excited fraction $f_1(t)$ is governed by $\dot{f}_1 = -2N[\Gamma_{00}^{11} + 2\Gamma_{20}^{11}]f_1^2$. Parity considerations forbid the transition $10 \rightarrow 00$ but not $20 \rightarrow 00$, so as $f_1 \rightarrow 0$ the $n=1$ decay rate per atom $\dot{f}_1/f_1 \rightarrow 0$, but as $f_2 \rightarrow 0$ the corre-
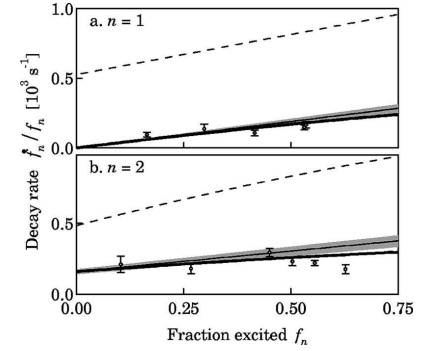

FIG. 3. Initial decay rates. (a) Initial population in $n=1$. (b) Initial population in $n=2$. The thin lines represent the result of our model with no adjustable parameters, integrated over the distribution of pancakes expected from Thomas-Fermi approximation. The gray regions reflect the variation in this model due to experimental number uncertainty. The thick solid lines include the estimated effect of secondary scattering, using a 75% probability of a second event, and the long-dashed lines are the expected decay rate in the absence of 2D confinement.

sponding $n=2$ rate is nonzero. For atoms excited to $n=2$, a pair of coupled equations describe the evolution of $f_2(t)$ and $f_0(t)$.

The excited-state population as a function of t_{hold} is found from a series of side-view images like those in Fig. 1. Integrating over x gives the atomic distribution along $\hat{z}$. To extract populations, we fit the data to a distribution, flat within each BZ, convolved with a Gaussian. The width of the Gaussian is fixed by applying this model to data in which only the ground state (first BZ) was occupied. Repeating the fitting process for different t_{hold} yields the fractional population as a function of time. We extract rates by fitting the first 2 ms to the expected solutions $f_1(t)$ and $f_2(t)$ [29].

The resulting rates per atom at $t=0$ are shown in Fig. 3. For comparison we plot the predicted rates at $t=0$ (thin solid line), where the gray band reflects the experimental atom number uncertainty. The agreement, with no free parameters, is good even though we neglected corrections from secondary collisions. The presence of atoms not on the rings (Figs. 1 and 2) indicates that around 75% atoms rescatter, consistent with our theoretical estimates. These processes decrease the atomic density, and hence reduce the overall decay rate at late times. (In separate experiments with lower density thermal samples, we indeed observe significantly lower rates: below 40 s^{-1}.) The effect should be more significant for large initial excited fractions, a trend consistent with the data. The thick solid lines in Fig. 3 show the estimated effect of secondary scattering from outgoing atoms which decayed during the 1 ms Raman pulse. This lowest-order estimate assumes that each decayed atom can rescatter at most once, and if it does scatter, its secondary-collision partner does not itself rescatter. We suspect that the neglected higher-order collision processes are in part responsible for the excess suppression in Fig. 3(b) for $f > 0.5$.

The reduced dimensionality suppresses the total scattering rate in a manner similar to the suppression of spontaneous emission in a planar cavity [13]. A comparison between confined and unconfined decay can be made by considering a situation where the final states of the atomic scattering are unconstrained. For confined final states, the total deexcitation rate Γ_{2D} is given by a discrete sum over energetically allowed final vibrational states, times the (energy-independent) 2D density of in-plane states. For unconfined final states, the total deexcitation rate Γ_{3D} is proportional to the 3D density of final states, which increases as the square root of the scattering energy. Note that, unlike the case of spontaneous emission in a planar cavity, the initial states and energies here are determined by the confining potential, so Γ_{3D} must include the zero-point energies $\hbar\omega_z/2$ of each atom. Figure 3 shows Γ_{3D} (long dashes). For a 100% excited fraction of $n=2$ atoms, $\Gamma_{3D}/\Gamma_{2D} \approx 2.4$, and for $n=1$ atoms, $\Gamma_{3D}/\Gamma_{2D} \approx 2.9$. In the absence of 2D confinement, the parity restriction which suppressed the decay of $n=1$ atoms as $f \rightarrow 0$ is lifted, so in this case Γ_{3D}/Γ_{2D} diverges [as seen in Fig. 3(a)].

In conclusion, we measured a confinement-induced suppression of the transition rates between different vibrational states in a deep 1D optical lattice using a new, single-shot, spectrographic technique. Additional suppression of the rates would be achieved by further modifying the final density of states [6], for example by confining the atoms into 1D tubes [16], or in analogy with photonic band-gap materials, by applying an additional in-plane lattice to open suitably placed band gaps. The long lifetimes are expected to be useful in the context of producing correlated atomic systems.

[1] A. Görlitz *et al.*, Phys. Rev. Lett. **87**, 130402 (2001).

[2] C. Orzel *et al.*, Science **291**, 2386 (2001).

[3] J. H. Denschlag *et al.*, J. Phys. B **35**, 3095 (2002).

[4] G. Schmid and M. Troyer, Phys. Rev. Lett. **93**, 067003 (2004).

[5] V. W. Scarola and S. D. Sarma, e-print cond-mat/0503378.

[6] A. Isacsson and S. M. Girvin, e-print cond-mat/0506622.

[7] E. Charron, E. Tiesinga, F. Mies, and C. Williams, Phys. Rev. Lett. **88**, 077901 (2002).

[8] K. Eckert *et al.*, Phys. Rev. A **66**, 042317 (2002).

[9] J. V. Porto *et al.*, Philos. Trans. R. Soc. London, Ser. A **361**, 1417 (2003).

[10] D. S. Petrov and G. V. Shlyapnikov, Phys. Rev. A **64**, 012706 (2001).

[11] M. Olshanii, Phys. Rev. Lett. **81**, 938 (1998).

[12] I. Bouchoule, M. Morinaga, C. Salomon, and D. S. Petrov, Phys. Rev. A **65**, 033402 (2002).

[13] R. G. Hulet, E. S. Hilfer, and D. Kleppner, Phys. Rev. Lett. **55**, 2137 (1985).

[14] N. R. Thomas, N. Kjærgaard, P. S. Julienne, and A. C. Wilson, Phys. Rev. Lett. **93**, 173201 (2004).

[15] Ch. Buggle, J. Léonard, W. von Klitzing, and J. T. M. Walraven, Phys. Rev. Lett. **93**, 173202 (2004).

[16] B. L. Tolra *et al.*, Phys. Rev. Lett. **92**, 190401 (2004).

[17] Y. B. Ovchinnikov *et al.*, Phys. Rev. Lett. **83**, 284 (1998).

[18] H. Perrin, A. Kuhn, I. Bouchoule, and C. Salomon, Europhys. Lett. **42**, 395 (1998).

[19] A. Kastberg *et al.*, Phys. Rev. Lett. **74**, 1542 (1995).

[20] H. Stecher *et al.*, Phys. Rev. A **55**, 545 (1997).

[21] E. G. M. van Kempen, S. J. J. M. F. Kokkelmans, D. J. Heinzen, and B. J. Verhaar, Phys. Rev. Lett. **88**, 093201 (2002).

[22] All uncertainties herein reflect the uncorrelated combination of single-sigma statistical and systematic uncertainties. Shot-to-shot fluctuations are the largest source of uncertainty in lattice depth and atom number.

[23] The nearly counterpropagating lattice beams are generated by a Ti:sapphire laser tuned to $\lambda = 809.5$ nm, intersecting at $\theta = 162(1)°$.

[24] The Raman beams have a $1/e^2$ radius $w_0 = 1.2$ mm and are canted from $\hat{z}$, leading to a small momentum kick of $0.06k_R$ in the 2D plane.

[25] The Raman chirp is essentially an adiabatic rapid passage. Since the anharmonicity makes the energy spacing $E_{n+1} - E_n$ between consecutive levels decrease as n increases, a downgoing chirp is successively resonant with higher transitions, exciting undesired vibrational levels. This is avoided by chirping from below.

[26] After TOF, the atom distribution maps final position to initial momentum. The TOF used in the computation of momentum is increased by 0.5 ms, accounting for the 1 ms window during which the atoms decay.

[27] The 200 ms turn-on procedure is adiabatic with respect to all time scales except inter pancake tunneling. Such a system fills the relevant BZ due to the fact that the essentially random phases develop in different pancakes via spatial variations in mean-field shifts and trapping potentials.

[28] The 3D scattering is largely unaffected by confinement since $a_s = 5.3$ nm is much smaller than $\sigma_z \approx 44$ nm [10].

[29] Our model assumes that decayed atoms leave the system forever; in reality the experiment was performed in a ~ 50 Hz harmonic trap. To assure the validity of our assumptions, we confined our analysis to times much shorter than the trap's 5 ms quarter-period—generally 2 ms. To achieve better signal to noise, we fit the first 5 ms for the $n=1$, $f_1 \approx 0.2$ data point.

BIBLIOGRAPHY

[1] M. H. Anderson, J. R. Ensher, M. R. Matthews, C. E. Weiman, E. A. Cornell, Science **269**, 198 (1995).

[2] O. Penrose and L. Onsager, Phys. Rev. Lett. **104**, 576 (1956).

[3] V. Bagnato, D. E. Pritchard, and D. Kleppner, Phys. Rev. A **35**, 4354 (1987).

[4] V. Bagnato and D. Kleppner, Phys. Rev. A **44**, 7439 (1991).

[5] G. V. Shlyapnikov, C. R. Acad. Sci. Paris, t.2, Serie IV, 407 (2001).

[6] E. H. Lieb and W. Liniger, Phys. Rev. **130**, 1605 (1963).

[7] E. H. Lieb and W. Liniger, Phys. Rev. **130**, 1616 (1963).

[8] M. Girardeau, J. Math. Phys. (NY) **1**, 516 (1960).

[9] M. Girardeau, Phys. Rev. **139**, B500 (1965).

[10] K. V. Kheruntsyan, D. M. Gangardt, P. D. Drummond, and G. V. Shylapnikov, Phys. Rev. Lett. **91**, 040403 (2003).

[11] G. V. Shylapnikov (private communication).

[12] J. W. Kane and L. P. Kadanoff, Phys Rev. **155**, 80 (1967).

[13] J. W. Kane and L. P. Kadanoff, J. Math. Phys. **6**, 1902 (1965).

[14] V. L. Berezinskii, Sov. Phys. JETP **32**, 493 (1971).

[15] V. L. Berezinskii, Sov. Phys. JETP **34**, 610 (1972).

[16] J. M. Kosterlitz and D. J. Thouless, J. Phys. C. **6**, 1181 (1973).

[17] J. M. Kosterlitz, J. Phys. C. **7**, 1046 (1974).

[18] A. Einstein, Sitzungsber Kgl. Preuss. Akad. Wiss. **1924**, 261 (1924).

[19] A. Einstein, Berl. Ber. **22**, 261 (1924).

[20] A. Einstein, Berl. Ber. **23**, 3 (1925).

[21] A. Einstein, Berl. Ber. **23**, 18 (1925).

[22] S. N. Bose, Z. Phys. **26**, 178 (1924).

[23] F. Dalfovo, S. Giorgini, L. P. Pitaevskii, and S. Stringari, Rev Mod. Phys. **71**, 463 (1999).

[24] A. Leggett, Rev. Mod. Phys. **73**, 307 (2001).

[25] See, for example, H. J. Metcalf and P. van der Straten, *Laser Cooling and Trapping* (Springer, 1999).

[26] Even though the cooling transition is on the $F = 2 \rightarrow F' = 3$ (stretched state) cycling transition, off-resonant transitions to $F' = 2$ can occur which can lead to decay to $F = 1$, thus requiring repumping.

[27] J. Dalibard and C. Cohen-Tannoudji, J. Opt. Soc. Am. B **6**, 2025 (1989).

[28] A. Aspect, E. Arimondo, R. Kaiser, N. Vansteenkiste, and C. Cohen-Tannoudji, JOSA B **6**, 2112 (1989).

[29] M. Kasevich and S. Chu, Phys. Rev. Lett **69**, 1741 (1992).

[30] E. L. Raab, M. Prentiss, A. Cable, S. Chu, and D. E. Pritchard, Phys. Rev. Lett. **59**, 2631 (1987).

[31] See, for example, K. Huang, *Statistical Mechanics* (John Wiley & Sons, 1987).

[32] C. Salomon, J. Dalibard, A. Aspect, H. Metcalf, C. Cohen-Tannoudji, Phys. Rev. Lett. **59**, 1659 (1987).

[33] M. Ben Dahan, E. Peik, J. Reichel, Y. Castin, and C. Salomon, Phys. Rev. Lett. **76**, 4508 (1996).

[34] Y. Castin and R. Dum, Phys. Rev. Lett, **77**, 5315 (1996).

[35] P. Cladé, Doctoral Thesis, Laboratoire Kastler Brossel, Conservatoire National des Arts et Metiers,(2005), http://tel.ccsd.cnrs.fr/tel-00010730.

[36] S. R. Wilkinson, C. F. Bharucha, K. W. Madison, Q. Niu, and M. G. Raizen, Phys. Rev. Lett. **76**, 4512 (1996).

[37] R. Grimm and M. Weidemüller, Y. B. Ovchinnikov, Adv. At. Mol. Opt. Phys. **42**, 95 (2000).

[38] S. Chu, L. Hollberg, J. E. Bjorkholm, A. Cable, and A. Ashkin, Phys. Rev. Lett. **55**, 48 (1985).

[39] V. S. Letokhov, JETP **7**, 272 (1968).

[40] C. I. Westbrook, R. N. Watts, C. E. Tanner, S. L. Rolston, W. D. Phillips, and P. D. Lett, P. L. Gould, Phys. Rev. Lett. **65**, 33 (1990).

[41] P. Verkerk, B. Lounis, C. Salomon, and C. Cohen-Tannoudji, J. -Y. Courtois and G. Grynberg, Phys. Rev. Lett. **68**, 3861 (1992).

[42] P. S. Jessen, C. Gerz, P. D. Lett, W. D. Phillips, S. L. Rolston, R. J. C. Spreeuw, and C. I. Westbrook, Phys. Rev. Lett. **69**, 49 (1992).

[43] A. Hemmerich and T. W. Hänsch, Phys. Rev. Lett. **70**, 410 (1993).

[44] A. Günther, S. Kraft, C. Zimmermann, and J. Fortagh, arxiv:cond-mat/0603631 (2006).

[45] J. E. Simsarian, J. Denschlag, M. Edwards, C. W. Clark, L. Deng, E. W. Hagley, K. Helmerson, S. L. Rolston, and W. D. Phillips, Phys. Rev. Lett. **85**, 2040 (2000).

[46] A. Kastberg, W. D. Phillips, S. L. Rolston, and R. J. C. Spreeuw, Phys. Rev. Lett. **74**, 1542 (1995).

[47] W. Ketterle and N. J. van Druten, Phys. Rev. A **54**, 656 (1996).

[106] N. D. Mermin and H. Wagner, Phys. Rev. Lett. **17**, 1133 (1966).

[49] F. S. Cataliotti, S. Burger, C. Fort, P. Maddaloni, F. Minardi, A. Trombettoni, A. Smerzi, and M. Inguscio, Science **293**, 843 (2001).

[50] M. Greiner, O. Mandel, T. Esslinger, T.W. Hänsch, and I. Bloch, Nature **415**, 39 (2002).

[51] H. Moritz, T. Stöferle, M. Köhl, and T. Esslinger, Phys. Rev. Lett. **91**, 250402 (2003).

[52] T. Stöferle, H. Moritz, C. Schori, T. Esslinger, Phys. Rev. Lett. **92**, 130403 (2004).

[53] W. D. Phillips, J. H. Huckans, B. Laburthe Tolra, K. M. O'Hara, J. V. Porto, S. L. Rolston, and M. Anderlini, Laser Spectroscopy, Proc. of the XVI International Conference, World Scientific, 124 (2004).

[54] B. Laburthe Tolra, K. M. O'Hara, J. H. Huckans, W. D. Phillips, S. L. Rolston, J. V. Porto, Phys. Rev. Lett. **92**, 190401 (2004).

[55] T. Kinoshita, T. Wenger, D. S. Weiss, Science **305**, 1125 (2004).

[56] B. Paredes, A. Widera, V. Murg, O. Mandel, S. Fölling, I. Cirac, G. V. Shylapnikov, T. W. Hänsch, and I. Bloch, Nature **429**, 277 (2004).

[57] See, for example, N. W. Ashcroft and N. D. Mermin, *Solid State Physics* (Holt, Rinehart and Winston, 1976).

[58] See, for example, J. D. Jackson, *Classical Electrodynamics* (John Wiley & Sons, 1999).

[59] See, for example, L. Allen and J. H. Eberly, *Optical Resonance and Two-Level Atoms* (Wiley, 1975).

[60] See, for example, C. Cohen-Tannoudji, B. Diu, F. Laloe, *Quantum Mechanics* (Wiley-Interscience 1977).

[61] See, for example, C. Cohen-Tannoudji, J. Dupont-Roc, G. Grynberg, *Atom-Photon Interactions: Basic Processes and Applications* (John Wiley & Sons 1992).

[62] A. F. Bernhardt, B. W. Shore, Phys. Rev. A. **23**, 1290 (1981).

[63] C. Keller, J. Schmiedmayer, A. Zeilinger, T. Nonn, S. Durr, G. Rempe, Appl. Phys. B **69**, 303 (1999).

[64] S. Altshuler, L. M. Frantz, R. Braunstein, Phys. Rev. Lett. **17**, 231 (1966).

[65] T. Pfau, Ch. Kurtsiefer, C. S. Adams, M. Sigel, and J. Mlynek, Phys. Rev. Lett. **71**, 3427 (1993).

[66] D. Jaksch *et. al.*, Phys. Rev. Lett. **82**, 1975 (1999).

[67] G. K. Brennen, C. M. Caves, P. S. Jessen, and I. H. Deutsch, Phys. Rev. Lett. **82**, 1060 (1999).

[68] D. Jaksch *et. al.*, Phys. Rev. Lett. **85**, 2208 (2000).

[69] Y. B. Ovchinnikov, J. H. Muller, M. R. Doery, E. J. D. Vredenbregt, K. Helmerson, S. L. Rolston, W. D. Phillips, Phys. Rev. Lett. **83**, 284 (1999).

[70] M .Lucas and P. Biquard, J. Phys. Radium **3**, 464 (1932).

[71] O. Nomoto, Bull. Kobayasi Inst. Phys. Res. **1**, 42 (1951).

[72] O. Nomoto, Bull. Kobayasi Inst. Phys. Res. **1**, 189 (1951).

[73] U. Janicke and M. Wilkens, Phys. Rev. A **50**, 3265 (1994).

[74] C. V. Raman and N. S. N. Nath, Proc. Indian Acad. Sci. A **2**, 406 (1935).

[75] C. V. Raman and N. S. N. Nath, Proc. Indian Acad. Sci. A **2**, 413 (1935).

[76] C. V. Raman and N. S. N. Nath, Proc. Indian Acad. Sci. A **3**, 75 (1936).

[77] C. V. Raman and N. S. N. Nath, Proc. Indian Acad. Sci. A **3**, 119 (1936).

[78] Simply stated, ignoring the kinetic energy term in the Hamiltonian constitutes the Raman-Nath approximation. This implicitly means that the density of atoms is unchanged during the diffraction on the length scale of the lattice. This can be interpreted physically in two ways. In the first way, no substantial population of atoms moves a distance of order d. Alternately, applying our classical intuition, an atom will have time to oscillate less than one-quarter period in a nearly harmonic potential.

[79] M. V. Berry and D. H. J. O'Dell, J. Phys. A: Math. Gen. **32**, 3571 (1999).

[80] M. V. Berry and N. L. Balazs, J. Phys. A: Math. Gen. **12**, 625 (1979).

[81] M. V. Berry and C. Upstill, Prog. Optics **18**, 258 (1980).

[82] M. V. Berry, *The Diffraction of Light by Ultrasound* (Academic Press, 1966).

[83] I wish to thank M. V. Berry for graciously permitting use of the images in Figure 7.7.

[84] V. I. Arnol'd *Catastrophe Theory* (Springer-Verlag, 1984).

[85] V. I. Arnol'd, Uspekhi Mat. Nauk **30**, 3 (1975).

[86] R. Thom, *Structural Stability and Morphogenesis* (Benjamin Inc., 1975).

[87] T. Pearcey, Phil. Mag. **37**, 311 (1946).

[88] The NIST *Digital Library of Mathematical Functions* (http://dlmf.nist.gov/) which is scheduled for completion this year (to be published on-line) will have a chapter devoted to these special functions.

[89] H. Trinkaus and F. Drepper, J. Phys. A **10**, L11 (1977).

[90] P. E. Moskowitz, P. L. Gould, S. R. Atlas, D. E. Pritchard, Phys. Rev. Lett. **51**, 370 (1983).

[91] S. Kunze, S. Durr, K. Dieckmann, M. Elbs, U. Ernst, A. Hardell, S. Wolf, G. Rempe, J. Modern Opt. **44**, 1863 (1997).

[92] P. L. Gould, G. A. Ruff, D. E. Pritchard, Phys. Rev. Lett. **56**, 827 (1986).

[93] See, for example, E. Hecht, *Optics* (Addison Wesley Longman, 1998).

[94] D. M. Giltner, R. W. McGowan, S. A. Lee, Phys. Rev. Lett. **75**, 2638 (1995).

[95] M. Kozuma, L. Deng, E. W. Hagley, J. Wen, R. Lutwak, K. Helmerson, S. L. Rolston, W. D. Phillips, Phys. Rev. Lett. **82**, 871 (1999).

[96] G. Timp, R. E. Behringer, D. M. Tennant, J. E. Cunningham, M. Prentiss, K. K. Berggren, Phys. Rev. Lett. **69**, 1636 (1992).

[97] J. J. McClelland, R. E. Scholten, E. C. Palm, R. J. Celotta, Science **262**, 877 (1993).

[98] M. E. Gehm, K. M. O'Hara, T. A. Savard, and J. E. Thomas, Phys. Rev. A **58** 3914 (1998).

[99] GSI Lumonics Product Number VM500 Optical Scanner. Citing of this product in no way represents an endorsement.

[100] OSLO Light Edition 6.1. Citing of this product in no way represents an endorsement.

[101] Melles Griot Product Number 06 LAI 009 Diode Laser Doublet, F 80 ∅ 25. Citing of this product in no way represents an endorsement.

[102] See, for example, L. I. Schiff, *Quantum Mechanics* (McGraw-Hill, 1968).

[103] P. S. Julienne, C. J. Williams, Y. B. Band, Marek Trippenbach (2004), cond-mat/0412639.

[104] S. Peil, J. V. Porto, B. Laburthe Tolra, J. M. Obrecht, B. E. King, M. Subbotin, S. L. Rolston and W. D. Phillips, Phys. Rev. A, **67**, 051603(R) (2003).

[105] D. S. Petrov, M. Holzmann, and G. V. Shlyapnikov, Phys. Rev. Lett. **84**, 2551 (2000).

[106] N. D. Mermin and H. Wagner, Phys. Rev. Lett. **17**, 1133 (1966).

[107] P.C. Hohenberg. Phys. Rev. **158**, 383 (1967).

[108] D. J. Bishop and J. D. Reppy, Phys. Rev. Lett. **40**, 1727 (1978).

[109] G. Agnolet, D. F. McQueeney, and J. D. Reppy, Phys. Rev. B **39**, 8934 (1989).

[110] A. I. Safonov, S. A. Vasiliev, I. S. Yasnikov, I. I. Lakashevich, and S. Jaakkola, Phys. Rev. Lett. **81**, 4545 (1998).

[111] J. E. Lorenzo et. al., Europhys. Lett. **45**, 45 (1999).

[112] S. Fassbender, M. Enderle, K. Knorr, J. D. Noh, and H. Rieger, Phys. Rev. B **65**, 165411-1 (2002).

[113] M. A. Krzyzowski et. al., Phys. Rev. B **50**, 18505 (1994).

[114] Gorlitz et. al., Phys. Rev. Lett. **87**, 130402 (2001).

[115] V. Schweikhard, I. Coddington, P. Engels, V. P. Mogendorff, and E. A. Cornell, Phys. Rev. Lett **92**, 040404 (2004).

[116] D. Rychtarik, B. Engeser, H. -C. Nagerl, and R. Grimm, Phys. Rev. Lett. **92**, 173003 (2004).

[117] N. L. Smith, W. H. Heathcote, G. HechenBlaikner, E. Nugent, and C. J. Foot, J. Phys. B **38**, 223 (2005).

[118] C. Orzel, A. K. Tuchman, M. L. Fenselau, M. Yasuda, and M. A. Kasevich, Science **291**, 2386 (2001).

[119] S. Burger et. al., Europhys. Lett. **57**, 1 (2006).

[120] Z. Hadzibabic, S. Stock, B. Battelier, V. Bretin, and J. Dalibard, Phys. Rev. Lett. **93**, 180403 (2004).

[121] M. Kohl, H. Moritz, T. Stoferle, C. Schori, and T. Esslinger, J. Low Temp. Phys. **138**, 635 (2005).

[122] I. B. Spielman, P. R. Johnson, J. H. Huckans, C. D. Fertig, S. L. Rolston, W. D. Phillips, and J. V. Porto, Phys. Rev. A **73**, 020702(R) (2006).

[123] I. B. Spielman, W. D. Phillips, and J. V. Porto, arxiv:cond-mat/0606216 (2006).

[124] S. Stock, Z. Hadzibabic, B. Battelier, M. Cheneau, and J. Dalibard, Phys. Rev. Lett. **95**, 190403 (2005).

[125] Y. B. Band and Marek Trippenbach, Phys. Rev. A **65**, 053602 (2002).

[126] Z. Hadzibabic, P. Kruger, M. Cheneau, B. Battelier, and J. Dalibard, Nature **441**, 1118 (2006).

[127] J. P. Fernandez and W. J. Mullin, J. Low Temp. Phys. **128**, 233 (2002).

[128] J. O. Andersen, U. Al Khawaja, and H. T. C. Stoof, Phys. Rev. Lett. **88**, 070407 (2002).

[129] D. S. Petrov, D. M. Gangardt, and G. V. Shlyapnikov, J. Physique IV France **116**, 5 (2004).

[130] T. P. Simula, M. D. Lee, and D. A. Hutchinson, Phil. Mag. Lett. **85**, 395 (2005).

[131] M. Holzmann, G. Baym, J. -P. Blaizot, and F. Laloe, Preprint cond-mat/0508131 at ¡http.arxiv.org¿ (2005).

[132] T. P. Simula, P. B. Blakie, Phys. Rev. Lett. **96**, 020404 (2006).

[133] S. T. Bramwell and P. C. W. Holdsworth, Phys. Rev. B **49**, 8811 (1994).

[134] D. Hellweg, L. Cacciapuotti, M. Kottke, T. Schulte, K. Sengstock, W. Ertmer, J. J. Arlt, Phys. Rev. Lett. **91**, 010406 (2003).

[135] A. Polkovnikov, E. Altman, E. Demler, Proc. Natl. Acad. Sci. USA **103**, 6125 (2006).

[136] R. Kenna, Preprint cond-mat/0512356 at ¡http.arxiv.org¿ (2005).

[137] S. Ashhab, Phys. Rev. A **71**, 063602 (2005).

[138] G. Cennini, C. Geckeler, G. Ritt, and M. Weitz, Phys. Rev. A **72**, 051601(R) (2005).

[139] W. H. Wing, Prog. Quantum Electronics **8**, 181 (1984).

[140] C. Zener, Proc. Royal Soc. of London Series A, 137, 696 (1932).

[141] J. R. Rubbmark, M. M. Kash, M. G. Littman, and D. Kleppner, Phys. Rev. A **23**, 3107 (1981).

[142] D. E. Pritchard, Phys. Rev. Lett. **51**, 1336 (1983).

[143] D. B. Montgomery and J. Terrell, *Some Useful Information for the Design of Air-Core Solenoids*, Air Force Contract AF19(604)-7344 (1961).

[144] K. Dieckmann, Doctoral Thesis, Van der Waals - Zeeman Institute, Faculty of Science, University of Amsterdam (2001).

[145] J. A. Giordmaine and T. C. Wang, J. Appl. Phys. **31**, 463 (1960).

[146] U. Schünemann, H. Engler, R. Grimm, M. Weidemüller, and M. Zielonkowski, Rev. Sci. Inst. **70**, 242 (1999).

[147] M. Krämer, C. Menotti, L. Pitaevskii, and S. Stringari, Eur. Phys. J. D. **27**, 247 (2003).

[148] M. Greiner, Doctoral Thesis, Physics Department, Ludwig-Maximilians-Universität-München (2003).

[149] This lattice was part of the 2D double well lattice described in this reference. Its lattice constant was known to better than 0.01 based on a deviation from beam orthognality less than 7 mrad. J. Sebby-Strabley, M. Anderlini, P. S. Jessen, and J. V. Porto, Phys. Rev. A **73**, 033605 (2006).

[150] J. Gea-Banacloche, A. M. Rey, G. Pupillo, C. J. Williams, C. W. Clark, Phys. Rev. A **73**, 013605 (2006).

[151] A. M. Rey, G. Pupillo, C. W. Clark, C. J. Williams, Phys. Rev. A **72**, 033616 (2005).

[152] G. Pupillo. A. M. Rey, C. J. Williams, C. W. Clark, New. J. Phys. **8**, 161 (2006).

[153] M. Rigol, V. Rousseau, R. T. Scalettar, and R. R. P. Singh, Phys. Rev. Lett. **95**, 110402 (2005).

[154] J. Ruostekoski and L. Isella, Phys. Rev. Lett. **95**, 110403 (2005).

[155] A. Polkovnikov, E. Altman, E. Demler, B. Halperin, M. D. Lukin, Phys. Rev. A **71**, 063613 (2005).

[156] H. P. Büchler, G. Blatter, W. Zwerger, Phys. Rev. Lett. **90**, 130401 (2003).

[157] R. B. Diener, G. A. Georgakis, J. Zhong, M. Raizen, Q. Niu, Phys. Rev. A **64**, 033416 (2001).

[158] K. M. O'Hara (private communication).